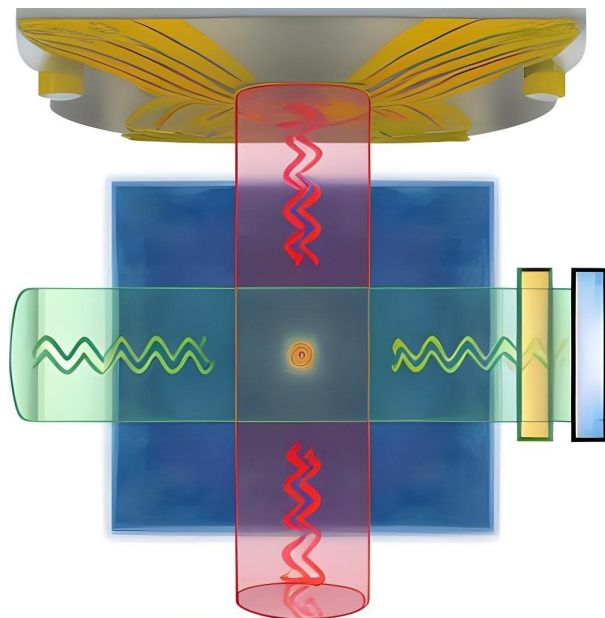

ATOM INTERFEROMETRY WITH ULTRACOLD ATOMS FOR INERTIAL SENSING



Artistic interpretation of the coherent manipulation of an ultracold atomic cloud by two retro-reflected light fields

PhD thesis by Matthias Gersemann

ATOM INTERFEROMETRY WITH ULTRACOLD ATOMS
FOR INERTIAL SENSING

Von der QUEST-Leibniz-Forschungsschule der
Gottfried Wilhelm Leibniz Universität Hannover
zur Erlangung des Grades

Doktor der Naturwissenschaften
- Dr. rer. nat. -
genehmigte Dissertation von

M.Sc. Matthias Gersemann

Referent:

Prof. Dr. Ernst M. Rasel
Institut für Quantenoptik
Leibniz Universität Hannover

Korreferent:

Prof. Dr. Enno Giese
Institut für Angewandte Physik, Theoretische Quantenoptik
Technische Universität Darmstadt

Korreferent:

Dr. habil. Sven Herrmann
ZARM - Zentrum für angewandte Raumfahrttechnologie und Mikrogravitation
Universität Bremen

Vorsitzender der Prüfungskommission:

Prof. Dr. Michael Kues
HOT – Hannoversches Zentrum für Optische Technologien
Leibniz Universität Hannover

Tag der Disputation: 12.10.2023

Abstract: Atom interferometry with ultracold atoms for inertial sensing

In light pulse atom interferometry wave packets are spatially separated and recombined in a coherent manner by interacting with laser pulses. Typically, two photon transitions are used to perform Rabi oscillations between two internal or/and external states to construct atom-optical elements, like beam splitters or mirrors. The phase difference accumulated between two atomic trajectories can be used to measure quantities such as accelerations or rotations. The velocity distribution and size of the employed atomic sources can significantly limit the efficiency of the atom-light interactions and thus the performance of the interferometer. To overcome this limitation, ensembles with momentum distributions far below the recoil of a photon are used, such as collimated Bose-Einstein condensates (BEC).

Exploiting the properties of a BEC opens up a wide range of possibilities for new techniques and concepts, especially for increasing the sensitivity of measurements performed in small volumes. This work presents some of these novelties. The technique of an innovative (re-)launch mechanism helps to effectively increase the available interferometry time in compact gravimeter setups. A symmetric large momentum transfer in the form of a twin-lattice enables the enclosure of large space-time areas suitable for rotation measurements with high sensitivities. The exploitation of a BEC in combination with momentum transfer by double Bragg diffraction contributed to the development of a new concept. Using a single BEC, it is possible to create two simultaneous interferometers, which are employed to differentiate between rotations and accelerations. Its symmetry allows this geometry to be extended to form the basis of a six-axis quantum inertial measurement unit. Last but not least, the (re-)launch in combination with the symmetric splitting also provides the basis for a multi-loop atom interferometer. With this concept, an area can be enclosed that offers unique scalability for rotational sensors.

Each atom interferometer is affected by the quality of its interrogating light fields. Therefore specific detrimental effects are pointed out in this work and possible mitigation strategies are presented subsequently. One way to reduce the susceptibility of light beams to distortions at apertures is to change their profile from the commonly used Gaussian profile to a more locally limited intensity distribution. For this purpose, the application of flat-top beam profiles is investigated. This brings the added benefit of a uniform power distribution, which helps to increase the beam area in which the ensemble of atoms can be manipulated with the same properties. Imperfections can also lead to position-dependent dipole forces that have a parasitic effect on the output of an interferometer. Especially for large momentum transfer techniques this has proven to be a limitation which can necessitate a compensation mechanism. To this end, a laser system is constructed that achieves the required high laser powers and includes additional frequency components.

Many of the interferometry methods and concepts introduced are well suited for compact or transportable systems. For this purpose, a laser system based on telecommunication fiber components is presented, which represents an all-in-one solution for the generation, preparation and subsequent beam splitting of ultracold atoms. Inspired by all of the above, the future vision of a quantum sensor for inertial navigation applications is discussed.

Key words: Atom interferometry, Bose-Einstein condensates, inertial sensing

Contents

1 Introduction	1
2 A brief introduction to atom interferometry with ultracold atoms	7
2.1 Bose-Einstein condensates	7
2.1.1 Atom-chip based generation	9
2.1.2 State preparation of atomic ensembles	11
2.2 The Mach-Zehnder-type atom interferometer	13
2.2.1 Stimulated Bragg transitions	15
2.2.2 Double Bragg diffraction	17
2.2.3 Stimulated Raman transitions	18
2.2.4 Double Raman diffraction	19
2.3 Sensitivity function formalism	21
3 Advanced atom interferometry methods for inertial sensing	28
3.1 Atom-chip fountain gravimeter	29
3.2 Twin-lattice atom interferometry	32
3.2.1 Proof of principle performance	34
3.2.2 Contrast reduction analysis	39
3.3 Differential interferometry using a Bose-Einstein condensate	41
3.3.1 Multi-axis operation	44
3.3.2 Proof of principle performance	48
3.3.3 Sensitivity limit estimation	52
3.4 Multi-loop atomic Sagnac interferometry	54
3.5 Similarities and unique features of the methods and concepts	58
4 Tackling detrimental effects in the atom-light interaction	60
4.1 Flat-top beams for the coherent manipulation of atoms	61
4.1.1 Flat-top beam shaping optics	64
4.1.2 Flat-top intensity profile	66
4.1.3 Influence of the intensity profile	67
4.1.4 Influence of the phase profile	71
4.1.5 Comparison with a Gaussian light field	76
4.2 High power lattice laser system with active light shift compensation	81
4.2.1 Beam superposition	85
4.2.2 Alternative ways of generating light shift compensated lattice light fields	87

4.3 Compact fiber-based laser system for coherent manipulations	87
4.3.1 Non-inertial phase noise contributions	96
4.3.2 Implementation of double Raman diffraction	97
4.3.3 Performance summary	102
5 Summary	103
6 Outlook	106
6.1 Hybrid inertial navigation	106
6.2 Experimental platform of a gyro-stabilized quantum navigation sensor	109
Bibliography	113
Appendix	133
Abbreviations and acronyms	134
Open Access	135
Publications	136
Curriculum Vitae	138

CHAPTER 1

Introduction

In his doctoral thesis defended in 1924, Louis Victor Pierre Raymond, 7th Duc de Broglie (1892-1987) developed the idea that *for matter as well as for radiation, especially for light, it is required to introduce the corpuscle and the wave concept simultaneously* [Bro24]. He formulated the hypothesis that also particles can be assigned a wavelength which depends on its momentum p . For the associated wavelength λ named after him, he postulated the well-known formula $\lambda = h/p$, where h denotes Planck's constant. According to this definition, matter waves were defined analogous to light waves. The existence of this wave-like behavior was demonstrated for the first time in 1927 in the famous Davisson-Germer experiment by Clinton Joseph Davisson and Lester Halbert Germer in the form of experimental evidence of interference phenomena with electrons [Dav27]. Such experiments were crucial to the field of matter-wave interference, which is now at the center of quantum physics, but they also revealed two major challenges. First, due to the relatively high temperature of the most accessible particles, the typical de Broglie wavelengths λ are much smaller than a nanometer and thus several orders of magnitude smaller than those of visible light. This makes it difficult to observe the wave-like behavior of heavier particles. Second, particles are usually scattered or absorbed by solid matter, which complicates the realization of coherent manipulations as well.

One step in the direction of overcoming the first problem was based on the use of a thermal atomic beam that could be split, sent on two or more paths, and recombined to overlap and interfere in space and time using small mechanical transmission structures [Kei88; Kei91; Car91]. The second challenge was addressed with the development of laser cooling, trapping of neutral atoms, and exploiting the electric dipole interaction with near resonant light fields to diffract atoms on gratings called *optical lattices* rather than solid matter [Ash78; Phi85; Raa87]. This opened up new possibilities for the construction of atomic interferometers and laid the foundation for their use in measuring inertial forces with high accuracy and precision. As a first application in this direction, a gravimeter based on the interference of laser-cooled sodium atoms was demonstrated [Kas91]. The basis for atom interferometry is the generation of superposition states of massive particles, which can subsequently be made to interfere. A single particle follows two space-time trajectories during an interferometer sequence, which can be influenced by a variety of effects. All interactions that take place with the particle during this time affect the measured output phase difference at the end of the sequence. With appropriate evaluation, this phase measurement can make it possible to determine quantities like for example the acceleration due to gravity. This makes interferometry a useful technique

for investigating a wide range of possible applications, ranging from fundamental physics to inertial navigation.

Shortly after the appearance of de Broglie's work, another, no less amazing quantum effect was predicted by Albert Einstein in 1925 [Ein25]. Based on the work of Satyendra Nath Bose, it was possible to postulate an extreme aggregate state of a system of indistinguishable particles in which the vast majority of particles are in the same quantum mechanical state, today known as a Bose-Einstein condensate (BEC) [Bos24]. In contrast to the matter waves postulated by de Broglie, it was not until 70 years later that this state could be produced in a real experiment in an atomic gas. In 1995, this was achieved three times in different groups for small ultracold, dilute gas clouds of rubidium [And95], lithium [Bra95], and sodium [Dav95]. Bose-Einstein condensation can be explained using the wave-like behavior of particles described by de Broglie's wavelength definition. At thermal energies, gaseous atoms move at high velocities, and the wavelengths are tiny compared to all other relevant length scales. Therefore, quantum effects are usually negligible under these conditions. However, if the atomic velocity is reduced sufficiently and the motion of the atoms in a gas is greatly slowed down, the quantum wave nature begins to play a crucial role, since the matter waves of the individual atoms are no longer independent but begin to overlap. In simplified terms, the de Broglie wavelengths of the atoms become about as large as the average distance between the individual atoms.

Interference between two freely expanding Bose-Einstein condensates (BEC) was observed for the first time by their overlap [And97]. This experiment validated the notion of the BEC as a macroscopic matter wave source for atom interferometers providing benefits in the form of a slowly expanding wave function, large spatial coherence, and possibilities of using a larger number of coherent manipulation techniques. [Den00; Bir95; Bon03]. Thanks to the availability of exceptional control over these ultracold ensembles, a wide range of techniques opened up: from strategies for preparing the initial example to the use of methods capable of transmitting large portions of photon momentum [Chu86; Ben96; Amm97; Chi11; McD14].

While BECs can overcome many problems that limit the performance of interferometers operated with ensembles of higher effective temperatures there are still challenges remaining. These can be due to the properties of the atomic source itself, the applied light fields, or the measurement environment. For example, any force that accelerates, expands, or shifts the ultracold atomic ensemble places a constraint on the interferometer [Szi12; Dic13].

For that matter the extent and homogeneity of the interrogating light fields themselves play an important role. The atom-light interaction in such an optical potential that contains two counter-propagating frequency components can typically only transfer momentum along its propagation. Simplified, one can assume now two cases: The atomic ensemble has a forward velocity parallel or perpendicular to this momentum transfer. Figure 1.2 illustrates this concept, showing on the left side an ensemble moving along the direction of the light fields (black arrow), which then transfers momentum in the same or opposite direction (red arrows).

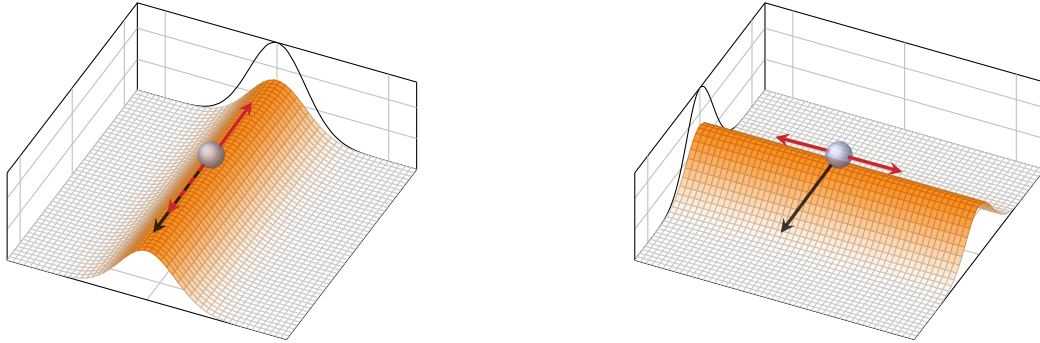


Figure 1.1: Idealized interrogation of an atomic ensemble within an optical potential consisting of the collimated propagation of a normal distribution and containing two counter-propagating frequency components. **Left:** The atomic ensemble moves along the direction of the propagated potential (black arrow) while in turn momentum is transferred in the same or exactly opposite direction (red arrow) **Right:** The ensemble moves perpendicular to the propagating potential (black arrow) and the momentum is therefore also transmitted perpendicular to it (red arrows).

On the right side, where the ensemble moves instead perpendicular to the light field (black arrow), momentum is therefore transferred perpendicular to this direction (red arrows). A conceptual difference is that the direction of momentum transfer is not selective, but occurs simultaneously on both sides, since there is no preferred direction as in the parallel motion of atoms along the propagated potential. This distinction illustrates in a simple way how different center-of-mass motions can have an effect on the interferometer relying on this interaction. An optical manipulation of the atoms is only possible as long as they are at a position with sufficient optical power. Therefore, the normal distribution shown here as an example with an intensity decreasing towards the edge provides only a suboptimal choice with that respect.

The conceptual model can also be extended to multidimensional manipulations. The most simple route is to combine two light fields with different propagation directions, as shown schematically in figure 1.2. In this way, the optical potentials can be used either sequentially, for example separated in time, or simultaneously for momentum transfer. If the ensemble is interrogated multiple times at different positions within the optical potential, a more uniformly distributed intensity can be desirable. An idealized example is shown in figure 1.2 on the right, where two so-called flat-top intensity distributions illustrate the concept of creating a region of constant intensity. Such a configuration can be advantageous because it greatly simplifies intensity-dependent optical manipulations while providing sharper intensity gradients at the edges. [Mie18].

Apart from the overall determining shape of the intensity and phase distribution, perturbations of the light field also have a great influence on the atom-light interaction. The (relative) phase of the light field is an especially important factor and wavefront aberrations are one of the largest uncertainty factors in today's atom interferometers [Lou11; Sch15; Bad18; Böh22].

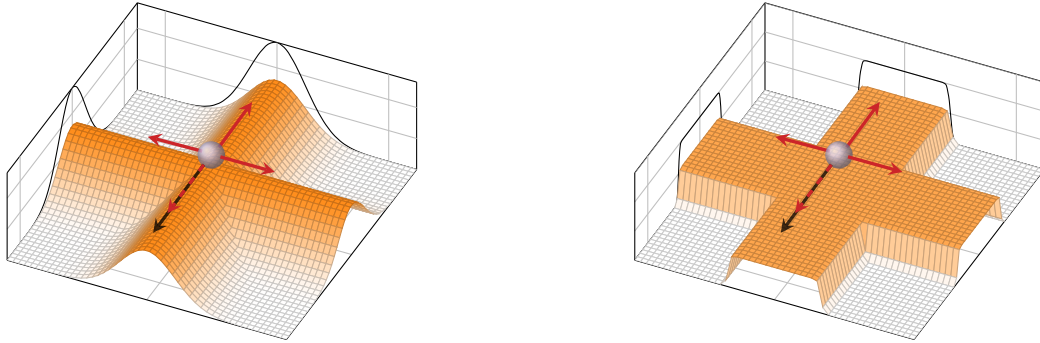


Figure 1.2: Idealized interrogation of an atomic ensemble in a crossed optical potential consisting of the collimated propagation of two different intensity distributions, each direction containing two oppositely propagating frequency components. **Left:** In a simple approach momentum can be imparted individually to the atomic ensemble in four different directions. Either along or against the direction of motion or perpendicular to it. **Right:** When the two gaussian shaped optical potentials are replaced by flat-top distributions a region of more constant intensity is created. Such a configuration provides advantages for intensity-dependent optical manipulations while providing sharper intensity gradients at the edges.

Another important aspect affecting performance are parasitic influences caused by less than ideal measurement environments. In the past, many approaches have been taken to overcome limitations like common-mode vibration noise or systematic effects in order to increase the precision and/or accuracy of the performed measurements. Differential or gradiometric concepts have emerged that rely on the formation of pairs of atomic ensembles, preferably from a single source than from separate sources. This has been prominently implemented at large baselines [Ove22]. However, in combination with ultracold atoms, there are also many advantages in more compact setups, especially for controlled initial splitting with subsequent manipulations [Per19; Mül08a; Bar19].

A large number of today's applications of atom interferometers are based on the measurement of accelerations and/or rotations derived from the detected phase difference. All of them have in common that their sensitivity scales with the time used for the interferometer, the transferred photonic momentum and, in the case of rotations, with the enclosed area by the interferometer trajectories. With the right choice of parameters, they have gained the ability to detect small changes in inertial quantities, which has led to the development of numerous applications such as the measurement of geophysical effects [Pet01; Mén18; Sav18; Sto11; Ber15], navigation [Hog07; Che18], or even a proposed measurement of gravitational waves [Dim09; Lor19a].

Following on from all these developments and discoveries, the results presented in this thesis are intended to further advance atom interferometry with BECs. First, its basic concepts, including prerequisites and employed techniques, are discussed in **chapter 2**. Based on these principles, four different publications are presented in **chapter 3** which can be subdivided into two methods and two schemes. The first of those methods is the realization of a compact

fountain gravimeter that utilizes an innovative launch mechanism based on Bloch oscillations and double Bragg diffraction to effectively increase the available interferometry time [Abe16]. The second method provides a symmetric large momentum transfer by a twin lattice enclosing large space-time areas suitable for rotation measurements with high sensitivities [Geb21]. Both methods employ beam-splitting light fields in a single direction only, either, along the direction of gravitational acceleration or perpendicular to it. The use of an initial double diffraction pulse in this horizontal direction followed by three successive pulses in the vertical direction allows the construction of two simultaneous interferometers. Within such a geometry, it is then possible to distinguish between rotational and acceleration components based on their combined initial phases [Ger20]. Due to the symmetry of this scheme it can be extended to a six-axis quantum inertial measurement unit. The combination of the method of the above-mentioned (re-)launch with the symmetric splitting enables still another scheme. This has led to the concept of a multi-loop atom interferometer with scalable area [Sch21]. Here, the atoms are again coherently manipulated by two perpendicular aligned optical lattices, with a vertical light field serving only for relaunch, while a horizontal field realizes splitting, redirection and recombination.

The above concepts and schemes are generally influenced by the quality of the laser light field used for the atom-optical manipulations. Therefore, performance limitations based on the detrimental effects are pointed out and possible mitigation strategies are presented subsequently in **chapter 4**. In an effort to generate a laser beam with a uniform intensity and phase distribution, a flat-top beam shaping optic is presented and characterized. It follows the idea that such a beam shape offers many advantages for atom interferometry, such as less susceptibility to distortion at apertures than the commonly used Gaussian beams and a uniform power distribution, which is useful when the atomic ensemble is interrogated at different positions within the beam. Despite all efforts to improve the beam quality, a realistic optical potential will still show small disturbances. When using high intensity laser beams, which are often required for large momentum transfer techniques within optical lattices, those imperfections can lead to position-dependent dipole forces that parasitically affect the output of an interferometer. The remainder of this chapter presents a high-power laser system that incorporates a compensation mechanism for this effect. Since the laser sources are one of the most important and complex components for atom interferometry, many efforts are also being made to simplify and miniaturize these systems. Thanks to an intensive and decade-long development in the field of optical fiber components for telecommunication, all optical manipulation and preparation techniques described in the beginning for the atomic species of rubidium can be realized with the help of these components. In the last section of this chapter, a laser system inspired by this concept is presented, that allows to generate ultracold atoms, combine different beam splitting methods, and detect the output phase of the interferometer as an all-in-one solution.

In **chapter 5**, the findings and results of this thesis are summarized. Furthermore, it describes the respective advantages of the presented techniques in the context of compact application possibilities and provides an estimation of the individually achievable sensitivities from the point of view of the current state of the art.

The final **chapter 6** highlights a potential application based on the differential BEC interferometer, in the form of multi-axis inertial sensing. The goal here is the technological development of a compact, hybrid six-axis quantum inertial measurement unit. It plans to utilize both a compact fiber-based laser system based on the concept presented in this thesis and flat-top-shaped interrogation beams.

CHAPTER 2

A brief introduction to atom interferometry with ultracold atoms

This chapter first introduces the concept of Bose-Einstein condensation, explains how to create such ensembles experimentally and prepare them as a suitable matter wave source for interferometry. This is followed by explanations of coherent atom-light interactions in terms of Raman and Bragg diffraction and their application in a Mach-Zehnder like atom interferometer. The two aforementioned techniques have differences and similarities, for example, Bragg diffraction has a relatively strong velocity selectivity of the process due to the rather low energy splitting of the involved momentum states. Therefore, it is particularly dependent on the low velocity dispersion of ultracold ensembles for the achievable manipulation fidelity. In addition, Bragg pulses leave the atoms in the same electronic state, which can make the interferometer phase more insensitive to influences acting in this regard. Raman pulses, on the other hand, are suitable for much broader thermal distributions and leave the atoms in a superposition of different electronic states. This can have advantages at the expense of noise resistance, such as going in favor of easier and faster readout or sensitivity towards state dependent effects.

2.1 Bose-Einstein condensates

Historically cold atom interferometers have been mostly operated with thermal sources at a temperature equivalent on the order of $1\ \mu\text{K}$ or less. While such sources allow high atomic flux, they typically have a large momentum width. In recent years many interferometric applications have shown the need for lower momentum widths to reach high fidelities for beamsplitting operations. A simple approach to achieve this goal was to velocity select the source cloud, which resulted in a smaller momentum width but reduced the atomic flux [Mül08a; Pet01]. A different approach is to create a source with a lower momentum width from the start, for example a Bose-Einstein condensates (BEC) at the cost of lower cycle rates [Hug07]. This has historically led to more complexity due to the additional number of steps required.

A complete theoretical description of BECs will be owed in this section. It should therefore only be mentioned that reference [Pes95] provides a good introduction using quantum field theory. For use as a source for atom interferometry, it is often sufficient to approximate the correlations between the particles by the mean-field theory and to neglect fluctuations of the bosonic field [Mey01]. BECs show potential especially when the state of the art for precision measurements is challenged. Particularly in combination with long interrogation times and/or large momentum transfer [Hen21]. It represents an extreme state of matter, where a large

fraction of bosons occupy the lowest quantum state. In the wave-duality picture single particles can be described by the so-called *thermal de Broglie wavelength* with

$$\lambda_T = \sqrt{\frac{2\pi\hbar^2}{mk_B T}}, \quad (2.1)$$

where m defines the mass of the particle, \hbar the reduced Planck constant and k_B the Boltzmann constant. As the temperature T decreases, microscopic quantum mechanical phenomena, in particular wavefunction interference, become macroscopically visible. Bose-Einstein condensation occurs when the individual wave packets begin to spatially overlap and the total system can be described by one single wave function. To achieve this for a uniform three-dimensional Bose gas consisting of N non-interacting particles in a volume V with the particle density $n = N/V$, a critical temperature for the transition can be defined as follows [Pet08]

$$T_C = \left(\frac{n}{\zeta(3/2)} \right)^{2/3} \frac{2\pi\hbar^2}{mk_B}, \quad (2.2)$$

with the Riemann zeta function $\zeta(3/2) \approx 2.6124$. The transition to the BEC takes place below this critical temperature. To simplify the definition, the phase space density $\rho = n\lambda_T^3$ can be introduced as the number of particles contained within a volume equal to the cube of the thermal de Broglie wavelength. According to equation 2.2 the phase transition to a BEC now occurs at $\rho = \zeta(3/2)$. This helps to see that low temperatures and high particle densities are both necessary for condensation.

One advantage of using BECs as a source for atom interferometry is that the expansion rate of the freely evolving atomic cloud after its formation is significantly reduced, so that its size during the interferometry time does not become too large compared to its initial size. Sub-recoil velocities allow individual momentum-separated ports to be detected one at a time. The low expansion rate also offers the possibility for precise position control and helps to circumvent systematic effects such as wavefront distortions. If the initial rates are not sufficiently low, they can be further reduced by using collimation techniques, as explained in the next section 2.1.2. With these properties, coherent manipulations such as Bragg (for reference see subsection 2.2.1) or Raman (for reference see subsection 2.2.3) diffraction or Bloch oscillations [Ben96; Cla06; Mül09; Cla09; McD13] can be employed with high fidelity. An upper limit to the sensitivity of atom interferometers is found in the quantum projection noise or so-called standard quantum limit (SQL), which scales with $1/C$ defined by the contrast of the interferometer and $1/N$ defined by the number of atoms involved .

The atomic flux of BEC experiments is typically lower compared to velocity filtered or even thermal clouds. An often mentioned disadvantage herefore is the time-consuming evaporation process and the resulting higher loss of atoms. This triggered the development of faster [Rud15; Ven22] or even continuous [Che22] BEC generation. But to date, only a few measurements

with high sensitivity below the SQL [Gau09; Sor14; Jan22] have been performed. When atom numbers N cannot or should not be increased further, achieving sensitivities beyond this limit requires the preparation of entangled atomic ensembles. Surpassing the SQL with measurements based on internal degrees of freedom has been demonstrated for ultracold atomic ensembles [Ler10; Lou10; Hos16] and specifically also Bose-Einstein condensates [Gro10; Rie10; Lüc11]. To preserve the nonclassical correlations during interferometry, high efficiency of the coherent manipulations is required, which can be made possible thanks to the coherence properties of a BEC. Instead of entangling internal states, it was recently shown that the preparation of momentum-entangled sources can also be achieved by transferring entangled twin-Fock states in the spin degree of freedom of a BEC into the momentum space of momentum-entangled atoms [And21]. However, the control or suppression of noise sources above the SQL is not trivial and often already requires special care [Yve03].

2.1.1 Atom-chip based generation

To generate a cloud of cold atoms and further evaporate them until condensation a dedicated setup is needed. Since the first generation of a BEC in 1995, most experiments have shared the need to generate trapping potentials that use magnetic and optical fields. Additionally the atoms are placed under high-vacuum (HV) or ultra-high vacuum (UHV) conditions, to reduce collisions with background particles. Therefore, preparation and manipulation often takes place in actively pumped chambers using Non-Evaporable Getter pumps (NEG) and/or Ion Getter Pumps (IGP). A solution to generate most of the relevant magnetic field gradients and curvatures with high trap frequencies up to the kHz regime are so-called atom chips. An example of a setup utilizing this technology is the device explained below, which was used to obtain the experimental results presented in this thesis. To generate a BEC of ^{87}Rb atoms in this setup, the following steps are performed: First of all the atoms are captured from a thermal background, generated by a rubidium dispenser, and slowed down in successive cooling stages, starting with Doppler cooling in a 3D magneto-optical trap. A process based on the polarization gradient cooling effect, often called optical molasses, helps to address atoms below the achievable effective Doppler temperature limit of $T_D = \hbar\gamma/(2k_B)$ with velocities comparable to a few multiples of the recoil velocity $v_r = \hbar k/m$. Here γ defines the natural linewidth of the used transition and k the wave number of the employed laser light field. After optically pumping the atoms to the Zeeman state with the highest possible magnetic moment, they are transferred into an Ioffe-Pritchard type magnetic potential, which contributes to the compression of the atomic cloud and to the increase of its density. Finally, various evaporative cooling stages remove the 'hottest' particles from the cloud, and subsequent re-thermalization by elastic collisions leads to an increased phase space density. At the end of this sequence, phase transition to a BEC is achieved, followed by an optional adiabatic decompression of the trap.

The entire device whose operation is described here is called QUANTUS-1. The name is derived from the project name *QUANT*engase *Unter Schwerelosigkeit*, which translates as *quantum gases under microgravity* and refers to a long-standing collaborative project between several

German universities funded by the German Aerospace Center (Deutsches Zentrum für Luft- und Raumfahrt). The total setup includes everything that is needed to generate ultracold atoms and perform matter-wave interferometry. Over time, it was used for various experiments, resulting in a considerable number of publications [Abe16; Geb21; Zoe10; Mün13; Ahl16; Kan21], to name some of them. Most of the assembled components are located inside a capsule that can be used for experiments under microgravity conditions in the drop tower at the Zentrum für angewandte Raumfahrttechnologie und Mikrogravitation (ZARM) located in Bremen. In the center of the capsule, surrounded by coils, is the ultra-high vacuum chamber containing an atom chip device. A depiction can be seen in figure 2.1. Together with macroscopic pairs of coils, the atom chip provides the magnetic fields necessary to trap and manipulate atoms by providing high-gradient magnetic potentials near its surface through microfabricated current-carrying wires. Typically the atoms are located several hundred micrometer from the chip's surface at this time. To cool the atoms to condensation, high densities are required, which in turn requires strong confinement. Such a configuration therefore allows very efficient evaporative cooling of the ensemble at comparably low currents.

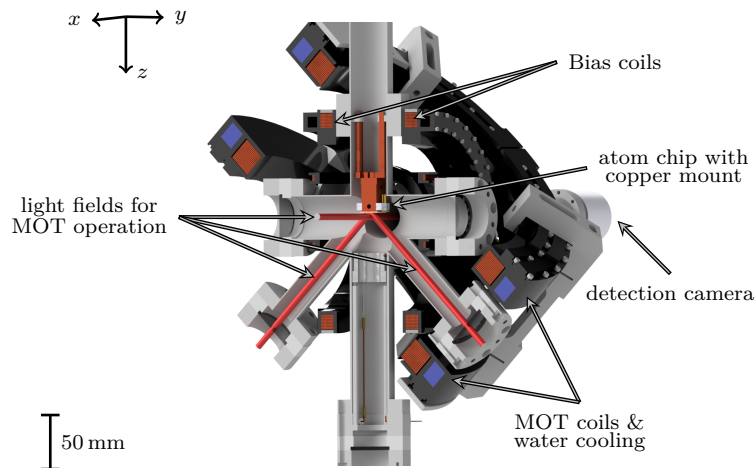


Figure 2.1: Section through the y-z plane of the vacuum chamber of the QUANTUS-1 experiment. It consists of a six-way cross made of non-magnetic steel extended by two tubes at a 45 degree angle and is surrounded by magnetic coils with an atom chip in the center. Optical access for cooling, trapping and manipulating the atoms is provided through viewports equipped with anti-reflection coated windows from seven directions and is only blocked from the top by the atom chip. The laser light beams for the operation of the MOT are depicted in red and components are labeled with arrows, while others are omitted for better visibility.

The atom chip itself is mounted on a copper structure that provides sufficient thermal management, and features various geometric wire structures that are used to control different magnetic potential shapes. As an additional feature its surface is coated with a reflective layer so that it can act as a mirror for an applied light field. There are a total of four pairs of coils on the chamber, three of them for providing homogeneous fields and one pair for generating a magnetic field gradient. The largest of them, the magneto-optical-trap (MOT) coil pair, is oriented in an

anti-Helmholtz configuration and generates a quadrupole field. Due to the applied current, the coils heat up during operation, so a water cooling circuit helps to control the temperature. The other three pairs are smaller and connected in Helmholtz configuration to provide homogeneous offset fields in all three directions. The largest pair of this set, labelled bias coils, is located inside the MOT coil pair as highlighted in figure 2.1. The remaining two pairs are smaller and closer to the center of the assembly.

The pressure in the vacuum chamber is maintained at a constant level below 1×10^{-11} mbar with the help of an ion getter pump and a non-evaporable getter material. The chamber consists of a six-way cross made of non-magnetic steel extended by two tubes at a 45-degree angle thus providing optical access through viewports. Four of them are used to direct the light fields for the operation of the MOT to a position just below the atom chip. The beams are shown in figure 2.1, with two of them aligned along the x -axis in the opposite direction and two at a 45 degree angle between the y - and z -axis. The propagation axis of the light field in the x -direction is shared with the detection light field and the first camera for absorption imaging. A second imaging axis is shared with the beams in the 45 degree direction and shown in more detail later in figure 4.2. The detection mechanism itself can be understood as a projection of the shadow of the atom cloud onto the camera sensor. By subtracting this image from an identically taken image without the presence of the atoms, corrected by a dark image, the two-dimensional atom density distribution can be reconstructed. The four cooling light fields, which decelerate the atoms in all three spatial directions, are operated in a mirror MOT configuration in which two of the beams reflect off the surface coating of the atom chip. There are three other optical access points used for the coherent manipulation operations required for interferometry. One of these is aligned along the y -axis and the other two along the z -axis, in the chosen coordinate system. To serve as a source for supplying a current controlled atomic vapor to the vacuum chamber, a rubidium dispenser is attached inside the bottom part of the chamber. Magnetic stray fields can adversely affect the preparation of the atoms, the interferometry or other coherent manipulation steps. Consequently the vacuum assembly is surrounded by a magnetic shield from a material with a very high relative permeability, which is used to significantly suppress influences of external magnetic fields. Only in some places holes remain for the electrical and fiber connections as well as for the vacuum tube in the upper part, which is connected to the vacuum pumps. The shielding consists of individual, overlapping components and can be removed individually to gain access to the chamber.

2.1.2 State preparation of atomic ensembles

The creation of an ensemble optimally prepared for atom interferometry begins with the release of the condensate from its final trap. Typically, remaining offset velocities or induced center of mass and size oscillations are unwanted effects. For example a non-zero velocity in the beam splitter direction can degrade the symmetry and fidelity of a following beam splitter operation. By tuning parameters such as the timing of the release and the trap fields used, these effects can be reduced. The release trap usually also determines the initial mean-field energy and thus the kinetic energy in the far-field of the ensemble expansion. If not sufficiently compensated,

atomic interactions can also lead to undesired phase shifts. After the release of the ensemble from its final magnetic trap subsequent state preparation helps to ensure optimal properties for atom interferometry. The techniques mentioned in the following help to reduce unwanted effects from residual magnetic fields and the expansion of the atomic cloud itself.

Adiabatic rapid passage

While the atoms are in a magnetically sensitive state for trapping and cooling, during interferometry this can be detrimental due to their susceptibility to possible parasitic magnetic fields. A robust and often used technique for coherent population transfer between quantum mechanical states, for example, Zeeman sublevels is the adiabatic rapid passage. This involves tuning the electromagnetic radiation above or below the resonant frequency of a particular transition and then sweeping it through the resonance [Cam84]. With this approach the atoms can be transferred into the non-magnetic m_F state. In practice, this transfer is realized in the QUANTUS-1 setup by sweeping a suitable radio frequency (RF), which is directly applied via a wire structure on the atom chip. The efficiency reaches more than 90%, resulting from losses at avoided crossings, and takes around 10 ms. Using the non-magnetic state removes the influence of magnetic fields to first order. Higher order contributions, like second-order Zeeman effects, are therefore still present and may not always be negligible.

Stern-Gerlach type deflection

The remaining atoms that are not transferred by the adiabatic rapid passage can still have detrimental effects for interferometry. Since they overlap spatially with the interfering states, they cannot be distinguished by an absorption detection system, which can lead to contrast loss or noise at the interferometer output. One solution is to apply an inhomogeneous magnetic field gradient that spatially separates all m_F sublevels of the hyperfine state, making them distinguishable by their density distributions. Thanks to the atom-chip design, such splitting can be conveniently realized by the large field gradients that can be generated. Since this technique makes use of the famous findings of Otto Stern and Walther Gerlach it is called Stern-Gerlach type deflection [Ger22].

Delta-kick collimation

The mean field energy from the atomic interactions of the condensate gets converted into kinetic energy until the expansion reaches a ballistic regime of only kinetic energy. Although low expansion rates of the atomic ensemble are desirable for atom interferometry, it is sometimes advantageous to start with a large expansion rate if a subsequent lensing mechanism is applied. This technique, called delta-kick collimation (DKC), reduces the atomic velocity by conversion of kinetic into potential energy. The expansion of the atoms is slowed down and ideally collimated by a position-dependent force. This can be generated by a harmonic potential applied after a certain expansion time, analogous to a lens in optics. In this way, the larger initial expansion for a short time leads to an adjustable cloud size tailored to a desired spatial extension with a resulting final small expansion. The concept is realized by applying a potential of either the initial magnetic trap or an optical field [Chu86; Amm97; Mün13; Mor99; Kov15a]. The expansion can be increased, decreased or ideally stopped by the choice of timing. A small

momentum width can lead not only to higher diffraction efficiency, but also to a smaller spatial extent, which reduces the systematic uncertainties associated with the size of the atomic cloud.

Feshbach resonances

The high density of an ultracold atomic ensemble above a certain atom number N can lead to unwanted atomic interactions and to the so-called mean-field shift, a non-linear bias shift in the interferometer. After sufficient time this potential energy converts to kinetic energy during free expansion and leads to a broadened velocity distribution. This can be mitigated by tuning the atomic interactions via magnetic fields to achieve Feshbach resonances [Fat08].

2.2 The Mach-Zehnder-type atom interferometer

Atom interferometry relies on the quantum superposition of different position and momentum states for the center-of-mass motion of single atoms or atomic ensembles. The foundation was laid by the so-called Ramsey experiment, in which an oscillating magnetic field was applied to a molecular beam for a certain time τ_p , turned off for a time T , and then applied again for a time τ_p [Ram50]. By choosing the proper frequency, time, and amplitude of the oscillating field, it was possible to create a superposition that could evolve at a different frequency than the electromagnetic field and accumulate a phase ϕ with respect to the driving electromagnetic radiation. The two interactions are called $\pi/2$ pulses because they represent a half transition probability to an excited state. The interaction that causes a complete transition is accordingly denoted π . In atom interferometry the roles of light and matter are reversed compared to traditional optical interferometers. Nowadays it is based on the interference of wave packets that are interrogated with individual laser pulses that act as beam splitters and mirrors. According to this principle it is possible to devise experiments that are suitable for high-precision measurements of fundamental constants such as the fine structure constant or inertial sensors like accelerometers and gyroscopes.

One common employed closed interferometer scheme is based on the Mach-Zehnder geometry. Here the incident wave packet is subsequently split, reflected, and recombined by interacting with three successive light pulses driving velocity-sensitive Bragg (see section 2.2.1) or Raman (see section 2.2.3) processes [Kas91]. The operating principle of the Mach-Zehnder-type like atom interferometer (MZI) is outlined in the figure 2.2. The incident cold or ultracold atomic wave packet is split onto two paths using an initial $\pi/2$ -pulse (I) that creates a superposition of two different momentum states $|p_0\rangle$ and $|p_1\rangle$. Those are reflected after a free propagation time T with a π -pulse (II), and superimposed after an additional time T with a second $\pi/2$ -pulse (III). The wave packets evolving along the two branches acquire a phase during the interferometry sequence which depends on their central position relative to the laser wavefronts when they are diffracted by the laser pulses. Each pulse is typically applied by two beams from opposite sides [Pet01]. At each process $j = \text{I, II or III}$, a phase ϕ_j is imprinted, giving rise to the so-called laser phase $\phi_L = \phi_I - 2\phi_{\text{II}} + \phi_{\text{III}}$ [Bor04]. In leading order, the total measured phase shift ϕ of the interferometer depends, apart from the laser phase ϕ_L , via two contributions ϕ_a and ϕ_r on the motion of the atoms with respect to a reference [Bon06].

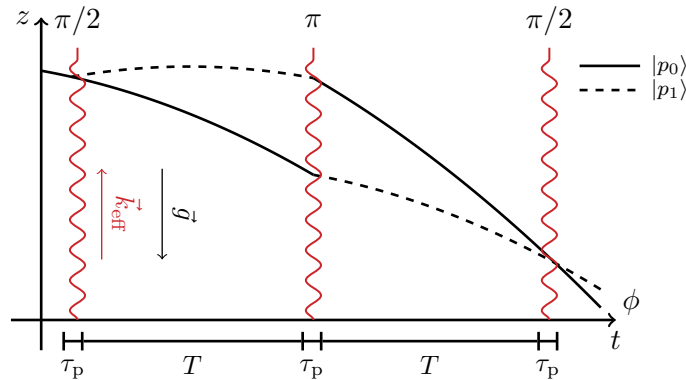


Figure 2.2: Space-time diagram of a Mach-Zehnder-type atom interferometer under the influence of the gravitational acceleration \vec{g} . The individual pulses are symbolized by wavy lines and the momentum states are represented by dashed, dotted and solid lines. The sequence is realised by three individual impulses symbolised by temporally separated wavy lines. It consists of a $\pi/2$ -pulse to split the atomic wave function, a π -pulse to mirror the imprinted momentum and a second $\pi/2$ -pulse to project the probability amplitudes onto classical populations. The trajectories of the individual interferometer states $|p_0\rangle$ and $|p_1\rangle$ are depicted by (dotted) lines.

The contribution ϕ_a can be identified with a shift due to accelerations, which is sensitive to forces in the direction of the beam splitters. The other shift ϕ_r , caused by rotations, depends on the enclosed areas of the interferometer trajectories. The response of the interferometer output also depends on other external (parasitic) influences that can lead to a change in phase $\delta\phi$. With the help of the sensitivity function formalism, explained in more detail in section 2.3, the influence of several noise contributions onto the interferometer can be calculated. Ideally, without the influence of external forces or noise contributions, the measured phase shift ϕ between the two arms is zero. Figure 2.2 shows a simplified space-time diagram of a Mach-Zehnder-type geometry under the influence of the gravitational acceleration along the z -axis, neglecting parasitic trajectories and assuming that the pulse interaction time τ is much smaller than the free propagation time T . In the example case shown here, two counter-propagating light fields (depicted in red) form an effective momentum transfer \vec{k}_{eff} , which is oriented opposite to the gravitational acceleration \vec{g} .

The measured phase shift due to this acceleration can be calculated as follows

$$\phi_a = \vec{k}_{\text{eff}} \vec{a} T^2. \quad (2.3)$$

As can be seen, the scaling of the interferometer phase shift depends on two adjustable parameters. First, linearly with the transferred momentum $n\vec{k}_{\text{eff}} \approx 2n\vec{k}$ and second, quadratically with the free evolution time T , which describes the time between each diffraction process. Here $k = 2\pi/\lambda$ denotes the wavenumber of a n -th order diffraction process, which describes the number of photon pairs of the process involved, driven by counter-propagating laser beams.

The approximation is explained in the next section 2.2.1. Summarized it can be said that the displacement of the wave packets is determined mainly by the amount of momentum transmitted during the sequence and its duration.

The second leading order phase contribution ϕ_r , linked to rotations $\vec{\Omega}$, only arises when the interferometer encloses an area due to a non-vanishing mean velocity \vec{v} of the atoms, not aligned with \vec{k}_{eff} . This can be understood as the atomic Sagnac effect [Rie91]. The phase shift in this case calculates as follows

$$\phi_r(\vec{v}) = 2\vec{k}_{\text{eff}} \cdot (\vec{\Omega} \times \vec{v})T^2. \quad (2.4)$$

While it scales with the transferred momentum \vec{k}_{eff} and the free evolution time T as before, it also depends on the velocity \vec{v} of the atomic ensemble.

2.2.1 Stimulated Bragg transitions

Atom interferometers typically utilize stimulated two-photon transitions that are able to split or recombine the atomic trajectories. Compared to light interferometers, these transitions act as the matter wave analogue to beam splitters and mirrors. The following explanations in the rest of this chapter refer to the ^{87}Rb isotope used in this work. For more details on the energy level splittings see the D_2 transition hyperfine structure shown in figure 4.20.

The so-called Bragg diffraction, originates in the scattering of electromagnetic waves from crystals [Bir95; Kun96] but can also be applied to matter waves [Koz99; Tor00]. It can couple two atomic momentum states ($|p_0\rangle$ and $|p_1\rangle$) via a third and intermediate state. This coupling is typically realized with the help of two laser frequencies ω_1 and ω_2 that fulfill the following resonance condition of

$$\Delta\omega = \omega_1 - \omega_2 = \omega_{k_{\text{eff}}}. \quad (2.5)$$

Here $\omega_{k_{\text{eff}}} = \frac{\hbar k_{\text{eff}}^2}{2m}$ denotes the recoil frequency of the atomic species. For the process itself an atom in state $|F = 2\rangle$ absorbs a photon at frequency ω_1 and is transferred via the intermediate state $|F' = 1\rangle$ back to $|F = 2\rangle$ by emitting a photon at frequency ω_2 in the opposite direction. The energy difference $\hbar\Delta\omega$ of the process is given by the the two light fields involved, which is maximized for counterpropagating laser beams, when both wave vectors point in opposite directions. This stimulated Bragg diffraction can also be represented by a transition between the two momentum states $|p_0\rangle$ and $|p_1\rangle$, which equals a transfer of $2\hbar k$ on the energy-momentum parabola (see figure 2.3 on the left). Typically a global detuning Δ is introduced that is large compared to the effective coupling, given by the effective Rabi frequency [Mül08a; Mül08b]. This allows the population of the intermediate state to be largely neglected and spontaneous emission to be reduced.

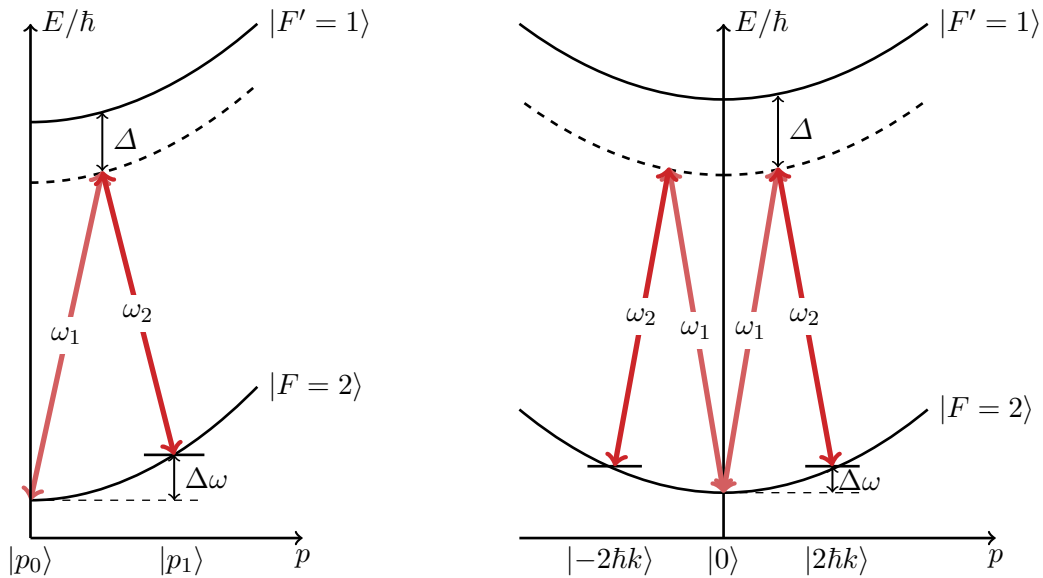


Figure 2.3: Energy-momentum diagrams for single and double Bragg transitions. **Left:** First-order single Bragg transition. An atom interacts with two counterpropagating light fields of frequencies ω_1 and ω_2 . It absorbs a photon with energy $\hbar\omega_1$ and emits a photon with energy $\hbar\omega_2$ in the opposite direction. Therefore, it changes its initial state $|F=2\rangle$ via the intermediate state $|F'=1\rangle$ to the final state $|F=2\rangle$. This causes a total energy difference of $\hbar\Delta\omega$, the recoil energy. This process transfers a total momentum of $\hbar k_{\text{eff}} \approx 2\hbar k$. **Right:** First-order double Bragg transition. If an atom interacts simultaneously with two pairs of counterpropagating light fields of frequencies ω_1 and ω_2 each, symmetric momentum transfer to the states $|\pm 2\hbar k\rangle$ is enabled. The resonance condition follows the same principles as for single Bragg diffraction, while the total momentum transfer is doubled. For both cases a global detuning Δ prevents population of the intermediate state. (The axis are not shown to scale)

In the case of such a transition, the frequency difference $\Delta\omega$ is typically on the order of kilohertz. For a Raman transition, as shown in subsection 2.2.3, this difference is larger and is of the order of gigahertz. Nevertheless, it is still relatively small compared to the absolute values of ω_1 and ω_2 , which are hundreds of terrahertz. This leads to the definition of the approximation of $\hbar|\vec{k}| \equiv \hbar|\vec{k}_1| \approx \hbar|\vec{k}_2|$. In the desired case of applying counter-propagating light fields $\vec{k}_1 = -\vec{k}_2$ to an atomic ensemble, the total momentum transfer can be expressed as $\hbar k_{\text{eff}} \approx 2\hbar k$. Moreover this difference is also very small compared to the absolute value of ω_1 and ω_2 and can therefore often be derived from a single laser source, for example by using acousto-optical modulation.

A first order diffraction process happens purely between the initial state $|F=2, p=p_0\rangle$ and the final state $|F=2, p=p_0+2\hbar k\rangle$. Any initial offset momentum must be taken into account, which can be intuitively explained as a Doppler shift resulting from the motion of the atoms relative to the light fields. It is zero for atoms at rest and otherwise shifts the initial state on the parabola, which changes the resonance condition to $\Delta\omega = \omega_{k_{\text{eff}}} + \omega_D$. Technically, this can be compensated, for example, by introducing an additional frequency component ω_D into the acousto-optical modulation.

The scheme in figure 2.3 does not depict higher-order or off-resonant transitions, which can in turn lead to unwanted populations of other states. In Bragg diffraction, these are most pronounced in the so-called Raman-Nath and Kapitza-Dirac regimes [Mül08b; Gad09]. Here the optical pulse durations are shorter and in the Kapitza-Dirac regime also the intensities are higher. Apart from unwanted off-resonant transitions, Bragg diffraction can also be realized by scattering n pairs of photons which corresponds to a transition between the momentum states $|p_0\rangle$ and $|p_n\rangle$ leading to higher order diffraction. The required resonance condition in this case changes to $\Delta\omega = n\omega_{k_{\text{eff}}}$, so any intermediate momentum state is not resonant and therefore should ideally not be populated.

2.2.2 Double Bragg diffraction

Due to energy momentum conservation the direction of the diffraction process is always oriented in the same direction as the light field with the higher absolute frequency value. For example in figure 2.3 case towards \vec{k}_1 , because $\omega_1 > \omega_2$. Applying a second set of opposite light fields with opposite directions, a combination of \vec{k}_1 and $-\vec{k}_2$ as well as $-\vec{k}_1$ and \vec{k}_2 is obtained. Now the atomic ensemble can interact with both frequency pairs simultaneously and symmetric momentum transfer is enabled. Such a coupling, called double Bragg diffraction [Chi11; Ahl16], is schematically shown in the energy-momentum diagram in figure 2.3 on the right side.

In the case of a first order diffraction process the initial state $|F = 2, p = 0\rangle$ is coupled to $|F = 2, p = \pm 2\hbar k\rangle$. The coupling strength for single and double diffraction is defined by intensity, pulse shape and time τ_p . The ratio of these parameters defines whether a clean oscillation from the initial to the target state is possible or if multiple states are populated. Because for double diffraction these oscillations take place in an effective three-level system, a higher velocity selectivity compared to single diffraction has to be taken into account. The frequency of the effective Rabi oscillation is also different and reads $\Omega_{\text{effDD}} = \sqrt{2}\Omega_{\text{eff}}$ [Gie13]. Note that in double diffraction a complete transfer from $|p = 0\rangle$ to $|p = \pm 2\hbar k\rangle$ is referred to a $\pi/2$ pulse, opposite to single diffraction where it denotes a superposition between $|p = 0\rangle$ and $|p = 2\hbar k\rangle$.

In order to technically realize the superposition of the required four frequency components, the overlap of two light beams propagating in opposite directions is a suitable solution. Another commonly used method is the retro-reflection of the superposition of two perpendicular polarized light fields \vec{k}_1 and \vec{k}_2 at a combination of a quarter-wave plate and a mirror. This configuration creates two perpendicular polarized sets of $\pm\vec{k}_1$ and $\mp\vec{k}_2$ and suppresses many unwanted systematic effects like disturbances due to copropagating transitions, standing waves or specific laser phase noise [Gie13]. In such a retroreflective arrangement, when the atomic ensemble is initially at rest, both counter-propagating optical lattices are equally relevant to the diffraction process, resulting in double diffraction. This process is therefore of particular importance for applications where the atoms are not naturally subjected to (large) accelerations, which is often the case in microgravity environments. But also for earthbound inertial sensors, whose beam splitter axis is aligned in horizontal direction orthogonal to gravity, the atoms normally have no

initial velocity in this direction. Achieving double diffraction for an initial ensemble that is not at rest is also possible but requires an additional frequency component, as shown in [Mal10].

2.2.3 Stimulated Raman transitions

The process of a stimulated Raman transition is similar to the Bragg transition described earlier in subsection 2.2.1. These type of beam splitters were first introduced for optical molasses [Phi91; Sal90]. The atom undergoes a two-photon scattering event controlled by two frequencies ω_1 and ω_2 , that fulfill the resonance condition $\Delta\omega = \omega_1 - \omega_2$. The transition is similarly represented on the two energy-momentum parabolas, as seen in figure 2.4 on the left. Note that in addition to the transition between the two momentum states $|p_0\rangle$ and $|p_1\rangle$, there is also a change of the internal state from $|F = 2\rangle$ to $|F = 1\rangle$, which is not the case for Bragg transitions.

When considering the individual one-photon transitions, the existence of spontaneous emission cannot be disregarded. In this case, atoms from the intermediate state $|F' = 1\rangle$ can also decay back to the initial state $|F = 2\rangle$. In order to maintain the coherence of the transition, this effect should not occur, which is why also in the Raman case a detuning Δ is chosen with respect to the intermediate state. Since energy and momentum have to be conserved the energy difference $\hbar\Delta\omega$ has to be equal to the kinetic energy $\hbar\omega_{k_{\text{eff}}}$ gained through the momentum transfer plus the energy difference of the internal states $\hbar\omega_{\text{HFS}}$, namely the hyperfine splitting between the coupled states $|F = 2\rangle$ and $|F = 1\rangle$. This definition assumes that no other effects shift the atomic energy levels. The total momentum transfer for a Raman transition is maximum for counter-propagating light fields $\vec{k}_1 = -\vec{k}_2$ and can be expressed as $\hbar k_{\text{eff}} \approx 2\hbar k$, as for the Bragg case. However, the resonance condition can be formulated somewhat differently, due to a non-negligible AC stark shift contribution ω_{AC} as

$$\Delta\omega = \omega_1 - \omega_2 = -\omega_{k_{\text{eff}}} + \omega_{\text{HFS}} + \omega_{\text{AC}}. \quad (2.6)$$

Note that here, as in the Bragg case, the initial momentum is assumed to be zero, otherwise the resonance condition must contain an additional Doppler term ω_{D} .

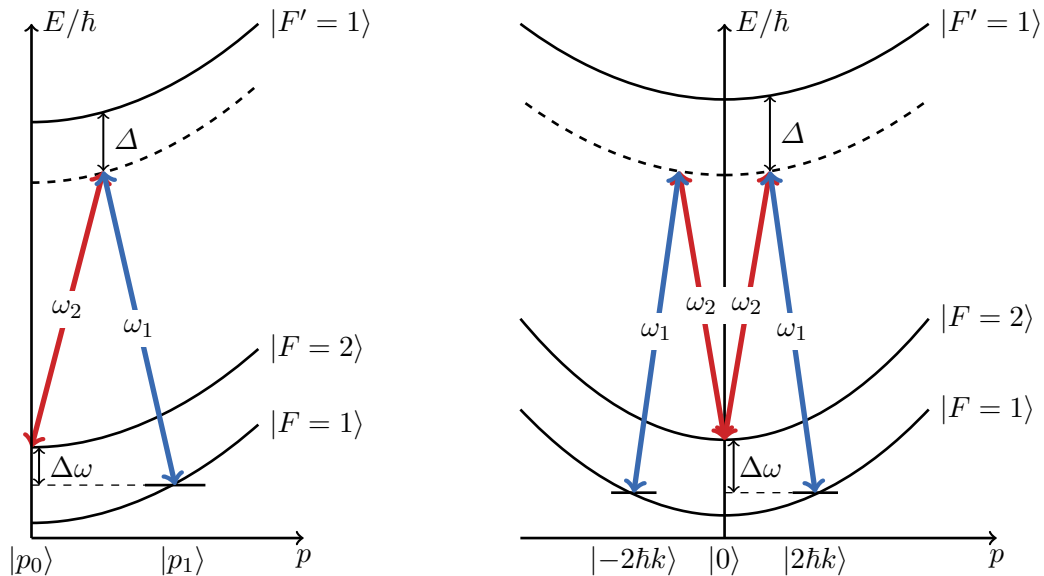


Figure 2.4: Energy-momentum diagrams for single and double Raman transitions. **Left:** First-order single Raman transition. The process is similar to Bragg scattering. Two counterpropagating light fields of frequencies ω_1 and ω_2 with a total energy difference of $\hbar\Delta\omega$ transfer a total momentum of $2\hbar k$. The main difference is found in the change of the internal state from $|F=2\rangle$ to $|F=1\rangle$ during the process. **Right:** First-order double Raman transition with symmetric momentum transfer to the states $|\pm 2\hbar k\rangle$. The same internal change of state occurs as in single Raman diffraction. To maintain the coherence of the transition, spontaneous emission must be suppressed. Therefore a detuning Δ is chosen with respect to the intermediate state $|F'=1\rangle$, analogous to Bragg diffraction. (The axis are not shown to scale)

The individual Raman light fields, defined by their orders of magnitude larger frequency difference compared to the Bragg case, exert energy shifts on the atomic system through non-resonant coupling. This changes the frequency of the two-photon transition by the so called one-photon AC-Stark shift. In the case of the atomic species ^{87}Rb this shift can be conveniently compensated by choosing a suitable intensity ratio I_2/I_1 of the two applied laser light fields. With the correct ratio the exerted energy shifts onto the atomic system can result in a differential shift of

$$\omega_{\text{AC}} \equiv \omega_{\text{AC},|F=1\rangle} - \omega_{\text{AC},|F=2\rangle} = 0. \quad (2.7)$$

It should be noted that the two-photon AC-Stark shift, caused by coupling of off-resonant two-photon transitions, can still lead to non-negligible effects like phase shifts during the interferometer sequence affecting its output phase.

2.2.4 Double Raman diffraction

Assuming that the atomic ensemble is at rest with an initial momentum $p_0 = 0$ in the direction of the interrogating light fields, double diffraction processes can also be realized for symmetric two-photon Raman transitions [Ber15; Mal10; Lévy09; Jaf18]. The energy-momentum parabola

in figure 2.4 on the right helps to visualize a first-order process. The two counterpropagating frequency pairs of ω_1 and ω_2 , are equally relevant for the process, leading to double diffraction. When an atom interacts with the two pairs of counterpropagating light fields of $\pm\vec{k}_1$ and $\mp\vec{k}_2$, it gains the same portions of momentum $2\hbar k$ as for single diffraction, associated to the recoil frequency $\omega_{k_{\text{eff}}}$. The additional pair of laser frequencies not only drives a process in the opposite direction, but also off-resonant transitions, which are not shown for better visibility.

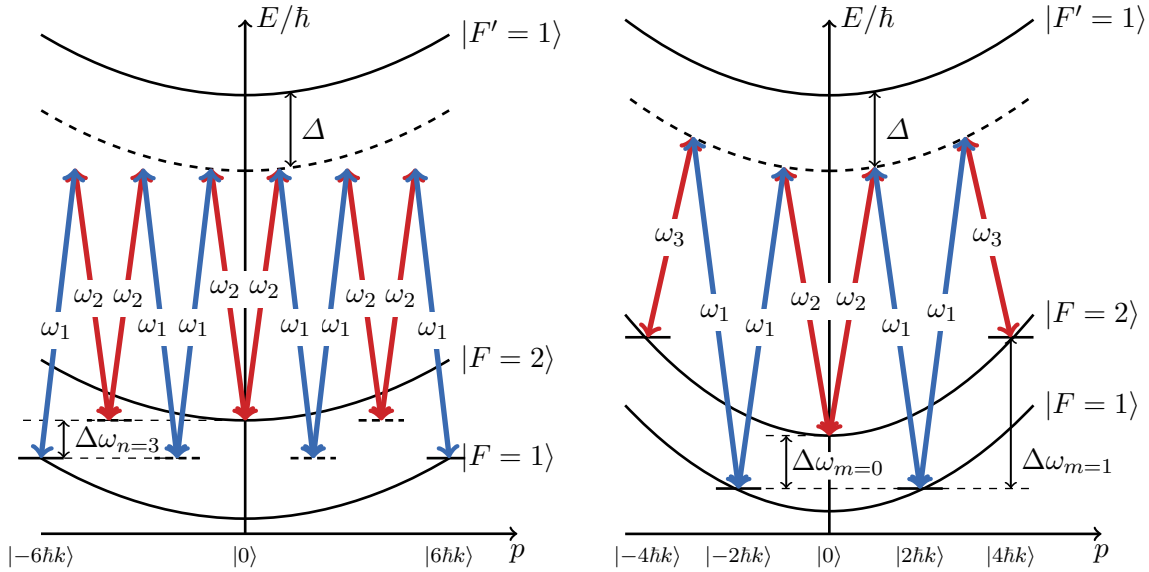


Figure 2.5: Two examples of higher order double Raman diffraction. **Left:** The energy-momentum level scheme illustrates a third order ($n = 3$) transition that transfers a total of $\pm 6\hbar k$ of momentum. Non-resonant states are represented by dashed levels. The final internal state has changed from $|F = 2\rangle$ to $|F = 1\rangle$. **Right:** An initial double diffraction beam splitter ($m = 0$) transfers the wave packet from the state $|p = 0\rangle$ to the state $|p = \pm 2\hbar k\rangle$, like a first order diffraction pulse ($n = 1$). Afterwards the sequential transfer ($m = 1$) to a total of $\pm 4\hbar k$ of momentum is shown. In this case the final internal state has not changed. Higher order transitions are possible, but like non-resonant transitions they are not displayed. (The axis are not shown to scale)

Compared to Raman single diffraction, these transitions are much more important since their detuning is on the order of $\Delta\omega$, similar to single Bragg diffraction, and must be considered for loss and efficiency reasons. For a first order Raman double diffraction process the initial state $|F = 2, p = 0\rangle$ is coupled to $|F = 1, p = \pm 2\hbar k\rangle$ if all relevant light field parameters are appropriately chosen. The coupling strength is hereby defined in the same way as for double Bragg diffraction. As indicated in the section 2.2.1 on Bragg single diffraction, it is possible to transfer momentum portions of $2n\hbar k$ by scattering n photon pairs. For illustration purposes, the process of sequential and higher-order double Raman diffraction is explained below as an example. The general resonance condition for a n^{th} order Raman transition is defined as

$$\Delta\omega_n = \omega_1 - \omega_2 = (-1)^n \cdot n\omega_{k_{\text{eff}}} + \omega_{\text{HFS}} + \omega_{\text{AC}}. \quad (2.8)$$

An energy-momentum level scheme is shown in figure 2.5 on the left and illustrates a third order ($n = 3$) transition that transfers a total of $\pm 6\hbar k$ of momentum [Har20]. The non-resonant states $|p = \pm 2\hbar k\rangle$ and $|p = \pm 4\hbar k\rangle$ are not populated in this case. The AC stark shift contribution ω_{AC} can be omitted if it is sufficiently compensated as described previously. The hyperfine splitting ω_{HFS} defines the splitting between $|F = 2\rangle$ and $|F = 1\rangle$, in the same way as for single Raman diffraction. Working with higher order transitions typically comes with two major disadvantages. The first is a quadratic increase in needed laser intensity $I_{1,2}^n$ and the second is a decrease in transfer efficiency [Mül08a; Gie16; Geb20]. Another option of increasing the transferred momentum is found in sequential transitions, where the need for higher laser intensities can be circumvented, but at the cost of using multiples of the pulse duration time $(m + 1) \cdot \tau_p$. To realize a m^{th} order sequential transition the resonance condition reads

$$\Delta\omega_m = \omega_1 - \omega_{m+2} = (-1)^{m+1} \cdot (2m + 1)\omega_{k_{\text{eff}}} + \omega_{HFS} + \omega_{AC}. \quad (2.9)$$

First of all, an initial double diffraction beam splitter ($m = 0$) transfers the wave packet from the state $|p = 0\rangle$ to the state $|p = \pm 2\hbar k\rangle$ ($m = 0$), like a first order diffraction pulse ($n = 1$). A subsequent Doppler-detuned effective single Raman diffraction pulse ($m = 1$) further transfers the population from $|p = \pm 2\hbar k\rangle$ to $|p = \pm 4\hbar k\rangle$. The energy-momentum level scheme in figure 2.5 on the right illustrates such a sequential transfer with a total of $\pm 4\hbar k$ transferred momentum. Higher order resonance conditions follow the relation from equation 2.9.

2.3 Sensitivity function formalism

The response function of an atom interferometer to time-varying phases, frequencies and chirps during interrogation can be described by the sensitivity function formalism [Che08; Bon15]. A change of phase for example from one beam splitter pulse to the next, caused by noise processes, would directly influence the difference laser phase ϕ_L and lead to a fluctuation of the output port population $P(\phi)$ of the interferometer, defined by the total occurring phase shift ϕ . The sum over all occurring phase changes $\delta P(\phi)$ during the total interferometer sequence duration $\tau_{\text{tot}} = 2T + 3\tau_p + 4m\tau_p$ is given by the following time integral

$$\delta P(\phi) = \frac{1}{2} \int_{\phi(t_0)}^{\phi(t_0 + \tau_{\text{tot}})} g(t) d\phi_L(t). \quad (2.10)$$

It introduces the sensitivity function $g(t)$, which describes the change in $P(\phi)$ after an infinitesimally small jump in phase $\delta\phi_L$ that occurs at time t after the start of the interferometer sequence. This function can be defined as

$$g(t) = 2 \lim_{\delta\phi_L \rightarrow 0} \frac{\delta P(\delta\phi_L, t)}{\delta\phi_L}. \quad (2.11)$$

In the case of the Mach-Zehnder sequence introduced in the section 2.2, the sensitivity function

for first-order diffraction ($m = 0$) reads

$$g_{\text{MZ}}(t) = \begin{cases} -\sin(\Omega_{\text{eff}}t) & 0 < t \leq \tau_{\text{p}} \\ -1 & \tau_{\text{p}} < t \leq T + \tau_{\text{p}} \\ \sin(2\Omega_{\text{eff}}(t - T - \frac{3}{2}\tau_{\text{p}})) & T + \tau_{\text{p}} < t \leq T + 2\tau_{\text{p}} \\ 1 & T + 2\tau_{\text{p}} < t < 2T + 2\tau_{\text{p}} \\ -\sin(\Omega_{\text{eff}}(t - 2T - 3\tau_{\text{p}})) & 2T + 2\tau_{\text{p}} < t \leq 2T + 3\tau_{\text{p}} \\ 0 & \text{otherwise.} \end{cases} \quad (2.12)$$

Where τ_{p} defines an equal time length of the three interferometry pulses of the sequence and $\Omega_{\text{eff}} = \frac{\pi}{2\tau_{\text{p}}}$ the corresponding fixed effective Rabi frequency. This definition is chosen analogous to calculations where Ω_{eff} is defined by the different pulse lengths in the interferometer, which determines whether they are $\pi/2$ - or π -pulses. In the here shown case this is realized by matching the amplitude of the pulse.

To measure absolute inertial effects using an interferometer, a reference is needed. Any motion on it directly couples inertial noise to the measured interferometer phase shift ϕ . The sensitivity function $g(t)$ shows how the resulting phase-continuous frequency changes of the laser or frequency shifts of the atomic resonances affect the interferometer phase and is related to the velocities of the atoms relative to their inertial reference. In an application case, this reference can be the retro-reflecting element of the interrogating laser light field. If its dynamic motion, for example vibrations of the mirror surface, is recorded during the time τ_{tot} and weighted according to the time dependent sensitivity function $g(t)$, the phase shift that occurred during that measurement cycle can be calculated. In this case the acceleration sensitivity function $f(t)$ provides the response from the phase continuous chirp of the laser and correlates the accelerations of the atoms relative to this reference. It is the integral of the sensitivity function and calculated for the ν -piecewise defined function as follows

$$f_{\nu}(t) = \int_{t_1}^t -g_{\nu}(t)dt + f_{\nu-1}(t_1) \quad \text{for } t_1 < t \leq t_2. \quad (2.13)$$

Any coupling through the inertial reference with a frequency larger than the interferometer cycle frequency f_{cycle} and lower than its corner frequency $f_{\text{corner}} = \frac{1}{\tau_{\text{tot}}}$ except for certain bands will distort the interferometer phase and decrease its measurement sensitivity. For the Mach-Zehnder sequence the piecewise defined acceleration sensitivity function $f(t)$ evaluates to

$$f_{\text{MZ}}(t) = \begin{cases} \frac{1}{\Omega_{\text{eff}}} (1 - \cos(\Omega_{\text{eff}} t)) & 0 < t \leq \tau_p \\ \frac{1}{\Omega_{\text{eff}}} + t - \tau_p & \tau_p < t \leq T + \tau_p \\ T + \frac{1}{\Omega_{\text{eff}}} (1 - \frac{1}{2} \cos(2\Omega_{\text{eff}} (T - t - \frac{3}{2}\tau_p))) & T + \tau_p < t \leq T + 2\tau_p \\ \frac{1}{\Omega_{\text{eff}}} + 2T + 2\tau_p - t & T + 2\tau_p < t < 2T + 2\tau_p \\ \frac{1}{\Omega_{\text{eff}}} (1 - \cos(\Omega_{\text{eff}} (t - 2T + \tau_p))) & 2T + 2\tau_p < t \leq 2T + 3\tau_p \\ 0 & \text{otherwise.} \end{cases} \quad (2.14)$$

Figure 2.6 shows example sensitivity functions $g_{\text{MZ}}(t)$ (left) and $f_{\text{MZ}}(t)$ (right). Interferometer geometries that seek to maximize their sensitivity may rely on increasing their differential kinetic momentum. As presented in section 3.2 this can be realized by using higher-order or sequential higher-order diffraction, as well as combinations with Bloch oscillations. In principle, this also changes the corresponding sensitivity functions due to the required additional atom-light interactions [D  c19]. The following case examines sequential first-order diffraction ($m = 1$), introducing a total of four additional pulses of equal length τ_p . This example is chosen because it corresponds to the twin-lattice sequence described later in section 3.2. Note that the additional momentum transfer due to Bloch oscillations is not considered in this treatment. The sensitivity functions $g(t)$ and $f(t)$ are modified in the following way,

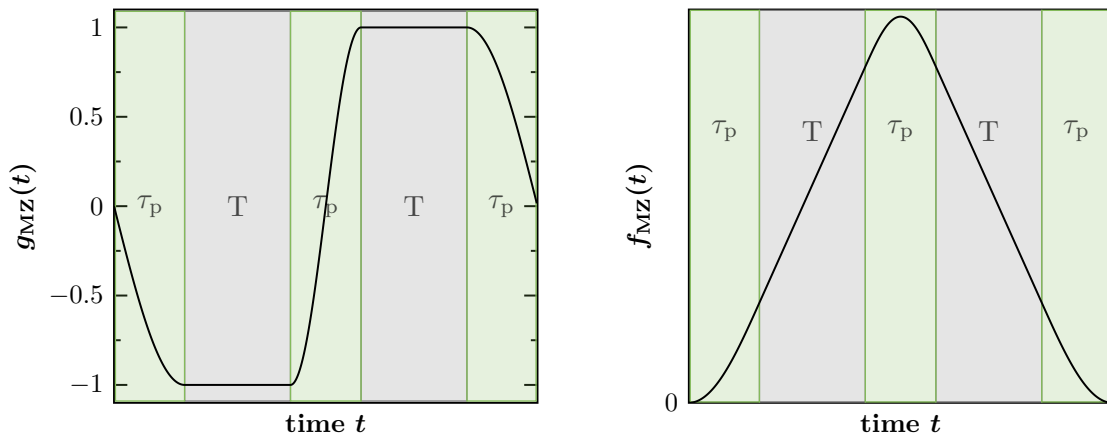


Figure 2.6: Sensitivity functions for a Mach-Zehnder type atom interferometer. **Left:** The time dependent sensitivity function $g_{\text{MZ}}(t)$ shows how phase-continuous frequency changes of the laser or frequency shifts of the atomic resonances, for example Zeeman or light shifts, affect the interferometer phase with respect to their occurrence. **Right:** The acceleration sensitivity function $f_{\text{MZ}}(t)$ is defined as the piecewise integral of the sensitivity function and provides the response from a phase-continuous chirp of the laser frequency and correlates the accelerations of the atoms relative to their inertial reference. The times τ_p of the individual pulses are shown strongly exaggerated compared to typical times for T to show the functional dependencies.

$$g_{\text{seqMZ}}(t) = \begin{cases} -\sin(\Omega_{\text{eff}}t) & 0 < t \leq \tau_p \\ -1 - \sin(\Omega_{\text{eff}}(t - \tau_p)) & \tau_p < t \leq 2\tau_p \\ -2 & 2\tau_p < t < T + 2\tau_p \\ -1 + \sin(\Omega_{\text{eff}}(t - T - 3\tau_p)) & T + 2\tau_p < t \leq T + 3\tau_p \\ \sin(2\Omega_{\text{eff}}(t - T - \frac{7}{2}\tau_p)) & T + 3\tau_p < t \leq T + 4\tau_p \\ 1 + \sin(\Omega_{\text{eff}}(t - T - 4\tau_p)) & T + 4\tau_p < t \leq T + 5\tau_p \\ 2 & T + 5\tau_p < t \leq 2T + 5\tau_p \\ 1 + \sin(\Omega_{\text{eff}}(t - 2T - 4\tau_p)) & 2T + 5\tau_p < t \leq 2T + 6\tau_p \\ \sin(\Omega_{\text{eff}}(t - 2T - 5\tau_p)) & 2T + 6\tau_p < t \leq 2T + 7\tau_p \\ 0 & \text{otherwise} \end{cases} \quad (2.15)$$

and

$$f_{\text{seqMZ}}(t) = \begin{cases} \frac{1}{\Omega_{\text{eff}}}(1 - \cos(\Omega_{\text{eff}}t)) & 0 < t \leq \tau_p \\ \frac{1}{\Omega_{\text{eff}}}(2 - \cos(\Omega_{\text{eff}}(\tau_p - t))) + t - \tau_p & \tau_p < t \leq 2\tau_p \\ \frac{2}{\Omega_{\text{eff}}} + 2t - 3\tau_p & 2\tau_p < t < T + 2\tau_p \\ T + \frac{1}{\Omega_{\text{eff}}}(2 + \cos(\Omega_{\text{eff}}(T + 3\tau_p - t))) + t - \tau_p & T + 2\tau_p < t \leq T + 3\tau_p \\ 2T + \frac{1}{2\Omega_{\text{eff}}}(6 + \cos(2\Omega_{\text{eff}}(T + \frac{7}{2}\tau_p - t))) + 2\tau_p & T + 3\tau_p < t \leq T + 4\tau_p \\ 3T + \frac{1}{\Omega_{\text{eff}}}(2 + \cos(\Omega_{\text{eff}}(T + 4\tau_p - t))) - t + 6\tau_p & T + 4\tau_p < t \leq T + 5\tau_p \\ 4T + \frac{2}{\Omega_{\text{eff}}} + 11\tau_p - 2t & T + 5\tau_p < t \leq 2T + 5\tau_p \\ 2T + \frac{1}{\Omega_{\text{eff}}}(2 + \cos(\Omega_{\text{eff}}(2T + 4\tau_p - t))) - t + 6\tau_p & 2T + 5\tau_p < t \leq 2T + 6\tau_p \\ \frac{1}{\Omega_{\text{eff}}}(1 + \cos(\Omega_{\text{eff}}(2T + 5\tau_p - t))) & 2T + 6\tau_p < t \leq 2T + 7\tau_p \\ 0 & \text{otherwise.} \end{cases} \quad (2.16)$$

Figure 2.7 shows example sensitivity functions $g_{\text{seqMZ}}(t)$ (left) and $f_{\text{seqMZ}}(t)$ (right).

To obtain the frequency dependence of the interference signal to a phase noise contribution of frequency ω_{ϕ_L} , the response function of the interferometer in Fourier space must be known. In the case of a measured electronic noise spectrum this can be obtained with the help of the Fourier transform of the sensitivity function. Based on the introduction of a modulation of the laser phase, that can be written down in the form of $\phi_L(t) = A_{\phi_L} \cos(\omega_{\phi_L}t + \theta_{\phi_L})$ [Bar14] and the interferometer phase is influenced as follows

$$\delta\phi = A_{\phi_L} \omega_{\phi_L} \text{Im}[G(\omega_{\phi_L})] \cos\theta_{\phi_L}. \quad (2.17)$$

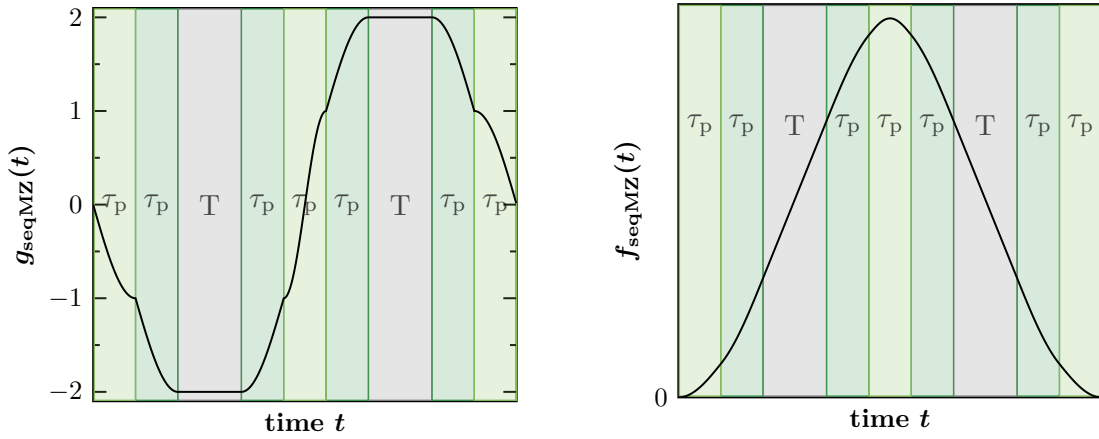


Figure 2.7: Sensitivity functions for a sequential Mach-Zehnder type atom interferometer. **Left:** The time dependent sensitivity function $g_{\text{seqMZ}}(t)$ shows a factor of two larger response compared to the function $g_{\text{MZ}}(t)$. **Right:** The shape of the acceleration sensitivity function $f_{\text{seqMZ}}(t)$ exhibits less modified behavior due to its more continuous pattern. Also here the times τ_p of the individual pulses are shown strongly exaggerated compared to typical times for T to show the functional dependencies.

Here $G(\omega_{\phi_L})$ is defined as the Fourier transform of the sensitivity function

$$G(\omega_{\phi_L}) = \int e^{-i\omega_{\phi_L}t} g(t) dt. \quad (2.18)$$

If the phase θ_{ϕ_L} , introduced as the modulation of the laser phase, is randomly distributed and can be averaged, it is possible to deduce a weight function. It is called the velocity transfer function and transforms the laser phase noise into interferometric phase noise as follows

$$H(\omega_{\phi_L}) = \omega_{\phi_L} G(\omega_{\phi_L}). \quad (2.19)$$

If the phase noise density $S_\phi(2\pi f_{\phi_L})$ is known or measured, its effect can be estimated by calculating the root mean squared phase of the interferometer phase as follows

$$(\sigma_\phi^{\text{rms}})^2 = \int_0^\infty |H(2\pi f_{\phi_L})|^2 S_\phi(2\pi f_{\phi_L}) df_{\phi_L}. \quad (2.20)$$

Typically atom interferometers are operated in a repetitive mode, yielding single phase measurements separated by a cycle time t_{cycle} . This allows to define the Allan variance [All66] for longer measurement series containing n_{tot} measurements with the cycle frequency $f_{\text{cycle}} = 1/t_{\text{cycle}}$ in the form of the following sum

$$\sigma_\phi^2(u \cdot t_{\text{cycle}}) = \frac{1}{u \cdot t_{\text{cycle}}} \sum_{n=1}^{\infty} |H(2\pi n_{\text{tot}} f_{\text{cycle}})|^2 S_\phi(2\pi n_{\text{tot}} f_{\text{cycle}}), \quad (2.21)$$

where $u \cdot t_{\text{cycle}}$ is the observation time typical for the Allan variance defined by an integer multiple u of the measurement cycle time t_{cycle} .

To get a complete expression of the transfer function as defined in equation 2.19 the Fourier transformed analytic form of the sensitivity function 2.12 can be calculated as defined in equation 2.18 to

$$G_{\text{MZ}}(\omega_{\phi_L}) = \frac{4i\Omega_{\text{eff}}}{\omega_{\phi_L}^2 - \Omega_{\text{eff}}^2} \sin\left(\frac{\omega_{\phi_L}(T + 2\tau_p)}{2}\right) \left(\cos\left(\frac{\omega_{\phi_L}(T + 2\tau_p)}{2}\right) + \frac{\Omega_{\text{eff}}}{\omega_{\phi_L}} \sin\left(\frac{\omega_{\phi_L}T}{2}\right) \right). \quad (2.22)$$

Also for the sequential Mach-Zehnder geometry the Fourier transformed function of equation 2.15 can be calculated and determined to

$$\begin{aligned} G_{\text{seqMZ}}(\omega_{\phi_L}) &= 2/(\omega_{\phi_L}^5 - 5\omega_{\phi_L}^3 + 4\omega_{\phi_L}\Omega_{\text{eff}}^4) \exp(i(T + (7\tau_p)/2)\omega_{\phi_L}) \\ &\cdot [(\omega_{\phi_L}^4 - 5\omega_{\phi_L}^2 + 4\Omega_{\text{eff}}^4) \cos((3\tau_p\omega_{\phi_L})/2) \\ &+ \omega_{\phi_L}(-\Omega_{\text{eff}}(\omega_{\phi_L}^2 - 4\Omega_{\text{eff}}^2 + (-3\omega_{\phi_L}^2 + 6\Omega_{\text{eff}}^2 - 2(\omega_{\phi_L}^2 - 4\Omega_{\text{eff}}^2) \cos(\tau_p\omega_{\phi_L}))) \cos(\tau_p\Omega_{\text{eff}})) \\ &\cdot \sin((\tau_p\omega_{\phi_L})/2) + \omega_{\phi_L} \cos((\tau_p\omega_{\phi_L})/2)(-3\Omega_{\text{eff}}^2 - 2(\omega_{\phi_L}^2 - 4\Omega_{\text{eff}}^2) \cos(\tau_p\omega_{\phi_L})) \sin(\tau_p\Omega_{\text{eff}})) \\ &+ (\omega_{\phi_L}^2 - 4\Omega_{\text{eff}}^2) \cos((\tau_p\omega_{\phi_L})/2)((\omega_{\phi_L} - \Omega_{\text{eff}})(\omega_{\phi_L} + \Omega_{\text{eff}}) + 2 \cos((T + 2\tau_p)\omega_{\phi_L}) \\ &\cdot (-\omega_{\phi_L}^2 + \Omega_{\text{eff}}^2 + i\omega_{\phi_L}\Omega_{\text{eff}} \cos(\tau_p\Omega_{\text{eff}}) + \omega_{\phi_L}^2 \sin(\tau_p\Omega_{\text{eff}})) \\ &- \omega_{\phi_L}(2i\Omega_{\text{eff}} \cos((T + 3\tau_p)\omega_{\phi_L}) \cos^2(\tau_p\Omega_{\text{eff}}) + 2\Omega_{\text{eff}} \sin((T + 3\tau_p)\omega_{\phi_L}) \sin^2(\tau_p\Omega_{\text{eff}}) \\ &+ \exp(i(T + 3\tau_p)\omega_{\phi_L})\omega_{\phi_L} \sin(2\tau_p\Omega_{\text{eff}}))]. \end{aligned} \quad (2.23)$$

If the source of noise is not derived from changes of the laser frequency ω_{ϕ_L} , but rather from inertial contributions like vibrations that manifest in the form of accelerations, the frequency ω_{ϕ_L} can be replaced by a Doppler detuning $\omega_D = \vec{k}_{\text{eff}}\vec{v}(t)$, in an analogous view. From the integration of the acceleration the time dependence of the velocity can be calculated and by averaging over all phase components the transfer function can be rewritten in the form of

$$H_a(\omega_{\phi_L}) = \frac{1}{T^4\omega_{\phi_L}^4} H(\omega_{\phi_L}). \quad (2.24)$$

The velocity and acceleration transfer functions for the Mach-Zehnder and sequential Mach-Zehnder geometry are visualized in figure 2.8 for an exemplary choice of the parameters

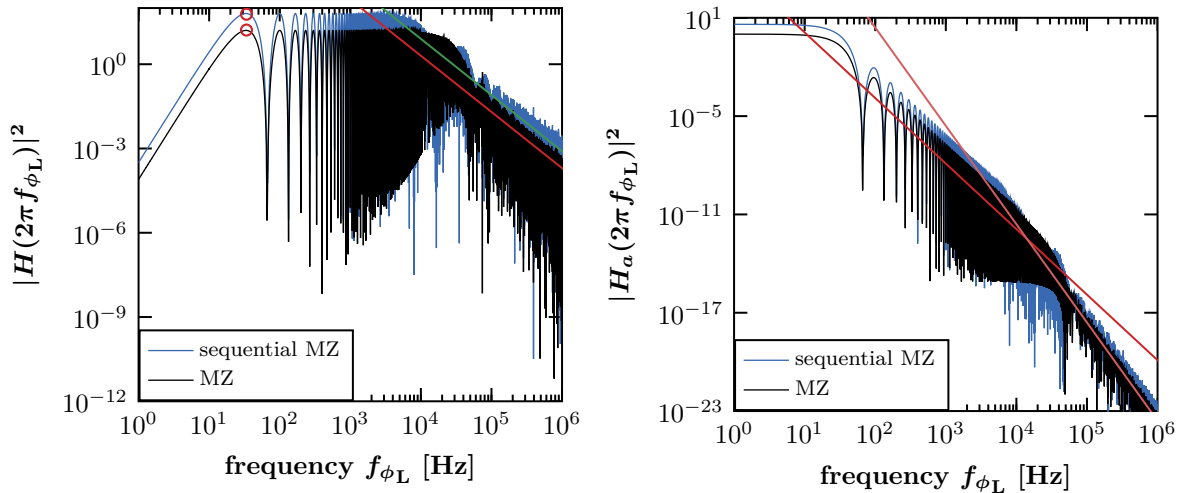


Figure 2.8: Sensitivity transfer functions for the Mach-Zehnder geometry compared to the sequential Mach-Zehnder geometry. The values chosen for the free evolution time are $T = 15$ ms and for the pulse time $\tau_p = 25$ μ s. For comparison the total interferometry time is set to be equal, realized by reducing the free evolution time T for the sequential geometry by $2\tau_p$. **Left:** Absolute square of the two velocity transfer functions $|H(\omega_{\phi_L})|^2$ with the conversion $\omega_{\phi_L} = 2\pi f_{\phi_L}$. The first sensitivity maximum for both is reached at the corner frequency $f_{\text{corner}} \approx 33$ Hz (red circles) and experiences minima which depend on the free evolution time T and pulse time τ_p . For high frequencies the function exhibits a low pass behaviour proportional to $\alpha(\Omega_{\text{eff}}/\omega_{\phi_L})^2$. **Right:** Absolute square of the two acceleration transfer functions $|H_a(\omega_{\phi_L})|^2$. It illustrates the same earlier low pass behaviour after the corner frequency f_{corner} proportional to $\alpha/(T^4\omega_{\phi_L}^4)$ until, in a second decline the sensitivity drops proportional to $2\alpha/(T^4\omega_{\phi_L}^4) \cdot (\Omega_{\text{eff}}/\omega_{\phi_L})^2$. Only the curves for $\alpha = 1$ are shown here for better visibility.

$T = 15$ ms and $\tau_p = 25$ μ s. On the left graph the absolute square of the two velocity transfer functions show a similar behaviour with the difference that the sequential function yields higher values due to the larger transferred momentum. The first sensitivity maximum for both is reached at the corner frequency f_{corner} and experiences minima which depend on the chosen values of the free evolution time T and the pulse time τ_p . For high frequencies the sensitivity drops proportional to $2\alpha(\Omega_{\text{eff}}/\omega_{\phi_L})^2$ illustrating the low pass behaviour. The parameter α takes the different amplitudes into account and evaluates to $\alpha = 1$ for the Mach-Zehnder and $\alpha = 4$ for the sequential Mach-Zehnder geometry. On the right graph the acceleration transfer functions shows the response to accelerations. As an example, one can consider the mirror motion, which is interpreted without correlation or compensation as the motion of the inertial reference in a retro-reflective geometry. It illustrates the earlier low pass behaviour after the corner frequency f_{corner} proportional to $\alpha/(T^4\omega_{\phi_L}^4)$ until, in a second decline the sensitivity drops proportional to $2\alpha/(T^4\omega_{\phi_L}^4) \cdot (\Omega_{\text{eff}}/\omega_{\phi_L})^2$.

CHAPTER 3

Advanced atom interferometry methods for inertial sensing

Expanding on the previously explained fundamentals of atom interferometry with Bose-Einstein condensates and the associated preparation and manipulation techniques, the following chapter presents results from four different publications that were published during my doctoral studies. These combine innovative realizations of different coherent optical manipulations of condensed atoms and interferometer concepts based on them.

Simplified, the achievable inertial sensitivity of an atom interferometer is proportional to the spatial separation of the wave packets and can be enlarged by increasing either the interaction time or the amount of transferred momentum as introduced in section 2.2. In the presence of a gravitational field the available time $2T$ between coherent splitting and recombination can be a limiting factor since it is constrained by the available free fall distance. This time can be further reduced significantly by additional operations. For example, by the time τ_{prep} needed for possible state preparation (see section 2.1.2), and the time τ_{det} needed for spatial separation of the output, for instance when using an absorption detection method. This is especially true when the employed setup features a short drop distance. This limitation has motivated efforts to achieve large sensitivities by confining and levitating matter waves in tight waveguides or traps and perform interferometry there [Ket92; Sau01; Arn04; Wu07; Moa20; Krz22]. As a result, long interrogation times can be achieved and large spatial separations are targeted. However, these methods usually bring additional challenges, often related to the enclosing potential. An alternative approach to increase the time the atoms remain in an interferometer without the need for levitation is presented in the following section 3.1. It relies on an efficient and versatile (re-)launch mechanism based on the coherent momentum transfer by Bloch oscillations combined with double Bragg diffraction.

A different way to enhance the inertial sensitivity scaling is to increase the velocity separation between the two interferometer arms. To achieve this, depending on the measured quantity or geometry, it can be advantageous to use double instead of single diffraction pulses or even higher order or sequential diffraction. The limitation for these different techniques is often given by atom loss caused by non-ideal beam splitter efficiencies. Another alternative approach is to increase the transferred momentum k_{eff} with the use of accelerated optical lattices, where the atomic ensemble suffers significantly less losses but is subject to dephasing effects due to light shifts [Mül09; Cla09; McD13]. In section 3.2 of this chapter a twin-lattice realization is presented. It is based on a combination of double Bragg beam splitters, which realize the

symmetric momentum splitting of the initial atomic ensemble, and accelerating them along both interferometer arms with the help of Bloch oscillations. Overall, this scheme provides opportunities for large momentum transfer on short time scales and can be of particular interest for increasing the sensitivity of rotational measurements. Thus, it also offers a perspective for inertial sensors of small size.

The third section 3.3 presents the studies on a scheme that can be used to measure and discriminate between rotations and accelerations from a single measurement sequence. For this purpose, the excellent motion control of BECs is combined with the precise momentum transfer by double Bragg diffraction. First, two counter-propagating ensembles are formed by symmetrically splitting an initial wave packet. These subsequently feed two simultaneously operated Mach-Zehnder interferometers driven by a second optical lattice moving perpendicular to the first one. This method helps to avoid the complexity of two independent BEC sources and can be extended using a third optical lattice, which is promising for the use in a six-axis quantum inertial measurement unit.

The last section 3.4 discusses a multi-loop geometry that combines the relaunch mechanism, with the symmetric momentum transfer of the twin lattice. Since the sensitivity to rotation based on the Sagnac effect scales with the enclosed area of the interferometer, it is advantageous to increase it by performing loops. To this end, the scheme uses two perpendicularly aligned lattice light fields, one carrying out the relaunch operation and the other performing the interferometer pulse sequence.

3.1 Atom-chip fountain gravimeter

On earth any object in free fall experiences a steady gain in speed, caused by the gravitational acceleration. This is also true for atoms used for interferometry and limits the time available to interrogate and detect them. Therefore, increasing the sensitivity by extending the free-fall time initially seems to contradict a compact setup. A possible solution here is provided by the implementation of a relaunch, similar to a vertical throw, which redirects the motion of the atoms and sends them on a parabolic trajectory in time. Based on this idea, an atom-chip based fountain gravimeter has been published in [Abe16]. Here, the available time before the relaunch is used exclusively for preparation (τ_{prep}), so that the remaining time after the launch can be used for interferometry ($2T$) and detection (τ_{det}) of the output ports. For a first overview, the flow diagram in figure 3.1 simplifies the necessary steps that have to be performed.

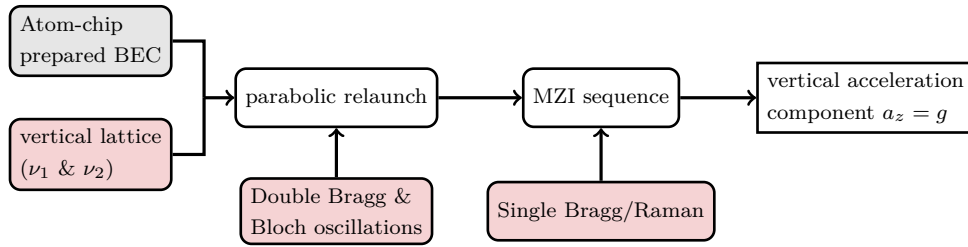


Figure 3.1: Flow diagram of the atom-chip fountain gravimeter sequence. The prepared BEC is manipulated by a vertical optical lattice with frequency components ν_1 and ν_2 . The individual applied techniques inside the lattice are highlighted by a red background.

First of all a BEC is generated by the atom chip source, explained in section 2.1.1. While its current-carrying wires are capable of generating the high magnetic gradients required for condensation, its coated surface acts as a retro-reflective mirror for the vertical optical lattice, which consists of two frequency components ν_1 and ν_2 . The coherent manipulations are realized with this optical lattice aligned along the z -axis, which coincides with the direction of gravity. These manipulations include the combination of double Bragg diffraction and Bloch oscillations. As well as single Raman or Bragg diffraction for the subsequently operated Mach-Zehnder like atom interferometer. The measured interferometric phase shift in the end can be related to the gravitational acceleration g .

A non-scale depiction of the geometric arrangement illustrates the used setup of the experimental realization, shown in figure 3.2 on the left hand side. It depicts the atom-chip at the top, the light field diameter in red and an exemplary image of the manipulated atomic ensemble in the form of an absorption image.

While so far only the very rough mode of operation has been shown, the details of the individual steps are explained in the following using example parameters. First an ultracold atomic ensemble is generated and released a few hundred micrometer below the atom chip surface. Afterwards state preparation is performed for a typical time of $\tau_{\text{prep}} \approx 33$ ms. This includes delta-kick collimation, adiabatic rapid passage to a non-magnetic state and the Stern-Gerlach-type deflection as theoretically introduced in section 2.1.2. During this time the condensate accelerates along the direction of gravity \vec{g} for a total distance of roughly 6 mm away from its initial position. To be able to read out the interferometer phase at the end of each sequence, absorption images are taken in the y - z -plane by a CCD camera. The light field required for this operation is aligned along the imaging axis (x -axis). The maximum detectable area is defined by the size of the camera sensor and the imaging system, thus limiting the time available before the atomic ensemble leaves this area. To extend the time of the Mach-Zehnder interferometer sequence, without increasing the free fall distance, the coherent relaunch is implemented. The corresponding space-time trajectories are depicted in figure 3.2 on the right.

The linearly polarized light fields of frequencies ν_1 and ν_2 driving the interferometer process are guided to the experimental vacuum chamber through a single-mode polarization-maintaining

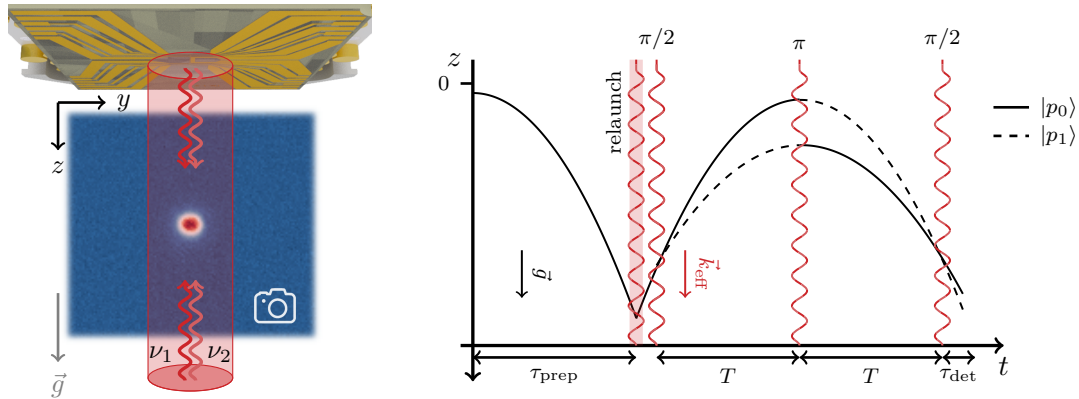


Figure 3.2: **Left:** Geometric representation of the vertical light field for the atom-chip gravimeter sequence. The magnetic fields of the chip are used for state preparation and its coating serves as a retro-reflector for light propagating in the z -direction thus creating moving lattices, which induce Bragg diffraction or Bloch oscillations. As an example of the detection method, one absorption image of a BEC in form of a density distribution is featured in the background. **Right:** Space-time trajectories of the wave packets of the atom-chip based fountain gravimeter with the relaunch after the time τ_{prep} and the subsequent Mach-Zehnder sequence. The individual pulses are symbolized by wavy lines. Note that beam splitter \vec{k}_{eff} points in the same direction as \vec{g} and no area is enclosed by the interferometer.

optical fiber and retro-reflected from the coating of the horizontally aligned atom chip surface. The retro-reflection helps to provide relative phase stability and accuracy for the two-photon processes and defines the surface of the atom chip as the inertial reference for the performed measurement. The absolute frequency $\Delta\nu(t)$ can be controlled by acousto-optical modulation which allows to compensate the frequency shifts of the free falling ensemble caused by Doppler detuning.

The relaunch mechanism itself can be divided into three steps that help to circumvent the large loss contribution of the atoms when crossing the zero momentum state $|p = 0\rangle$. This reversal point cannot be avoided in principle, but its influence can be reduced. First of all the ensemble of atoms is adiabatically loaded into a downward moving optical lattice, decelerated by chirping the frequency $\nu_2(t)$ and released to a momentum of $|p = -8\hbar k\rangle$. Afterwards a double Bragg diffraction pulse 2.2.2 drives a transition between the $|p = -8\hbar k\rangle$ and $|p = +8\hbar k\rangle$ momentum states, which allows a subsequent acceleration of the ensemble, but now in the opposite direction (upwards). If the atoms would be solely decelerated and accelerated by Bloch oscillations, without the double Bragg diffraction pulse in between, large losses due to the population of multiple different momentum states around zero relative momentum would occur. After this relaunch the ensemble is interrogated along the z -direction by a three pulse interferometer as described in section 2.2. At the end of the sequence, the output phase of the interferometer is measured by counting the atoms in each output port, which can then be related to the acceleration component $a_z = g$ following equation 2.3. Generally speaking, the

free fall rate of the BEC is measured by chirping the difference of the laser frequencies at a rate β so that the lattice motion exactly matches the acceleration of the atoms. It follows that the measured phase shift $\phi_a = (\vec{k}_{\text{eff}} \cdot \vec{a} - 2\pi\beta)T^2$ becomes zero independently of T for the special case of $\beta = \vec{k}_{\text{eff}} \cdot \vec{a}/(2\pi)$, in which only one output port of the interferometer is occupied.

In the proof-of-principle measurement presented in [Abe16] an intrinsic sensitivity limit of $(\Delta g/g)/\sqrt{\text{Hz}} = 1.7 \times 10^{-7}$ could be achieved. The available time for interferometry could be increased by a factor of 5 from $2T \approx 10$ ms to $2T \approx 50$ ms on the same baseline of $|z| \leq 7$ mm. The pulse time τ_p is neglected here because it is smaller by at least two orders of magnitude. This measurement is already limited by the largest systematic uncertainty given by the residual magnetic stray fields in the setup. With an improved parameter set, explained in more detail in [Abe16], achieving sensitivities on the order of $(\Delta g/g)/\sqrt{\text{Hz}} = 10^{-9}$ seem feasible.

In summary, this BEC-based fountain gravimeter is able to realize tens of milliseconds of free fall on a baseline of less than one centimeter. Not only does it show how to miniaturize an already compact scheme of an atom interferometer, but it also opens up the possibility of increasing its sensitivity at the same time. Because the relaunch technique is not exclusive to such compact setups, it also offers advantages for a transportable gravimeter, as presented in [Hei20] or the multi-loop scheme in section 3.4.

3.2 Twin-lattice atom interferometry

Another way to improve the sensitivity scaling of an atom interferometer is to increase the velocity separation between its arms. This can be achieved by increasing the transmitted momentum k_{eff} during beam splitter operations. One possibility for achieving this is to form symmetric interferometers featuring matter waves with large relative momentum Δp by employing two counterpropagating optical lattices. For this purpose, this section describes the individual steps of a so-called twin-lattice sequence implementation, as published in reference [Geb21]. The flow diagram in figure 3.3 visualizes the simplified steps schematically in the same way as in the other sections of this chapter. In the beginning the BEC is generated and prepared by the atom chip source. All subsequent optical manipulations are implemented with a single retro-reflected horizontal light field, consisting of the frequencies ω_1 and ω_2 , which is aligned perpendicular to gravity. Due to the beam being aligned horizontally there is a vanishing velocity in beam splitter direction, which directly entails symmetric diffraction through double Bragg 2.2.2 or double Raman processes 2.2.4. After the generation and release of the BEC, together with Bloch oscillations, they allow for a large symmetric momentum transfer and the generation of a Mach-Zehnder like sequence. The individual steps contain further details and are explained in the following section 3.2.1. The final measured output phase is sensitive to accelerations acting on the retro-reflection mirror and also to rotations around $\vec{g} \times \vec{e}_y$, where \vec{e}_y defines the unity vector pointing along the direction of the y -axis.

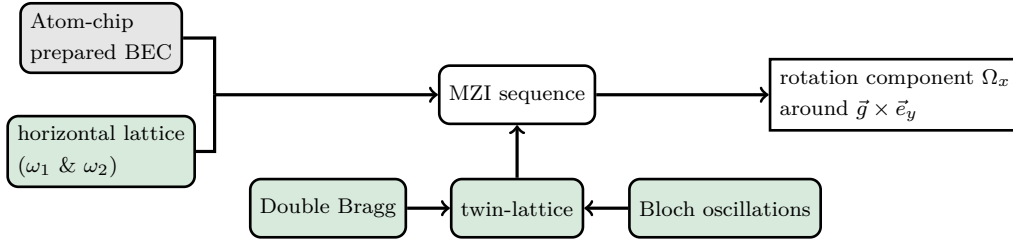


Figure 3.3: Flow diagram of the twin-lattice atom interferometer sequence. The prepared BEC is manipulated by a horizontal optical lattice containing the frequencies ω_1 and ω_2 . The individual applied techniques inside the lattice are highlighted by a green background.

The geometric realisation and the space-time diagram are summarized in figure 3.4. The two incoming frequencies ω_1 and ω_2 are directed into the vacuum chamber via an optical fiber so that they are combined into a single beam with orthogonally aligned linear polarizations. The total light field is retro-reflected on a combination of a quarter wave plate and a separate mirror, located outside the vacuum chamber, creating two counterpropagating optical lattices. This configuration helps to partially suppress losses caused by parasitic standing waves as well as systematic effects like laser phase noise and wavefront distortions. The symmetry of the geometry also lowers the laser power requirements compared to an asymmetric scheme. For the same momentum transfer, accelerating only a single interferometer arm would require larger optical lattice depths, which can result in higher atomic losses due to spontaneous scattering. The original atomic ensemble as well as the individual output ports are measured using absorption detection. On the right side of the figure 3.4 it can be seen that the atomic trajectories enclose a space-time area, which is also reflected in an actual geometric area A . Equation 2.4 shows how part of the output phase shift ϕ_r of the atom interferometer depends on rotations, which can be rewritten to show that the sensitivity to these rotations also scales with the enclosed area as

$$\phi_r = \frac{2E}{\hbar c^2} \vec{A} \vec{\Omega}, \quad (3.1)$$

which shows the linear dependency on the area vector \vec{A} . It can be concluded that a large enlargement of this area, as made possible by the twin-lattice technique, is advantageous for achieving higher measurement sensitivities. It is also clear from the formula that the measured phase shift depends on the energy value E . For optical interferometers this is $E_{\text{ph}} = \hbar\omega$ and for atom interferometers it reads $E_{\text{at}} = mc^2$. Here ω describes the angular frequency of the total employed laser light field, c the speed of light and m the mass of the exploited atomic species. Since typically $E_{\text{at}} \gg E_{\text{ph}}$, the induced rotational phase shift in an atom interferometer must be much larger than in its optical analogue for equal areas A .

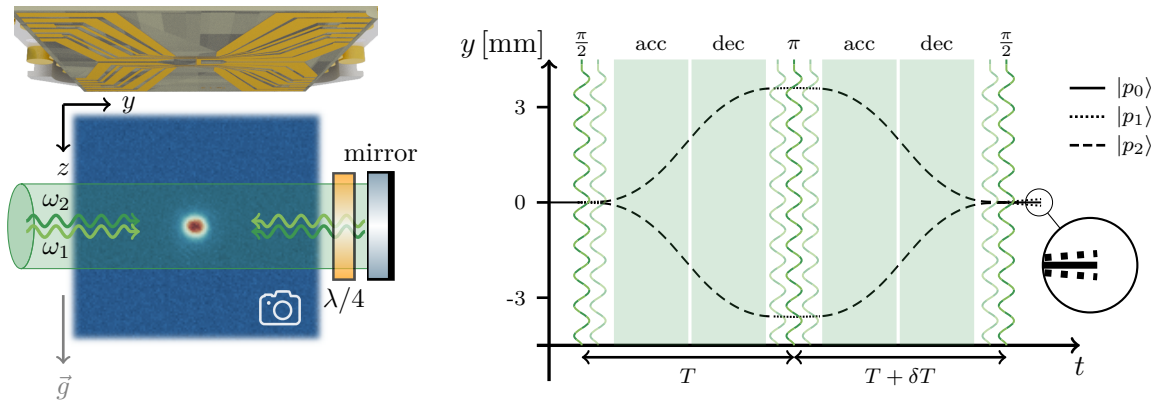


Figure 3.4: **Left:** Geometric representation of the horizontal light field for the twin-lattice interferometer sequence. The chip's magnetic fields are used for state preparation, but instead of using the surface coating as a retroreflector, as done in the fountain gravimeter, a combination of a mirror and a quarter wave located outside the vacuum chamber is used. The reflected beam containing two cross-polarized frequencies ω_1 and ω_2 propagates along the y -axis, creating two moving lattices. As an example of the detection method, one absorption image of a BEC showing its density distribution is featured in the background. **Right:** Space-time trajectories of the wave packets during the twin-lattice interferometer with the symmetric momentum transfer in $\pm y$ -direction, exemplarily depicted for a momentum transfers of $\Delta p = 408\hbar k$, a time $2T = 12.1$ ms and the time $\delta T = 0$. The individual pulses are symbolized by wavy lines and the momentum states are represented by dashed, dotted and solid lines. The y -axis is scaled in mm and the zoom in shows the three output ports separated in space. The space-time area enclosed by the interferometer also illustrates that a geometrical region is enclosed, allowing sensitivity to rotations.

So far, however, very different enclosed areas have been achieved. The twin-lattice interferometer achieved an area of $A = 7.6 \times 10^{-6} \text{ m}^2$ [Geb20], a juggling fountain configuration along with a four-pulse sequence an area of $A = 11 \times 10^{-4} \text{ m}^2$ [Sav18; Dut16] and a trapped-atom interferometer $A = 0.5 \times 10^{-6} \text{ m}^2$ [Moa20]. Comparing this to light interferometers, which have shown areas like $A = 16 \text{ m}^2$ [Sch11], there are obviously still orders of magnitude difference. Nevertheless, the smaller areas of atom interferometers can be realised much more compactly compared to their photonic counterpart and in principle offer higher sensitivities.

3.2.1 Proof of principle performance

In the following, an exemplary twin-lattice sequence is described to serve as a proof of principle. It begins with the generation of a BEC of up to 1.5×10^4 atoms of ^{87}Rb in the magnetic state $|F = 2, m_F = 2\rangle$ generated using the trapping and cooling functions of the atom chip, as detailed in section 2.1.1. After release a state preparation is performed, including delta-kick collimation followed by an adiabatic rapid passage to the non-magnetic state $|F = 2, m_F = 0\rangle$. The large momentum transfer itself is based on two counter-propagating lattices via Bloch oscillations [Ben96; Cla06; Mül09; Cla09; McD13], realized by sweeping the frequency difference between $\omega_1(t)$ and $\omega_2(t)$. Before the atoms are loaded into these lattices, the initial degeneracy between them must be lifted. This is done by a sequential double Bragg diffraction $\pi/2$ -pulse that creates an initial momentum superposition of $|p = \pm 4\hbar k\rangle$. Details of the involved steps and

limitations are also discussed in [Ahl16]. Although the beam splitting and recombination pulses can theoretically also be realized with Raman transitions, only Bragg transitions are used here. Subsequently, the two ensembles are adiabatically loaded into their respective co-propagating lattice counterpart for a time $\tau_{\text{load}} = 200 \mu\text{s}$ and then accelerated. In this way a maximum momentum separation between the two interferometer arms of up to $\Delta p = 408 \hbar k$ is achieved. These temporal steps are symbolized in figure 3.4 on the right with wavy lines for the double diffraction processes and shaded areas for the Bloch oscillations. To mirror the momentum states for the second half of the interferometer a three pulse combination is applied that inverts the atomic momentum to $|p = \mp 4\hbar k\rangle$ that can be summarized as a sequential double Bragg π -pulse. Afterwards the ensembles are accelerated again to the same momentum separation Δp as before and decelerated again down to $|p = \pm 4\hbar k\rangle$ to be able to close the interferometer with a final sequential double Bragg $\pi/2$ -pulse. The difference now is that the trajectories point towards each other to allow spatial overlap. The interferometer is closed by a final sequential double Bragg diffraction $\pi/2$ -pulse. After a waiting time of $\tau_{\text{det}} = 9 \text{ ms}$ the three wave packets leaving the interferometer have spatially separated and can be imaged using absorption detection. In the exemplary setup the twin-lattice sequence can be realized with a total interferometer time of up to $2T = 12.1 \text{ ms}$, of which the atoms spend up to 8 ms in the optical lattice.

A common technique to determine the performance of the interferometer in terms of amplitude, offset and contrast is the stepwise increase of the laser phase ϕ_L (see section 2.2) and then measure the sinusoidal oscillations of the output populations that occur. However, in the case of twin-lattice configuration this is not possible due to the symmetric imprinting onto both interferometer arms. Nonetheless, the inertial vibrations present on the non-vibration-isolated experimental apparatus, corresponding to a background noise of about $10^{-2} \text{ m/s}^2/\sqrt{\text{Hz}}$, shift the output phase ϕ of the interferometer by more than 2π from one experimental shot to the next. This effect is already visible for an interferometer without Bloch oscillations, a total momentum separation of $\Delta p = 8 \hbar k$ and a free evolution time of $2T = 10 \text{ ms}$.

Taking the assumption into account, that the random changes in phase are corresponding to white phase noise, one can still perform a statistical analysis to obtain the performance values [Gei11]. Repeating the same sequence for a sufficient amount of cycles creates a statistical distribution of the output port population, which can be split into equidistant intervals resulting in a histogram as also depicted in figure 3.5. The output phase ϕ can be extracted, modulo 2π , from the normalized output population in the following way

$$P(\phi) = P_0 - \mathcal{A} \cdot \cos(\phi) = \frac{N_A}{N_A + N_B}. \quad (3.2)$$

Here P_0 defines the offset of the distribution, \mathcal{A} its amplitude and N_A and N_B the populations of the inner and the two outer output ports. It is worth mentioning that in the case of interferometry with double diffraction, the atom numbers in the two outer ports are added and treated as one. Without additional influences, the population of those changes symmetrically. The visible double peak structure results from the fact that the probability to find an output

state at the top or bottom of a sinusoidal pattern is larger than at the mid position. As a fitting routine to this data set a kernel density estimation (KDE) is chosen [Rud82], which is shown in blue in figure 3.5. This routine helps to make more sophisticated statements about the population based on the finite data sample at hand, especially for the extracted amplitude, offset and contrast values. Its adjustable parameter is the bandwidth, which determines how smooth the output appears. For further analysis, the two peaks on either side of the distribution are represented by a Gaussian fit in green and red with

$$f_{\text{Gauss}}(P) = a_0 \cdot \exp\left(-\frac{(P - P_0)^2}{\sigma^2}\right). \quad (3.3)$$

Here a_0 defines the amplitude, P_0 the center shift, and σ^2 the standard deviation of the fit. Both fitted distributions show consistency with the KDE estimation. Therefore to extract the contrast $C = \mathcal{A}/P_0 = 0.87$ from this data set and the corresponding fit information, the offset P_0 and amplitude \mathcal{A} of the signal are calculated as depicted by the annotations in figure 3.5. In general, it can be assumed that the similar broadening of the Gaussian curves is dominated by technical and non-inertial noise contributions. One possibility to estimate the effect on the interferometer phase is based on the standard deviation as follows $\sigma_\phi = 2\sigma/C \approx 100$ mrad. This contribution appears relatively large, but in this case it is still smaller than the inertial contributions.

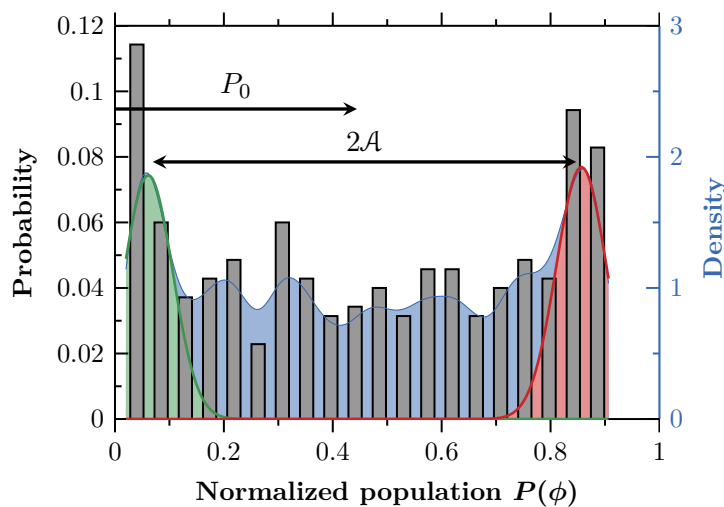


Figure 3.5: Histogram distribution (20 bins of equal distance) of the output signal of the twin-lattice interferometer sequence with a momentum transfer of $\Delta p = 8 \hbar k$ with a time $2T = 10$ ms for a total of 350 measurement cycles. The output phase ϕ of the interferometer is perturbed by more than 2π from one experimental shot to the next, leading to the formation of the double peak structure. From the offset P_0 and amplitude \mathcal{A} the contrast of $C = 0.87$ is calculated. The data set is fitted by a KDE (in blue) and two additional gaussian fits for the two peaks (green and blue) giving an estimate for the technical noise.

Statistical evaluations based on such histogram data require a sufficient number of points over typically several hundred experimental cycles. In addition it is necessary that the double peak structure can be sufficiently separated from each other. This may not always be given especially in the case of large technical noise or small amplitudes \mathcal{A} , which is observed for larger momentum separations Δp . An alternative way to make statements about the performance values of the interferometer is to add a temporal asymmetry δT , which changes the spatial overlap at the last beam splitter pulse [Kov15b]. This delay is added to the second duration of T and leads to a decrease of the spread of $P(\phi)$ and thus to a reduction of the contrast. The decrease itself depends on the coherence length of the atomic ensemble, while the remaining spread is dominated by non-inertial and technical noise components. For a sufficiently large asymmetry value δT , the interferometer is operated in an open configuration and the contrast C vanishes, leaving only those noise contributions.

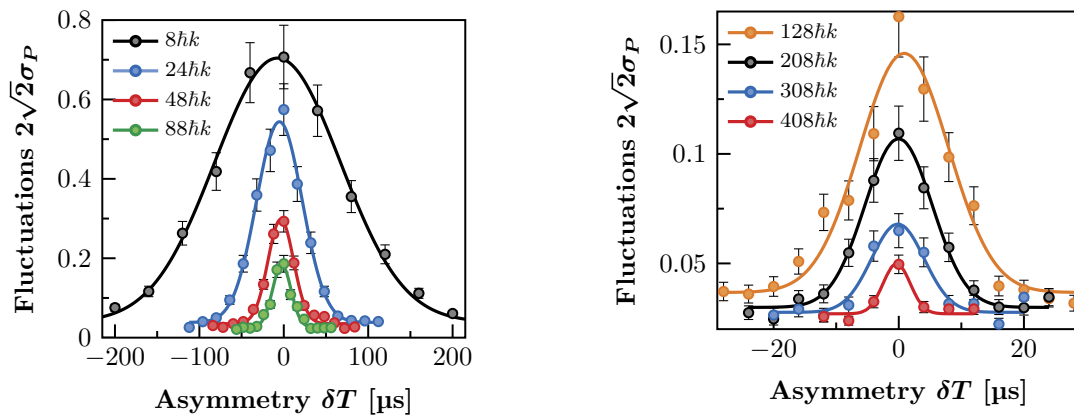


Figure 3.6: Measured atom number fluctuations $2\sqrt{2}\sigma_P$ at the twin-lattice interferometer in dependence of an introduced asymmetry δT for increasing maximum transferred relative momenta Δp and corresponding Gaussian fits for 40 data points each. The data sets are presented in two graphs with different axis scaling for better overview. The interferometer time is always fixed to $2T = 12.1$ ms. The contrast itself is proportional to the calculated values of σ_P . The asymmetry δT leads to a varying spatial overlap at the last beamsplitter pulse of the sequence. For larger values of maximum relative momenta Δp the widths and maxima of the fits decrease. (adapted from [Geb21])

For each individual value of δT , a corresponding contrast value can be estimated based on the standard deviation σ_P of the normalized population spread for a sufficiently large enough data set [Mül08a]. Figure 3.6 shows these measured fluctuations for twin-lattice sequences in terms of the calculated deviations $2\sqrt{2}\sigma_P$ as a function of the temporal asymmetry for different magnitudes of the maximum momentum separations Δp . The data sets are presented in two graphs with different axis scaling for better overview. For each momentum value, the asymmetry δT is varied and the different values of $2\sqrt{2}\sigma_P$ are fitted by Gaussian envelopes, analogous to equation 3.3, to obtain their widths $\sigma_{\delta T}(\Delta p)$. According to the publications [Geb21; Kov15b] the contrast and its dependance on the asymmetry δT can be directly related to the transferred

momentum Δp as follows

$$C(\Delta p, \delta T) = 2\sqrt{2}\sigma_P(\delta T) \cdot \exp\left(-\frac{1}{2}\left(\frac{\Delta p}{\hbar}\right)^2 \sigma_v^2 \delta T^2\right). \quad (3.4)$$

Here, the value for σ_v represents the momentum width of the atomic ensemble along the direction of the twin-lattice light field, which is measured to $\sigma_v = 0.18 \pm 0.03$ mm/s. The individual fits confirm that the largest value is always found near $\delta T = 0$, corresponding to a fully closed interferometer, and that its maximum is reduced for larger momentum values Δp . It is also observable that the width of these fits $\sigma_{\delta T}$ decreases for these values, which is a result of the lower spatial overlap of the wavepackets at the output ports for larger transferred momentum values.

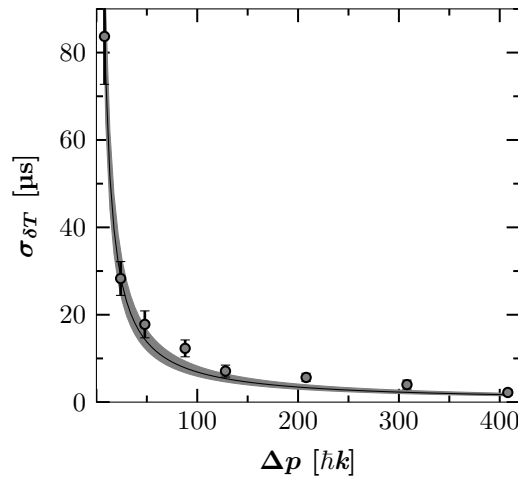


Figure 3.7: Coherence time evaluation for the twin-lattice interferometer. The calculated widths $\sigma_{\delta T}$ of the envelopes from figure 3.6 show a decay with the inverse of the maximum relative momentum Δp for a constant spatial coherence length. The line represents the theoretically calculated fit $\sigma_{\delta T} = \hbar/(\sigma_v \Delta p)$ with a value of $\sigma_v = (0.18 \pm 0.03)$ mm/s and the corresponding uncertainty as a gray shaded area. (adapted from [Geb21])

To better illustrate the dependencies of the individual widths $\sigma_{\delta T}$, obtained from the data sets shown in figure 3.6, they can be plotted as a function of the transferred momentum as depicted in figure 3.7. The emerging inverse proportionality shows not only how the width decreases, but also how the spatial coherence length is affected for higher transferred momentum values. The solid line depicts the corresponding theoretical values obtained with $\sigma_{\delta T} = \hbar/(\sigma_v \Delta p)$. The gray shaded area depicts the uncertainty of the momentum width σ_v . Overall the agreement between the theoretical calculated curve and the data points indicates that the performed coherent manipulations do not reduce the spatial coherence length of the atomic ensemble contributing to the interference signal.

3.2.2 Contrast reduction analysis

The atom number fluctuations $2\sqrt{2}\sigma_P$ for the realisations of the twin-lattice interferometers shown in figure 3.6 represent the sum of technical, or non-inertial noise sources plus inertial contributions. A decrease in peak contrast C was observed with increasing number of Bloch oscillations and thus maximum achieved momentum separation Δp . For further analysis, their dependence is shown in figure 3.8.

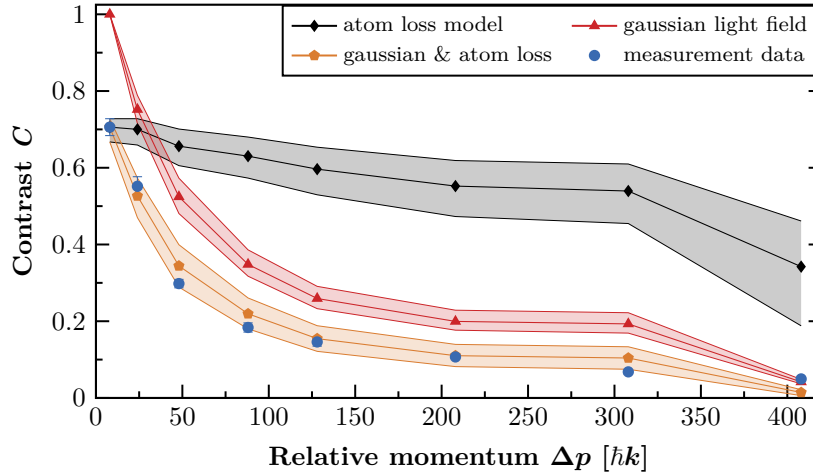


Figure 3.8: Dependence of the experimentally determined contrast C values (blue dots) on the maximum relative momentum Δp together with theoretical models based on atom losses due to non-adiabatic transitions (black diamonds) and local inhomogeneous dipole forces due to light field distortions (red triangles). Both combined (orange pentagons) are used to model the experimentally determined contrast. Only a single parameter describing the magnitude of the intensity perturbations was used for fitting. The best agreement was obtained with 9% variations of the lattice depth V_0 . The shaded areas represent confidence intervals of the simulation, determined by atom number and lattice depth uncertainty. (adapted from [Geb21])

Three main parameters change between the different experimental sequences. These are the remaining detected atomic number N , the lattice depth V_0 and the maximum relative momentum Δp , which leads to different spatial trajectories. Looking directly at the absorption images of the output ports, it can be found that fewer atoms N are detected for larger pulse separation sequences. A decreasing number of atoms is not only a reason for higher noise contributions, but also directly affects the achievable interferometric contrast [Chi11]. Nevertheless, it cannot alone explain the observed contrast loss. Instead, many additional effects related to the spatial quality of the applied light fields lead to loss of contrast in the interferometer and/or loss of interfering atoms.

In general, all atom-optical diffraction mechanisms suffer mainly from three types of imperfections: (i) The loss of output port populations, (ii) the emergence of spurious interferometer paths and (iii) additional phase errors [Jen22]. Since the gaussian shaped beam of the twin lattice is passing by design close to the atom chip source, a clipping of the beam can be observed.

The resulting imperfect laser beam profile leads to different dephasing processes, caused by the spatially varying intensity distribution. In this context, it is important to mention that the relevant perturbations are below the expansion size of the atomic ensemble. Consequently the atomic trajectories of the interferometer arms are differently influenced by these path-dependent effects. A more detailed numerical analysis of the influence of such spatially varying intensity fluctuations on the twin-lattice interferometer contrast can be found in the supplementary material of [Geb21] and in the doctoral thesis of J.-N. Kirsten-Siemß [Sie23]. In this thesis a model of an ideal Gaussian beam profile of the interferometry light beam is distorted by diffraction at the edge of the atom chip. The hereby arising path-dependent dipole forces act on the atoms via the gradient of the distorted beam potential. They are caused by the energy shift of an atomic state by an amount proportional to the local laser intensity. The potential can be written with the normalized intensity distribution as

$$U(j, \Delta p) = V_0(\Delta p) \frac{I(j)}{I_0}, \quad (3.5)$$

in dependence of the relative momentum separation Δp and the lattice depth V_0 . Integration of the dipole force for the duration $2T$ along the right and left arm of the interferometer can result in a differential momentum $\Delta m_{j,a} = m_{j,\text{left}} - m_{j,\text{right}}$ between them, with $j = \{y, z\}$ and $a = \{\text{left}, \text{right}\}$ defining the two arms. This yields

$$\begin{aligned} m_{j,a}(2T, \Delta p) &= - \int_0^{2T} \frac{\partial}{\partial j} U(y_a(t, \Delta p), z_a(t, \Delta p)) dt \\ &= - \frac{V_0(\Delta p)}{I_0} \int_0^{2T} \frac{\partial}{\partial j} I(y_a(t, \Delta p), z_a(t, \Delta p)) dt. \end{aligned} \quad (3.6)$$

This connection implies that the local intensity changes affect the differential momentum and in turn can lead to a spatially dependant phase difference $\delta\varphi_j = \Delta m_j \frac{j}{\hbar}$ that is linked to the initial density distribution of the atomic cloud. The effective interferometric contrast C for a particular $\Delta m_j(\Delta p)$ can be predicted by integrating the atomic density distribution

$$C(\Delta p) = \left| \iint |\Psi_{(0\hbar k, \pm 2\hbar k)}(y, z, t = 2T)|^2 \exp\left(-\frac{i}{\hbar}(\Delta m_y y + \Delta m_z z)\right) dy dz \right|. \quad (3.7)$$

This approach, using a parameter-dependent phase, is based on [Eks93]. The function $\Psi_{(0\hbar k, \pm 2\hbar k)}(y, z, t = 2T)$ describes the ensemble density of the interfering wave packets at the end of the sequence $t = 2T$ at the output ports with momenta $0\hbar k$ and $\pm 2\hbar k$ modeled by Thomas-Fermi density distributions. In theory, the initial spatial as well as the velocity distribution should be accounted for, but to simplify the problem, the effect of the initial velocity distribution on the different trajectories is neglected. To account for the spatial extent of the initial atomic ensemble, 1360 single particle trajectories with different positions at $t = 0$

inside the Thomas-Fermi radius are calculated. The final contrast values $C(\Delta p)$ are therefore providing averaged results of those individual, weighted contrast values. If the atoms propagate on different trajectories through a distorted light field the gradient $\frac{\partial}{\partial j}U(j)$ of the distorted beam potential lets them experience path-dependant dipole forces.

This model of the distorted gaussian light field is used in combination with the model for the atomic losses due to spontaneous emission and Landau-Zener losses to model the observed contrast behavior, as shown in figure 3.8 in orange. Only a single parameter describing the magnitude of the intensity perturbations was used for fitting. The best agreement was obtained with a value of rounded 9% of the lattice depth V_0 .

While the symmetric momentum transfer together with the observed spatial coherence up to a maximum splitting of $\Delta p = 408 \hbar k$ already represents one of the largest momentum separations in an interferometer reported to date, strategies can still be developed that should make it possible to go beyond this. Chapter 4 presents two of those, namely the application of a flat-top shaped beam profile with less susceptibility to distortions and a frequency compensation technique for light shift effects.

3.3 Differential interferometry using a Bose-Einstein condensate

Twin-lattice interferometry offers potential to be used for inertial sensing by forming symmetric interferometers featuring matter waves with large relative momentum. However, it is not able to distinguish between rotational phase shifts and those caused by accelerations of its inertial reference. In particular, in the presence of high vibrational noise, no measurement of rotations could be performed. If no vibration damping systems are available to suppress the movement of the reference, the acting accelerations could be measured with an external sensor and the inertia-induced phase shift can be calculated with a correlation algorithm (for reference see section 2.3). Such an approach not only increases the complexity of the system, but also requires good knowledge of mechanical transfer functions. Therefore, it seems beneficial to find ways to already intrinsically suppress such influences and to distinguish between inertial effects in a single measurement run.

For such a case, a differential measurement geometry is presented in the following, which is based on the combination of two perpendicular beam splitter axes. The main idea is to use two simultaneous interferometers generated from a single BEC and read out their two individual phases [Ger20]. In the following, it is referred to as a dual BEC interferometer, whose flow diagram in figure 3.9 illustrates the techniques used in the order described below.

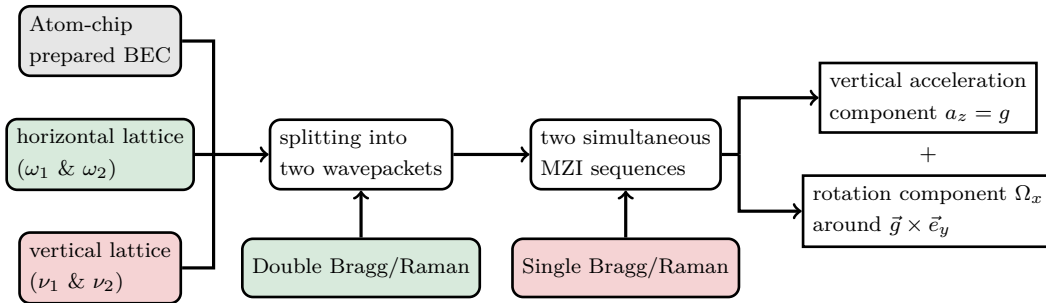


Figure 3.9: Flow diagram of a dual BEC atom interferometer sequence. The prepared BEC is manipulated by two perpendicular oriented optical lattices containing the frequencies ω_1 and ω_2 and ν_1 and ν_2 respectively. The horizontally aligned lattice (green) is used for an initial splitting, while the vertically aligned lattice (red) provides the necessary interrogation steps for two simultaneously operated interferometer sequences. With the help of the combined measured phase shifts, a distinction between rotation and acceleration components is made possible.

The experimental implementation of the used light fields can be understood as a combination of the individually described fields from sections 3.1 and 3.2. They consists of two retro-reflected combined optical lattices, as schematically shown in figure 3.10 on the left. In this illustration, the horizontally aligned lattice (ω_1 and ω_2) is used for an initial splitting, while the vertically aligned lattice (ν_1 and ν_2) provides the necessary interrogation steps for interferometry. Applying the first half of the concept from section 3.2, it is possible to split an initial BEC into two wave packets in horizontal direction using the precise momentum transfer of double Bragg diffraction with the possible addition of Bloch oscillations. Afterwards they separate apart from each other with a relative velocity \vec{v}_{sep} . The two ensembles can then be used for two Mach-Zehnder interferometers operated simultaneously. The approach of generating two sources for two interferometers from a single ensemble of atoms has also been of interest in previous publications [Per19; Mül08a; Bar19; Ase17]. It can avoid issues connected to using multiple sources, such as uncertainties in initial velocities and positions causing systematic errors in the differential output signal of the two interferometers [Ber15; Gau09; Dur06]. Since the splitting velocity \vec{v}_{sep} is orders of magnitude larger than the expansion rate of the ensembles, they can be well distinguished even after a time of flight on the order of milliseconds.

Figure 3.10 on the right shows how the trajectories of the two realized interferometers enclose two different regions (shaded areas), symbolized in a sketch below the atom chip representation. A detailed step-by-step overview of the sequence together with a proof of principle measurement follows in subsection 3.3.2. Nevertheless, the concept of phase sensitivities will already be explained here. In general, the output phase of each of the two interferometers is sensitive to a variety of effects, many of the unwanted ones are already suppressed in common mode due to the symmetrical nature of their origin. Section 2.2 only introduced and explained the basic concept how accelerations or rotations individually affect the measured interferometer phase shift ϕ . In the case of the dual BEC interferometer this can be exploited in a different way to differentiate between accelerations and rotations by adding or subtracting the half sum

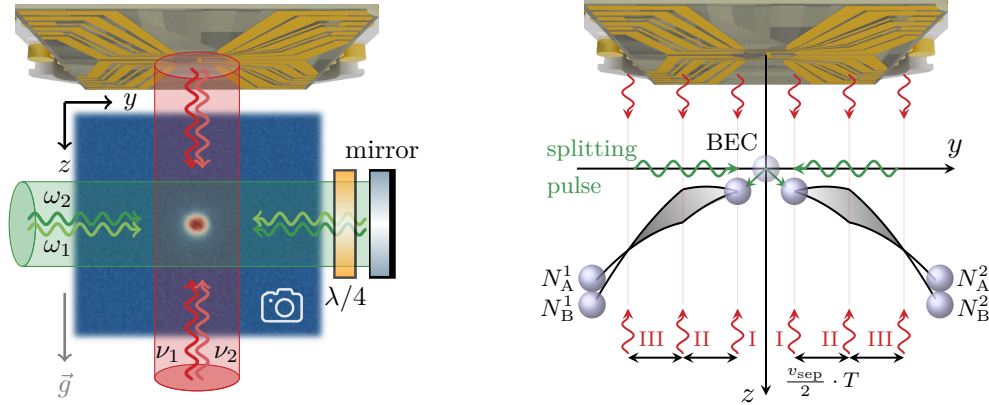


Figure 3.10: Left: Setup of the dual BEC atom interferometer. The combination of two vertically aligned retro-reflected light fields (red and green arrows) allows the manipulation of an atomic ensemble along two axes. **Right:** Schematic description of the dual BEC interferometer. The z -axis is aligned parallel to gravity \vec{g} . An initial BEC is split via double Bragg diffraction (green arrows) into two wave packets separating in y -direction with the velocity v_{sep} apart from each other. Two Mach-Zehnder-type interferometers are formed by three successive light pulses I, II and III (red arrows), separated by intervals of time T . The light pulses induce Bragg diffraction in an optical lattice retro-reflected from the atom chip located at the top. The enclosed areas of the interferometer trajectories are shown shaded in gray. The atomic densities at the output ports of the interferometers are detected via imaging the absorption of light propagating in the x -direction and pointing in the plane, and exploited to determine the number of atoms in the output ports $N_{A,B}^{1,2}$.

of the individual output phase shifts. This has the added advantage of suppressing ambient acceleration noise for the rotation phase and ambient rotation noise for the acceleration phase.

The total phase shift of the two interferometers can be formulated as $\phi_i = \phi_{a,i} + \phi_{r,i}(\vec{v}) + \phi_{L,i}$, where $\phi_{a,i}$ (see equation 2.3) denotes the phase contributions due to accelerations, $\phi_{r,i}$ (see equation 2.4) the contributions due to rotations and $\phi_{L,i}$ the laser phase contributions. If one calculates the half sum ϕ_{sum} and half difference ϕ_{diff} as follows

$$\begin{aligned}
 \phi_{\text{sum}} &= \frac{1}{2}(\phi_1(\vec{v}) + \phi_2(-\vec{v})) \\
 &= \frac{1}{2}(\vec{k}_{\text{eff}} \cdot \vec{a}T^2 + 2\vec{k}_{\text{eff}} \cdot \left(\vec{\Omega} \times \frac{\vec{v}_{\text{sep}}}{2}\right) T^2 + \phi_{L,1} \\
 &\quad + \vec{k}_{\text{eff}} \cdot \vec{a}T^2 + 2\vec{k}_{\text{eff}} \cdot \left(\vec{\Omega} \times -\frac{\vec{v}_{\text{sep}}}{2}\right) T^2 + \phi_{L,2}) \\
 &= \vec{k}_{\text{eff}} \cdot \vec{a}T^2 + \phi_{L,1} + \phi_{L,2},
 \end{aligned} \tag{3.8}$$

and

$$\begin{aligned}
\phi_{\text{diff}} &= \frac{1}{2}(\phi_1(\vec{v}) - \phi_2(-\vec{v})) \\
&= \frac{1}{2}(\vec{k}_{\text{eff}} \cdot \vec{a}T^2 + 2\vec{k}_{\text{eff}} \cdot \left(\vec{\Omega} \times \frac{\vec{v}_{\text{sep}}}{2}\right) T^2 + \phi_{L,1} \\
&\quad - \vec{k}_{\text{eff}} \cdot \vec{a}T^2 - 2\vec{k}_{\text{eff}} \cdot \left(\vec{\Omega} \times -\frac{\vec{v}_{\text{sep}}}{2}\right) T^2 - \phi_{L,2}) \\
&= 2\vec{k}_{\text{eff}} \cdot \left(\vec{\Omega} \times \frac{\vec{v}_{\text{sep}}}{2}\right) T^2, \tag{3.9}
\end{aligned}$$

one obtains two expressions that allow to distinguish between the rotation phase ϕ_r and the acceleration phase ϕ_a components, as they again resemble the original definitions of the equation 2.3 and 2.4. For the expression of ϕ_{diff} the laser phase contributions $\phi_{L,1}$ and $\phi_{L,2}$ are assumed to be equal due to the fact that both interferometers are operated in the same light field. Equation 3.9 shows that the differential phase ϕ_{diff} only depends on one velocity \vec{v}_{sep} . This is true to first order, because this velocity is solely generated by the well controllable momentum transfer of the splitting process. The output phase is therefore independent of any initial velocity \vec{v}_0 of the atomic ensemble. In the case of equation 3.8 for the sum phase ϕ_{sum} spurious contributions due to a non zero initial velocity \vec{v}_0 may arise. These are neglected in the formula, because they can be reduced by the well-controlled release of the BEC from its magnetic trap. It has been shown that this can be less than $\pm v_0 = 60 \mu\text{m/s}$ per shot [Rud16; Abe17].

3.3.1 Multi-axis operation

The concept of the dual BEC interferometer can be taken further to measure six degrees of freedom, more precisely Ω_x , Ω_y and Ω_z , as well as a_x , a_y and a_z . The most simple option is to create two wave packets along three perpendicular axes which can subsequently be used for interferometry. This leads to the scheme shown in figure 3.11. If these three sets are combined and successively measure all three components of $\vec{\Omega}$ and \vec{a} they form the basis for a complete quantum inertial measurement unit. As can be seen three perpendicular oriented optical lattice light fields are needed, ideally in a symmetric configuration. To explain the general concept in more detail, it is assumed in the following that the original atomic ensemble is at rest and that no (constant) accelerations or rotations are present. This corresponds to a microgravity environment such as would exist on the ISS or on a satellite [Agu14; Ave20; Fry21].

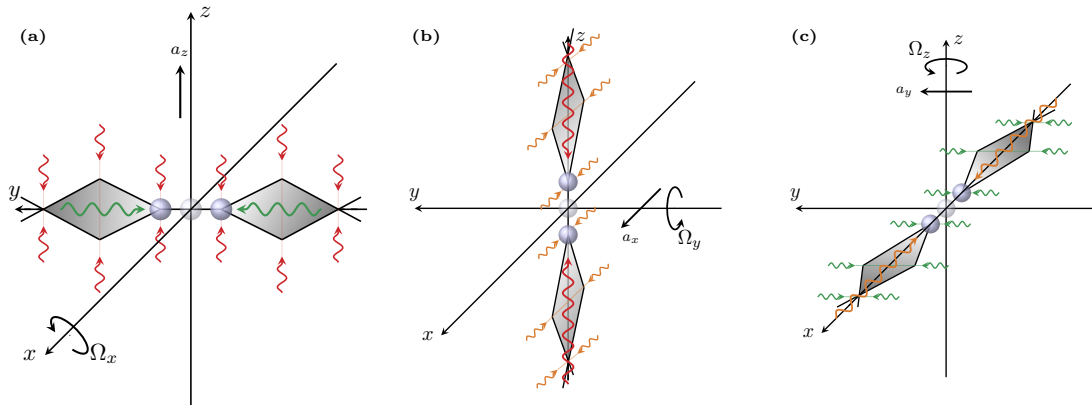


Figure 3.11: Three perpendicular oriented optical lattices in orange (along x -axis), green (along y -axis) and red (along z -axis) help to form an extension of the dual BEC scheme to successively detect all three components of $\vec{\Omega}$ and \vec{a} . For illustration purposes it is assumed that the original atomic ensemble is at rest and that no (constant) accelerations or rotations act on it. **(a)** This scheme shows the initial trajectories from figure 3.10 (right) without the influence of the gravitational acceleration \vec{g} . The output phase is sensitive to accelerations a_z and rotations Ω_x **(b)** Employing a double diffraction process to create two initial wave packets along the z -axis and an additional optical lattice (orange arrows) along the x -axis creates two interferometers that are in total sensitive to Ω_y and a_x . **(c)** In order to measure the remaining components Ω_z and a_y as well, the direction of the initial splitting process is changed again to generate the initial wave packets along the x -axis.

Since all three axes are occupied by beam-splitting light fields in this configuration, absorption imaging of the final population distributions can only be performed off-axis, e.g. under an angle of 45° with respect to any of the coordinate axes, by an additional light field. The projection of these on a single CCD camera would still be sufficient for all three geometries if the final separation is large enough. A typical initial ensemble has a size of roughly $20\ \mu\text{m}$ and an expansion rate of about $0.3\ \text{mm/s}$, corresponding to a delta-kick collimated BEC. With a separation velocity of $v_{\text{sep}} = 94\ \text{mm/s}$, the detected atomic clouds should therefore be well separated and individually resolvable after less than $1\ \text{ms}$. If the use of an additional light field is to be avoided, the detection of the output port populations can also be carried out with the aid of fluorescence detection, whereby the light field required for this can be applied via one of the existing optical access points.

In order to understand the exact functioning of the multi-axis operations, the individual steps are explained in more detail. First of all first-order or higher-order double diffraction generates two wave packets (see section 2.2.2 or 2.2.4), each with a velocity of $\vec{v}_{\text{sep}}/2$ and travelling perpendicular to the respective acceleration component that is to be measured. For an increase of the interferometry areas A_i , and consequently the achievable rotational phase sensitivity, transferring more momentum during this splitting can be preferable. In this context, the use of a twin lattice, as described in section 3.2, is an option. To achieve constant lattice depths during this operation, without the need of changing the overall laser power, exploiting non-gaussian beam profiles with more homogeneous intensity distributions is appealing.

For example, a flat-top, as shown in the section 4.1, would make this possible. After the initial wave packet splitting the Mach-Zehnder sequence is applied for all geometries using light pulses driving again either Bragg or Raman processes inside the second optical lattice. This lattice is perpendicular oriented to the respective \vec{v}_{sep} and the initial splitting. To enhance the sensitivity of one or all of the interferometers, employing higher order diffraction processes is also possible here. The measurement of all six degrees of freedom can potentially be performed in one single experimental run, but one has to take into account, that the individual diffraction orders may parasitically interact. The intended modus operandi of a six-axis inertial measurement is therefore sequential, helping to avoid problems associated with crosstalk between diffraction processes along different measurement axes and reducing the absolute demand for laser power.

As an example of such crosstalk, the first order diffraction pulse of geometry **(a)** in figure 3.11 along the z -axis (red arrows) that is meant to perform the beam splitting operation would also interact with the two wave packets created in geometry **(c)** as both wave packet sets have the same relative velocity along the splitting z -axis (in this case ideally zero). Therefore one would end up with more than the typical $n = 6$ interferometric output ports $N_{\text{A,B}}^n$.

In the presence of a constant acceleration, for example the gravitational acceleration \vec{g} acting along the direction of the z -axis, the geometry is changed as can be seen in figure 3.12. In order not to go beyond the scope of further consideration, it is assumed that the orientation of the geometry does not change during operation. In principle, with an active position adjustment, the coordinate system can always be oriented so that one axis points in the direction of the largest constant acceleration component. Perpendicular to gravity the retro-reflected light field naturally induces double diffraction, but in the direction of gravity this is true only when the atomic ensemble is not yet accelerated. As can be seen in figure 3.12 **(a)**, the two ensembles moving apart in the y -direction acquire an additional velocity component in the z -direction, so that the interferometry pulses (red arrows) lead to single instead of double diffraction processes. Due to the time taken by state preparation (see section 2.1.2) before the first splitting, the ensemble is usually also not at rest for the initial splitting. This presents a challenge for the geometry **(b)** from figure 3.12. Nevertheless, double diffraction can be achieved by adding an additional frequency component [Mal10].

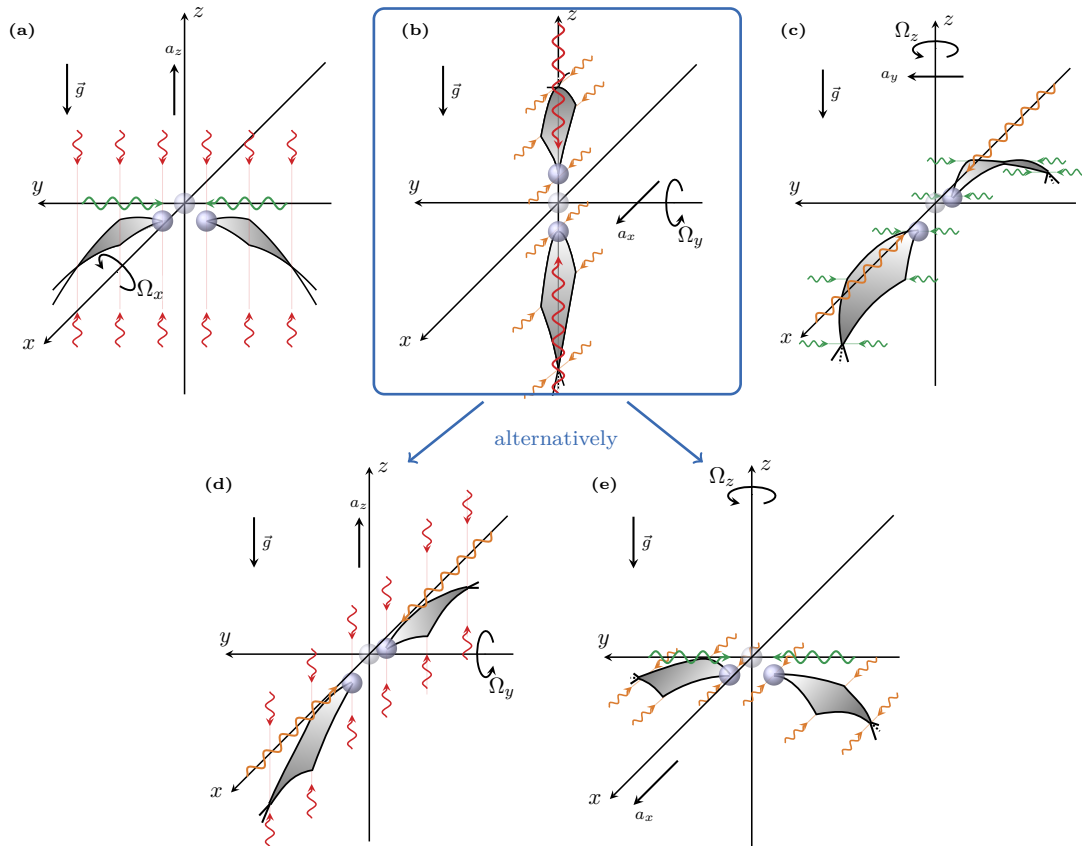


Figure 3.12: The geometries shown in figure 3.11 change in the presence of a constant acceleration acting, in this example gravity \vec{g} is pointing along the direction of the z -axis. The resulting changes are described individually. **(a)** The two ensembles moving apart in the y -direction acquire an additional velocity component in the z -direction, so that the interferometry pulses (red arrows) lead to single diffraction transitions instead of double diffraction processes. **(b)** The initial splitting cannot be performed without additional steps, like an accelerated optical lattice or a relaunch. Furthermore the enclosed geometric areas of the two interferometers are not equal. **(c)** The initial splitting and the Mach-Zehnder sequence can be applied largely unperturbed since \vec{g} is perpendicular to both interrogating light fields. As an alternative to the geometry **(b)**, the two geometries shown in **(d)** and **(e)** can be used. In this case the measurement of all six degrees of freedom of $\vec{\Omega}$ and \vec{a} can be performed with four measurements in total. The difference is that in this case Ω_z and a_z are determined twice. With the shown orientation, all initial splitting processes naturally occur with double diffraction, while only the interferometry pulses oriented in the z -direction lead to single diffraction. (adapted from [Ger20])

Another approach would be to implement the fountain sequence as described in section 3.1, which launches the initial ensemble back to the position of nearly zero relative velocity where double diffraction naturally occurs. Also, it is important to note that the enclosed areas of the two interferometers may not be equal ($A_1 \neq A_2$), resulting in imperfect suppression of rotational noise in the sum phase ϕ_{sum} . For the difference signal ϕ_{diff} the acceleration noise is still suppressed. To compensate for this drawback, a hybrid approach in the form

of a classical accelerometer could help to remove the influence of \vec{g} from this phase by correlation.

To circumvent the mentioned issues from geometry **(b)** in figure 3.12 it may make more sense to realize four measurements instead of three. Replacing **(b)** with **(d)** and **(e)** also yields a measurement set of all six degrees of freedom, with the difference that Ω_z and a_z are determined twice. Depending on the application, this double determination of the rotational component Ω_z can provide an additional advantage. In inertial navigation, for example, it is the most important component. With the orientation shown, all initial splitting processes naturally occur with double diffraction, while the interferometry pulses oriented in the z -direction lead to single diffraction.

When considering to use the presented scheme for navigation purposes, the additional influence of a dynamic environment must be considered. Chapter 6 deals with such an approach and therefore provides deeper explanations. An immediate effect is the modification of the interferometer trajectories in different, possibly unequal ways. One implication already visible under the influence of the gravitational acceleration can be seen in geometries **(c)** and **(e)** in figure 3.12. Because of the curvature there, the area vectors $\vec{A}_{1,2}$ do not point in the same direction. This means that the measured phase difference ϕ_{diff} based on equation 3.9 cannot be directly translated into the rotation component around the z -axis. Therefore in order to calculate the quantity Ω_z , it is also necessary to know the acceleration component along this axis, which shows that this information is needed from at least one other measurement.

3.3.2 Proof of principle performance

To demonstrate the correlation and noise reduction capabilities of the dual BEC interferometer, a sample measurement set is performed based on the geometry shown in figure 3.10 on the right. It starts with the generation of a BEC of up to 1.5×10^4 atoms of ^{87}Rb in the magnetic state $|F = 2, m_F = 2\rangle$ generated using the trapping and cooling functions of the atom chip. After release a state preparation is performed, including delta-kick collimation followed by an adiabatic rapid passage to the non-magnetic state $|F = 2, m_F = 0\rangle$. Afterwards the ensemble is symmetrically split using first-order double Bragg diffraction along the y -axis. After the splitting process, two wave packets travel apart from each other with a relative velocity of $v_{\text{sep}} = 4\hbar k/m$ along the direction of the splitting pulse, while being forced on a parabolic trajectory due to the gravitational acceleration \vec{g} acting along the z -axis. Here m denotes the atomic mass of ^{87}Rb . The two individual wave packets are interrogated by a common optical lattice travelling in vertical direction along the z -axis in the manner of three successive first-order Bragg processes (I, II and III) to realize a Mach-Zehnder type sequence, as introduced in section 2.2. The lattice itself is formed by retro-reflecting the light beam from the coating surface of the atom-chip, which is depicted in figure 3.10 on the left. While the Bragg light pulses are separated in time by T , an additional time τ_{det} is needed for the atomic wave packets to separate before their populations $N_{\text{A,B}}^{1,2}$ can be detected using absorption detection.

Table 3.1: Parameters of the dual BEC interferometer defined as follows: beam diameter d of the vertically aligned gaussian shaped beam (shown in red in figure 3.10); detected atom number N ; initial effective temperature of the ensemble; pulse separation time T ; mean contrast C ; separation velocity v_{sep} ; momentum $\hbar k_{\text{eff}}$ transferred within the Mach-Zehnder sequence; and experimental cycle time t_{cycle} . The parameter set is in principle limited by the achievable space-time area of the interferometer, bounded by the beam diameter, which represents the maximum distance at which optical manipulations are still possible.

d [mm]	N	eff. temp. [nK]	T [ms]	C	v_{sep} [$\hbar k/m$]	$\hbar k_{\text{eff}}$ [$\hbar k$]	t_{cycle} [s]
6.6	$7.5 \cdot 10^3$	50	5	0.64	4	2	15

The most important operating parameters are summarized in table 3.1. To obtain data on the contrast of the interferometer and its noise properties, repeated measurements of the above experimental sequence with a stepwise increase $2\pi/14$ between 0 and 2π of the laser phases $\phi_{L,i}$ are performed and the two sets of initial populations $P(\phi_i)$ are recorded. In the absence of forces, this stepwise increase would typically lead to a sinusoidal fringe pattern of the output port populations, as explained in section 3.2.1. However the experiment is performed at the same non-vibration-isolated experimental apparatus and, hence, the sinusoidal dependence is not visible. Still modulo 2π , the individual output phases ϕ_i can be extracted from the normalized output population analogously as follows

$$P(\phi_i) = P_0 - \mathcal{A} \cdot \cos(\phi_i) = \frac{N_A^i}{N_A^i + N_B^i}, \quad (3.10)$$

where N_A^i and N_B^i describe the atom numbers in the two output ports of the i -th interferometer and their sum $N = \sum_{i=1}^2 (N_A^i + N_B^i)$ represents the total detected number of atoms.

The obtained data points for 246 experimental cycles are shown in figure 3.13. On the left side the output populations of the two interferometers (black and blue points) are plotted against the step-wise increased relative laser phase. Subsequently they are binned into two histograms with 20 bins each. Due to the statistical nature of the scattered data two double peak structures are formed. To extract the amplitudes \mathcal{A} of the interferometric signal and its mean P_0 a kernel density estimation is applied (compare to section 3.2.1 and figure 3.5). While the offset value P_0 is determined to be the same for both data sets, the two amplitudes are different. This allows to determine two individual contrast values $C_1 = 0.67$ and $C_2 = 0.59$ and a mean contrast of $C = \mathcal{A}/P_0 = 0.64$. Limitations that reduce this contrast value are first of all the achievable efficiencies of the individual Bragg processes. Furthermore remaining atoms in magnetic sub-states $m_F \neq 0$ that are affected by the linear Zeeman effect, spontaneous emission processes during atom-light interaction and spurious thermal background atoms contribute as well.

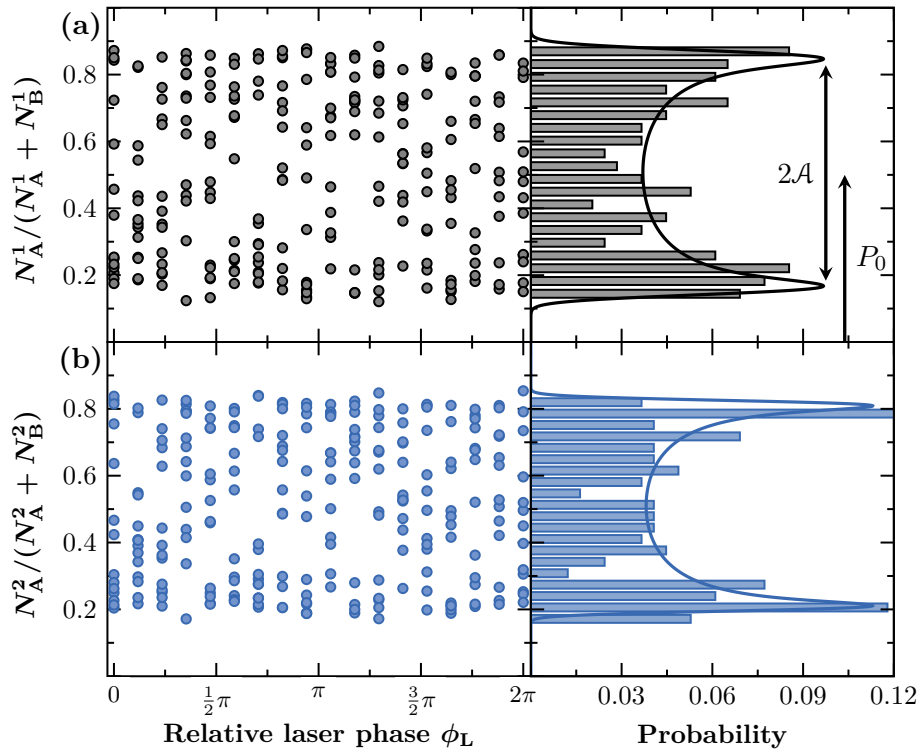


Figure 3.13: Output signals $P(\phi_i)$ of the two Mach-Zehnder interferometers from fig. 3.10 in the form of the normalized output port populations $N_A^i / (N_A^i + N_B^i)$. The signals are obtained by increasing the relative laser phase ϕ_L in steps of $2\pi/14$ between 0 and 2π . Due to the presence of vibrational noise the expected sinusoidal response is washed out (left-hand side). The histogram analysis with a corresponding fit based on a kernel density estimation (KDE) reveals a characteristic double peak structure reflecting the sinusoidal dependence of the interference signal on ϕ_L instead (right-hand side). The contrast $C = A/P_0$, given by the amplitude A of the signal divided by its mean P_0 , is extracted from the KDE fitting routine of the distribution analogous to section 3.2. (taken from [Ger20])

An additional problem may arise if the propagation of the Gaussian shaped interferometry beam is not completely centered on the z -axis, which corresponds to the release position of the BEC on the axis. This results in different pulse amplitudes for the Bragg processes and therefore affects their efficiency. In the here presented case the largest separation of the wave packets in y -direction is on the order of $600\ \mu\text{m}$, which is relatively small compared to the $6.6\ \text{mm}$ diameter of the beam. Consequently, only minor variations of the diffraction efficiency due to the different positions of the wave packets within the beam profile are expected, and the observed difference is more likely attributed to imperfections of the retro-reflection coating of the atom chip for the optical lattice, which is causing intensity fluctuations across the beam.

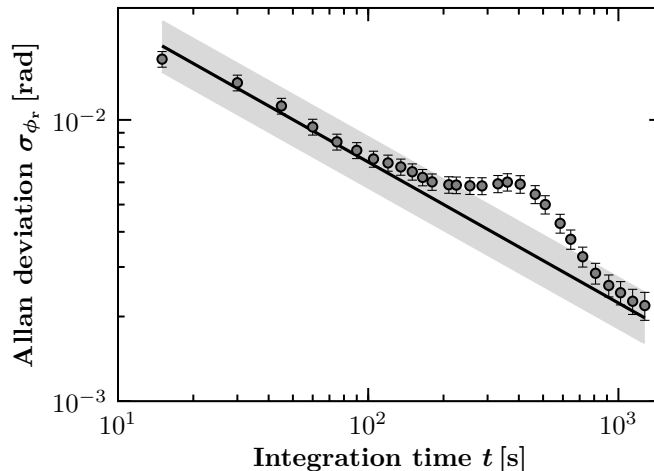


Figure 3.14: Overlapping Allan deviation of the differential phase ϕ_r for a dual BEC interferometer sequence with the parameters from table 3.1. The noise per experimental cycle can be estimated by the starting value of $\sigma_{\phi_r} = 16.4 \pm 2$ mrad. The solid line depicts an estimation of the quantum projection noise $\sigma_{\text{qpN}}(t)$, with the shaded area defining an uncertainty band due to the atom number determination in the experiment. The functional dependence of $1/\sqrt{t}$ agrees well with signal averaging in the presence of white noise. The peak at around 400 s, matches the modulation frequency of the air condition in the laboratory. (taken from [Ger20])

To calculate the differential phase ϕ_{diff} out of this data set the phases $\phi_{1,2}$ for each interferometer time series are calculated separately by solving equation 3.10 for ϕ_i and inserting the normalized populations P , offsets P_0 , and amplitudes \mathcal{A} , as depicted in figure 3.13. Afterwards taking the half difference according to equation 3.9 leads to one differential phase ϕ_{diff} per experimental cycle.

To assess information about the temporal characteristics of the signal the Allan deviation [All66] of this phase is calculated and shown in figure 3.14. From the starting point of this deviation, which is at the cycle time of $t_{\text{cycle}} = 15$ s, a single-shot phase noise equivalent of $\sigma_{\phi_r} = 16.4 \pm 2$ mrad can be obtained. Taking into account that the phase noise of the individual interferometer phases ϕ_1 and ϕ_2 is larger than 2π one can estimate that contributions from vibrational accelerations and the laser phase are suppressed by at least 22 dB in the differential phase ϕ_{diff} . At $t = 405$ s of integration time the Allan deviation shows a distinct peak or bump which matches the modulation frequency of the air condition present in the laboratory. After an integration time of $t = 1020$ s a value of $\sigma_{\phi_r} = 2.0 \pm 1$ mrad is reached.

To answer the question of what limits the measured phase sensitivities, they can be compared to the following estimate of quantum projection noise σ_{qpN} , which serves as an upper bound,

$$\sigma_{\text{qpN}}(t) = \frac{1}{2} \sqrt{\frac{1}{(C_1 \sqrt{N_A^1 + N_B^1})^2} + \frac{1}{(C_2 \sqrt{N_A^2 + N_B^2})^2}} \sqrt{\frac{t_{\text{cycle}}}{t}}. \quad (3.11)$$

Here t_{cycle} defines the time of experimental run and t the time of integration. The estimate is shown in figure 3.14 as a solid line with an uncertainty band in the form of a shaded area. This region is mainly determined by the uncertainty of the measured atomic number, which is estimated with a deviation of $\pm 50\%$ from the actual detected number of N_A^i and N_B^i . Overall, it is evident from the graph that the data points follow a $1/\sqrt{t}$ integration behavior and, except for the peak around $t = 405$ s, are close to the calculated limit defined by the quantum projection noise.

3.3.3 Sensitivity limit estimation

The calculated phase noise equivalents σ_{ϕ_r} can be used to estimate intrinsic sensitivities $\sigma_r(t)$ with respect to rotations. For this purpose, they must be multiplied by the response or scaling factor of the interferometer to rotational changes Ω , which is defined by the equation 3.9 and is as follows

$$\sigma_r(t) = \sigma_{\phi_r}(t) \cdot \frac{1}{k_{\text{eff}} v_{\text{sep}} T^2}. \quad (3.12)$$

This yields a single-shot sensitivity of $1.7 \cdot 10^{-3}$ rad/s at $t = 15$ s and a sensitivity of $2 \cdot 10^{-4}$ rad/s after $t = 1020$ s of integration time. The largest rotation contribution to the described measurement is the average angular speed of Earth's rotation. In an inertial reference frame it can be calculated to roughly $7.2 \cdot 10^{-5}$ rad/s, which means that in the shown measurement it is not resolvable.

To estimate the quantum projection noise limited sensitivity $\sigma_r(t)$, the same approach as in equation 3.12 can be followed, except that the phase noise equivalent σ_{ϕ_r} is replaced by the quantum projection noise $\sigma_{\text{qpn}}(t)$. This approach also applies analogously to accelerations and leads to the following equations

$$\begin{aligned} \sigma_r(t) &= \sigma_{\text{qpn}}(t) \cdot \frac{1}{k_{\text{eff}} v_{\text{sep}} T^2} \\ &= \frac{1}{2} \sqrt{\frac{1}{(C_1 \sqrt{N_A^1 + N_B^1})^2} + \frac{1}{(C_2 \sqrt{N_A^2 + N_B^2})^2}} \sqrt{\frac{t_{\text{cycle}}}{t}} \frac{1}{k_{\text{eff}} v_{\text{sep}} T^2}, \end{aligned} \quad (3.13)$$

$$\begin{aligned} \sigma_a(t) &= \sigma_{\text{qpn}}(t) \cdot \frac{1}{k_{\text{eff}} T^2} \\ &= \frac{1}{2} \sqrt{\frac{1}{(C_1 \sqrt{N_A^1 + N_B^1})^2} + \frac{1}{(C_2 \sqrt{N_A^2 + N_B^2})^2}} \sqrt{\frac{t_{\text{cycle}}}{t}} \frac{1}{k_{\text{eff}} T^2}. \end{aligned} \quad (3.14)$$

In the publication [Ger20] such sensitivity limits for two other scenarios based on different parameter sets of the dual BEC interferometer geometry are presented and calculated. As it turned out, one constraint that must be taken into account is the limited area defined

by the diameter of the lattice light beam $d \geq v_{\text{sep}} \cdot 2T$, symbolized by the red cylinder in figure 3.10 on the left. Assuming that the ensemble starts at the geometric center of the crossed beams and the available laser intensities are able to maintain coherent manipulations at the maximum distance for a given diameter d . Higher velocities v_{sep} imply a shorter time T and allow higher repetition rates which can be beneficial for an inertial navigation sensor. Of course, this only becomes important when the experimental cycle time t_{cycle} is of the same order of magnitude as the pulse separation time T . While extending the time T has in principle the advantage of increasing the acceleration and rotation sensitivity quadratically, to optimize a given system, the values for T and v_{sep} can be designed so that the atomic trajectories fit within the range given by the two crossed retro-reflected light fields (red & green).

Table 3.2: Two parameter sets for the calculated quantum projection noise limited sensitivities of the dual BEC interferometer $\sigma_a \sqrt{t}$ and $\sigma_r \sqrt{t}$. It should be noted that, for ease of comparison, these are presented as the slope of the functions defined in equation 3.14 and 3.13, which conveniently also reflect the value at $t = 1$ s. The input values are defined as the vertically aligned full-width-half-maximum of a flat-top shaped beam with diameter d , the detected atom number N , the pulse separation time T , a mean contrast C , a separation velocity v_{sep} , a momentum $\hbar k_{\text{eff}}$ transferred within the Mach-Zehnder sequence, and an experimental cycle time t_{cycle} .

d [mm]	N	T [ms]	C	v_{sep} [$\hbar k/m$]	$\hbar k_{\text{eff}}$ [$\hbar k$]	t_{cycle} [s]	$\sigma_a \sqrt{t}$ [(m/s ²)/ $\sqrt{\text{Hz}}$]	$\sigma_r \sqrt{t}$ [(rad/s)/ $\sqrt{\text{Hz}}$]
15	10^5	25	0.5	32	16	2	$1.1 \cdot 10^{-7}$	$5.9 \cdot 10^{-7}$
50	10^6	125	0.5	32	96	2	$2.3 \cdot 10^{-10}$	$1.2 \cdot 10^{-9}$

The choice of the two sets of parameters is explained below, and the values are summarized in table 3.2. For the first one, it is reviewed which realistic parameters can be chosen within an example volume of 4 cm^3 of a cube, which should contain all operations of the dual BEC interferometer. A separation velocity of $v_{\text{sep}} = 32 \hbar k$ and a time $T = 25 \text{ ms}$ are chosen such that the beam diameter $d = 15 \text{ mm}$ approximately corresponds to the (vertical) baseline of the interferometer ($\frac{1}{2}g(2T)^2 \approx 12 \text{ mm}$). To achieve a more uniform distribution of laser power, one could envision the use of a flat-top laser beam here, which is explored in more detail in section 4.1. The estimation for the contrast is based on the achieved values for the twin-lattice sequence, shown in figure 3.6. For a momentum transfer of $\hbar k_{\text{eff}} = 16 \hbar k$ it is reasonable to estimate it to be $C = 0.5$. The total cycle time of $t_{\text{cycle}} = 2 \text{ s}$ and atom number are based on the reported atomic flux of $N = 10^5$ per 1.6 s from the report [Rud15], which has a technologically similar setup based on an atom chip. These assumed parameters lead to a quantum projection noise limited acceleration sensitivity of approximately $\sigma_a \sqrt{t} \approx 10^{-7} \text{ (m/s}^2\text{)}/\sqrt{\text{Hz}}$ and a rotational sensitivity limit of approximately $\sigma_r \sqrt{t} \approx 10^{-7} \text{ (rad/s)}/\sqrt{\text{Hz}}$.

A navigation grade inertial measurement unit based on ring laser gyroscopes, achieves a noise density of $1.2 \times 10^{-6} \text{ (m/s}^2\text{)}/\sqrt{\text{Hz}}$ based on the angular random walk for accelerations and a noise density of $7.3 \times 10^{-7} \text{ (rad/s)}/\sqrt{\text{Hz}}$ for rotations [iNAT-RQT-4002, iMAR Navigation]. In comparison, the previously computed values alone are not directly outstanding, but they do

show possible applications in the field of inertial navigation, which is discussed in more detail later in the outlook section 6.1 of this thesis.

In contrast, higher sensitivities are often needed to study geophysical effects, such as the Earth's rotation. For these high-resolution can be performed by large ring laser structures [Sch11; Bev16], which can theoretically achieve sensitivities on the order of 10^{-11} (rad/s)/ $\sqrt{\text{Hz}}$. In order for the dual BEC interferometer to be competitive, the parameter set must be adjusted. An envisioned system in which it is implemented must be larger than the volume of the cube before with only a few cubic centimeters. The following values are chosen so that they do not appear completely unrealistic. The pulse separation time is therefore increased to $T = 125$ ms, which corresponds to a fall distance of about 35 cm for the atoms. Also the chosen beam diameter of the flat-top shaped laser beam is increased to $d = 50$ mm. An improved atom number of $N = 10^6$ and an enhanced momentum transfer of $\hbar k_{\text{eff}} = 96 \hbar k$ in the interferometer are assumed as well. This larger momentum transfer and beam diameter also require higher laser powers, which is, however, in the order of magnitude of the achievable powers of frequency-doubled fiber laser systems, as shown in section 4.2. In units, this would correspond to a laser power of 10 W which translates to a constant lattice depth of about $V_0 = 9 E_r$, in units of recoil energy, if 90% of the total power is uniformly distributed over the flat-top shaped beam.

With these challenging parameters at hand, quantum projection noise limited acceleration sensitivities on the order of $\sigma_a \sqrt{t} \approx 10^{-10}$ (m/s²)/ $\sqrt{\text{Hz}}$ and also rotation sensitivities of $\sigma_r \sqrt{t} \approx 10^{-9}$ (rad/s)/ $\sqrt{\text{Hz}}$ could be achievable with the presented dual BEC interferometer. At some point, however, the scaling of these values reaches its technical maximum, which in this estimate was limited by the diameter of the light beam. This in turn is defined by the available laser power, as mentioned above.

3.4 Multi-loop atomic Sagnac interferometry

It would be desirable to combine all the advantages of the approaches and techniques introduced in this chapter without their disadvantages or limitations. To move in this direction, a multi-loop atom interferometer in the following section employs the relaunch mechanism from section 3.1 combined with the large momentum transfer through a twin lattice from section 3.2, but is not restrained by small finite laser beam diameters as explained for the dual BEC interferometer in section 3.3.

To increase the measurement sensitivity of light interferometers without increasing the setup size, multiple loops can be formed. To realize an equivalent for matter-wave interferometers, several approaches have been proposed. One of them is to confine matter waves in tight waveguides, analogous to light in a fiber optic gyroscope. In this manner, long interrogation times and larger total enclosed areas, and thus higher sensitivities, can be achieved without having to increase the actual geometric area. Thus, compact but not always sensitive devices could be realized. [Arn04; Wu07; Moa20; Krz22]. While such fully guided or trapped systems have their benefits, they can also suffer from systematic effects of the guiding or trapping potential itself.

An alternative approach that attempts to take advantage of the same benefits, but without the constant confinement, is the multi-loop atom interferometer published in [Sch21] and presented here. It employs several different light pulses to form a scalable area.

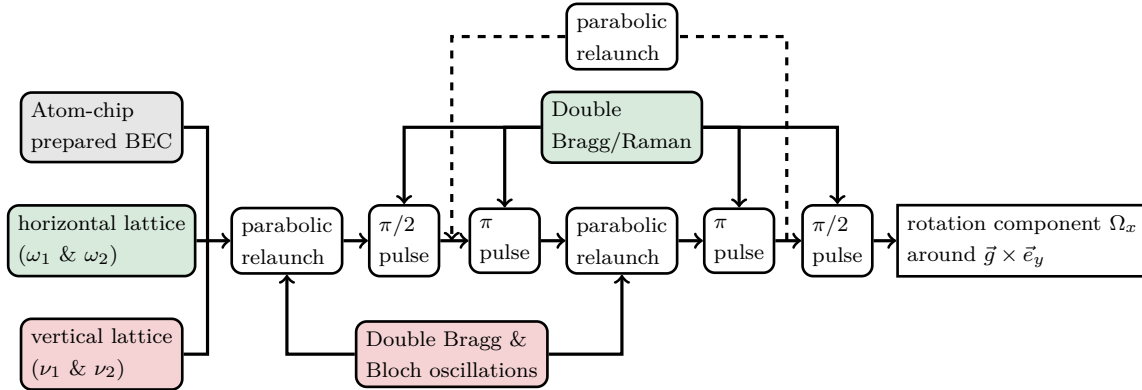


Figure 3.15: Flow diagram of a multi-loop atomic Sagnac interferometer sequence. The prepared BEC is manipulated by two perpendicular oriented optical lattices containing the frequencies ω_1 and ω_2 as well as ν_1 and ν_2 respectively. The individual techniques applied inside the lattice are highlighted by a green or red background. A four-pulse sequence ($\pi/2$ - π - π - $\pi/2$) is used instead of the Mach-Zehnder sequence frequently mentioned before. The relaunch process is always performed within the vertical lattice, while the interferometer pulses are applied within the horizontal lattice. The sequence can be repeated by forming $2n$ loop iterations, where $n = 1$ defines one loop in this flow diagram. For more details on the sequence, refer to the space-time diagram 3.17.

The approach uses free-falling atomic ensembles, implements a four-pulse interferometer sequence, and includes the ability to relaunch after each one, as shown in the flow diagram in figure 3.15. After each relaunch the atoms follow the same trajectories as before, multiplying the effectively enclosed geometric area. The geometry itself is shown in figure 3.16. It utilizes the same combination of light fields as before for the dual BEC interferometer from section 3.3. Under the simple assumption of neglecting loss of atoms and loss of contrast, which may scale with the number of loops due to imperfections in the atom-light interactions, a linear increase in the quantum projection noise limit of the sensitivity per cycle is obtained.

The detailed sequence can be understood as follows. First a BEC is generated below the atom chip, released from its trap and prepared as explained in section 3.2.1. After this step the atoms have moved a certain distance away from the horizontally aligned atom chip. Subsequently the ensemble is launched upwards by the light field consisting of ν_1 and ν_2 (red arrows) in the same way as explained for the fountain gravimeter in section 3.1. After the launched ensemble reaches the position (a) a horizontal beam splitting operation is applied with the retro-reflected light field consisting of ω_1 and ω_2 (green arrows), that interacts with the wave packet and forms two individual ones drifting apart with a momentum of $p = \pm\hbar k/(2m)$. After the drift time T , the two ensembles have reached the points (b) and (d) and the horizontal light field is applied again to invert their momentum. After having reached these two outermost points of the geometry the atoms drop until they reach the position (c) at a time $2T$. Here, at their lowest point their

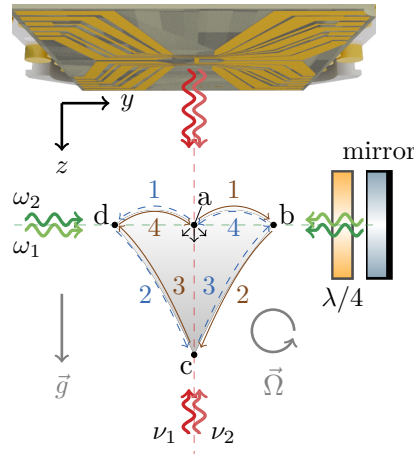


Figure 3.16: Trajectories of the multi-loop scheme within the the atom chip setup as employed in sections 3.1, 3.2 and 3.3. First, the atomic ensemble is created and prepared, during this time it falls in the direction of z . Afterwards it is launched upwards towards position (a) where a beam splitting pulse leads to a coherent superposition of two momentum states (blue, brown) that separate symmetrically apart (1). After they reach positions (b) and (d), their momentum is reversed and they are deflected toward each other (2). Arriving at position (c), another relaunch sends the wave packets back on their way (3). At position (b) and (d) a mirror operation directs them back to the start (4). At this position (a), after the interferometer has enclosed the area A (shaded region) twice, it can either be closed with a final beam splitter, or another relaunch starts a new loop. After a number of $2n$ loop iterations, the output ports below position (a) can be seen in the form of three black arrows. Adapted from [Sch21].

momentum is reversed again by a relaunch operation. Following the trajectories of the first loop upwards again the ensembles reach the position of horizontal momentum reversal again after a time $3T$ and are directed back towards the starting position (a) of the initial splitting operation. This completes the second loop after the time $4T$ and opens up two possibilities at this point. Either the interferometer is closed by a final beam splitting operation that afterwards allows for the detection of three output port populations, or all previous operations are repeated to form another $2n$ loop.

As described, the two light fields used serve different purposes. While one focuses on the launch process, the other applies beam-splitting and recombination pulses. With some adaption such a scheme is also of interest for operation with a high-finesse optical resonator. In this case the beam-splitting and recombination light field is enhanced by the cavity setup to improve spatial filtering of the coherent manipulation beam [Ber21].

An important quantity for rotational measurements based on the Sagnac effect is the effective enclosed area. In the case of this multi-loop scheme, it is enclosed by the atomic trajectories,

as shown in gray in figure 3.16, and can be calculated to

$$A = n \frac{\hbar \vec{k}_{\text{eff}}}{m} \vec{g} T^3, \quad (3.15)$$

with the effective wave vector \vec{k}_{eff} originating from the green light field (ω_1 and ω_2) and \vec{g} defining the local gravitational acceleration.

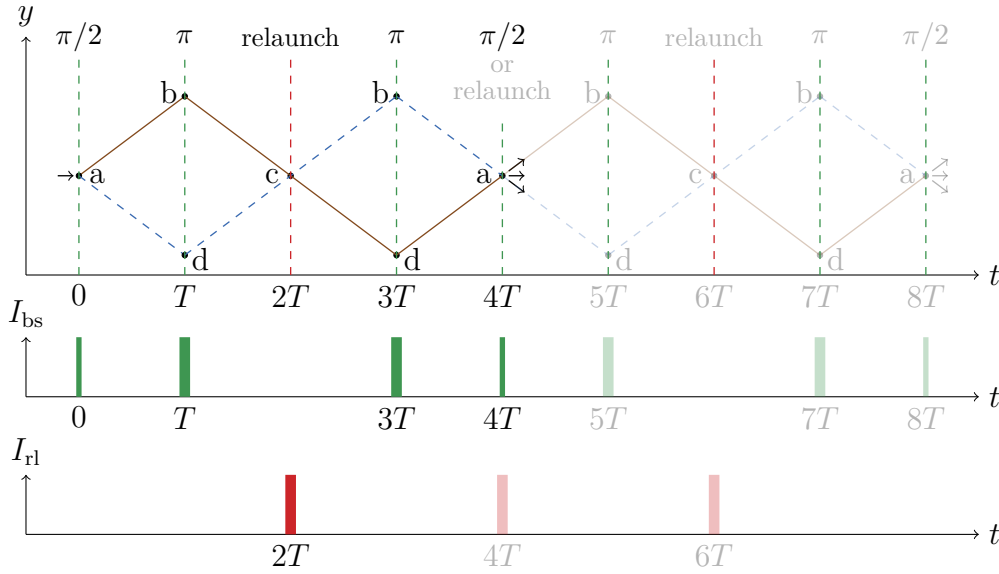


Figure 3.17: Space-time diagram of the multi-loop ($n = 1$) geometry together with the timings of the intensities of the interferometer pulses ($\pi/2$ and π) applied in the horizontal lattice (green) and the relaunch in the vertical lattice (red). The positions (a), (b), (c), and (d) correspond to their respective equivalents in Figure 3.16. The entire sequence takes the time $4T$, with the relaunch halfway through this at $2T$. The space-time trajectories of a possible second loop ($n = 2$) are shown opaque. Preparation and detection time of the atoms, as well as the initial launch at the beginning of the sequence are neglected. Adapted from [Sch21].

For a better visualization of the individual steps and timings of the sequence, a space-time diagram with two loops ($n = 1$) and the possible extension to four loops ($n = 2$) is shown in figure 3.17. The phase shift measured by an atom interferometer originating from the Sagnac effect is generally described in equation 3.1. In the present case for this explicit scheme it is similarly calculated to

$$\phi_r = 2n(\vec{k}_{\text{eff}} \times \vec{g}) \vec{\Omega} T^3. \quad (3.16)$$

An interesting detail to note here is that the manipulations within the vertical light field (ν_1 and ν_2) are used only for the relaunch process and therefore need to be considered only indirectly for this calculation.

Analogous to the calculation for the dual BEC interferometer sequence in section 3.3.3, the potentially achievable rotation sensitivity for the multi-loop geometry, limited by the quantum projection noise, can be estimated based on the measured phase shift from equation 3.16 as follows

$$\sigma_r(t) = \frac{1}{C\sqrt{N}2n(k_{\text{eff}}gT^3)} \sqrt{\frac{t_{\text{cycle}}}{t}}. \quad (3.17)$$

The presented multi-loop scheme implicitly assumes that the velocity vector of the relaunch is aligned parallel to gravity, which can lead to undesired phase shifts in case of a non-ideal alignment. Due to the inherent symmetry many other spurious shifts are already suppressed, but still timing jitter or gravity gradients may degrade the sensitivity of the measurement. A detailed analysis of different requirements on these parameters can be found in [Sch21].

3.5 Similarities and unique features of the methods and concepts

In order to try to compare the described methods and concepts with each other, individual advantages and limitations are listed in the table 3.3. However, these points represent only a limited selection of the most prominent properties and do not allow an equal comparison. Nevertheless, this shows that depending on the targeted measurement, a selection can be made in which existing disadvantages may not come into play. Some obvious applications, such as the use of the re-launch process in a fountain gravimeter or the twin-lattice interferometer for a highly sensitive rotation sensor, seem clear. However, these are not limited to such uses and can therefore also be useful in other areas. Another application example from the field of inertial navigation is presented later in section 6.1 and describes the use of the multi-axis dual BEC interferometer concept in a compact sensor setup.

Table 3.3: Summary of the benefits and limitations of the different interferometry methods and concepts presented in this chapter. The points represent a limited selection of the most prominent properties and do not provide an equivalent comparison. They show distinctive characteristic features which can help to identify possible applications or implementations.

Benefits	Limitations
Fountain	
<ul style="list-style-type: none"> • relaunch operation helps to increase available interferometer time • compact, retro-reflected lattice light beam configuration 	<ul style="list-style-type: none"> • output phase sensitive to accelerations, but rotations can cause systematic effects • atom-chip coated surface defines quality of light field
Twin lattice	
<ul style="list-style-type: none"> • large enclosed area A due to the symmetric momentum transfer Δp • area tunable by parameters T and Δp • retro-reflection of lattice light beam can suppress systematic effects 	<ul style="list-style-type: none"> • major advantage for rotational measurements only • distortions of the light field have shown to limit the sensitivity scaling
Dual BEC	
<ul style="list-style-type: none"> • single initial BEC based differential scheme • vibration noise suppressed rotation measurement • rotation noise suppressed acceleration measurement • easily extendable to multi-axis operation 	<ul style="list-style-type: none"> • achievable beam sizes limit the interferometer area and thus the achievable sensitivities under the influence of gravitational acceleration • dynamic environments influence the differential readout method
Multi-loop	
<ul style="list-style-type: none"> • enclosed area A can be tuned to either operate larger scale or compact sensors • only requires single beam splitting zone of finite size • multiple loops n increase area A and sensitivity, but not size • can be extended to measure the local gravitational acceleration or tilts 	<ul style="list-style-type: none"> • high relaunch efficiency is crucial for multi-loop operation • non-ideal alignment of relaunch direction can lead to undesired phase shifts

CHAPTER 4

Tackling detrimental effects in the atom-light interaction

Measurement of inertial signals with an atom interferometer can be negatively influenced by different effects, some of them can be common-mode suppressed, while others cannot. In the case of the geometries presented in chapter 3, these can be vibrations of the inertial reference, laser phase noise, temporal and spatial intensity fluctuations of the laser beam. The so-called detection noise can usually be decomposed into contributions with different scalings with respect to the atomic number N [Ita93; San99]. For example, contributions from technical noise such as noise in electronics or scattered light fluctuations scale with the inverse of the atomic number $1/N$. Contributions dominated by quantum projection noise, as an expression of the probabilistic nature of measuring a quantum superposition, scale with $1/\sqrt{N}$. Other contributions arising for example from optical noise due to laser frequency and intensity fluctuations scale independent of N .

The optical noise can be a dominant negative effect for the atom-light interaction. In chapter 3.2.2, this was strongly demonstrated by the contrast loss in the twin-lattice interferometer, where the perturbations of the laser light field used for the atom-light interactions limit an even larger momentum transfer. In addition, the (relative) phase of the light field should not be neglected either, and even today wavefront aberrations are one of the major uncertainty factors in atom interferometers [Lou11; Sch15; Bad18; Böh22]. To date, the supply of laser frequencies with the required agility for quantum optical experiments has often been provided by large laboratory setups. For the future, the need has arisen to move such setups from the laboratory to field applications in the form of transportable or mobile experiments. Here, the environment and the desired compactness pose further challenges [Bar14; Hei20; Fry21; Bec18; Bon19].

Therefore it seems to be an important task to reduce the influence of technical shortcomings of the employed light fields. Some methods already exist, such as common-mode suppression or the implementation of high-finesse optical resonators [Ber21; Pan23a], which in turn increase the complexity of the setup and also set limits depending on the application. In the case of an optical resonator, for example, one limit is the tunable frequency range. In the following chapter, three further topics are presented, which are dedicated to individual problems of light field generation, but are not mutually exclusive.

1. **Generation of a collimated homogeneous beam profile based on flat-top shaping optics [Mie18]:** For this purpose, an aspherical lens based beam shaping setup is analysed with respect to its applicability for atom interferometry. The measured intensity and phase profiles are presented and their influences on an atom interferometer are explained. Finally, the comparison with a Gaussian light field is made and the temporal stability is investigated.
2. **Compensation of light shift effects based on the combination of two oppositely detuned light fields away from the atomic resonance frequency [Kov15b]:** This method is integrated into a laser system that enables detuning of several hundred GHz while generating high optical powers and multiple frequencies. Its performance is presented with special attention to low-loss light beam superposition.
3. **Stable generation of all laser frequencies required for the production of a cold atomic ensemble or quantum degenerate gas and the subsequent coherent manipulation in the form of Raman and Bragg transitions via single and/or double diffraction:** This is to be realized in a compact laser system that combines the reliability and robustness of telecom components with frequency doubling by Periodically Poled Lithium Niobate (PPLN) crystals. It provides the ability to combine internal and external state manipulations with only a single laser source. This enables for example the removal of spurious atoms through blow-away pulses and interferometer topologies that are sensitive to the gravitational redshift. As an application example, double Raman processes of different order are realized and their performance is presented.

4.1 Flat-top beams for the coherent manipulation of atoms

Since the sensitivity and accuracy of atom interferometers, especially when employing large momentum transfer techniques, crucially depends on the spatial beam profile and phase uniformity of the applied light field, it seems logical to investigate and try to improve it. The commonly used interrogation light field for atom interferometry is based on the propagation of a collimated Gaussian beam, as is true for all measurements presented in chapter 3. Instead, the use of a collimated flat-top beam profile may offer the advantage of providing constant light intensities for interacting atoms at different positions in the beam. This is a good basis for coherent manipulations which typically scale with the optical potential. It also has the advantage of being less susceptible to distortion at apertures or edges than a Gaussian beam profile, since the amplitude of the flat top decreases much faster at edges. Avoiding distortions is crucial since they immediately decrease the interferometer contrast, and ultimately lead to a loss in signal-to-noise ratio. Moreover, they can also cause phase inhomogeneities and lead to systematics or diffraction phase effects that are not negligible. In the case of multiple atom-light interactions that imprint different phases in each operation, for example when using techniques with large momentum transfer, such effects are amplified. Therefore, it is important to obtain a homogeneous intensity and phase profile.

The size of the interrogated cold atomic ensemble is also of importance, because when it reaches the order of magnitude of distortions in the light field, the transition probability distributions

are broadened and more effects are sampled. For comparison with quantitative results obtained later, it is mentioned that this size can range from a few micrometers (typical for BECs) to centimeters (typical for laser cooled atom clouds) and depends on effective temperatures, expansion rates, and observation times.

Theoretically a flattened Gaussian beam can be expressed as a finite sum of N Laguerre-Gauss beams, whose field can be written as

$$U_N(\rho) = A_0 \sum_{n=0}^N c_n^{(N)} L_n \left(\frac{2(N+1)\rho^2}{w_0^2} \right) \exp \left(-\frac{(N+1)\rho^2}{w_0^2} \right), \quad (4.1)$$

where ρ is the radial coordinate and w_0 the radius of the beam [Gor94; Bag96; Bor01]. L_n describes the n -th Laguerre polynomial and the corresponding coefficient is defined as

$$c_n^{(N)} = (-1)^n \sum_{m=n}^N \frac{1}{2^m} \binom{m}{n}. \quad (4.2)$$

In contrast to a Gaussian beam, a flat-top beam is not a free-space mode, meaning that the shape of its intensity profile will change. While a Gaussian beam with few high spatial frequencies, will tend to keep its shape during propagation, a beam that is flat in intensity with sharp edges is likely to see its profile deteriorate more quickly for the same propagation distance.

A different approach to better compare the propagation of the intensity profile of a flat-top beam to a Gaussian beam is to express its shape with the Fermi-Dirac (FD) function

$$g_{\text{FD}}(\rho) = g_0 \left(1 + \exp \left(\beta \left(\frac{\rho}{w_0} - 1 \right) \right) \right)^{-1}, \quad (4.3)$$

with w_0 setting the length scale, equivalent to a Gaussian beam, and the dimensionless parameter β defining the shape of the function, where $\beta \rightarrow \infty$ represents a perfect flat square. The normalization constant g_0 can be adequately approximated for $\beta \gg 1$ by a Taylor expansion

$$g_0^{-1} = \pi w_0^2 \left(1 + \exp(-\beta)^{-1} + \frac{1}{3} \pi^2 \beta^{-2} + \mathcal{O}(\beta^{-4}) \right), \quad (4.4)$$

which is the case of interest [Hof00].

If one assumes that the output beam from the beam shaping optics is a plane wave, the propagating beam can be modelled by using Kirchhoff's diffraction theory and the Fresnel approximation [She06].

The optical amplitude of the radial beam profile r is calculated after passing the initial output

aperture with a radius w_{\max} after the propagation distance d to

$$u(r, N_F) = \int_0^{w_{\max}} g_{\text{FD}}(r) J_0 \left(2\pi N_F \frac{r\rho}{R_0^2} \right) \exp \left(i\pi N_F \left(\frac{\rho}{R_0} \right)^2 \right) \frac{\rho}{R_0} d\rho. \quad (4.5)$$

Here $J_0(x)$ is the Bessel function of order zero and N_F describes the dimensionless Fresnel number

$$N_F = \frac{w_0^2}{\lambda d}, \quad (4.6)$$

with λ as the optical wavelength. This number is the main parameter for the diffraction theory and therefore has a large influence on the propagation behaviour. An overall phase was omitted and the intensity was normalized to its plateau. For better representation, the modelled shapes before and after propagation for different values of β and the initial parameters $w_0 = 7.7$ mm Full Width at Half Maximum (FWHM) and 780.24 nm, which correspond to the technical data of the beam shaping optics used later, are shown in figure 4.1.

After propagation ring-shaped structures appear at the edges of the beam. These structures amplify after longer propagation distances and are more distinct for flat-top beams with steeper edges, respective larger β parameters, as visible for the two different simulated beam propagations. Finally, at large propagation distances, these ring-shaped structures will reseal

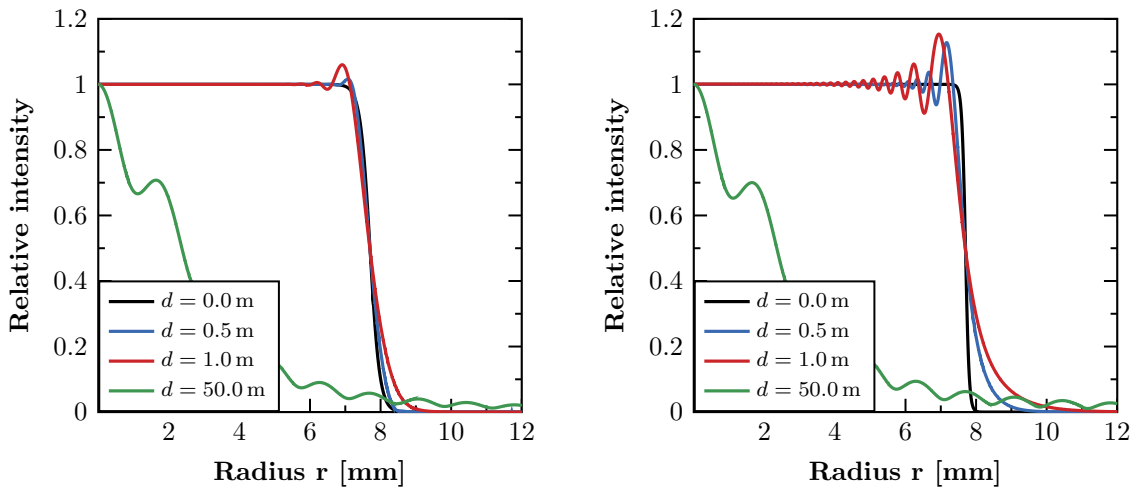


Figure 4.1: Theoretical prediction of a flat-top beam profile after propagation of distances $d = 0$ m, $d = 0.5$ m, $d = 1$ m and $d = 50$ m. The model is based on the Fermi-Dirac function and Kirchhoff's diffraction theory with the Fresnel approximation and initial parameters $w_0 = 7.7$ mm and $\lambda = 780.24$ nm. **Left:** Normalized optical amplitude of the radial beam profile with the parameter $\beta = 56$. In a simplified picture this parameter describes the steepness of the slope of the flat-top profile. **Right:** For a larger value of $\beta = 150$, the propagated beam profile exhibits larger distortions that start at the edges and increase as the propagation progresses.

and the beam shape will resume a Gaussian-like intensity distribution. Additionally these structures appear after much shorter propagation distances for smaller beam diameters. All of the aforementioned points clearly illustrate the importance of controlling the output intensity shape of the flat-top beam to obtain a useful range of propagation. The choice of initial beam diameter and β parameter directly influence the degradation of the propagated profile.

4.1.1 Flat-top beam shaping optics

As mentioned in the introduction of this chapter clipping mechanisms at edges or apertures close to the optical beam path can have a severe influence on an atom interferometer. In the vacuum chamber setup shown in figure 4.2, the light beam (displayed in red) propagates horizontally below the atom chip. Due to the atom chip's property of generating high magnetic field gradients close to its surface, the prepared atomic ensemble is located only a few hundred micrometers below it. Thanks to the vertically oriented gravitational field the atomic ensemble starts to accelerate towards the center of the beam after its release from the magnetic trap. For ground-based setups that do not use trapped or guided geometries [Arn04; Krz22], the interrogation time T is ultimately limited by the detectable free fall distance, with exceptions such as through the schemes presented in sections 3.1 and 3.4.

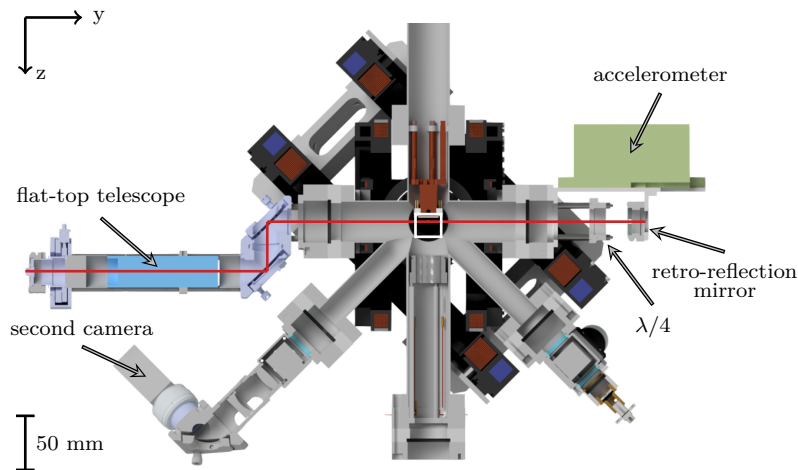


Figure 4.2: Half-section through the y - z plane of the experimental vacuum chamber with externally attached components. This includes an additional detection axis along the 45 degree angle relative to the horizontal plane shared with the light fields for MOT operation. The flat-top telescope assembly is connected horizontally and is opposite to the retroreflection combination consisting of mirror and quarter-wave plate. A commercially available accelerometer [Titan TACCL-N1, Nanometrics] attached to the top of the mirror can measure vibrations acting on it. The path of the light beam is shown by a red line and the detectable interferometer area under the atom chip is roughly shown by a white rectangle.

The idea of making compact interferometers possible by moving the optical beam path close to the production site (for example the atom chip) therefore seems favourable. This may come with the tradeoff of creating perturbations that induce spatially variable dipole forces and can ultimately lead to a contrast and sensitivity loss, as explained in subsection 3.2.2. A flat-top

beam has the advantage of being less susceptible to such distortions than a Gaussian beam, since the amplitude of its spatial profile decreases much faster at its edges.

A simple approach for achieving a flat-top beam is by transmitting a Gaussian shaped beam through an apodizing filter. It locally reduces the intensity of an incident beam in order to achieve the desired distribution. This filtering is not very efficient since it intrinsically generates a large loss of intensity. Alternatively, a set of aspheric optical components can be used to redistribute the intensity of the beam as it propagates through the assembly. Different properties of the diffractive elements are used to modify the shape of the incident collimated Gaussian wave to obtain a desired intensity distribution after a certain propagation. Typically, aspheric lenses are effective in producing complex intensity distributions in a given plane, but are not optimal for obtaining a constant profile, like a flat-top, after long propagation distances. The commercially available TopShape LongDistance beam shaper by the Asphericon GmbH [TSM25-10-LD-B-780, Asphericon] advertises a collimated flat-top beam output up to a working distance of at least 1 m. Its principle is based on the refractive beam shaping concept, introduced by Frieden and Kreutzer [Fri65; Kre69], and consists of two plano-aspheric lenses. The first aspheric surface changes the incoming plane wave with a Gaussian intensity profile by ray mapping, so that an uniform intensity distribution is generated. The second aspheric surface collimates the output beam again to obtain the flat-top beam profile. Important points that affect the output quality of the flat-top beam are the size, collimation and relative position of the input beam. Therefore a mechanical assembly as shown in figure 4.3 is constructed to mount the beam shaping optics.

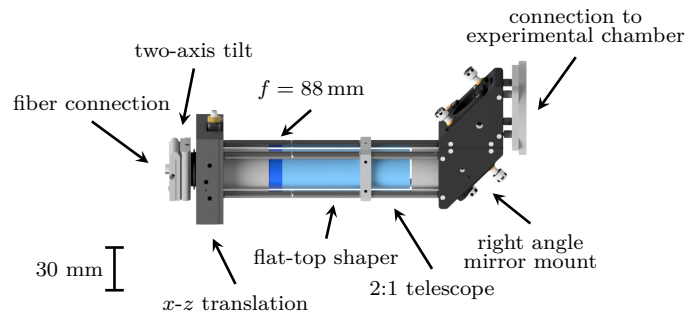


Figure 4.3: Mechanical assembly of the flat-top beam shaping optics for connection to the experimental vacuum chamber. A single large mode area photonic crystal fiber outputs light from a FC/PC fiber connection. The divergent output light is collimated by a custom designed aspheric lens with an EFL of $f = 88$ mm connected to and serving as an input for the flat-top beam shaper. To obtain a symmetric output profile the position of the fiber connector can be adjusted by a two-axis tilt and a two-axis x - z translation. The output of the flat-top beam shaper is demagnified by a 2:1 telescope which is mounted directly at the output side. Two right angle mirrors enable the adjustment, especially beam walking, of the flat-top beam with respect to the interrogated atomic ensemble.

In the case presented here, a single photonic crystal fiber with a large mode area [LMA-PM-10, NKT Photonics] and a mode-field diameter of $1/e^2 = 8.5 \pm 0.1 \mu\text{m}$ outputs light with a

wavelength of 780 nm at a FC/PC connector that is mounted inside an adapter [SM1FC, Thorlabs]. The divergent output light is collimated by a custom aspheric lens [200286-000-03A, Asphericon], designed with an Effective Focal Length (EFL) of $f = 88$ mm to a theoretical Gaussian beam width of $1/e^2 = 10.000 \pm 0.015$ mm. The calculated wavefront map of the designed lens demonstrates a value of the wavefront error which is below the RMS value for a lens with a diffraction limited performance. Therefore, a point source assumed to be the output of the single mode fiber and located at the front focal point of the lens should be ideally collimated.

To be able to obtain a symmetric flat-top beam profile after collimation, the relative position of the fiber output with respect to the lens is adjusted in two stages. The first stage is a flexure mount [IXF1.0, siskiyou] that provides a two-axis tilt alignment with minimum controllable motion of $\pm 0.001^\circ$ for pitch and yaw. The second stage [ST1XY-A/M, Thorlabs] allows for x - z translation in the plane of the lens that centers the tilt compensated input wavefront to the geometrical center of the lens. The collimation lens itself is directly connected to the flat-top beamshaper [TSM25-10-LD-B-780, Asphericon], mounted together in a 30 mm cage system assembly and positioned by translation in y -direction at a distance of 88.0 ± 0.1 mm. The FWHM of the flat-top beam is specified to be between 15.2 mm to 15.7 mm and demagnified by a 2:1 telescope [BeamExpander, Asphericon] which is also mounted directly at the output side of the flat-top beam shaper. This optional reduction relaxes the requirement of achievable maximum laser power for coherent manipulations, since it effectively increases the intensity on the flat-top plateau by a factor of four. The last part of the mechanical assembly consists of two right angle mirror mounts [KCB1E/M, Thorlabs] with mounted elliptical mirrors [BBE1-E03, Thorlabs]. They enable the adjustment, especially beam walking, of the flat-top beam with respect to the interrogated atomic ensemble. The full setup is connected with an adapter plate to the experimental vacuum chamber as shown in figure 4.2. In the following sections, values of the generated flat-top beam such as collimation, intensity and phase profile are quantified and their influence on atom interferometry is discussed.

4.1.2 Flat-top intensity profile

In reality, the propagation shape of the intensity and phase profile is determined by many more factors than the propagation theory explained in the previous section can predict. Most effects can be listed under the collective term of production tolerances and resulting imperfections. Depending on the number of optical elements and manufacturing techniques, these differ in size and shape. Experimentally, this usually leads to more distortions of the beam profile.

In figure 4.4 the measured flat-top profile after a propagation distance of $d = 0.243$ m is shown and compared to the theoretic prediction from equation 4.5 with the parameter $\beta = 95$ chosen to match the experimentally determined slope of the profile for different propagation distances. It should be noted that in the setup, as explained in the section before, the 2:1 telescope reduces the initial radius parameter w_0 by a factor two. The intensities of both the experimental and the theoretical beam profile are normalized to the plateau of the non-propagated flat-top beam. The $\beta = 95$ parameter is obtained by matching the measured experimental slope to the

calculated profile from equation 4.5. This chosen value for the optic design lies between the two shown in figure 4.1 and therefore provides a compromise between steepness of the slope and flatness of the plateau. For the theoretical profile at propagation distances of up to 0.5 m, the largest intensity changes occur only at the edges of its plateau, with 80% of the profile being changed by less than 5%. From the comparison of the measured data with this theoretical profile, it becomes clear that the dominant deviations must come from something other than the propagation simulated by the diffraction theory, quite possibly the optical imperfections of the beam shaping optics used.

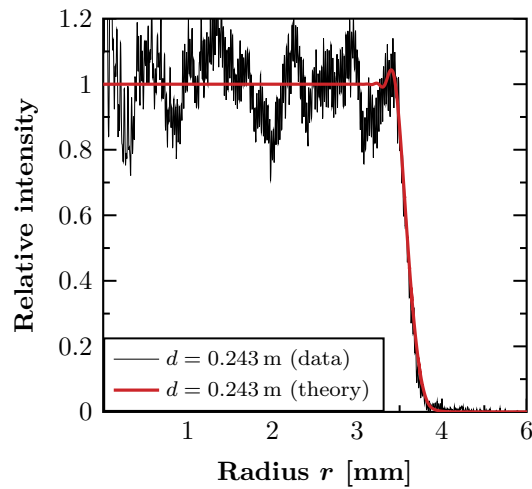


Figure 4.4: Theoretical prediction of the propagated flat-top beam profile compared to an experimentally obtained profile after a propagation distance of $d = 0.243$ m. The initial parameters $w_0 = 3.7$ mm and $\lambda = 780.24$ nm are obtained experimentally. The value for $\beta = 95$ is matched according to the measured experimental slope. This value seems to be a good compromise between a steep slope and flatness of the plateau. However, it is obvious that the simulated propagation using diffraction theory cannot model the perturbations on the intensity profile alone.

4.1.3 Influence of the intensity profile

To measure the quality of the intensity distribution of the flat-top beam a simple optical setup is devised. The assembly of the components for beam shaping, described in subsection 4.1.1 and shown in figure 4.3, is placed on an optical table and its output profile measured at different distances. A schematic overview is shown in figure 4.5.

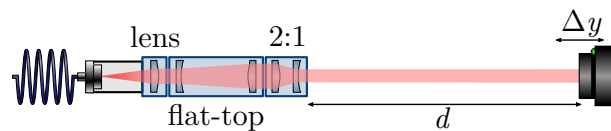


Figure 4.5: Schematic setup of the intensity profile measurement of the flat-top beam. The output profile is measured at a fixed propagation distance d by a beam profiler placed on a translation stage with an adjustable distance Δy . It should be noted that the exact lens configuration inside the flat-top beam shaper and the beam reducer is subject to actual conceptual implementation by the manufacturer.

The beam is detected by a beam profiler with an active area of 11.3×11.3 mm [S-WCD-LCM, DataRay], which captures individual images of the 2D intensity distribution in the x - z -plane of the propagation direction at a distance d . The camera itself is placed on a translation stage that is controlled by a motorized actuator [LTA-HS, Newport] and a motion controller [ESP300, Newport]. The actuator allows for a maximum total travel distance $\Delta y = 50$ mm with a resolution of 0.035 μm and a guaranteed directional repeatability of 0.5 μm . In a first measurement, the beam profile is evaluated at two different fixed points. Those roughly correspond to the optical distances the light has to travel until the two-photon interrogation position with the atomic ensemble at $d_1 = 243$ mm and $d_2 = 615$ mm after retro-reflection. From these two positions, the beam collimation is calculated to a divergence beam half-angle of $0.0204 \pm 0.0028^\circ$ by measuring the radial distance of the points where the intensity has dropped to $1/e^2$ of its maximum. Additionally, the profile is measured with $\pm\Delta y = 4$ mm and a step size of 40 μm to obtain more pictures in the direction of propagation and be able to compile a profile in the y - z -plane. The area defined by $\pm\Delta y$ incorporates the largest separation of the trajectories generated by a relative momentum of $\Delta p = 408\hbar k$ of the twin-lattice interferometer introduced in section 3.2. The obtained x - z and y - z intensity distributions can be seen in figure 4.6. The left picture displays the normalized distribution after the propagation distance of $d_1 = 243$ mm and the right picture the normalized intensity distribution along the propagation direction $d_1 \pm \Delta y$ with four example trajectories of a twin-lattice interferometer with different relative momentum transfers. The two-dimensional intensity distribution shows various features, for example concentric ring-shaped structures, which are created by the polishing process during the manufacture of the aspherical beam shaping optics. The apparent periodic structure of peaks and valleys on these rings is also due to induced oscillations during polishing and thus represents a technical limitation of the manufacturing process. In addition, the characteristic hexagonal structure of the fiber is visible in the center of the beam, even after 1 m of propagation. On the left side of the intensity profile, an additional interference pattern covers the beam profile, which will be explained in subsection 4.1.5. In addition, smaller dots identified as dust particles interfere with the pattern, but can be neglected since they are located on the camera screen.

Overall, the intensity pattern varies spatially up to $\pm 20\%$ but much less along the direction of light travel, as seen in figure 4.6 on the right. On the scale of atomic trajectories of the twin-lattice interferometer, the propagated intensity distribution varies less than $\pm 1\%$. The working distance of the beam shaping optics is advertised with up to 1 m, which is more than the measured distance $d_2 = 0.615$ m. In this region, the fluctuations of the intensity pattern are increased up to $\pm 25\%$, but the enveloping profile and especially the slope are consistent with the theoretical prediction.

To analyze the influence of the intensity distribution on the interferometer, the measured profile is compared to the model of a clipped beam from subsection 3.2.2. In this context, it should be noted that wavefront distortions appear as amplitude fluctuations after propagation because spatial phase and amplitude fluctuations mix during this process [Bad18; Rou14]. The flat-top light field is represented by a two-dimensional map of the measured intensity distribution as

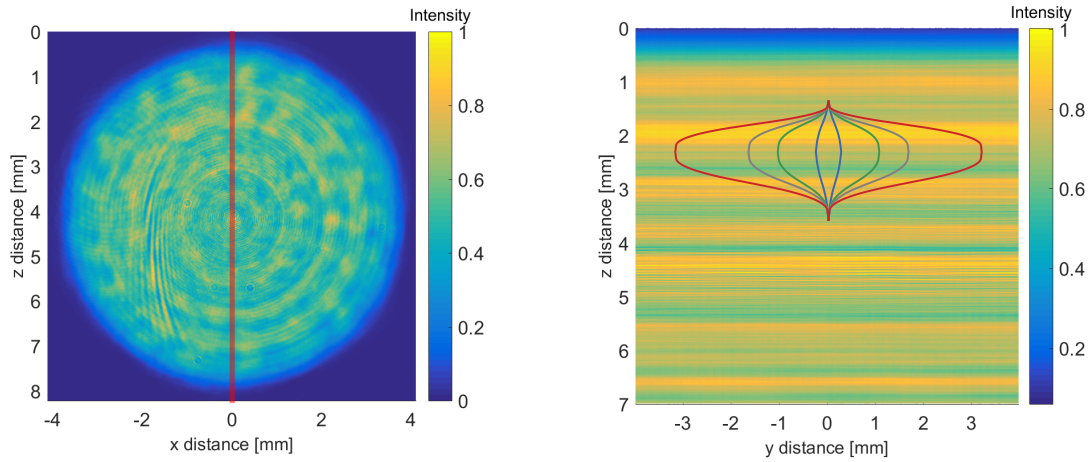


Figure 4.6: Sections through the measured intensity profiles of the flat-top beam along the x - z plane and the y - z plane. **Left:** Two-dimensional representation of the intensity profile after a propagation distance of 243 mm. **Right:** Cut along the red line of the left profile in the direction of beam propagation through 200 individual images of the intensity profile. The example trajectories for a twin-lattice interferometer, introduced in section 3.2, with a relative momentum transfer of $\Delta p = 24\hbar k, 128\hbar k, 208\hbar k,$ and $408\hbar k$ are plotted for order of magnitude, starting with smaller and then increasing separation. The intensity is normalized to the maximum pixel value.

displayed in figure 4.6 on the right. Due to the small atomic movement in x -direction the beam profile is assumed to be constant in this direction. A three-dimensional simulation including this data is possible, but beyond the scope of this analysis.

The modelled data grid in [Geb21] based on the Gaussian beam clipped at the edge of the atom chip is populated with points at distances below the Thomas-Fermi radius. This translates into a grid size in the y -direction of $3.9\ \mu\text{m}$ and in the z -direction of $0.5\ \mu\text{m}$. To achieve the comparable sampling rate as in the simulation with the Gaussian light field, the grid size of the measured data must be interpolated. Of course, distortions smaller than the originally grid size are then neglected. For the measured profile of the flat-top beam, it is interpolated in the y -direction from $40\ \mu\text{m}$ by a factor of 10 to $4\ \mu\text{m}$ and in the z -direction from $5.5\ \mu\text{m}$ by a factor of 5 to $1.1\ \mu\text{m}$.

Nevertheless, the grid size in z -direction is already smaller than the calculated Thomas-Fermi radius of the initial propagated ensemble of about $30\ \mu\text{m}$. The changes of the profile in the y -direction, which is direction of propagation, can be estimated as small at these distances. The result from the simulated contrast values from equation 3.7 in dependence of the relative transferred momentum Δp is shown in figure 4.7. The modelled dependence of the contrast on the light field is combined with the same atom loss model, as described in the supplement of reference [Geb21] and shown in figure 3.8 to account for the two presumed dominant effects contributing to the experimentally observed loss of contrast.

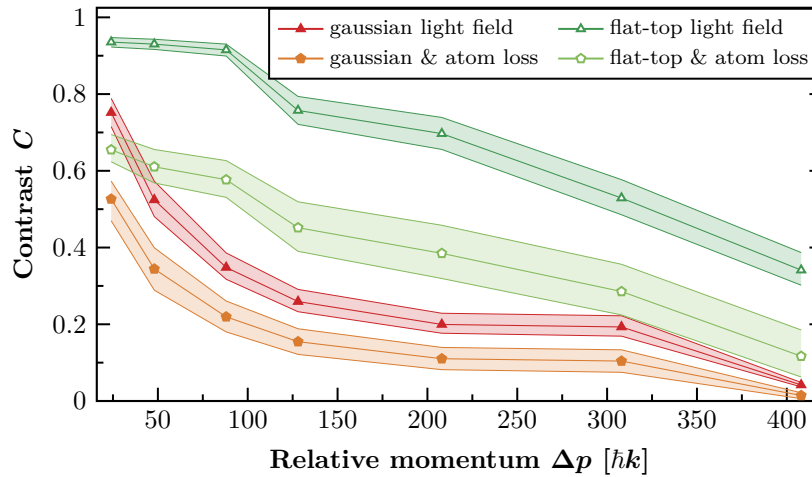


Figure 4.7: Theoretical analysis of the achievable contrast values C for a twin lattice interferometer with different momentum transfers Δp operated with a flat-top beam or a distorted Gaussian beam. The input for the simulations are the measured flat-top profile shown in figure 4.6 on the right or a simulated Gaussian beam profile clipped at the edge of the atom chip. The atomic loss model is calculated for both light fields with the same parameters from section 3.2. The shaded areas represent confidence intervals of the simulations, determined by atom number and lattice depth uncertainties.

This comparison shows an overall expected lower contrast loss for the flat-top case. However, it should be taken with special caution, since it is based on the one hand on a numerical simulation of a clipped Gaussian beam profile whose distortion was adjusted to an experimentally observed contrast loss, and on the other hand on a measured flat-top profile. It remains to be seen to what extent the contrast loss for the latter can be confirmed experimentally.

There is an additional assumption that needs to be taken into consideration when comparing these simulations to measured data, which is the aspect of retro-reflection. The optical lattice is generated through the superposition of two counter-propagating light fields, realized by the reflection of an incoming laser beam featuring two frequencies with linear orthogonal polarizations at a quarter-wave plate and mirror combination, see figure 3.4 for reference. The input for the contrast loss curves presented, in the form of the simulated and the measured light field, represents only the incident light field and neglects the influence of the reflected component. Measuring the overlapped light field with a beam profiler is more difficult, but could be realized by taking two sets of intensity data at $d_1 \pm \Delta y$ and $d_2 \pm \Delta y$, which are added together. In this case, special attention would have to be paid to the quality of the alignment, since the combined light field should be optimized either with a set of pinholes or by feedback into the optical fiber. If the acquired data sets do not reflect this fact, the combined light fields are not a good substitution.

4.1.4 Influence of the phase profile

Atom interferometers measure parameters of interest by comparing the phase accumulated by atoms as they traverse either of two trajectories, known as the arms of the interferometer. During two-photon interactions, the relative phase of the counter-propagating laser light fields is imprinted on the matter wave, giving rise to the laser phase ϕ_L . This phase directly influences the measured output phase of the interferometer (for reference see section 2.2). Ideally, the relative phase of the counter-propagating beams should be zero, which is not always the case in reality. To determine this, the propagated wavefronts can be measured. This can be typically done using the two methods of light interferometry and direct wavefront sensing. To characterize the profile of the presented flat-top beam shaping optics setup and estimate its influence for an atom interferometer both methods are explored.

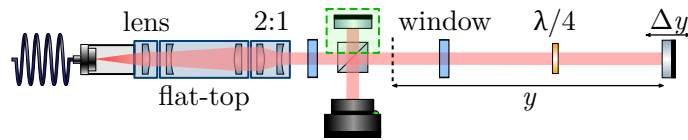


Figure 4.8: Schematic setup of the phase profile measurement of the flat-top beam. The setup in principle resembles an optical Michelson interferometer where the length of one of the arms can be adjusted by a translation stage by Δy . In this configuration, the interference pattern resulting from the beam overlap at the central polarizing beam splitter and detected by a beam profiling camera can be used to extract the phase information. Alternatively, if the upper arm is blocked (green box), a Shack-Hartmann sensor can be used to obtain information about the propagated wavefront. To model the optical configuration for twin-lattice interferometry, comparable optical elements in the form of two vacuum viewports, a quarter-wave plate, and two mirrors are used in the setup.

For this reason, the measurement setup shown in figure 4.8 and described below is used in two different configurations. The first is based on a Michelson interferometer and the second utilizes a Shack-Hartmann Sensor (SHS). To measure the same accumulated phase difference for both, the setup presented must include slight modifications. If a SHS is placed as the sensor in the figure, the light from the top arm is blocked (green part in figure 4.8), while two corresponding wavefront images at two positions d_2 and d_1 are captured. Afterwards these two images are subtracted from each other.

The Michelson interferometer, on the contrary, evaluates single beam images with a beam camera as a sensor. The evaluation procedure is explained in detail later in this section. In principal this allows to compare two independent measurements of the same measurand (wavefront aberrations) without having to make major changes to the setup. Two exemplary wavefront images, one taken with the SHS method and one with the Michelson setup, are presented in figure 4.9 and suggest a comparable performance.

The SHS measures wavefronts with an array of lenslets. Different local inclinations can be measured and the entire wavefront can be reconstructed by an automated software algorithm. The sensor [SHScam UHR, Optocraft] used for the measurement consists of a CCD camera

head [TM 4200 CL, Pulnix] with 2048×2048 pixels of size $7.4 \mu\text{m} \times 7.4 \mu\text{m}$ and a matrix of 100×100 microlenses with $f = 4.73 \text{ mm}$ and a size of $150 \mu\text{m} \times 150 \mu\text{m}$ each, optimized to a wavelength of 780 nm together with an anti-reflective coating. The image evaluation is carried out by the proprietary software, which outputs a set of 36 Zernike polynomials. When using the flat-top beam at the experimental vacuum chamber, as shown in figure 4.2, the first distance between the exit aperture of the telescope (depicted in light blue) and the atomic ensemble (located inside the white rectangle) is roughly $d_1 = 243 \text{ mm}$. This corresponds to the common path the wavefront has traveled and is adjusted in the measurement setup to the position where the light hits the sensor for the first time. The second distance the light travels after being retro-reflected and reaching the ensemble again is $d_2 = 615 \text{ mm}$. Therefore the distance over which the phase difference is accumulated is set to $y = (d_2 - d_1)/2 = 186 \text{ mm}$. When the longer arm of the setup is moved by Δy , the relative phase between two different propagation distances is measured in addition to the optical defects. The optical elements used in the measurement setup correspond to the components at the experimental vacuum chamber in type and quality. Nevertheless, differences due to contamination of the surfaces or deformation of the windows by the vacuum itself cannot be excluded.

To generate wavefront data from the signal measured with the Michelson interferometer a phase extraction sequence must be performed. The applied technique is based on a Fourier-spectrum analysis of the measured fringe pattern, as developed in reference [Tak82]. The distance y over which the phase difference is accumulated is adjusted as described before for the SHS measurement. Instead of the SHS, the beam camera [S-WCD-LCM, DataRay] used for the characterization of the intensity profile is positioned as the sensor. As already mentioned, rather than taking two separate images, only one image is taken. The fringe pattern created by the interference of the light from the two arms can be seen in figure 4.10 on the top left. Horizontally aligned fringes covering the intensity profile of the flat-top beam, with superimposed interference fringes due to optical reflections can be seen. Some overlaying intensity modulations due to dust particles are also visible. Such a pattern is created only when one of the arms is slightly tilted with respect to the other, which is otherwise oriented perpendicular to the sensor. In general the interference pattern is a superposition of the phase $\phi_{1,2}$ and amplitude $E_{1,2}$ of the two individual beams coming from the two arms. For field and intensity this gives [Mie19]

$$E(x,z) = E_1(x,z) \exp(i\phi_1(x,z)) + E_2(x,z) \exp[i\phi_2(x,z)] \quad (4.7)$$

$$I(x,z) = E_1^2(x,z) + E_2^2(x,z) + 2E_1(x,z)E_2(x,z) \cos[\phi_1(x,z) - \phi_2(x,z)]. \quad (4.8)$$

If the amplitudes of the two light fields are uniform, the phase difference can be directly inferred. However, when the amplitude of the beam varies, the extracted phase information is modulated. Therefore it is difficult to recover only the relative phase of the two beams. The introduced tilt helps to eliminate this modulation and allows to choose a suitable and resolvable value for the distance between each fringe. The two-dimensional pattern can be described by the following expression

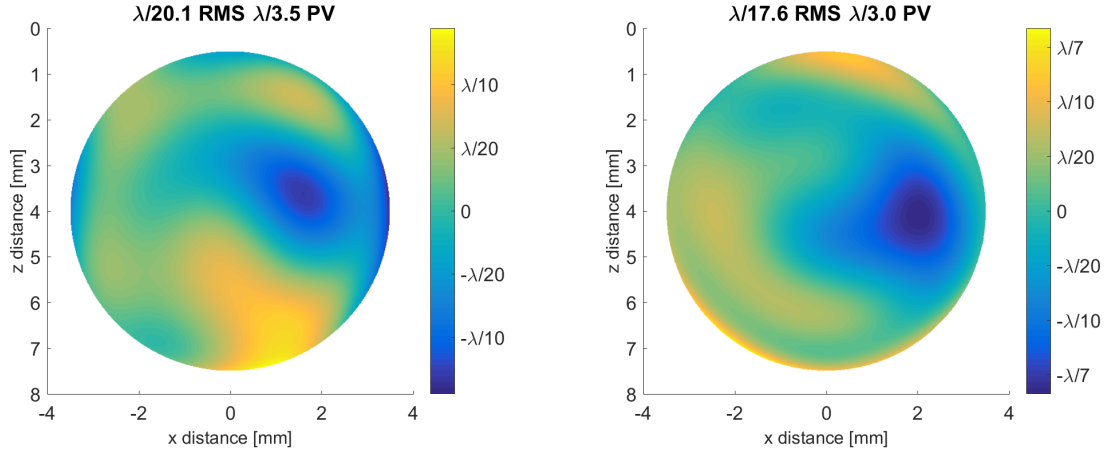


Figure 4.9: Comparison of two phase profiles as measured by the SHS and the phase extraction from the Michelson interference pattern. The corresponding root-mean-square (RMS) and peak-to-valley (PV) values are noted at the top of the images. **Left:** Two images captured by the SHS at the positions d_2 and d_1 are subtracted from each other. The resulting image illustrates the accumulated phase difference over the propagation distance y . **Right:** Wavefront image as obtained from the algorithm schematically explained in figure 4.10. It should be noted that the two profiles were not obtained on the same day, which could have resulted in different absolute values due to thermal changes of the alignment of the setup.

$$g(x, z) = a(x, z) + b(x, z) \cos[2\pi f_0 x + \phi(x, z)], \quad (4.9)$$

where the desired phase information is stored in the term $\phi(x, z)$, f_0 denotes the spatial frequency of the fringes and $a(x, z)$ and $b(x, z)$ represent unwanted variations due to imperfect intensity profiles of the beams. Typically these variations and the phase term $\phi(x, z)$ vary much slower than the frequency f_0 , which makes it easy to separate them in Fourier space. The equation 4.9 can be rewritten as

$$g(x, z) = a(x, z) + b(x, z) \exp[2\pi f_0 x] + c^*(x, z) \exp[-2\pi f_0 x], \quad (4.10)$$

where $*$ denotes the complex conjugate and

$$c(x, z) = \frac{1}{2} b(x, z) \exp[i\phi(x, z)]. \quad (4.11)$$

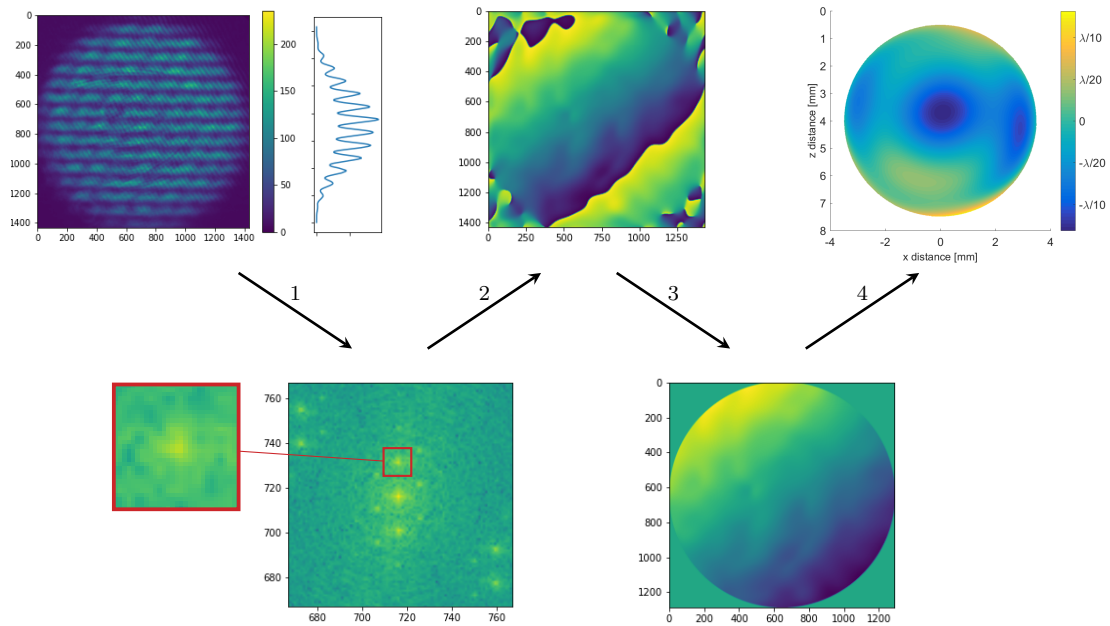


Figure 4.10: Algorithm for wavefront aberration analysis based on Michelson interference fringe detection using the setup shown in figure 4.8. The following steps are performed: The measured interference pattern is aligned horizontally. A 2D Fourier transformation is performed (1). The first order detectable maximum is selected and an inverse 2D Fourier transformation is performed (2). To remove phase discontinuities and ensure that all appropriate multiples of 2π are included in the signal, a phase unwrapping algorithm is applied (3). The final wavefront image is obtained by subtracting the first three Zernike polynomials (4).

The 2D Fourier transform of equation 4.10 yields

$$G(f_x, f_z) = A(f_x, f_z) + C(f_x - f_0, f_z) + C^*(f_x + f_0, f_z), \quad (4.12)$$

with f_x and f_z denoting the spatial frequencies in the respective directions and G , A and C represent the Fourier transformed signals of g , a and c . The visual representation of this transformation can be seen in figure 4.10 on the bottom left, where the spatial separation becomes visible. One of the side spectra is selected, for example $C(f_x - f_0, f_z)$, and shifted by f_0 towards the origin $C(f_x, f_z)$. The inverse Fourier transform of this selected part helps to obtain $c(x, z)$ without the unwanted background variations of $a(x, z)$. With the help of the complex logarithm of equation 4.11, the phase in the imaginary part can also be completely separated from the unwanted amplitude variations of $b(x, z)$ as follows

$$\log[c(x, z)] = \log[(1/2)b(x, z)] + i\phi(x, z). \quad (4.13)$$

The top middle plot in figure 4.10 shows the output of this operation. The obtained phase is indeterminate to a factor of 2π . To remove the visible non-physical discontinuities and obtain a continuous phase distribution a correction algorithms often labelled as 'phase unwrapping' is applied. To recover the information sampled in the discrete wrapped phase, the algorithm

searches for the correct integer number of phase cycles to add to each phase measurement to obtain the correct slant range distance. The result is displayed at the bottom right and decomposed into a set of 36 Zernike polynomials. In a final step, the first three of these polynomials, associated with piston, x -tilt and z -tilt are subtracted. This compensates incorrect centering of the chosen area of interest before the inverse Fourier transformation. The resulting phase distribution, as shown in the plot on the top right, constitutes the obtained relative phase difference over the distance $y = 186 \text{ mm} \pm \Delta y$. It should be noted that both presented methods are technically limited by resolution and are therefore not suitable for resolving all high frequencies of phase noise or phase discontinuities.

Following the phase extraction method explained above, based on the Michelson interference setup, an obtained wavefront image after $y = 186 \text{ mm}$ is shown in figure 4.11 on the left and a stack of multiple images over a distance of $\Delta y = \pm 4 \text{ mm}$ with a step size of $250 \mu\text{m}$ between two neighboring images on the right. The wavefront distortion or equivalently transmitted wavefront error is often quantitatively described by deviations from a perfectly plane wave and typically specified in dependence of $\lambda = 780 \text{ nm}$, which describes the nominal wavelength. Its Peak-to-Valley (PV) value at a fixed y position is measured to $\lambda/3.8$ and the Root-Mean-Square (RMS) value to $\lambda/20.6$, which are two common units typically used to measure surface accuracy of optics. The PV value only compares two local points of the profile and ignores curvature,

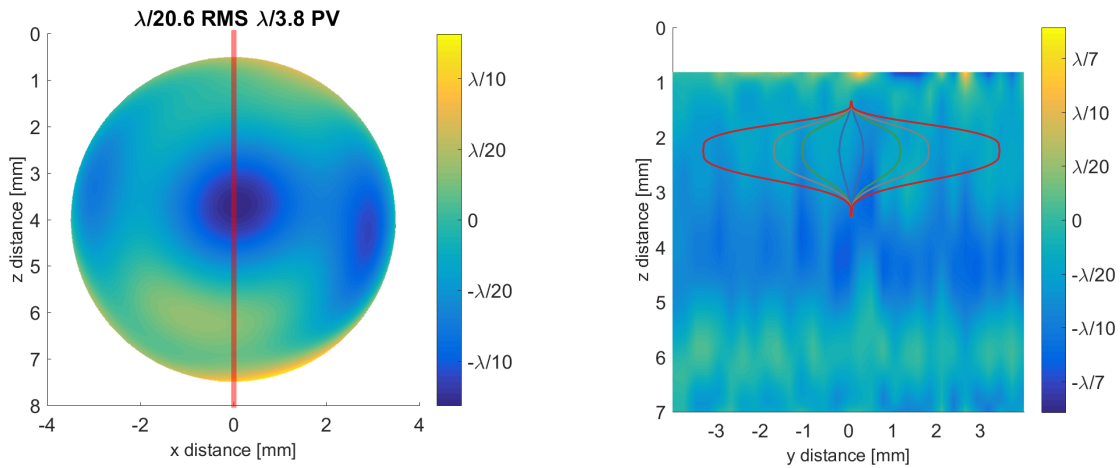


Figure 4.11: Sections through the measured phase profiles of the flat-top beam along the x - z plane and the y - z plane. **Left:** Two-dimensional representation of the wavefront after a propagation distance of the difference phase of $y = 186 \text{ mm}$, as obtained by the phase extraction algorithm explained in 4.10. **Right:** Cut along the red line of the left profile in the direction of beam propagation in the form of an extrapolated stack of multiple images over a distance of $\Delta y = \pm 4 \text{ mm}$ with a step size of $250 \mu\text{m}$ between two adjacent images. The example trajectories of a twin lattice interferometer are plotted for order of magnitude as done in figure 4.6.

therefore it is difficult to give an accurate representation of the phase front profile. The RMS on the other hand is calculated using the standard deviation of the height relative to a reference using all of the data points.

Most commercial optical components are typically only specified with a PV value at a reference wavelength and a so-called scratch-dig value that refers to the cosmetic quality of the optical surface. Optic tests beyond these specified values or classifications according to other more quantitative approaches are more costly and are therefore often only performed after appropriate custom order. Nevertheless, it still seems important to mention at least these values, since all defects of the wavefront caused by transmission or reflection are included in the measurement. Table 4.1 summarizes the individual specifications of the optics used. Since the values are on the order of the measured wavefront error they should not be neglected and show currently imposed limitations. Furthermore, it is shown that the flat-top wavefront is not limited by the original profile of the fiber and the subsequent beam shaping optics.

Table 4.1: Specified surface quality of commercially available optical components used for the phase profile measurement. These values are generally described by manufacturers as high to very high. It should be mentioned that these are by no means achievable qualitative limits, but improvements over them require significantly more complex manufacturing and are therefore usually not available from stock.

	vacuum win- dow/viewport	quarter-wave plate ($\lambda/4$)	mirror
PV @633 nm	$< \lambda/8$	$< \lambda/4$	$< \lambda/10$
scratch-dig	20-10	60-40	10-5

On the right side of figure 4.11, the evolution of the wavefront over the same range as the intensity profile in figure 4.6 shows larger relative deviations along the y -direction. The most likely reason for this behavior are vibrations, which affects the underlying interference pattern used for phase extraction more than the intensity profile. Nonetheless adapting the same model as explained in paragraph 4.1.3 and integrating the difference phase along the atomic trajectories leads to an estimated differential phase uncertainty of < 60 mrad for the largest relative momentum transfer Δp of $408 \hbar k$. For an initial calculated position jitter of $\pm 20 \mu\text{m}$ this value deviates by a maximum of ± 3 mrad. However, it remains to be mentioned that the step size of the phase measurement, which is by a factor of 6.25 larger than that of the intensity measurement, and the above-mentioned undetectable high-frequency phase fluctuations limit this estimate.

4.1.5 Comparison with a Gaussian light field

To illustrate the differences in the performance of a Gaussian beam compared to the previously studied flat-top beam shaping optics, the individual profiles are measured after propagation through the vacuum setup as presented in subsection 4.1.1. By placing a beam profiling camera [S-WCD-LCM, DataRay] at the position of the retro-reflection mirror, the beam profile can be captured after it has passed all apertures of the chamber and the edge of the atom chip.

With an alignment procedure that moves the beam down parallel to the z -axis, which is aligned with the surface of the atom chip, it is possible to achieve a position far enough away that almost no clipping effects are observed for either beam shape.

For a Gaussian beam with a measured $1/e^2$ diameter of 5 mm, diffraction effects are still visible even after a parallel shift of the center of the beam of more than 4.4 mm below the chip surface centered at $z = 0$. A visual representation can be seen as a normalized intensity distribution in figure 4.12 where clipping effects between a distance of 0 mm to 3 mm can be observed.

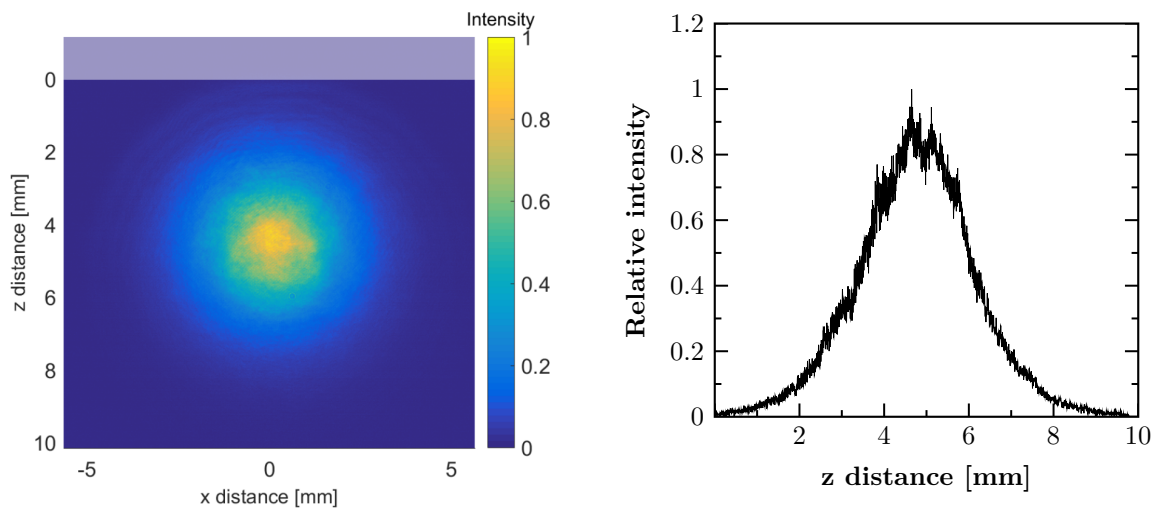


Figure 4.12: **Left:** Normalized intensity profile of the Gaussian beam with a $1/e^2$ radius of 2.5 mm after propagation through the vacuum chamber, as illustrated in figure 4.2 shown by the red line. The beam is horizontally aligned at a distance of $z = 4.4$ mm below the atom chip, which is positioned at $z = 0$. This distance is chosen so that the visible overlapping effects are almost no longer visible. Only a barely visible diffraction pattern remains in the distance between the beam center and the atom chip. **Right:** Integrated normalized intensity profile of the Gaussian beam along the x -axis.

For a flat-top beam with a radius parameter of $w_0 = 3.7$ mm whose center is positioned only 3.7 mm below the chip's surface large diffraction effects are visible as shown in figure 4.13 on the left in the form of a normalized intensity distribution. Shifting the beam parallel downward by an additional 0.8 mm yields a distribution without visible parasitic patterns, as seen in figure 4.13 on the right. To put this in perspective, compared to the Gaussian beam profile, a flat-top beam can be positioned much closer to the surface with even less visible distortions of its distribution.

Another important note in this regard is that real collimating optics used for Gaussian beam

propagation can show deviations compared to the theoretical model of a Gaussian envelope. In particular, for the light amplitude farther from the center, the measured value tends to be higher than predicted by a pure Gaussian profile. Such behavior amplifies any negative influences caused by clipping at apertures or edges.

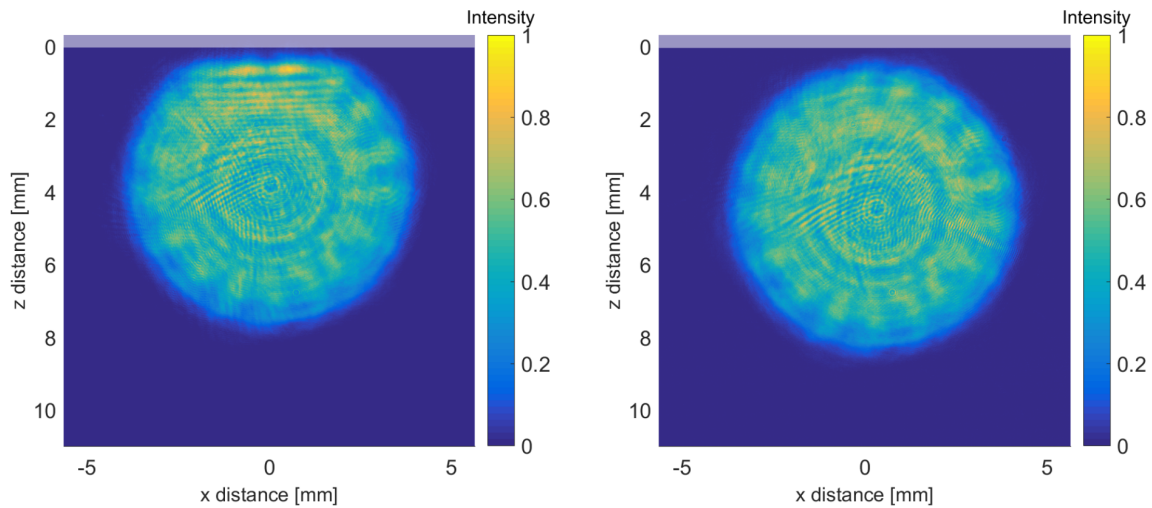


Figure 4.13: Normalized intensity profile of the flat-top beam with a radius parameter of $w_0 = 3.7$ mm after propagation through the vacuum chamber, as illustrated in figure 4.2. **Left:** The beam is horizontally aligned at a distance of $z = 3.7$ mm below the atom chip which is positioned at $z = 0$. At this position diffraction effects are clearly visible. **Right:** A horizontal shift of the beam by 0.8 mm to a position of $z = 4.5$ mm results in an intensity profile that no longer shows visible diffraction patterns.

To measure the effect of the individual intensity distributions for beam splitter operation, the population transfer of a double Bragg process into the states $|p = \pm 2\hbar k\rangle$ is measured. The process is not adjusted to resemble a $\pi/2$ or π transition but rather to map fluctuations of the individual beam profiles in the form of varying normalized output port population $P_{\pm 2\hbar k}$. A BEC is generated below the atom chip and released from its final magnetic trap. After a certain stepwise adjusted free fall time, defining the distance z , a light pulse with constant intensity is applied. Figure 4.14 shows the results for a flat-top profile versus a Gaussian profile. Each scan is repeated three times and the corresponding standard deviations are shown as error bars. The enveloping profiles verify the z -distance to the surface of the atom chip measured by beam profile camera, determined by the known relative position of the final trap and the free fall time. For the flat-top beam, the intensity plateau is reached after less than 2 mm, confirming that it is positioned much closer to the chip surface than the Gaussian beam. Since the population transfer depends on the light field intensity and the duration of the applied pulse, from a simple theoretic assumption it should be possible to achieve higher transfer efficiencies with the Gaussian profile near the chip surface by increasing one or both of these parameters. Comparing the two beam profiles presented, more than a factor of 2.5 higher power is required

to achieve the same intensity at the $1/e^2$ position of the Gaussian beam as at any position on the plateau of the flat-top beam. In reality time and power cannot be adjusted independently from other possibly unwanted effects like velocity selectivity or stray light effects.

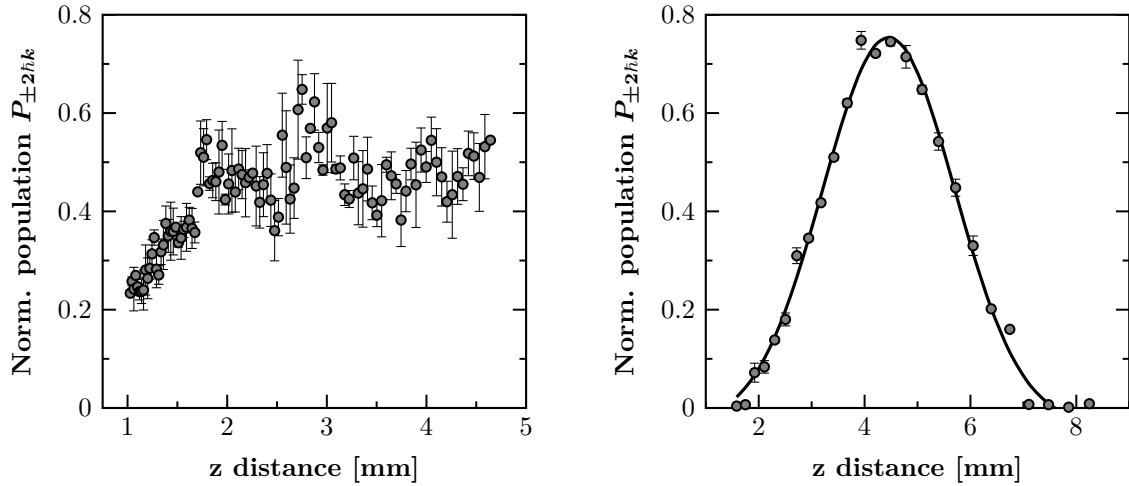


Figure 4.14: Comparison of the beam splitter capabilities in an atom interferometer between the flat-top and the Gaussian beam profiles. The laser intensity is kept constant while the free fall time is stepwise adjusted, resulting in an increasing fall distance of the atomic ensemble in the beam. This way fluctuations of the individual beam profiles are mapped in the form of a varying normalized output port population $P_{\pm 2\hbar k}$. **Left:** The flat-top profile shows fluctuations with an average standard deviation of $\sigma = 0.044$ for repeated measurements. The plateau of the flat-top is reached after a distance of $z = 1.7$ mm with $P_{\pm 2\hbar k} = 0.545 \pm 0.055$. Since intensity and time of the pulse were not adjusted to a specific transfer, this value does not represent the maximum achievable efficiency. **Right:** The profile is fitted by a Gaussian envelope (analogous to equation 3.3) and shows fluctuations with an average standard deviation of $\sigma = 0.010$ for repeated measurements. At distances larger than 7.5 mm, the fitting algorithm is no longer able to reliably distinguish the individual atomic clouds from each other due to the small separation time available, resulting in an underestimation of the normalized population.

On the one hand, the varying population transfer may map the intensity distribution of the retro-reflected field, similar to the profile shown in figure 4.4. On the other hand the fluctuations, as represented by the standard deviations, are larger than with the Gaussian beam. Finding a clear explanation is difficult, as there can be different reasons for this behavior. Many of them can be ruled out based on common features, since the same laser light coupled into the individual fibers shares a common source and the same optics are used at the experimental vacuum chamber. One possible difference lies in the design of the beam shaping optics. While the Gaussian collimator consists of a two-lens system within a common non-magnetic steel housing, the flat-top optics are more modular, for reference see subsection 4.1.1. This setup was chosen so that the system would be flexible enough to adjust the two-axis tilt and x - y displacement to an optimized wavefront profile. However, this makes the system more susceptible to perturbations, which affects the relative position of the optical components to each other.

To quantify these, the temporal stability of the Gaussian beam used as input for the flat-top beam shaper and the actual flat-top beam shaper is analyzed by taking two sets of 50 images. Each image is separated in time by the typical experimental repetition rate of $t_{\text{cycle}} = 15\text{ s}$. They are generated by illuminating the beam profiling camera for a typical pulse duration of $220\text{ }\mu\text{s}$.

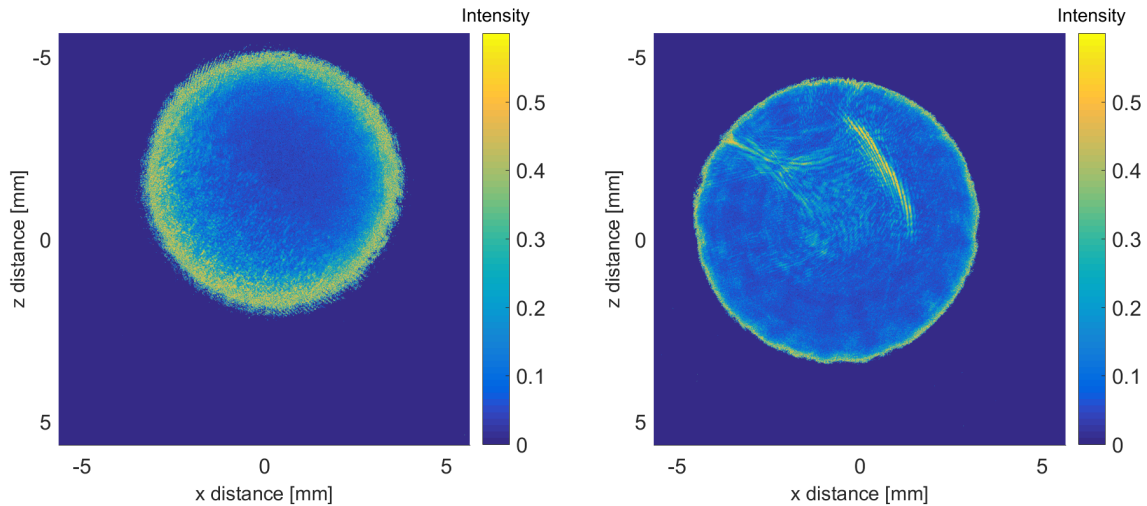


Figure 4.15: Comparison of the temporal-spatial stability of the Gaussian beam used as input for the flat-top beam shaper and the actual flat-top beam shaper output. The images are generated by illuminating the beam profile camera for a pulse duration of $220\text{ }\mu\text{s}$. The average of 50 of these images is calculated and subtracted from a single reference image. The intensity scale shows the difference between the mean and the individual picture divided by the pixel values of the mean picture. **Left:** Temporal variations of the Gaussian beam with large changes at the edges of the profile, which is attributed to a large uncertainty due to the low illuminance at this location. **Right:** Temporal deviations of the flat-top beam with changes at the edge for the same reason, but also with interference-like patterns closer to the center with large deviations.

To determine the deviations, the average of these 50 images is calculated and subtracted from the individual images. Two images generated in this way, showing the deviation from the mean in a normalized manner, are shown in figure 4.15. For both, the deviations at the edges of the profile seem to be large, which is due to a large uncertainty caused by the low illuminance at these positions. In the middle region of the Gaussian beam, however, the deviations from the mean are apparently more constant and smaller in amplitude than in the middle region of the flat-top beam. The apparent interference pattern can already be observed on the images in figure 4.13 but less prominent. This temporally unstable pattern has a large effect on the amplitude of the beam splitter and therefore suggests a more stable and rigid structural beam shaper. The determined critical component was found in the described setup between fiber output and first collimating lens. An ideal future setup would therefore first reduce the wavefront error to a minimum by adjusting the relative positions of the individual optical

components and afterwards tightly fix the connection between them to eliminate the observed temporal spatial instabilities.

4.2 High power lattice laser system with active light shift compensation

Light field imperfections can lead to different dephasing processes caused by a spatially varying intensity distribution and variable dipole forces along the interferometer arms [Mor93; Mül95; Dei08; Cro09]. The atomic trajectories governed by the spatial distribution of atoms are differently influenced by these often path-dependent effects. One direct observation is the loss of contrast as shown in subsection 3.2.2 and 4.1.3. Reasons for existing imperfections are manifold and can range from mere clipping of the light beam over manufacturing tolerances of the beam shaping optics or transmissive elements in the optical path to the evolution of the wavefront (for reference see subsection 4.1.2).

The spatial profile of the light field affects the atom-light interaction in a position dependent manner and consequently the measured phase of the interferometer. The static influence of intensity and phase imperfections was studied in the sections before. In the following, an active suppression of the resulting light shifts is presented by adding a light field of the same power that introduces a shift of opposite sign so that the frequency dependent shift of the other field is approximately compensated.

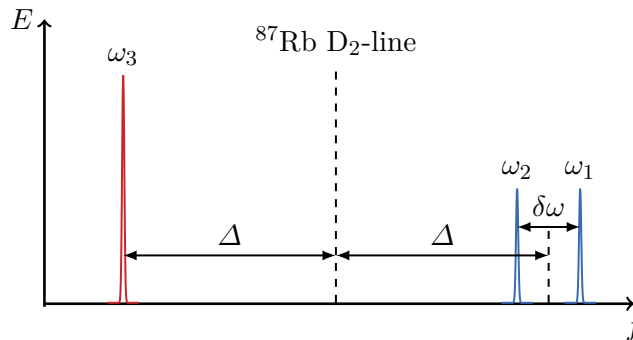


Figure 4.16: Required frequencies to realize a light shift compensation mechanism for a twin lattice. The combined light field should contain two of the frequencies (ω_1 and ω_2) with linear orthogonal polarization, that generate the lattice potential and a third component ω_3 . The power of the third frequency component is equal to their sum and enables the compensation. The frequencies are oppositely tuned from the ^{87}Rb D₂-line resonance by Δ , with the relation $\Delta \gg \delta\omega$. The frequency axis f is shown not to scale.

Atom-optical operations like higher-order Bragg diffraction as well as manipulations in an optical lattice via Bloch oscillations typically require coherent light sources with high optical powers. This is especially true for the large momentum transfer techniques developed within the twin lattice (see section 3.2). In addition, sufficient global detuning Δ away from the atomic resonance to reduce spontaneous emission and high quality of the optical mode field become relevant.

One experiment realizing atom interferometers with long interaction times and large momentum beam splitters has demonstrated the importance of absolute light shift compensation [Kov15b]. There the quantum superposition principle was studied on the half-meter scale, and the observed contrast almost completely disappeared when working without compensation. A direct outcome was the development of a laser system with low phase noise, large optical output power, frequency flexibility from tens to hundreds of megahertz, and an optical spectrum that contains multiple frequency components separated by tens of gigahertz or more [Kim20].

For example, operation of a light-shift compensated twin-lattice interferometer in a retro-reflected configuration requires three separate frequencies combined into a single beam. The above mentioned requirements must be met, and the total light field should contain two of the frequencies (ω_1 and ω_2) with linear orthogonal polarization, and a frequency component ω_3 with equal power. As shown in the figure 4.16, these frequencies need to be oppositely tuned from the ^{87}Rb D₂-line resonance by Δ , with the relation $\Delta \gg \delta\omega$.

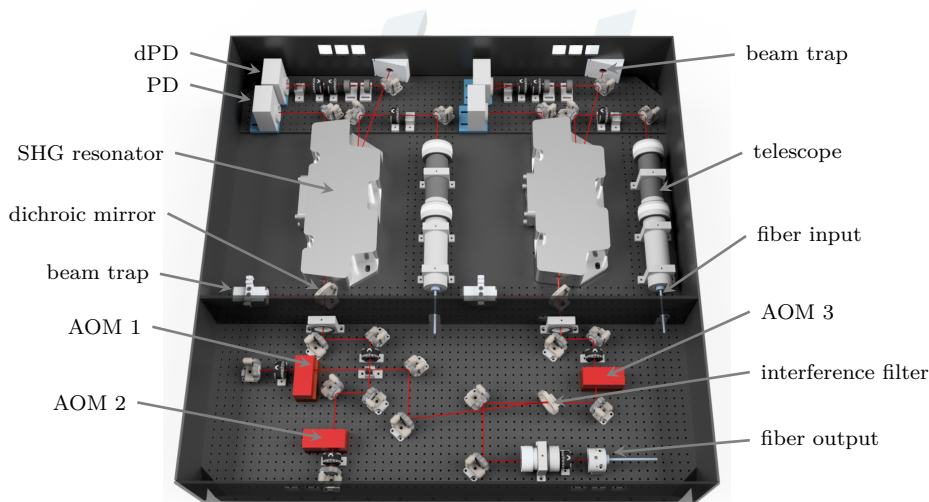


Figure 4.17: Setup for frequency doubling, distribution and overlapping of two individual laser beams on a custom honeycomb breadboard (600 mm \times 600 mm) to generate a single high power, light shift compensated laser beam. The main components are labelled with the following abbreviations: differential Photodiode (dPD), Photodiode (PD), Second Harmonic Generation (SHG), Acousto-Optical Modulator (AOM).

To realize this, a laser system is set up based on two commercially available fiber lasers [ADJUSTIK C15, NKT Photonics], with a narrow linewidth of less than 15 kHz, that are amplified in two separate fiber amplifiers [Koheras BOOSTIK, NKT Photonics] to an optical power of 15 W and 10 W. The output wavelength of these lasers is at the C-band of optical communications technology at a wavelength of $\lambda \approx 1560$ nm and can be thermally tuned by up to 1000 pm.

This established technology makes it relatively easy to acquire high optical output powers. A disadvantage is that the typically interrogated hyperfine transitions of rubidium are not close to this wavelength, but can be reached after a frequency doubling, which is also explained and exploited in section 4.3. The thermal fine tuning of the fundamental wavelengths of the two lasers is manufactured in a way that they can be oppositely detuned by Δ between 100 GHz to 260 GHz. For the maximum value this corresponds to 779.71 nm and 780.77 nm, which is commonly referred to as the blue and red detuned light fields. Without any external stabilization, the two fiber lasers already provide an absolute frequency stability of changes below 10 MHz for roughly one hour at laboratory room temperature with approximately 20.0 ± 0.1 °C. This is significantly less than their absolute frequency difference in the range of several hundred GHz.

For the purpose of frequency doubling, distribution and overlapping of the two individual laser beams an optical assembly is set up on a custom honeycomb breadboard. A more detailed overview of the system can be found in the reference [Che21]. It consists of two stages, the first of which is used for frequency doubling of the fundamental light fields ($\lambda \approx 1560$ nm). The second stage is employed for frequency as well as amplitude modulation and distribution of the frequency-doubled light fields ($\lambda \approx 780$ nm). The first stage can be seen in figure 4.17 in the top part and features a mirror set up of two bow-tie cavities [custom SHG resonator, Agile Optic] that serve the purpose of Second Harmonic Generation (SHG) of the two fundamental light fields [Han18; Sha21]. To realize this doubling process, a MgO:PPLN crystal is placed inside the cavity, on which the light field is focused. To this end, the fiber output of the amplified fundamental light field is connected to a two stage telescope assembly that focuses the beam to a beam waist of 280 μm at the position of the crystal inside the bow-tie cavity. Before entering the cavity housing the light field's polarisation is cleaned by a Polarizing Beam Splitter cube (PBS) and matched with one of the crystal axis by an optical half wave plate ($\lambda/2$). To enable stable frequency doubling, the optical path inside the cavity is stabilized with respect to the coupled fundamental wavelength. This is done by means of a piezoelectric actuator attached to one of the four cavity mirrors and controlled by a proportional-integral (PI) controller. The herefore required error signal is generated using a Hänsch-Coulliaud lock scheme [Han80]. For this purpose a dispersion-type error signal is generated from the phase shift upon reflection of the light from the cavity detected by a differential Photodiode (dPD). An additional single photodiode (PD) is monitoring a fraction of the frequency-doubled light and helps to identify the correct lock position of the error signal. As long as the resonance condition is fulfilled the entire fundamental pump light is coupled into the cavity. If this is not the case the cavity turns reflective and the majority of the light is dumped in a beam trap [BT620/M, Thorlabs] for safety reasons. One SHG cavity frequency doubles the 15 W input for the purpose of creating the needed power for all optical lattice operations, while the second cavity doubles the 10 W input to create a light field with opposite light shift nulling the total light shift. To distinguish these two from each other they will be referred to 'lattice light field' and 'compensation light field' in the following. Their individual output powers can be seen in figure 4.18, with a notable difference in conversion efficiency.

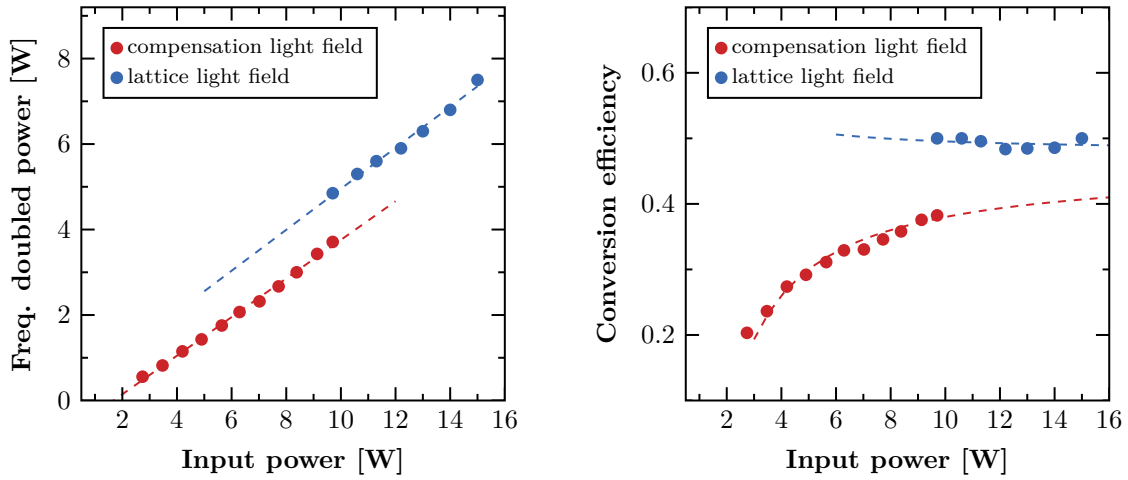


Figure 4.18: Comparison of the conversion efficiencies of the frequency doubling cavities. **Left:** Frequency-doubled output power as a function of input power for each cavity. The maximum input power of 10 W for the compensation light field is frequency doubled to 3.7 W and 15 W for the lattice light to 7.5 W, respectively. The dashed lines represent the linear trend (fit) as a guide to the eye. Due to the detectable power range of the DPD, the doubling of the lattice light could not be operated below 10 W for a selected lock set point. **Right:** Conversion efficiency (corresponding to frequency doubled power divided by input power) in dependence of the input power for each cavity. The dashed lines show the estimated trend for the conversion efficiencies and represent the same fit as in the left graph. This more clearly indicates an underperforming frequency-doubled output power for the compensation light field.

This could not be linked to the comparable parameters of incoupling efficiency 86 % to 94 % and finesse $\mathcal{F} = 85.6$ to 86.2 for both cavities. Thus, an underperforming frequency doubling in the PPLN crystal is the most likely candidate to explain this deviation.

The two cavities emit frequency-doubled as well as fundamental laser light. Therefore, before entering the second stage of the system, as seen in figure 4.17 in the bottom part, those are separated at a dichroic mirror [DMSP1180, Thorlabs]. More than 99.7 % of the fundamental light is reflected and directed towards a beam trap [BTC30, Thorlabs], where it is absorbed. The dichroic mirror also has a $> 97.9\%$ transmission for the frequency-doubled light. To operate a light shift compensated twin-lattice interferometer, the three separate frequencies are generated and controlled as follows. Two of them ω_1 and ω_2 are generated from the output of one of the cavities with the help of double pass setups using two Acousto-Optical Modulators (AOM) 1 and 2. Afterwards they are overlapped at a PBS with orthogonal polarizations. The third frequency ω_3 , the compensation light field, is generated from the other cavity output and modulated onto by AOM 3 in a single pass configuration. The main purpose of these modulators is twofold. On the one hand, they ensure that the frequency of the laser light field always remains in resonance with the desired atom-optical manipulations and on the other hand, they allow the overall power to be adjusted. In addition, the double-pass configuration helps to reduce the angular dependence of frequency modulations that affects the beam path and

reduces beam overlap and fiber coupling efficiency. While acousto-optic frequency modulation is on the order of kHz or MHz (δ_ω), the frequency spacing Δ between the lattice light frequencies and the compensation frequency can be set in the much larger range of 100 GHz to 260 GHz. For optimal operation, the magnitude of the optical power of the two lattice light fields ω_1 and ω_2 should be equal, as well as their sum should be equal to the power of the compensation light ω_3 . The superposition of these three frequencies is explained in detail in the following section 4.2.1. After superposition the combined light field is mode matched by a telescope assembly to a fiber collimator and coupled into a single large mode area photonic crystal fiber [LMA-PM-10, NKT Photonics] that is able to guide high optical powers of up to 6 W to the vacuum chamber containing the atomic clouds to be interrogated.

4.2.1 Beam superposition

To realize the light shift compensation using the additional light field of frequency ω_3 it must be superimposed with the actual lattice light field. With orthogonal polarization of ω_1 and ω_2 , which must be preserved, the use of a polarizing beam splitter is not an option. Alternatively, a non-polarizing beamsplitter comes with the cost of losing 50 % optical power. Another possibility would be a dichroic mirror, as employed in the section before to separate the fundamental and frequency-doubled light, but its transmission/reflection bandwidth is not spectrally narrow enough.

As a proposed new solution an interference filter in the form of a substrate coated by Ion Beam Sputtering (IBS) with a narrow transmission line, tunable by the incident angle of the beam, is used [IF 780 nm/6° (B-06650), LASEROPTIK]. The beam superposition itself is done by transmitting the frequencies ω_1 and ω_2 through the interference filter, while simultaneously reflecting ω_3 . The coating of the filter is designed for a center wavelength of $\lambda \approx 780$ nm. Due to the difference of 1 nm between the lattice and compensation light field the performance away from the design optimum must be investigated. Since the reflection bands to the left and right of the transmission peak of the filter are spectrally broader, the reflection adjustment is easier compared to the transmission at an angle of $6 \pm 2^\circ$. A Lorentz fit of the measured transmission data helps to quantify its bandwidth following

$$f_{\text{Lorentz}}(x) = a_0 \frac{\left(\frac{1}{2}\Gamma\right)^2}{(x - x_0)^2 + \left(\frac{1}{2}\Gamma\right)^2}, \quad (4.14)$$

where a_0 defines the amplitude of the curve, x_0 its center shift and Γ the FWHM, calculated to $\Gamma = 11.25 \pm 0.22$ mrad. To be able to supply enough optical power the transmission is tested successfully with up to 3.8 W of laser light at a wavelength of $\lambda = 780.77$ nm with a collimated Gaussian beam waist of 1.4 ± 0.1 mm. By tuning the wavelength of the laser light and setting the mirror angle to maximum transmittance, a linear relationship between the two can be demonstrated for the operating range. The corresponding coefficient is calculated to 28.43 mrad/nm and allows to determine the wavelength dependent transmission relation as shown in figure 4.19 on the left. The corresponding FWHM of the Lorentz fit, analogous

to equation 4.14, yields a value of $\Gamma = 0.396 \pm 0.004$ nm, which is much smaller than the separability of a dichroic mirror, for example.

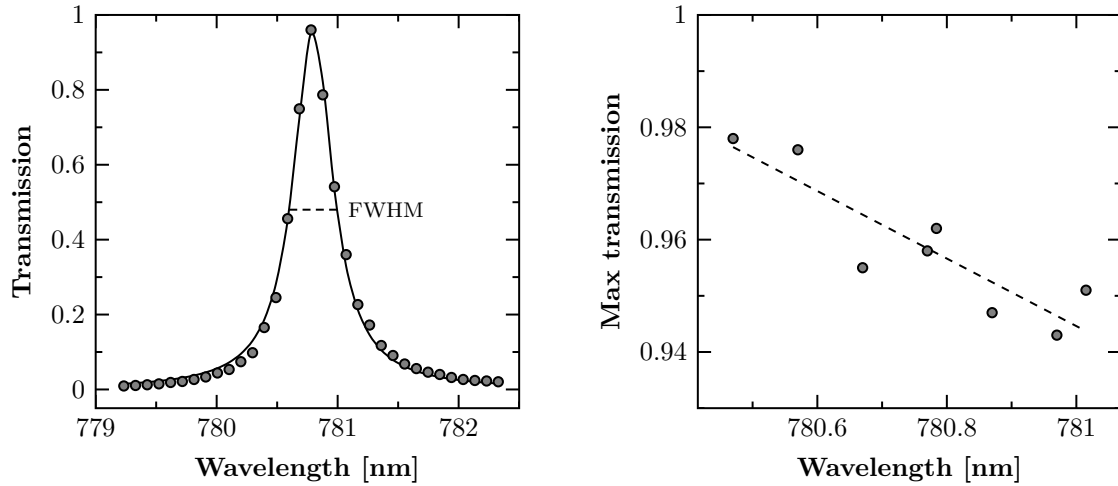


Figure 4.19: Performance of the interference filter for the superposition of the lattice light field with the compensation light field. **Left:** Normalized transmission in dependence of the incoming wavelength for a fixed incident angle of the beam. The corresponding FWHM of a Lorentz fit returns a value of $\Gamma = 0.396 \pm 0.004$ nm. **Right:** Maximum transmission values for different wavelengths and individually optimized incident angles, corresponding to the maximum of the Lorentz fit on the left graph. The transmission percentage decreases further away from the design wavelength of the interference filter. Assuming a linear dependency for this range a maximum transmission between 98 % and 94 % is obtained.

By setting the transmission wavelength to different values and optimizing the incidence angles individually, the corresponding maxima of the Lorentz fits can be plotted as shown in 4.19 on the right. It is observable that the transmission percentage decreases further away from the design wavelength, which is expected. Assuming a linear dependency for this small range of 0.55 nm a maximum transmission between 98 % and 94 % is obtained.

In the presented case the frequencies ω_1 and ω_2 are transmitted through the interference filter and frequency ω_3 is reflected. In principle, these roles can also be reversed, since no significant difference in the conservation of the individual polarization-extinction ratios is found for either transmission or reflection. As a quantitative measure of overlap, the efficiency of coupling into a polarization-maintaining single-mode fiber is performed as a test. The coupled power depends strongly on the angle and position of the beam relative to the coupling lens and fiber facet [Tom81] and can therefore serve as an ideal metric for beam overlap. Comparing the two light field powers before the superposition with the powers in the coupled fiber results in an overall fraction of 85 % for the transmitted light field and 89 % for the reflected light field. Taking into account the losses at the additional optical elements in the optical beam path after superposition (see figure 4.17), the finite mode matching quality to the fiber and the loss

channel due to the Fresnel reflection, this represents an overall low-loss realization. For the requirements of optical powers of more than 1 Watt and relative polarisation preservation, the superposition at an interference filter provides a unique and effective solution.

4.2.2 Alternative ways of generating light shift compensated lattice light fields

An alternative way to create a single lattice light beam containing all necessary frequency components for light shift compensation is to overlap the frequency-doubled compensation light field ($\lambda \approx 780$ nm) with the fundamental input light of the lattice light field before it is itself frequency-doubled ($\lambda \approx 1560$ nm). At this point, a dichroic mirror can be used, which is technically less demanding because the individual wavelengths are separated by many hundreds of nanometers. This would mean that the compensation light field additionally needs to pass through the second resonator once again without being frequency doubled. Whereby the combined output beam would then be a superposition of two frequency-doubled light fields. One drawback of this setup is that the subsequent modulation by AOMs 1 and 2, which generates the frequencies ω_1 and ω_2 as before, is applied to both light fields, creating an additional (unwanted) lattice pair. Furthermore, the optical path length of the compensation light field is significantly extended and additional effort is required to achieve the ideal minimization of the path length difference.

The design presented in [Kim20] follows a similar approach, with the difference that initially a total of four individually modulatable light fields are generated at a wavelength of $\lambda \approx 1560$ nm. Subsequently, two of them are frequency-doubled (single pass through PPLN non-linear crystals) and each superimposed with one of the other two. In this way, individually controllable, so-called negatively detuned 'red' and positively detuned 'blue' Bragg pairs are obtained. For technical reasons, such a system can in principle enable higher optical powers and generates a total of four optical frequencies in the final beam, but it also requires twice the number of fiber amplifiers and doubling stages. Since all of the proposed approaches have individual advantages and disadvantages, it remains a case-by-case decision which path to take.

For reference, it should be mentioned that the subsection 4.3.2 explains more theoretical background of the differential light shift and its compensation for the case of a light field used for (double) Raman diffraction.

4.3 Compact fiber-based laser system for coherent manipulations

To perform atom interferometry experiments with ultracold atoms different optical frequency components are necessary. The range of their applications extends from the capture and cooling of the atomic ensemble to its manipulation and detection. Most of the laser systems built to date for this purpose take up a lot of space on optical tables and suffer from environmental perturbations, for example in the form of dealignment or coupling to noise sources. A promising solution to improve this situation can be the use of fiber-based telecommunication components. In particular, when using atomic rubidium as a source for atom interferometry, which has favorable transition frequencies close to the wavelength of $\lambda = 780$ nm. The system described

in the following enables the generation of all optical frequencies displayed in the hyperfine structure diagram in figure 4.20.

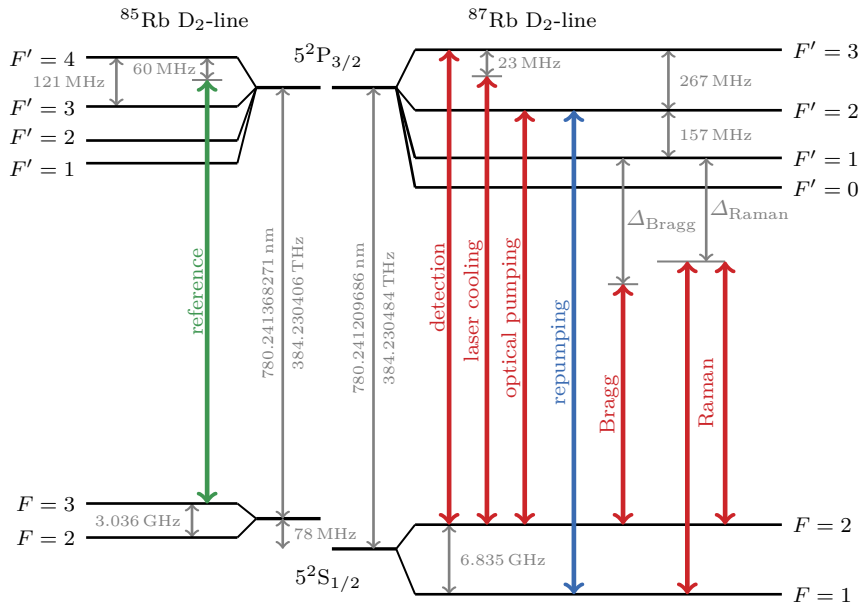


Figure 4.20: D₂ transition hyperfine structure of ⁸⁵Rb and ⁸⁷Rb, with frequency splittings between the hyperfine energy levels. The colored arrows depict all transitions employed for the initial cooling, trapping and manipulation of the ⁸⁷Rb atoms. The respective splits are based on the amount of the shifts, but are not shown to scale. The color coding (green, red, blue) reflects three different laser sources, with each task labeled next to the transition.

A notable advantage of this system is the flexibility to drive Raman and Bragg transitions via single and/or double diffraction in a retro-reflective setup without the need for modifications other than electronic sequence control. This makes it easy to study interferometry topologies based on a combination of Raman and Bragg beam splitters by utilizing control over both internal and external states and exploit their complementary advantages [Ber15; Say22]. The following list gives a few examples where such investigations are of interest. They illustrate why the use of a flexible laser system as presented in this section can be advantageous.

- Tests of quantum-clock interferometry in a twin paradox like experiment with a superposition of two different internal states and magic Bragg diffraction [Lor19b]
- Testing the universality of the gravitational redshift by creating an internal superposition within the interferometer sequence, corresponding to an initialization of a clock [Rou20]
- Atom-interferometric tests of the universality of free fall and gravitational redshift without a superposition of internal states using double Raman and double Bragg diffraction [Ufr20]
- Removal of spurious paths in Mach-Zehnder like atom interferometers by utilizing Raman diffraction as blow-away pulses [Pet01; Har20]

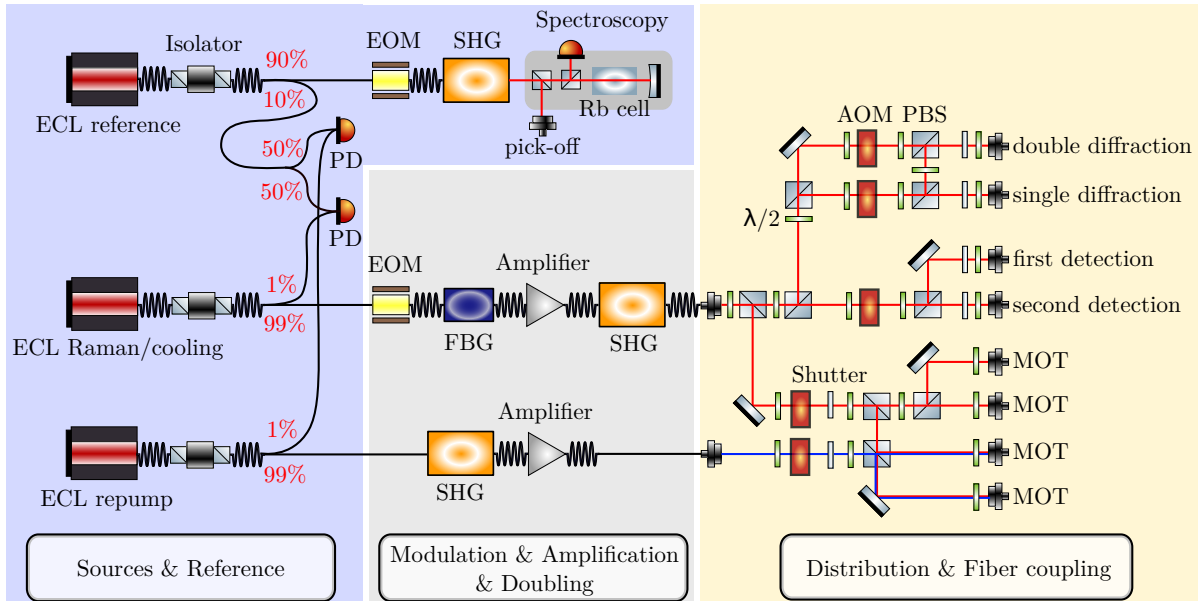


Figure 4.21: Schematic setup of the fiber based generation of all transition frequencies shown in figure 4.20. Fiber connections are shown in black color, the red and blue lines show the propagation of the laser light in free space. The system is divided into three color coded modules which take on different tasks of the laser system. The blue shaded area on the left contains three single-frequency lasers emitting light in the C-band of optical communications technology. One of them is locked to the ^{85}Rb D_2 line as a reference, and the other two are offset locked onto it. In the gray shaded area the light of one path is frequency modulated, frequency filtered, amplified and finally frequency doubled. In the other path the light is first frequency doubled and afterwards amplified. The last module in orange on the right side shows the distribution to eight different optical fibers, which guide the individual amplitude and frequency modulated light fields to the experimental chamber. Any electric and electronic connections between the components are neglected for better visibility. The individual components are labelled with the following abbreviations: External Cavity single-frequency Laser (ECL), Electro-Optical Modulator (EOM), Photodiode (PD), Second Harmonic Generation (SHG), Fiber Bragg Grating (FBG), Acousto-Optical Modulator (AOM), Polarizing Beam Splitter (PBS), half wave plate ($\lambda/2$), Magneto Optical Trap (MOT).

The following part of this section will mostly focus on its design, setup, characterization and implementation. As a first demonstration, the capabilities for double Raman diffraction are presented in the end. The scheme of this fiber based setup in figure 4.21 shows the three color coded modules with different purposes. The blue shaded area on the left contains three laser sources in the form of pigtailed External Cavity single-frequency Lasers (ECL) [SFL1550P-CUS-1560.5NM, Thorlabs] with a typical linewidth of 50 kHz and output power of 40 mW mounted in butterfly laser diode mounts [LM14S2, Thorlabs]. They are powered by current drivers developed at the Institute of Quantum Optics in Hannover. These drivers are designed to fit into an 8-bit parallel bus system and can be connected to other cards for different purposes to create a stack. While the hardware part of this system is based around the bus system to enable a simple hardware interface, the software part allows for a user interface and translates the user commands to hardware instructions. In the following this will be referred to as the TBus system.

The ECLs are connected to temperature controllers [TEC-1091, Meerstetter], which allow the diodes to be temperature stabilized to better than 0.01 °C. Furthermore the tuning of these temperatures allows to shift the setpoint of the output wavelength of the emitted laser light fields to the desired values at a wavelength of $\lambda \approx 1560$ nm. The three output light fields are fiber coupled by design and pass three separate optical isolators [IO-G-1550-APC, Thorlabs] with an isolation better than 30 dB. The first light field serves as an absolute reference to which the employed other two lasers can be offset locked to. For that reason its frequency is stabilized onto the crossover transition of $|5^2S_{1/2}, F = 3\rangle \rightarrow |5P_{3/2}, F = 4\rangle$ of ^{85}Rb with the help of frequency modulation transfer spectroscopy. This locking is realized by modulating the laser light at 12.5 MHz with a fiber-connected 1550 nm band 10 GHz Electro-Optical phase Modulator (EOM) [MPZ-LN-10, iXblue Photonics]. The modulation signal is provided by a frequency controller card that is located inside the TBus system, which also provides the necessary infrastructure to frequency stabilize the reference laser light.

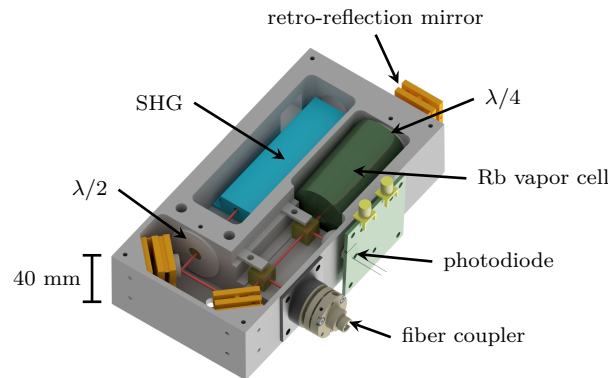


Figure 4.22: Setup of the spectroscopy unit for the generation of an absolute frequency reference based on the ^{85}Rb D₂ line. The input light is connected via a fiber to a wavelength conversion module, where it is frequency doubled. After passing through a half-wave plate, a small portion of the light output is split at a PBS and coupled into a single-mode fiber. The remaining light passes through a rubidium vapor cell, is retroreflected at a quarter-wave plate and a mirror combination, and finally passes back through the PBS to a photodiode where the spectroscopy signal can be electronically recorded.

Since all transitions shown in figure 4.20 are close to the wavelength of $\lambda \approx 780$ nm, the light emitted by all ECLs must be frequency doubled. In the case of the reference laser this is done with a wavelength conversion module [RMA1702010010, HC Photonics]. This waveguide mixer is based on the principle of second harmonic generation (SHG) inside a PPLN. After this doubling the laser beam probes ^{85}Rb atoms contained as a vapor inside a glass cell in the configuration shown in figure 4.22. Here also additional optical elements like half- and quarter-wave plates ($\lambda/2$ and $\lambda/4$), three adjustable mirror mounts with mirrors and two PBS are shown. Additionally a portion of the light inside this module is coupled into an optical fiber [PMC-780-5.1-NA012-3-APC-100-P, Schäfter + Kirchhoff] for monitoring the frequency

spectrum of the reference laser light and debugging purposes. The second part of the light beam is detected after retro-reflection on a photodiode whose signal is fed back to the frequency controller card. This signal is demodulated and the zero crossing of the obtained error signal, with a signal-to-noise ratio of around 20, is used as input for a PI controller to modulate the current of the initial laser diode. In this way the output wavelength of the 'ECL reference' is stabilized onto the ^{85}Rb atomic transition mentioned before and can serve as an absolute frequency reference.

Due to technical limitations of the electronics used, the absolute position of the locking point may shift by a few hundred kHz over time, but since the FWHM of the natural linewidth $\Gamma = 2\pi \cdot 6.065 \text{ MHz}$ of the ^{87}Rb D_2 transition used is relatively wide, this is acceptable. The control bandwidth is sufficient for all operations shown in figure 4.20 with their respective single photon detunings. The long-term stability is given by the frequency reference used, which can be the signal of the 100 MHz oscillator also used later [DLR-100-50G SN 11FR07-05, Wenzel Associates]. For this application, its deviations are in a negligible order of magnitude.

To be able to address the specific atomic transitions, the other two ECLs are to be stabilized against this reference frequency, and for this reason 10% of the light from the reference laser is diverted and combined with 1% from each of the other lasers. These lasers are called by different names corresponding to their main tasks in the system. The two new resulting light fields are detected on two fiber-coupled photodiodes [FGA01FC, Thorlabs]. Their electronic beat outputs individually pass through a powered Bias-Tee [ZX85-12G-S+, Mini-circuits] whose RF output port is connected to an amplifier [ZJL-7G, Minicircuits]. The amplifier output frequency is divided by a factor of two by a prescaler [FPS-2-12, RF BAY] for the 'ECL Raman/cooling' and by a factor of six [FPS-6-12, RF BAY] for the 'ECL repump'. The outputs from the two prescalers are at the end used as input to the frequency controller card, which in addition already has the task of locking the reference laser. This input is converted using a frequency counter on the board and used as input to a control loop that outputs changes in laser current that are added to or subtracted from the output of each laser current driver depending on defined setpoints. In this way, the laser frequencies of the two ECLs are locked with respect to the absolute frequency reference supplied by the 'ECL reference'. The repump ECL diode is locked with an offset of 2710.932 MHz, which can be calculated from the difference in transition frequencies as shown in blue in figure 4.20. Apart from the division factor of six mentioned above, it must also be taken into account that all light fields undergo a frequency doubling before driving the transitions shown in the figure. Additionally an amount of 80 MHz must be added for the two offset locked lasers due to diffraction by AOMs explained later in this paragraph. This leads to an actual detected beat frequency of 451.489 MHz. The Raman/cooling ECL diode can not be locked with a constant offset value since it needs to perform more than one task. These tasks, represented by the red transition arrows in the figure 4.20, are called optical pumping (beat frequency of 353.205 MHz), laser cooling (beat frequency of 292.292 MHz), detection (beat frequency of 286.542 MHz) and Raman or Bragg diffraction (Δ_{Raman} and Δ_{Bragg}). Therefore its lock setpoint is dynamically changed

during successive operations. The biggest frequency jump is defined by the global detuning values $\Delta_{\text{Raman,Bragg}}$. In the here presented case the maximum achievable values are around $\Delta_{\text{Raman,Bragg}} < 2 \text{ GHz}$ on time scales of the order of milliseconds, limited by the detectable beat frequency.

The grey shaded area in figure 4.21 defines the second stage of the full laser system and serves three main purposes: modulation, amplification and frequency doubling. Two of the ECL diodes from the first stage, the repump ECL and Raman/cooling ECL, are fiber connected to this module. The light field of the repump ECL is frequency doubled inside a wavelength conversion module [WH-0780-000-F-B-C, NTT Electronics] and afterwards amplified by a high-gain semiconductor optical amplifier [SOA-780-20-YY-30dB, Innolume GmbH] to a typical output power of 120 mW before leaving the module fiber-coupled. In parallel the light from the Raman/cooling ECL is undergoing a more complex modulation scheme, which is detailed in figure 4.23.

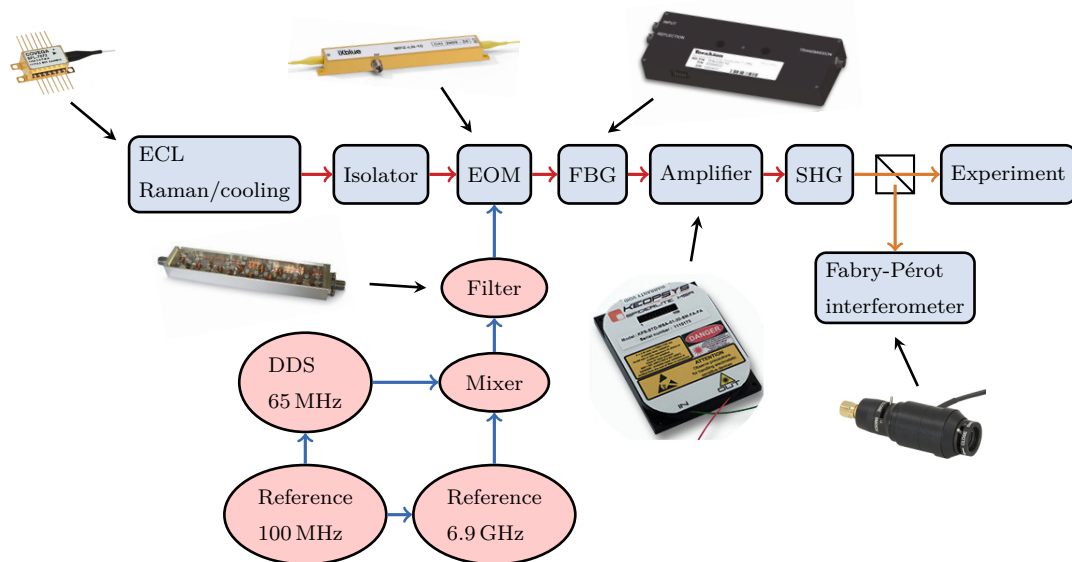


Figure 4.23: Flowchart of the steps to generate the frequencies needed for Raman diffraction based on electro-optical modulation. The optical components are highlighted by a blue background and the electronic components by a red background. Red arrows symbolize fiber connections, orange arrows free space propagation and blue arrows electronic connections. Briefly, the original light field is first modulated by an EOM supplied with a frequency of 6.835 GHz, creating sidebands. An optical filter in the form of an FBG suppresses all unwanted sidebands, leaving the carrier and only one sideband. These are frequency doubled by generating the sum frequency and the second harmonic. The output spectrum is monitored by a Fabry-Pérot cavity and fed to the experiment.

To drive the process of a stimulated Raman transition usually two phase-locked laser light fields are required, typically derived from two separate sources. A complementary approach is to make use of the electro-optic effect [Kaw07], for example with an EOM or its more elaborate

version the I/Q modulator for single-sideband generation [Zhu18; Pan23b]. Especially a low-phase noise implementation for the hyperfine splitting is mandatory. In the implementation presented here, an EOM with a bandwidth of up to 12 GHz [MPZ-LN-10, iXblue Photonics] is used, which can add a modulation frequency of 6.835 GHz. It is supplied by a frequency reference of 100 MHz generated by stress-compensated-cut ovenized oscillators [DLR-100-50G SN 11FR07-05, Wenzel Associates]. From an earlier measurement, a phase noise of less than -90 dBc/Hz was determined [Wen10]. Its integrated phase noise density as well as those of the other used components is shown in table 4.2. The output of 100 MHz is multiplied by a factor of 69 within a frequency chain [GMU69124LN, RUPPtronik] to reach 6.9 GHz. This frequency is mixed [M3005LE, Advanced Microwave] with 65 MHz from a Direct Digital Synthesizer (DDS) [AD9958, Analog Devices], which is located on a DDS card module inside the above mentioned TBus system. The resulting electronic spectrum is filtered to feature only the frequency of 6.835 GHz, which is realized with a combline bandpass filter [CB 6776, BSC Filters Ltd] that suppresses the unwanted frequencies produced in the mixing process, as well as the fundamental frequencies. Mainly the frequency at 6.9 GHz is still visible but suppressed by more than 24 dBc, while 6.966 GHz is suppressed by more than 26 dBc and 6.768 GHz by more than 30 dBc. An even higher suppression would be achieved if the mixing would be done with a frequency of 7 GHz. The not suppressed frequency of $\lambda_{\text{RF}} = 6.835$ GHz is afterwards amplified by a low phase noise amplifier [AMF-5F-04000800-07-10P-LPN, NARDA-MITEQ] and fed to the EOM.

However, the so modulated light field also features unwanted frequency components in the form of parasitic sidebands that are detrimental to atom interferometers, as they produce both a systematic measurement bias and spatial variations in fringe contrast [Car12; Wan17; Sar22; Jia22]. The here presented system features a solution where these frequencies are filtered optically with the help of an ultra-narrowband tunable optical filter based on the concept of a Fiber Bragg Grating (FBG) [TFN-1560.482-N6.8-IL3.5-20-C1P-C, TeraXion] [Mac21].

To be able to drive Raman transitions for ^{87}Rb between the ground state hyperfine levels $|5^2S_{1/2}, F = 2\rangle$ and $|5^2S_{1/2}, F = 1\rangle$, two frequencies are needed whose difference corresponds to the frequency spacing between the states (for reference see section 2.2.3). Therefore the filter bandwidth is custom designed with a center wavelength at $\lambda = 1560.482$ nm, a tuning range of ± 20 GHz and a reflection bandwidth of 19 GHz with -20 dB suppression. In this way, the filter can be tuned by temperature to a setpoint where only the carrier frequency and one of the modulated sidebands are selected to pass through to the following fiber amplifier [CEFA-C-B0-HP, Keopsys], which amplifies the two frequencies to an optical power of up to 1 W. If additional suppression is needed multiple FBGs can be used to further increase the attenuation of undesired frequencies [Ram20]. Subsequently, the light field is frequency doubled in a wavelength conversion module [WH-0780-000-F-B-C, NTT Electronics] in the same way as the other light fields before, with the difference that the two frequencies now contribute not only to the second harmonic generation, but also to Sum Frequency Generation (SFG). With the help of a scanning Fabry-Pérot interferometer [SA210-5B, Thorlabs] with a Free Spectral

Range (FSR) of 10 GHz the generated optical spectrum can be observed, as can be seen in figure 4.24. Apart from the spectral properties, the amplitudes and amplitude ratios of the individual frequencies can be measured, assuming a linear response of the used Si photodiode, which is similar to the model [FDS100, Thorlabs]. Normally, the photocurrent of a such a diode can be assumed to be linear with respect to the incident light at the optical powers used. At a normal operating point the achievable range of linearity can be higher than nine orders of magnitude, as stated in reference [Ham14].

The frequencies ω_1 and ω_2 represent the ones labelled with 'Raman' in figure 4.20. Their intensity ratio I_1/I_2 is chosen so that the resulting differential AC Stark shift ω_{AC} becomes zero for a chosen global detuning Δ_{Raman} . The other, unwanted visible peaks ω_{-2} , created by SFG between the carrier and the imperfectly filtered sideband frequency, and ω_{2S} , created by SHG of the unfiltered sideband, are suppressed by more than 21 dB. The remaining two frequency components (ω_1 and ω_2) can additionally be power stabilized [Wan22]. One of the reasons why an unfiltered spectrum is undesired is the presence of multiple pairs of frequencies that can drive resonant two-photon Raman transitions. In this case the effective Rabi frequency contains a spatial dependence with a periodicity of $\lambda_{RF}/2$. With the present filtering this dependency can typically be reduced below an experimental noise level [Zhu18]. The unwanted sidebands can also induce a position dependent phase shift in the atom interferometer signal, which can be numerically calculated [Car12], if the herefore needed parameters can be estimated. But with the shown optical filtering, this is not necessary.

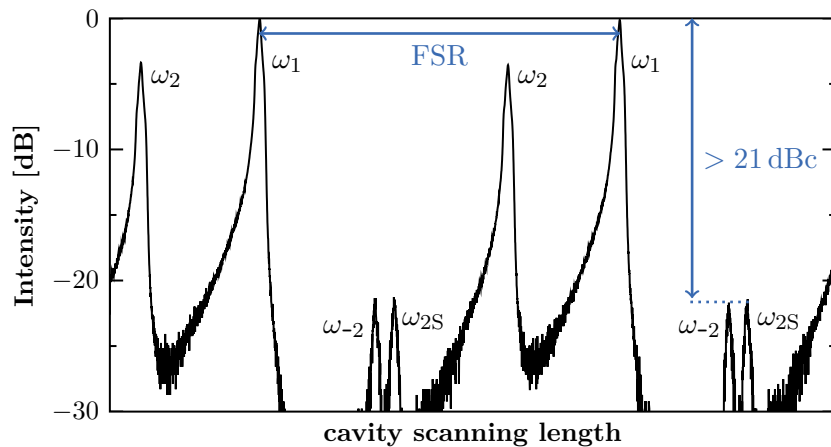


Figure 4.24: Optical spectrum obtained with the Fabry-Pérot interferometer shown in figure 4.23 including the Raman frequencies ω_1 and ω_2 . The other, unwanted visible peaks ω_{-2} , created by SFG between the carrier and the before filtered sideband frequencies, and ω_{2S} , created by SHG of the unfiltered sideband, are suppressed by more than 21 dB. The distance between two identical peaks is known as the free spectral range (FSR) of the scanning interferometer. The asymmetric shape of the peaks is technically due to the scanning piezo crystal on the cavity mirror. The width of the peaks is also limited by the finesse of the cavity, which is not important in this case.

The third and final stage shaded in yellow in figure 4.21 serves the purpose of frequency and amplitude modulation as well as distribution of the light fields into eight different optical fibers [PMC-800-5.1-NA012-3-APC-660-P, Schäfter + Kirchhoff]. This is realized by splitting and overlapping the two incoming beams with a PBS and $\lambda/2$ combination. To direct the individual beams, dielectric mirrors inside long-term stable, kinematic mirror mounts [POLARIS-K05, Thorlabs] are employed. The five AOMs [MT80-A1.5-VIS, AA Opto Electronic] are used to generate the frequencies required for Bragg transitions and to control the amplitude of the light fields. The AOMs are supplied by RF frequencies from DDS card modules inside the TBus system amplified by 1 W power amplifiers [AMPA-B-30, AA Opto Electronic]. By controlling the amplitude of these RF fields the pulse shape of the individual diffraction pulses can be adjusted. In addition, custom built mechanical shutters based on stepper motors [AM 1020-V-3-16-01, Faulhaber] and controlled by a dedicated card inside the TBus system block light beams as needed during certain parts of the experimental sequence. The light fields coupled into the eight optical fibers serve different purposes that are explained in the following.

- **MOT:** Four fibers are reserved for the different optical steps for the generation of Bose-Einstein condensates that include laser cooling, trapping and optical pumping. Since these steps are crucial for the operation of the Magneto-Optical Trap (MOT) they are labelled with this abbreviation. Two of the fiber-coupled light fields are previously superimposed with the required frequencies for repumping. The four light fields are guided via the polarisation maintaining fibers to the respective viewports of the experimental vacuum chamber and allow the operation of a mirror-MOT configuration [Rei99].
- **First/Second Detection:** Two fibers enable the detection of the final atom population $P(\phi)$ through absorption imaging at the end of every sequence. Herefore two light fields are guided to two different viewports at the experimental chamber. The image itself is acquired with a collimated resonant light field that is pulsed in the direction of the atomic ensemble onto a CMOS camera sensor [Grasshopper GS3-U3-89S6M-C, FLIR]. To obtain not only 2D but 3D information about the atomic distribution a second absorption picture can be taken in a subsequent, identical experimental sequence from a different angle of observation. Therefore the second light field is connected to a different view port opposite to a CCD camera sensor [Grasshopper GS3-U3-15S5M-C, FLIR].
- **Diffraction capabilities:** Two polarization-maintaining optical fibers guide individual light fields into the experimental chamber, allowing single or double diffraction techniques to be performed. The incoupled light fields differ in the fact that one contains the frequency and amplitude modulated output signal from one AOM and the other contains two superimposed output signals from two individual AOMs. Therefore, the first coupled light field is meant to enable single and double Raman or single Bragg diffraction. The second additionally enables double Bragg diffraction in the twin-lattice configuration with two perpendicularly polarized light fields. Since both light fields are guided in a single fiber, a retro-reflective setup is assumed for implementation.

4.3.1 Non-inertial phase noise contributions

The light field most affected by phase noise is the one used for Raman diffraction and generated as described in the previous section. In the further course it is referred to as the Raman light field. To find a measure of this influence on the interferometer phase, the sensitivity function formalism from section 2.3 can be applied. To quantify these non-inertial phase noise contributions the standard deviation of the phase noise density [Che08] of the light field and the used electronic components are measured with a commercial phase noise analyzer [FSWP8, Rohde & Schwarz]. In total the phase noise densities of the local oscillator, the stable reference frequency of 100 MHz, the reference chain at 6.9 GHz, the used Direct Digital Synthesizer (DDS) at 65 MHz and the Raman light field at 6.835 GHz are investigated. Afterwards, they are weighted as derived in equation 2.20 with the help of the transfer function defined in equation 2.19 to calculate σ_ϕ^{rms} . The free evolution time of the interferometer chosen for this purpose is $T = 15$ ms and the pulse duration $\tau_p = 25$ μ s in agreement with the order of magnitude of the values given in chapter 3.

The measurement setup for the beat frequency of the light field at 6.835 GHz consists of a fiber-coupled photodiode [FGA01FC, Thorlabs], supplied with a bias voltage [ZX85-12G-S+, Mini-circuits] and amplified with two amplifiers [ZVE-8G+, Mini-circuits and ZJL-7G+, Mini-circuits]. The output beat signal is then used to measure the phase noise density with the commercial phase noise analyzer. The spectra of the weighted and unweighted phase noise density can be seen in figure 4.25.

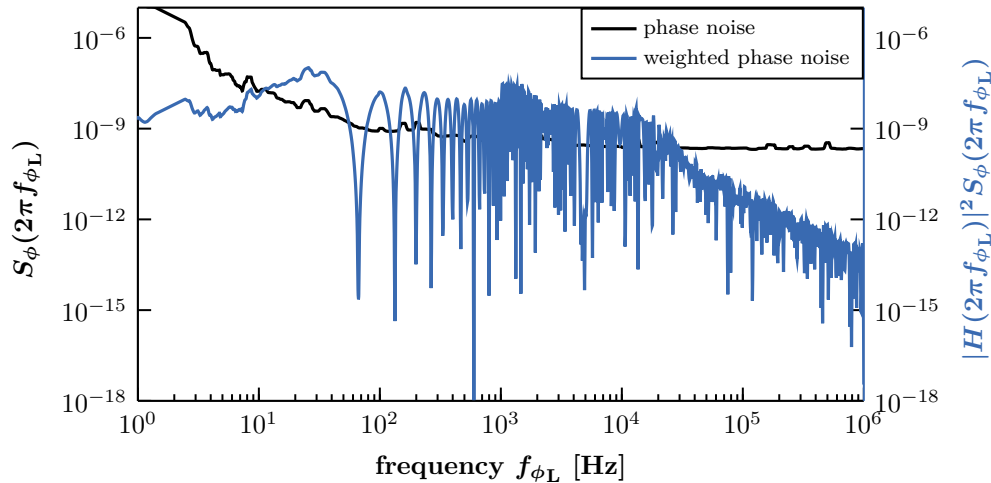


Figure 4.25: Phase noise density of the beat frequency of the Raman light field, detected with a photodiode [FGA01FC, Thorlabs] and measured with a commercial phase noise analyzer [FSWP8, Rohde & Schwarz]. The measured phase noise density, shown in black, is weighted with the sensitivity transfer function for a Mach-Zehnder type interferometer. The resulting weighted phase noise density is shown in blue. The chosen free evolution time of the interferometer is $T = 15$ ms and the pulse duration time $\tau_p = 25$ μ s. The integrated weighted phase noise density over the measurement range shown is calculated as $\sigma_\phi^{\text{rms}} = 6.21$ mrad.

The measured weighted (σ_ϕ^{rms}) and unweighted ($\int S_\phi df_{\phi_L}$) integrated phase noise densities of the crucial electronic components used to generate the Raman light field, as detailed in figure 4.23, and the values for its beat are summarized in table 4.2. More details on the individual measurements can be found in the reference [Ris18].

Table 4.2: Table of the integrated phase noise densities of the electronic components that are part of the optical frequency generation (see figure 4.24) and the values measured for the Raman light field.

	stable reference (100 MHz)	reference chain (6.9 GHz)	DDS (65 MHz)	light field (6.835 GHz)
unweighted $\int S_\phi df_{\phi_L}$	0.04 mrad	1.81 mrad	2.58 mrad	16.49 mrad
weighted σ_ϕ^{rms}	0.02 mrad	0.66 mrad	1.47 mrad	6.21 mrad

4.3.2 Implementation of double Raman diffraction

Comparing the two different mechanisms of Bragg and Raman diffraction, as introduced in subsections 2.2.1 and 2.2.3, the latter can offer advantages, such as state-selective manipulation and detection without spatial resolution. A case to be highlighted here is interferometry with the symmetric case of double Raman diffraction [Mal10; Lévo9; Zho15], where the interfering atoms remain in the same internal electronic state during the sequence, allowing electronic readout, noise suppression, and elimination of spurious paths by Raman blow-away pulses [Har20]. To support such an interesting approach, the performance of (higher order) double Raman diffraction processes is demonstrated below as an application example of the system.

As explained in subsection 2.2.3 the herefore necessary transition frequencies are affected by the one-photon AC-Stark shift. To experimentally cancel this differential shift for the used atomic species ^{87}Rb the following steps are taken. Considering

$$\omega_{\text{AC}} \equiv \omega_{\text{AC},|e\rangle} - \omega_{\text{AC},|g\rangle} = 0, \quad (4.15)$$

it is needed to tune $\omega_{\text{AC},|e\rangle} = \omega_{\text{AC},|g\rangle}$. Since these terms both include the single light field Rabi frequencies Ω_1 and Ω_2 it is possible to calculate an optimal ratio. Solving the AC-Stark couplings for the relation Ω_2/Ω_1 and making use of the proportionality $\Omega_i \propto \sqrt{I_i}$, where I_i defines the individual light field intensities, the following intensity ratio is obtained using the Clebsch-Gordon coefficients [Ste01]

$$\frac{I_2}{I_1} = \frac{\Omega_2}{\Omega_1} = \frac{\left(\frac{1}{60(\Delta + \omega_{\text{eg}})} + \frac{1}{4(\Delta - D_{12} + \omega_{\text{eg}})} + \frac{2}{5(\Delta - D_{13} + \omega_{\text{eg}})} \right) - \left(\frac{5}{12\Delta} + \frac{1}{4(\Delta - D_{12})} \right)}{\left(\frac{5}{12(\Delta - \omega_{\text{eg}})} + \frac{1}{4(\Delta - D_{12} - \omega_{\text{eg}})} \right) - \left(\frac{1}{60\Delta} + \frac{1}{4(\Delta - D_{12})} + \frac{2}{5(\Delta - D_{13})} \right)}. \quad (4.16)$$

For better readability, the following temporary definition is used in this formula $\Delta \doteq \Delta_{\text{Raman}}$. The values D_{12} and D_{13} define the fixed transition frequencies from the $|5^2\text{P}_{3/2}, F=1\rangle$ to the $|5^2\text{P}_{3/2}, F=2\rangle$ state and respectively to $|5^2\text{P}_{3/2}, F=3\rangle$. Additionally, $\omega_{\text{eg}} \approx \omega_{\text{HFS}}$ specifies

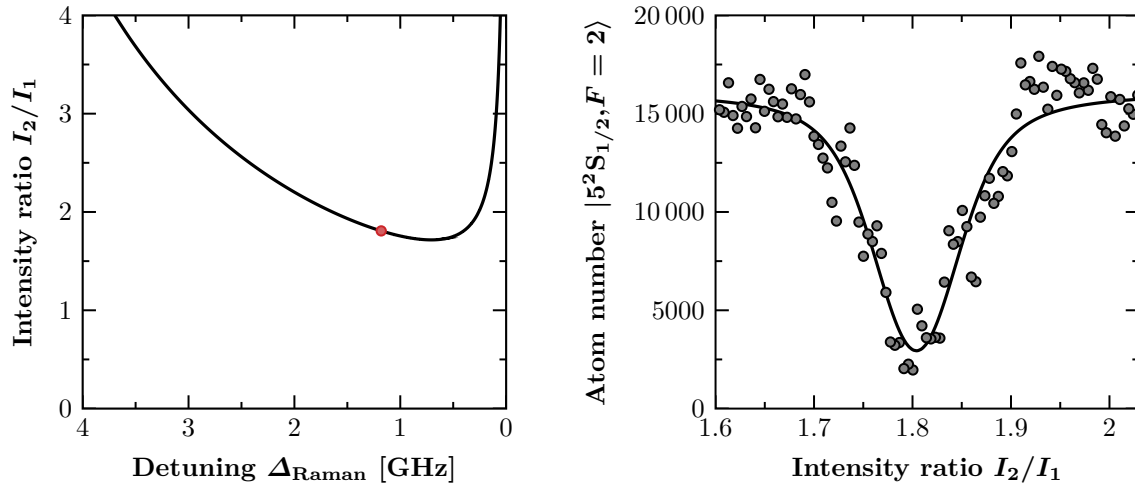


Figure 4.26: Compensation of the differential AC-Stark shift ω_{AC} in a Raman light field. **Left:** Sideband intensity ratio I_2/I_1 as a function of the detuning Δ_{Raman} required to satisfy the equation $\omega_{AC,|e\rangle} = \omega_{AC,|g\rangle}$ for the respective energy levels of ^{87}Rb . The red point marks a detuning of $\Delta_{\text{Raman}} = 1.18$ GHz, which translates into a theoretical sideband ratio of $I_2/I_1 = 1.80749$. **Right:** A microwave pulse with the transition frequency of $\omega_{\text{HFS}} = 6.834682$ GHz depopulates the initial state $|5^2S_{1/2}, F=2\rangle$. Additionally applying a non-resonant Raman light field with an intensity ratio I_2/I_1 creates an AC-Stark shift that reduces the amount of transferred atoms, resulting in more remaining atoms in the initial state. The maximum depopulation is realized at an intensity ratio of $I_2/I_1 = 1.804 \pm 0.065$, fitted by a Gaussian envelope.

the hyperfine splitting between $|5^2S_{1/2}, F=1\rangle$ and $|5^2S_{1/2}, F=2\rangle$, neglecting Zeeman shift contributions. This relation can be represented as a function of Δ_{Raman} in figure 4.26 in the graph on the left. To reduce spontaneous emission and have relatively equal light intensities a convenient working spot can be found for example at $\Delta_{\text{Raman}} = 1.18$ GHz, marked by a red point, which translates into a theoretical sideband ratio of $I_2/I_1 = 1.80749$. Experimentally the intensity ratio can be controlled by the modulation amplitude applied to the EOM. The resulting spectrum can be observed with the Fabry-Pérot interferometer as explained in section 4.3 and is shown in figure 4.24. The experimentally matching intensity ratio that achieves $\omega_{AC,|e\rangle} = \omega_{AC,|g\rangle}$ for a fixed detuning Δ_{Raman} can be found in the following way. A microwave pulse with the correct pulse length and a transition frequency of $\omega_{\text{HFS}} = 6.834682$ GHz can properly depopulate the initial state $|5^2S_{1/2}, F=2\rangle$ to $|5^2S_{1/2}, F=1\rangle$. Additionally applying a non-resonant Raman light field with an arbitrary intensity ratio I_2/I_1 creates an AC-Stark shift that reduces the amount of transferred atoms, resulting in more remaining atoms in the initial state. The light field itself is detuned by 1 MHz away from the desired transition frequency to avoid stimulated two-photon Raman processes. Changing the intensity ratio as shown in figure 4.26 on the right indicates a minimum at $I_2/I_1 = 1.804 \pm 0.065$, fitted by a Gaussian envelope analogous to equation 3.3.

To reduce the effects of unwanted residual magnetic fields, as explained in subsection 2.1.2, the following shown measurements are exclusively operated with $m_F = 0$ states and Doppler-insensitive transitions with $\Delta m_F = 0$. Therefore the linear Zeeman shift vanishes, but the second-order Zeeman shift induces an additional contribution $\Delta\omega_{\text{clock}}$ to the transition frequency ω_{HFS} between the $m_F = 0$ sublevels of the two hyperfine ground states, often referred to as 'clock transition'. This becomes apparent by a measured difference frequency between the theoretical value ω_{HFS} of the microwave pulse and the experimentally adjusted one. Using the Breit-Rabi formula

$$\Delta\omega_{\text{clock}} = \frac{(g_J - g_I)^2 \mu_B^2}{2\hbar\Delta E_{\text{HFS}}} B^2, \quad (4.17)$$

with the fine structure Landé factor g_J , the nuclear g -factor g_I , the Bohr magneton μ_B and the hyperfine splitting $\Delta E_{\text{HFS}} = A_{5^2S_{1/2}}(I + 1/2)$, this difference can be linked to a clock transition Zeeman shift of $\Delta\omega_{\text{clock}}/B^2 = 2\pi \cdot 575.146 \text{ Hz/G}^2$. The measured difference frequency of $7 \pm 1 \text{ kHz}$ translates therefore to a magnetic field value of $B \approx 3.5 \pm 0.1 \text{ G}$. This value contains the contribution of the homogenous quantization field value generated at the experiment by a pair of coils in Helmholtz configuration and residual field contributions like the Earth's magnetic field.

As a demonstration, first-order double Raman beamsplitters are realized in the following. The experimental setup is analogous to that of the twin lattice from section 3.2 and features retro-reflection at the $\lambda/4$ and mirror combination. The transfer itself is generated by two pairs of counter-propagating frequencies ω_1 and ω_2 . The pairs can be distinguished by their polarization combination, so that in the retro-reflective arrangement, the two frequencies are first applied in parallel polarization and then rotated by the $\lambda/4$ plate to suppress spurious coupling. For more information, see section 2.2.4 and the energy level scheme in figure 2.4 on the right. Before detection of the output port population, a Stern-Gerlach type deflection pulse is applied to prevent atoms with nonzero magnetic moment from overlapping with the zero momentum output port. The deflection is realized by applying an inhomogeneous magnetic field gradient perpendicular to the direction of diffraction that spatially separates the different $m_F \neq 0$ sub-states. Figure 4.27 on the left represents a final density distribution obtained from the absorption image after applying a first order ($n = 1$) double Raman $\pi/2$ pulse. The different m_F states are highlighted by white circles and the symmetric splitting into the $|F = 1, p = \pm 2\hbar k\rangle$ is indicated by arrows. Since the absorption detection is resonant only for atoms in the $|F = 2\rangle$ state, additional repumping cycles totaling $200 \mu\text{s}$ are required to transfer them from $|F = 1\rangle$ to $|F = 2\rangle$ before the detection light field is applied (see level scheme in figure 4.20). Due to this, the detected spatial distribution is broadened for the $|F = 2, p = \pm 2\hbar k\rangle$ states compared to the $|F = 2, p = 0\hbar k\rangle$.



Figure 4.27: Examples of atomic density distributions after double Raman diffraction. **Left:** Final distribution in the form of an absorption image taken after applying a first order ($n = 1$) double Raman $\pi/2$ pulse and a subsequent Stern-Gerlach type deflection pulse. Different m_F states are highlighted by white circles and the symmetric splitting into the $|F = 1, p = \pm 2\hbar k\rangle$ states is indicated by arrows. The distribution is broadened for the $|F = 1, p = \pm 2\hbar k\rangle$ states due to the absorption detection only working on the $|F = 2\rangle$ state, which needed additional repumping cycles before the application of detection light. **Right:** Density distribution after a first order sequential transfer $m = 1$ of two consecutive pulses into the $|F = 2, p = \pm 4\hbar k\rangle$ states, including the Stern-Gerlach splitting for residual m_F -states.

For a closer analysis the effective Rabi frequency Ω_{effDD} is determined by measuring the oscillation between $|F = 1, p = \pm 2\hbar k\rangle$ and $|F = 2, p = \pm 4\hbar k\rangle$. To first occupy the $|F = 1, p = \pm 2\hbar k\rangle$ states, an initial $\pi/2$ pulse is applied, symmetrically transferring atoms there from the $|F = 2, p = 0\hbar k\rangle$ state. Afterwards a second pulse of time τ_p is applied, sequentially transferring the population to $P_{\pm 4\hbar k}$. The corresponding energy level scheme can be seen in figure 2.5 on the right. Since the atoms in the $|F = 1\rangle$ state can only be detected with the additional repumping cycles, a measurement can also be performed by observing the population in $P_{\pm 4\hbar k}$ alone. To compensate for changes in the initial amount of atoms the residual, non-diffracted atoms N_0 in the $|F = 2, p = 0\rangle$ state are included in the following definition

$$P_{\pm 4\hbar k}(\tau_p) = \frac{N_{\pm 4\hbar k}(\tau_p)}{N_{\pm 4\hbar k}(\tau_p) + N_0} \equiv \frac{\sin(\Omega_{\text{effDD}}\tau_p)^2}{\sin(\Omega_{\text{effDD}}\tau_p)^2 + n_0}, \quad (4.18)$$

where n_0 defines the reduced oscillation amplitude linked to the atom number N_0 . The atom number N_0 includes the spurious amount of atoms in the $m_F \neq 0$ states. These remaining atoms can potentially be spatially separated by a Stern-Gerlach splitting, which was not done for the presented measurement, which limited the maximum transfer to $\max(P_{\pm 4\hbar k}(\tau_p)) \approx 0.8$. Therefore, the maximum amplitude of this oscillation is not a good indicator for the fidelity of the diffraction processes.

The separation of the momentum states is exemplary shown in figure 4.27 on the right in the form of an absorption image of the respective atomic density distributions taken at the time of maximum population transfer into $|F = 2, p = \pm 4\hbar k\rangle$. For reference, it should be mentioned here that the total time of a pulse in the sequence is $8 \cdot \tau_p$, due to the definition of the temporal Gaussian pulse width as $\sigma_{\tau_p} = \tau_p/8$ at the experimental control.

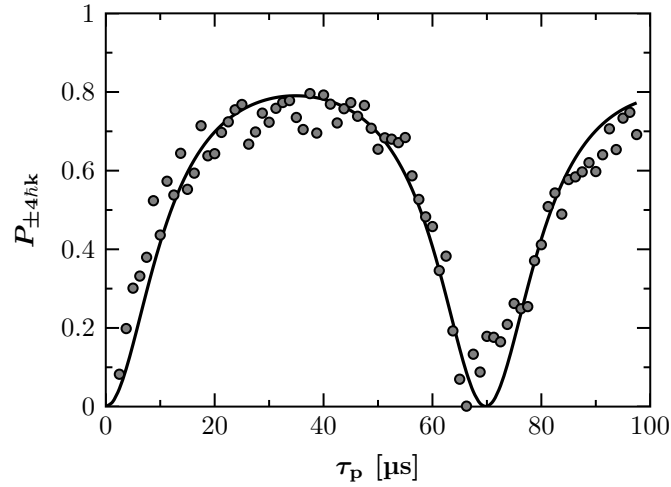


Figure 4.28: Measured population oscillations of $P_{\pm 4\hbar k}(\tau_p)$ in dependence of the pulse time τ_p of the second pulse for first order sequential $m = 1$ double Raman diffraction. The fit follows the definition from equation 4.18. From it the time τ_π is determined and the effective Rabi frequency is calculated according to equation 4.19 to $\Omega_{\text{effDD}} = 2\pi \cdot 7.165 \pm 0.033$ kHz.

The resulting oscillation of $P_{\pm 4\hbar k}(\tau_p)$ can be seen in figure 4.28. From the applied fit function, the first minimum can be determined to be at a time $\tau_\pi \approx 70 \mu\text{s}$. Subsequently, the effective Rabi frequency can be calculated as follows

$$\Omega_{\text{effDD}} = \frac{\pi}{\tau_\pi} = \frac{\pi}{69.78 \pm 0.32 \mu\text{s}} = 2\pi \cdot (7.165 \pm 0.033 \text{ kHz}). \quad (4.19)$$

Finally to demonstrate third order Raman double diffraction, atoms are transferred from $|F = 2, p = 0\hbar k\rangle$ into the states $|F = 1, p = \pm 6\hbar k\rangle$ as shown in the energy level scheme in figure 2.5 on the left. To visualize the atomic density distributions additional repumping cycles totaling $200 \mu\text{s}$ are applied to transfer atoms from $|F = 1\rangle$ to $|F = 2\rangle$ before the detection light field is applied. The corresponding final distributions are displayed in figure 4.29 through absorption imaging. Since the time τ_p is not optimised for a specific transfer, a considerable number of atoms remain in the state $|F = 2, p = 0\hbar k\rangle$. Moreover, visible losses exist, possibly into the $|F = 1, p = \pm 2\hbar k\rangle$ states.

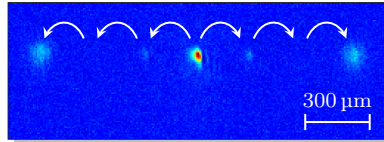


Figure 4.29: Density distribution in the form of an absorption image after applying a third order ($n = 3$) double Raman diffraction pulse. The symmetric splitting is symbolized by arrows indicating the in principle non-populated states $|F = 1, p = \pm 2\hbar k\rangle$ and $|F = 1, p = \pm 4\hbar k\rangle$, with visible losses. The distributions appear broadened for the targeted $|F = 1, p = \pm 6\hbar k\rangle$ states due to the additionally needed repumping cycles before the application of the detection light.

4.3.3 Performance summary

Overall, important points about the performance of the laser system and its exemplary application for Raman double diffraction can be summarized as follows. The Raman light field exhibits comparable phase noise to that shown in [Ram20], which uses a similar setup with a single-sideband via an IQ modulator. This is limited mainly in the RF design and in the choice of microwave components that drive the modulation. In particular, a gain could be obtained by choosing a DDS with lower phase noise. Significant phase shifts also result from differential light shifts due to a changing ratio between sideband and carrier power. These were not measured, but were estimated to be as high as a few percent. Therefore, a stability analysis of the compensation point I_2/I_1 and a possible stabilization based on this analysis is suggested.

Altogether, the system is able to provide all laser frequencies needed for the generation of ultracold atoms and to perform Bragg and Raman diffraction with them. Examples of different cases of double Raman diffraction, including higher order diffraction, show a flexible spectrum of possible applications. The performance shown with BECs indicates that high beam splitting efficiencies can be achieved with an applied Stern-Gerlach deflection, which is a good basis for high-contrast atom interferometry. Overall, it shows that such a system is very well suited for coherently manipulating the atomic species rubidium, as it provides the tunable, phase-stable and efficient light sources necessary for this purpose.

CHAPTER 5

Summary

The work presented in this thesis aims to improve interferometry with ultracold atomic ensembles and its use for inertial sensing by exploiting novel atom-optical manipulation techniques and schemes. Achievable inertial sensitivities are proportional to the spatial separation of the employed wave packets and can be enlarged by increasing either the interaction time or the amount of transferred momentum. To this end, a (re-)launch mechanism effectively helped to increase the available interferometry time and allowed the realization of a compact fountain gravimeter. To achieve a symmetric large momentum transfer, an optical twin-lattice potential enables large space-time areas suitable for rotation measurements with high sensitivities across short baselines. A common feature of both methods are the light fields that are applied from only a single direction, either along gravity or perpendicular to it.

Efforts to implement the previously presented methods in new atom interferometer concepts led to the creation of a so-called dual BEC and a multi-loop scheme. For this purpose, at least two perpendicularly aligned light fields were combined in each case. The first implementation introduced a differential interferometer scheme formed from a single Bose-Einstein condensate. The use of an initial double diffraction pulse from one direction, followed by three successive pulses, allowed the discrimination between rotational and acceleration components using the combined output phases of two interferometers. In this way, the complexity of two BEC sources is avoided and the measurement can be extended to six-axis due to its symmetry. The combination of the above mentioned method of the (re-)launching mechanism with symmetric splitting allowed a second implementation in the form of the concept of an atomic Sagnac interferometer with multiple loops. By using loops, the enclosed space-time area can be effectively increased without requiring a larger setup, analogous to light interferometers that use multiple fiber loops. Neglecting contrast and atomic losses, which can scale with the number of loops due to imperfections in the atom-light interactions, the result is a linear increase in the quantum projection noise limited sensitivity per cycle.

In view of such potential limitations caused by the quality of the employed light fields, possible mitigation strategies were investigated. A motivating factor was the loss of contrast observed for the twin-lattice interferometer. Spatial distortions were shown to limit the current beam splitter efficiency and thus the scaling of the method. In search of optical potentials propagating with uniform intensity and phase distribution without being susceptible to distortion, a flat-top shaped beam was investigated. Due to the shape of the intensity distribution, it is less prone to

clipping at apertures, and its uniform power distribution can be useful for addressing the atomic ensemble equally at different positions in the beam. The shaping optics studied have shown that collimated beam profiles useful for atom interferometry can be produced at propagation distances up to 1 m. However the profile still featured intensity distortions stemming from the aspherical shaping components themselves. The measured phase front deviations are on the order of $\lambda/20$ for root-mean-square values and of $\lambda/3$ for peak-to-valley. This is on the same order of magnitude as specified for the high quality optical components typically employed in atom interferometer experiments. The study also found that the relative positions of each beam shaping component to each other have a critical influence on the wavefront profile. Only rigid fixed connections between them can eliminate temporal and spatial instabilities. Even with such a monolithic approach, it cannot be ruled out that spatially fixed imperfections still remain in the light field. Those can, among other things, lead to position-dependent dipole forces that have a parasitic effect on the output of an interferometer. To compensate for these light-shift based effects, the generation of two light fields detuned by hundreds of GHz in opposite directions with respect to the atomic resonance frequency and several watts of power was presented. By superimposing three individually frequency and amplitude controllable light fields in a single beam, the necessary optical lattice depths for large momentum transfer techniques with active light shift compensation can be generated.

Inspired by the concept of providing a relatively compact and robust all-in-one solution for the generation of ultracold atoms, combination of different beam-splitting techniques, and detection of the output phase of the interferometer, a fiber-based laser system was built. It offers the reliability and robustness of frequency-doubled telecommunication components and the ability to combine internal and external state manipulations with only a single laser source. As a demonstration, the novel technique of a modulation-based and optically filtered light field for sequential and third-order double Raman diffraction was shown.

All of the techniques and schemes presented in this work share the ability to achieve competitive measurement sensitivity for atom interferometers operating in comparatively compact devices. The fountain gravimeter, for example, realized tens of milliseconds of free fall on a distance of less than 1 cm. With a differential momentum of 408 photon recoils, the twin-lattice interferometer enclosed an area of more than 7 mm^2 on a baseline of less than 3 mm in fewer than 13 ms. To draw a comparison between the different interferometer types presented in this thesis, a square area of 1 cm^2 is chosen as the basis for their geometries, neglecting the comparably small spatial extent of the atomic ensembles. The constraint is such that all manipulations and detection of the output phase signal must be based in this area. With this, the individual shot-noise-limited achievable sensitivities to accelerations and rotations are calculated. The results and the underlying parameters are summarized in table 5.1. Since some of the concepts use a combination of atom-light interactions generated by light fields propagating in perpendicular directions, those that imprint laser phase contributions for the interferometer phase are highlighted in red. Although the chosen area may seem small, it turns out that the achievable sensitivity limits are in the order of $10^{-8} (\text{m/s}^2)/\sqrt{\text{Hz}}$ for accelerations

Table 5.1: Sensitivity limit estimations for accelerations ($\sigma_a\sqrt{t}$) and rotations ($\sigma_r\sqrt{t}$) for the four different geometries presented in this thesis. The calculations are based on the operation with ^{87}Rb atoms, a number of N detected atoms, an interferometer pulse separation time T , a contrast C , $2n$ loops, and two effective wave numbers $k_{\text{eff},\uparrow}$ and $k_{\text{eff},\leftrightarrow}$ for their respective directions of momentum transfer. The two values for the fountain represent the transfer during relaunch and MZI sequence. The atom-light interactions that contribute to the measured total phase shift ϕ are highlighted in red. The parameters are chosen with the overall constraint of performing all manipulations and detecting the output phase signal within the area of 1 cm^2 . For simplicity finite pulse durations are neglected and a cycle time of 1 s is assumed, which is in the same order of magnitude as the atomic flux achievable with current atom chip based BEC sources [Rud15].

	N	T [ms]	C	n	$\hbar k_{\text{eff},\uparrow}$ [$\hbar k$]	$\hbar k_{\text{eff},\leftrightarrow}$ [$\hbar k$]	$\sigma_a\sqrt{t}$ [(m/s ²)/ $\sqrt{\text{Hz}}$]	$\sigma_r\sqrt{t}$ [(rad/s)/ $\sqrt{\text{Hz}}$]
Fountain	10^5	35.0	0.7	-	60 & 8	-	$5.7 \cdot 10^{-8}$	-
Twin lattice	10^5	24.2	0.5	-	-	808	-	$8.0 \cdot 10^{-9}$
Dual BEC	10^5	25.0	0.5	-	16	32	$7.9 \cdot 10^{-8}$	$4.2 \cdot 10^{-7}$
Multi-loop	10^5	24.0	0.5	6	60	64	-	$7.5 \cdot 10^{-9}$

and 10^{-7} to 10^{-9} (rad/s)/ $\sqrt{\text{Hz}}$ for rotations. Depending on the application, such sensitivities can already be considered sufficient, which is put into perspective using the example of quantum inertial navigation in the outlook section 6.2.

One promising candidate for such an application is the dual BEC geometry with the possibility of extending its measurement along all three axes. The other techniques presented in this thesis still offer individual advantages for compact deployment. These include, for example, the relaunch capability implemented in the multi-loop and fountain geometry, which allows the same baseline to be used over and over again, or the optimal use of available space through scalable large momentum transfer in a twin lattice. In particular, the application range of the twin-lattice and multi-loop geometry is not limited to compact devices. Rather, they offer an excellent perspective for achieving unprecedented sensitivities on longer baselines. Especially in combination with delta-kick collimated BECs, the potential in the field of metrology increases significantly.

CHAPTER 6

Outlook

The position of an object in space at a given time can be considered as a spatial and temporal information. Often great efforts are made to obtain them as accurately as possible. Nowadays, the need for navigation is increasing, the dependency on location services is growing and their applications are constantly expanding. Although the use of Global Navigation Satellite Systems (GNSS), often represented by the Global Positioning System (GPS), is widespread, problems with accuracy, availability and also security have begun to come to the fore in current practical applications. Indoors, underground, or even in cities, GPS cannot provide continuous and accurate services due to signal loss or overlap. Therefore, the biggest challenge for next-generation navigation technology is high availability and credibility.

To tackle this challenge and to be able to navigate without a GNSS link, the construction of an inertial measurement unit (IMU) based on (ultra)cold atoms is a promising option. Such a unit should measure the acceleration and angular velocity along all three axes of motion, representing the fundamental part of inertial navigation. To date, few attempts have been made to fully explore the potential of atom interferometers for field applications or to make them useful as a technology for navigation. There have been recent efforts to bring quantum sensors based on atom interferometry out of the laboratory to real-world applications [Bon19; Abe23], as well as advances toward field-ready atom interferometers [Nar22]. However, the actual design and, in particular, the implications of its use in dynamic environments is a relatively new area [Boc17; Bla20].

In the following, this outlook addresses the questions why hybridization of an inertial measurement can be a useful tool and how an implementation of a gyro-stabilized quantum navigation sensor based on the dual BEC interferometer can look like.

6.1 Hybrid inertial navigation

Most atom interferometers sense along one direction, for example only a single axes of rotation and/or acceleration is measured at a time. However, for full inertial navigation, it is necessary to reconstruct the three-dimensional trajectory of a moving body. Therefore, only the simultaneous measurement of accelerations and rotations in three mutually orthogonal directions forms the basis of a complete inertial measurement unit. Recent concepts have been tackling this problem [Bar19; Ger20], but are typically operated in a pulsed manner. Therefore, they have a smaller bandwidth than mechanical devices used for navigation and suffer from low

repetition rates. This also results in dead times during which inertial measurements cannot be performed. There are efforts to circumvent this problem based on a common interrogation scheme [Sav18; Dut16] or recapturing the atoms after the interferometer sequence [Rak14], but they are accompanied by increased instrument and sequence complexity.

The performance of atom interferometers is often limited by the characteristics of the employed laser light field. A directly observable effect is the efficiency and stability of the individual beam splitters, which require a strict phase relationship between the counter-propagating light fields. Changes in this relationship directly influence the measured phase difference. Therefore, it is a requirement to generate the light fields with the necessary stability and quality within robust setups. An example of a fiber-based laser system, which is supposed to provide the necessary capabilities for navigation purposes, is shown in the following section in figure 6.3.

An additional related challenge in dynamic or seismically noisy environment, typically encountered in navigation scenarios, is that the influence of inertial effects acting on the matter waves and the phase reference of the interferometer are indistinguishable. Vibrations coupling into a retro-reflection mirror shift the wave-front phase relative to the incoming beam and add an additional phase contribution. As a consequence, seismic noise contributes significantly to the instability of quantum inertial sensors and often inhibits the interferometer readout due to phase ambiguities. In addition to the contributions of quantum projection noise and technical noise, this contribution of inertial noise is a dominant factor in phase uncertainties. To counteract or reduce this influence, there are two common techniques: first, vibration attenuation systems that reduce the amount of spurious movement of the inertial reference, and second, post-correction methods that detect the motion with an external sensor and apply a transfer function (see section 2.3) to calculate the inertially induced phase shift. The additional use of a classical external sensor can bring further advantages in the form of hybridization, as shown by the flow diagram in figure 6.1 and explained below.

The classical sensors often exhibit broader bandwidths, but suffer from long-term bias and scale factor drifts. This is where they can benefit from quantum sensors. The combination of their signals enables the correction of systematic errors (for example with the help of the Kalman filter formalism [Che18]), offsets and drifts of the classical sensor by providing a hybrid signal with no such bias. This hybridization therefore provides continuous measurements without dead times and a high dynamic range. In fact, commercially available classical sensors such as the Titan Accelerometer or the Trillium Seismometer from Nanometrics Inc. have already been employed in combination with atom interferometers [Gei11; Le 08; Lau14; Bar16; Ten21; Tem22]. Recently a new class of optomechanical sensors with small form factors has shown potential to perform well in portable and compact quantum inertial sensor units [Guz14; Hin20; Ric20].

When developing a navigation-compatible quantum sensor, it must be taken into account that the ensemble of atoms used will be accelerated in different directions for short periods of time.

For the application of beam splitters, the relative velocity between the freely falling atoms and the moving reference frame must be known to some degree to control the phase measurement. A common method is to apply a phase-continuous chirp to maintain the transition resonance condition as the atoms accelerate relative to their inertial reference. However, if the system experiences multiple translational accelerations, this chirp must be changed from cycle to cycle. By applying a high-pass filter to the acceleration signal measured by a classical sensor, the AC acceleration can be used to adjust the laser frequencies accordingly. This can be implemented by a real-time solution [Tem22], as shown in figure 6.1 on the left. Doing so is particularly important if there is otherwise a risk of signal loss or degradation, for example due to phase ambiguity or reduced contrast. An ultimate limitation is that it is impossible to extract the phase information when the atomic trajectories leave the laser beam due to the experienced acceleration before the interferometer is closed.

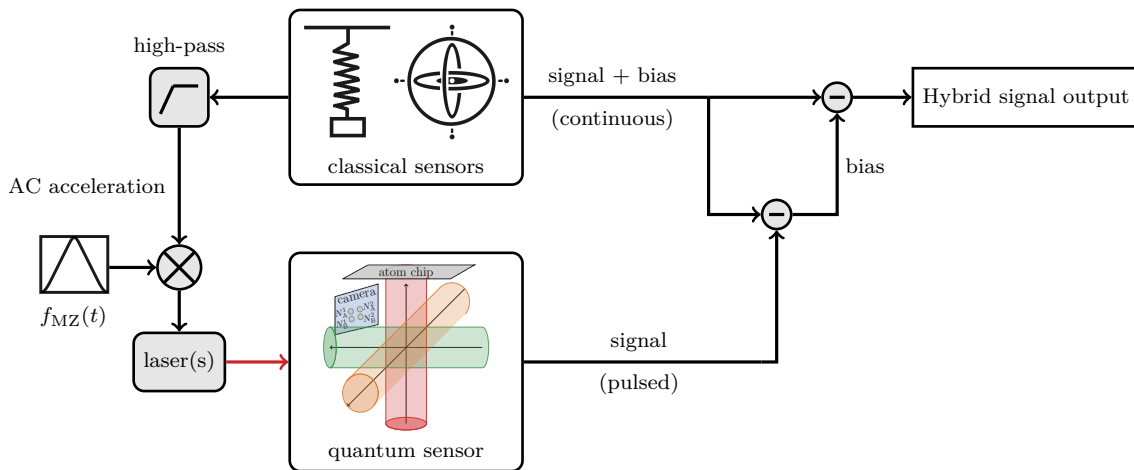


Figure 6.1: Flow diagram of the operating principle of a hybrid inertial navigation system. Classical sensors typically allow for continuous measurements, but suffer from long-term bias. These can be isolated and discarded/corrected by correlation with a quantum sensor to produce a hybrid signal. Furthermore, a real-time system can help to detect AC accelerations by high-passing. Through calculation of the response using the transfer function $f_{MZ}(t)$, laser frequency and phase can be adjusted accordingly.

Another effect to consider results from rotations that change the direction of the beam-splitting light pulses and impart offset velocities to the atoms. This can result in the wave packets not overlapping at the last pulse and the interferometer not being able to close completely, resulting in a loss of interferometric contrast. A common solution is to use a tilting mirror as an inertial reference. It has been shown that this can eliminate, for example, the influence of the Coriolis force caused by the Earth's rotation [Lan12]. Alternatively, an inertial platform, often called a gyroscopic platform, can be used to hold the sensor in a fixed orientation in space despite rotational changes. Such an approach can also be understood as a form of hybridization, since a classical gyroscope can provide the input for the orientation of the inertial platform, while the quantum sensor measures and corrects the remaining rotational components.

6.2 Experimental platform of a gyro-stabilized quantum navigation sensor

In the practical development of a navigation-compatible (hybrid) quantum inertial measurement unit, many challenges must be considered that are not present in static laboratory setups. This starts with compactness, which is critical for such an application, and continues with reduced complexity and power consumption. Yet all the influences of the dynamic environment, described in the section before, should also be taken into account. A sensor design and setup that tackles these challenges is discussed in the following.

The basis for this development is the multi-axis scheme of the dual BEC interferometer presented in subsection 3.3.1. An idea of what the future sensor head for its implementation might look like is shown in figure 6.2. As explained in chapter 5, considerable sensitivities can already be achieved in areas the size of square centimeters. Nowadays, the available technology still mostly determines the size of the device. Nevertheless, the sensor head presented here constitutes already a significant compactification.

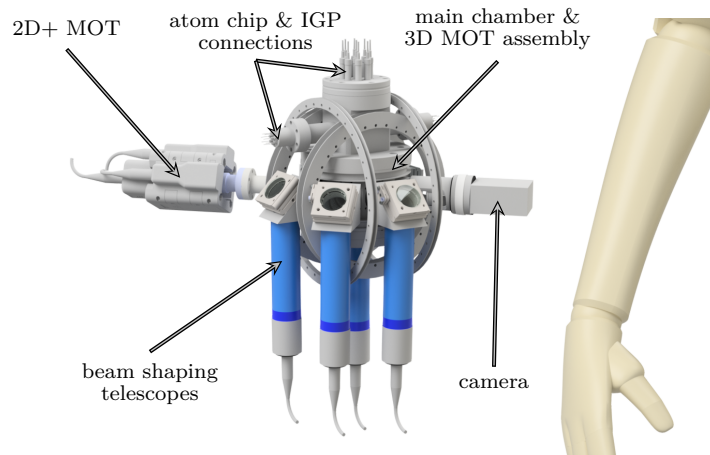


Figure 6.2: Construction model of the sensor head of the experimental platform within an outer support frame. The structure shown includes all vacuum components, which consist mainly of the 2D+ MOT and the 3D MOT chamber with the atom chip inside. Components attached to it such as the four beam shaping optics and the detection camera are also shown. The main missing components are an enclosing magnetic shield, and the gyro stabilized base, which are not shown for display reasons. The human arm on the right illustrates the size of the setup.

The chosen design goal of this setup is to achieve an absolute acceleration accuracy below $1 \times 10^{-6} \text{ (m/s}^2\text{)}/\sqrt{\text{Hz}}$ and an absolute rotation rate accuracy below $5 \times 10^{-9} \text{ (rad/s)}/\sqrt{\text{Hz}}$. The most demanding component is the rotation requirement (compare to table 5.1). As a comparative example, a navigation grade IMU based on ring laser gyroscopes [iNAT-RQT-4002, iMAR Navigation] achieves a noise density of $7.3 \times 10^{-7} \text{ (rad/s)}/\sqrt{\text{Hz}}$ based on the angular random walk and a bias instability of $4.8 \times 10^{-9} \text{ (rad/s)}/\sqrt{\text{Hz}}$. In addition a tactical grade

IMU based on MEMS technology [3DM-GQ™-45, LORD Corporation] achieves a noise density of 3.4×10^{-5} (rad/s)/ $\sqrt{\text{Hz}}$ and a bias instability of 2.4×10^{-5} (rad/s)/ $\sqrt{\text{Hz}}$. Therefore, it is a much greater challenge to overcome the performance of the former.

The goal is to compete with the above values while targeting lower bias instabilities with hybridization to open up a field of applications not covered by conventional sensors alone. To achieve this, new developments and innovations are needed in the areas listed below:

1. Miniaturized vacuum technology components
2. Gyro-stabilized platform for position control
3. Atom-chip technology
4. Optomechanical acceleration sensors for integration with mirror reference surfaces
5. Laser system with integrated fiber optics
6. Monolithic flat-top beam shaping optics
7. Control electronics

The following brief overview discusses the state of the art in these important areas, as well as the challenges and limitations to date.

1. Miniaturized vacuum technology components

For atom interferometry ultra-high vacuum environments are often necessary. Therefore, miniaturization of the vacuum chamber and the required pumping system are critical to the realization of a compact sensor. To make this possible, different miniaturization concepts are used, for example the use of non-evaporable getter material, which is applied to the inside of the vacuum chamber by means of cathode sputtering and a compact integrated ion getter pump. The use of low-outgassing, non-adhesive and vacuum-compatible joining techniques to produce customized vacuum chambers will also contribute. Additively manufactured chambers have been shown to operate at a pressure below 10^{-10} mbar [Coo21]. As this technology advances, it will be possible to achieve increasingly smaller form factors.

2. Gyro-stabilized platform

An inertial platform, also called a gyroscopic platform or stabilized platform, uses gyroscopes to hold a platform in a fixed orientation in space despite movement of the mount to which it is attached. This can then be used to stabilize the mounted inertial quantum measurement unit [Bid18]. While this stabilization can be limited, the atom interferometer allows the residual rotational components to be measured.

3. Atom-chip technology

Atom chips represent a robust and mature technology for the generation of BECs. In combination with laser cooling techniques, they generate magnetic field configurations so that the atoms can be trapped, cooled and manipulated. Atom chips benefit from new developments, particularly in surface quality, thermal management, the use of non-magnetic materials with low outgassing rates, novel wire structures and the use of new types of coatings [Chr19; Kas19].

4. Optomechanical acceleration sensors

The technology of optomechanical accelerometers [Guz14; Hin20; Ric20] is a promising approach to implement an accelerometer directly at the reference surface of the atom interferometer. In the application case these are the mirror surfaces and the atom chip. Only sensors with a small form factor make this possible. The volume of only a few cubic millimeters of such sensors therefore offers great opportunities for miniaturization. Current designs include a drum head resonator shape whose movement can be read out optically directly behind the mirror surface.

5. Laser system with integrated fiber optics

Based on the design of the fiber laser system from section 4.3, a new commercial prototype system [KVANTUM, NKT Photonics] is developed and shown in figure 6.3. It is based on a modular approach, where each module is assigned an individual task. The modules, powered via a common backplane, are designed to contain electro- and acousto-optical components and are interconnected with optical fibers. Narrow-band laser sources in the telecommunications wavelength range are used with subsequent amplification, modulation, optical filtering and frequency doubling. Together they provide the necessary light fields, required for the production of a quantum degenerate gas and its subsequent coherent manipulation. In addition to compactness, the main focus lies also on power consumption and frequency and amplitude stability of the produced light fields.

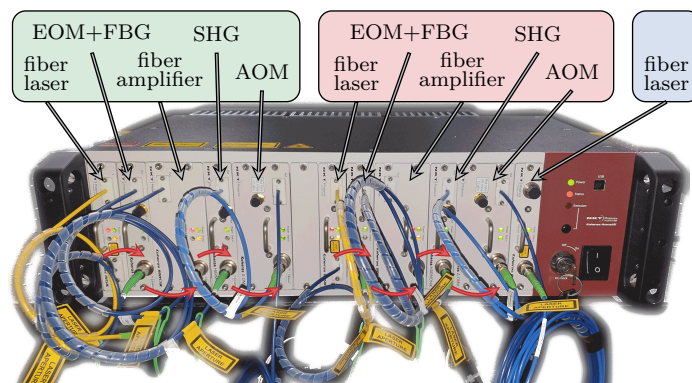


Figure 6.3: Fully fiber-based laser system consisting of a series of modules interconnected with optical polarization-maintaining fibers (from left to right). Each module performs an individual task, step by step and analogously to the section 4.3. The same abbreviation notation is used in the image as in this section. Shortly summarized, three individual fiber laser sources (red, green, and blue shaded areas) provide the necessary light fields, required for the production of a BEC and its subsequent coherent manipulation. The total system fits into a standard 19-inch rack module.

6. Monolithic flat-top beam shaping optics

Based on the concept from section 4.1 and the need to maximize the interferometry volume in a small setup, flat-top beams are chosen. The results obtained in section 4.1.5 regarding temporal and spatial intensity instability suggest the construction of a monolithic beam shaping element, which should be less susceptible to vibrations.

7. Control electronics: **A**dvanced **R**eal-**T**ime **I**nfrastructure for **Q**uantum physics (ARTIQ)

Much of the overall development of compact electronics for experiment control is already implemented within the ARTIQ framework [Kul18; Kas20]. The sequence code is compiled and executed on dedicated Field-Programmable Gate Array (FPGA) hardware with nanosecond timing resolution and sub-microsecond latency. The time-critical code (a kernel) running on the FPGA (the core device) can then be interfaced via programming language from a computer using a Remote Procedure Call (RPC) mechanism. First and foremost, the following hardware must still be developed: Current drivers, piezo drivers, electronics for laser control and the corresponding firmware. In addition, real-time capable control boards as well as boards for the generation of high-frequency signals and boards for digital and analog inputs and outputs are required.

At the end of this section, it remains to mention that the previously listed areas only cover parts of a fully functioning sensor system. There are still many open challenges and subtleties to master. In particular, the operating principle of the signal readout, the hybridisation with the optomechanical acceleration sensors and the gyro-stabilised platform require a more detailed investigation and explanation. Together with the associated position and sequence control, all this would go beyond the scope of this outlook.

This being said, it can be claimed that throughout the history of technology, there have always been methods that have replaced earlier ones. However, such processes often take time and require extensive development and qualification. Sensors based on atom interferometry are now at a stage where they can be used in the fields of inertial and gravity measurements. In recent years, transportable commercial quantum gravimeters have been developed, by the companies AOsense [AOS], M Squared Lasers [Las] and Muquans [Muq]. It therefore remains to be seen when the first quantum navigation compatible sensors will appear on the market.

Bibliography

- [Bro24] L. D. BROGLIE: ‘Recherches sur la théorie des Quanta Louis de Broglie’. PhD thesis. Migration-université en cours d’affectation, 1924 (cit. on p. 1).
- [Dav27] C. J. DAVISSON and L. H. GERMER: ‘The Diffraction of Electrons by a Crystal of Nickel’. *Phys. Rev.* (1927), vol. 30(705): pp. 90–105 (cit. on p. 1).
- [Kei88] D. W. KEITH, M. L. SCHATTENBURG, H. I. SMITH, and D. E. PRITCHARD: ‘Diffraction of atoms by a transmission grating’. *Physical Review Letters* (1988), vol. 61(14): pp. 1580–1583 (cit. on p. 1).
- [Kei91] D. W. KEITH, C. R. EKSTROM, Q. A. TURCHETTE, and D. E. PRITCHARD: ‘An interferometer for atoms’. *Physical Review Letters* (1991), vol. 66(21): pp. 2693–2696 (cit. on p. 1).
- [Car91] O. CARNAL and J. MLYNEK: ‘Youngs double-slit experiment with atoms: A simple atom interferometer’. *Physical Review Letters* (1991), vol. 66(21): pp. 2689–2692 (cit. on p. 1).
- [Ash78] A. ASHKIN: ‘Trapping of atoms by resonance radiation pressure’. *Physical Review Letters* (1978), vol. 40(12): pp. 729–732 (cit. on p. 1).
- [Phi85] W. D. PHILLIPS, J. V. PRODAN, and H. J. METCALF: ‘Laser Cooling and Trapping of Neutral Atoms’. *Opt. Soc. Am. B* (1985), vol. 2(11): pp. 1751–1767 (cit. on p. 1).
- [Raa87] E. L. RAAB, M. PRENTISS, A. CABLE, S. CHU, and D. E. PRITCHARD: ‘Trapping of Neutral Sodium Atoms with Radiation Pressure’. *Physical Review Letters* (1987), vol. 59(23): pp. 2631–2634 (cit. on p. 1).
- [Kas91] M. A. KASEVICH and S. CHU: ‘Atomic interferometry using stimulated Raman transitions’. *Physical Review Letters* (1991), vol. 67(2): pp. 181–184 (cit. on pp. 1, 13).
- [Ein25] A. EINSTEIN: ‘Quantentheorie des einatomigen idealen Gases’. *Sitzungsberichte der Preussischen Akademie der Wissenschaften* (1925), vol. 23: pp. 13–14 (cit. on p. 2).
- [Bos24] S. BOSE: ‘Plancks Gesetz und Lichtquantenhypothese’. *Zeitschrift für Physik* (1924), vol. 26: pp. 178–181 (cit. on p. 2).
- [And95] M. H. ANDERSON, J. R. ENSHER, M. R. MATTHEWS, C. E. WIEMAN, and E. A. CORNELL: ‘Observation of bose-einstein condensation in a dilute atomic vapor’. *Science* (1995), vol. 269(5221): pp. 198–201 (cit. on p. 2).
- [Bra95] C. C. BRADLEY, C. A. SACKETT, J. J. TOLLETT, and R. G. HULET: ‘Evidence of Bose-Einstein Condensation in an Atomic Gas with Attractive Interactions’. *Physical Review Letters* (1995), vol. 75(9): pp. 1687–1690 (cit. on p. 2).

- [Dav95] K. B. DAVIS, M.-O. MEWES, M. R. ANDREWS, N. J. van DRUTEN, D. S. DURFEE, D. M. KURN, and W. KETTERLE: ‘Bose-Einstein Condensation in a Gas of Sodium Atoms’. *Physical Review Letters* (1995), vol. 75(22): pp. 3969–3973 (cit. on p. 2).
- [And97] M. R. ANDREWS, C. G. TOWNSEND, H. J. MIESNER, D. S. DURFEE, D. M. KURN, and W. KETTERLE: ‘Observation of interference between two bose condensates’. *Science* (1997), vol. 275(5300): pp. 637–641 (cit. on p. 2).
- [Den00] J. DENSCHLAG, J. E. SIMSARIAN, D. L. FEDER, C. W. CLARK, L. A. COLLINS, J. CUBIZOLLES, L. DENG, E. W. HAGLEY, K. HELMERSON, W. P. REINHARDT, S. L. ROLSTON, B. I. SCHNEIDER, and W. D. PHILLIPS: ‘Generating solitons by phase engineering of a Bose-Einstein condensate’. *Science* (2000), vol. 287(5450): pp. 97–101 (cit. on p. 2).
- [Bir95] G. BIRKL, M. GATZKE, I. H. DEUTSCH, S. L. ROLSTON, and W. D. PHILLIPS: ‘Bragg scattering from atoms in optical lattices’. *Physical Review Letters* (1995), vol. 75(15): pp. 2823–2826 (cit. on pp. 2, 15).
- [Bon03] K. BONGS, S. BURGER, D. HELLWEG, M. KOTTKE, S. DETTMER, T. RINKLEFF, L. CACCIAPUOTI, J. ARLT, K. SENGSTOCK, and W. ERTMER: ‘Spectroscopy of dark soliton states in Bose-Einstein condensates’. *Journal of Optics B: Quantum and Semiclassical Optics* (2003), vol. 5(2): p. 124 (cit. on p. 2).
- [Chu86] S. CHU, J. E. BJORKHOLM, A. ASHKIN, J. P. GORDON, and L. W. HOLLBERG: ‘Proposal for optically cooling atoms to temperatures of the order of 10^{-6} K’. *Optics Letters* (1986), vol. 11(2): pp. 73–75 (cit. on pp. 2, 12).
- [Ben96] M. BEN DAHAN, E. PEIK, J. REICHEL, Y. CASTIN, and C. SALOMON: ‘Bloch oscillations of atoms in an optical potential’. *Physical Review Letters* (1996), vol. 76(24): pp. 4508–4511 (cit. on pp. 2, 8, 34).
- [Amm97] H. AMMANN and N. CHRISTENSEN: ‘Delta kick cooling: A new method for cooling atoms’. *Physical Review Letters* (1997), vol. 78(11): pp. 2088–2091 (cit. on pp. 2, 12).
- [Chi11] S.-w. CHIOW, T. KOVACHY, H. C. CHIEN, and M. A. KASEVICH: ‘ $102 \hbar k$ Large Area Atom Interferometers’. *Physical Review Letters* (2011), vol. 107(13): p. 130403 (cit. on pp. 2, 17, 39).
- [McD14] G. D. McDONALD, C. C. N. KUHN, K. S. HARDMAN, S. BENNETTS, P. J. EVERITT, P. A. ALTIN, J. E. DEBS, J. D. CLOSE, and N. P. ROBINS: ‘Bright solitonic matter-wave interferometer’. *Physical Review Letters* (2014), vol. 113(1): p. 013002 (cit. on p. 2).
- [Szi12] S. S. SZIGETI, J. E. DEBS, J. J. HOPE, N. P. ROBINS, and J. D. CLOSE: ‘Why momentum width matters for atom interferometry with Bragg pulses’. *New Journal of Physics* (2012), vol. 14: p. 023009 (cit. on p. 2).
- [Dic13] S. M. DICKERSON, J. M. HOGAN, A. SUGARBAKER, D. M. S. JOHNSON, and M. A. KASEVICH: ‘Multiaxis inertial sensing with long-time point source atom interferometry’. *Physical Review Letters* (2013), vol. 111(8): p. 083001 (cit. on p. 2).

- [Mie18] N. MIELEC, M. ALTORIO, R. SAPAM, D. HORVILLE, D. HOLLEVILLE, L. A. SIDORENKOV, A. LANDRAGIN, and R. GEIGER: ‘Atom interferometry with top-hat laser beams’. *Applied Physics Letters* (2018), vol. 113(16): p. 161108 (cit. on pp. 3, 61).
- [Lou11] A. LOUCHET-CHAUVET, T. FARAH, Q. BODART, A. CLAIRON, A. LANDRAGIN, S. MERLET, and F. P. D. SANTOS: ‘The influence of transverse motion within an atomic gravimeter’. *New Journal of Physics* (2011), vol. 13(6): p. 065025 (cit. on pp. 3, 60).
- [Sch15] V. SCHKOLNIK, B. LEYKAUF, M. HAUTH, C. FREIER, and A. PETERS: ‘The effect of wavefront aberrations in atom interferometry’. *Applied Physics B* (2015), vol. 120(2): pp. 311–316 (cit. on pp. 3, 60).
- [Bad18] S. BADE, L. DJADAOJEE, M. ANDIA, P. CLADÉ, and S. GUELLATI-KHÉLIFA: ‘Observation of Extra Photon Recoil in a Distorted Optical Field’. *Physical Review Letters* (2018), vol. 121(7): p. 073603 (cit. on pp. 3, 60, 68).
- [Böh22] S. BÖHRINGER: ‘Matter Wave Interferometry with Realistic Optical Fields’. PhD thesis. Universität Ulm, 2022 (cit. on pp. 3, 60).
- [Ove22] C. OVERSTREET, P. ASENBAUM, J. CURTI, M. KIM, and M. A. KASEVICH: ‘Observation of a gravitational Aharonov-Bohm effect’. *Science* (2022), vol. 375(6577): pp. 226–229 (cit. on p. 4).
- [Per19] I. PERRIN, Y. BIDEL, N. ZAHZAM, C. BLANCHARD, A. BRESSON, and M. CADORET: ‘Proof-of-principle demonstration of vertical-gravity-gradient measurement using a single-proof-mass double-loop atom interferometer’. *Physical Review A* (2019), vol. 99(1): p. 013601 (cit. on pp. 4, 42).
- [Mül08a] H. MÜLLER, S.-w. CHIOU, Q. LONG, S. HERRMANN, and S. CHU: ‘Atom interferometry with up to 24-photon-momentum-transfer beam splitters’. *Physical Review Letters* (2008), vol. 100(18): p. 180405 (cit. on pp. 4, 7, 15, 21, 37, 42).
- [Bar19] B. BARRETT, P. CHEINEY, B. BATTELIER, F. NAPOLITANO, and P. BOUYER: ‘Multidimensional Atom Optics and Interferometry’. *Physical Review Letters* (2019), vol. 122(4): p. 043604 (cit. on pp. 4, 42, 106).
- [Pet01] A. PETERS, K. Y. CHUNG, and S. CHU: ‘High-precision gravity measurements using atom interferometry’. *Metrologia* (2001), vol. 38(1): pp. 25–61 (cit. on pp. 4, 7, 13, 88).
- [Mén18] V. MÉNORET, P. VERMEULEN, N. LE MOIGNE, S. BONVALOT, P. BOUYER, A. LANDRAGIN, and B. DESRUELLE: ‘Gravity measurements below 10^{-9} g with a transportable absolute quantum gravimeter’. *Scientific Reports* (2018), vol. 8(1): p. 12300 (cit. on p. 4).
- [Sav18] D. SAVOIE, M. ALTORIO, B. FANG, L. A. SIDORENKOV, R. GEIGER, and A. LANDRAGIN: ‘Interleaved Atom Interferometry for High Sensitivity Inertial Measurements’. *Science Advances* (2018), vol. 4(12): eaau7948 (cit. on pp. 4, 34, 107).

- [Sto11] J. K. STOCKTON, K. TAKASE, and M. A. KASEVICH: ‘Absolute geodetic rotation measurement using atom interferometry’. *Physical Review Letters* (2011), vol. 107(13): p. 133001 (cit. on p. 4).
- [Ber15] P. BERG, S. ABEND, G. TACKMANN, C. SCHUBERT, E. GIESE, W. P. SCHLEICH, F. A. NARDUCCI, W. ERTMER, and E. M. RASEL: ‘Composite-light-pulse technique for high-precision atom interferometry’. *Physical Review Letters* (2015), vol. 114(6): p. 063002 (cit. on pp. 4, 19, 42, 88).
- [Hog07] J. M. HOGAN, D. M. S. JOHNSON, and M. A. KASEVICH: ‘Light-pulse atom interferometry’. *Proceedings of the International School of Physics "Enrico Fermi" on Atom Optics and Space Physics*. Ed. by E. ARIMONDO, W. ERTMER, W. P. SCHLEICH, and E. M. RASEL. Vol. 168. 2007: pp. 411–447 (cit. on p. 4).
- [Che18] P. CHEINEY, L. FOUCHÉ, S. TEMPLIER, F. NAPOLITANO, B. BATTELIER, P. BOUYER, and B. BARRETT: ‘Navigation-Compatible Hybrid Quantum Accelerometer Using a Kalman Filter’. *Physical Review Applied* (2018), vol. 10(3): p. 034030 (cit. on pp. 4, 107).
- [Dim09] S. DIMOPOULOS, P. W. GRAHAM, J. M. HOGAN, M. A. KASEVICH, and S. RAJENDRAN: ‘Gravitational wave detection with atom interferometry’. *Physics Letters, Section B: Nuclear, Elementary Particle and High-Energy Physics* (2009), vol. 678(1): pp. 37–40 (cit. on p. 4).
- [Lor19a] S. LORIANI, D. SCHLIPPERT, C. SCHUBERT, S. ABEND, H. AHLERS, W. ERTMER, J. RUDOLPH, J. M. HOGAN, M. A. KASEVICH, E. M. RASEL, and N. GAALLOUL: ‘Atomic source selection in space-borne gravitational wave detection’. *New Journal of Physics* (2019), vol. 21: p. 063030 (cit. on p. 4).
- [Abe16] S. ABEND, M. GEBBE, M. GERSEMANN, H. AHLERS, H. MÜNTINGA, E. GIESE, N. GAALLOUL, C. SCHUBERT, C. LÄMMERZAHL, W. ERTMER, W. P. SCHLEICH, and E. M. RASEL: ‘Atom-chip fountain gravimeter’. *Physical Review Letters* (2016), vol. 117(20): p. 203003 (cit. on pp. 5, 10, 29, 32).
- [Geb21] M. GEBBE, J.-N. SIEMSS, M. GERSEMANN, H. MÜNTINGA, S. HERRMANN, C. LÄMMERZAHL, H. AHLERS, N. GAALLOUL, C. SCHUBERT, K. HAMMERER, S. ABEND, and E. M. RASEL: ‘Twin-lattice atom interferometry’. *Nature Communications* (2021), vol. 12(1): p. 2544 (cit. on pp. 5, 10, 32, 37–40, 69).
- [Ger20] M. GERSEMANN, M. GEBBE, S. ABEND, C. SCHUBERT, and E. M. RASEL: ‘Differential interferometry using a Bose-Einstein condensate’. *European Physical Journal D* (2020), vol. 74(10): p. 203 (cit. on pp. 5, 41, 47, 50–52, 106).
- [Sch21] C. SCHUBERT, S. ABEND, M. GERSEMANN, M. GEBBE, D. SCHLIPPERT, P. BERG, and E. M. RASEL: ‘Multi-loop atomic Sagnac interferometry’. *Scientific Reports* (2021), vol. 11(1): p. 16121 (cit. on pp. 5, 55–58).
- [Hug07] K. J. HUGHES, B. DEISSLER, J. H. T. BURKE, and C. A. SACKETT: ‘High-fidelity manipulation of a Bose-Einstein condensate using an optical standing wave’. *Physical Review A* (2007), vol. 76(3): p. 035601 (cit. on p. 7).

- [Pes95] M. E. PESKIN and D. V. SCHROEDER: *An Introduction To Quantum Field Theory*. Boca Raton: CRC Press, 1995 (cit. on p. 7).
- [Mey01] P. MEYSTRE: *Atom optics*. Springer Science & Business Media, 2001 (cit. on p. 7).
- [Hen21] T. HENSEL, S. LORIANI, C. SCHUBERT, F. FITZEK, S. ABEND, H. AHLERS, J. SIEMSS, and K. HAMMERER: ‘Inertial sensing with quantum gases : a comparative performance study of condensed versus thermal sources for atom interferometry’. *The European Physical Journal D* (2021), vol. 75(3): p. 108 (cit. on p. 7).
- [Pet08] C. PETHICK and H. SMITH: *Bose–Einstein Condensation in Dilute Gases*. Cambridge: Cambridge University Press, 2008 (cit. on p. 8).
- [Cla06] P. CLADÉ, E. DE MIRANDES, M. CADORET, S. GUELLATI-KHÉLIFA, C. SCHWOB, F. NEZ, L. JULIEN, and F. BIRABEN: ‘Determination of the fine structure constant based on Bloch oscillations of ultracold atoms in a vertical optical lattice’. *Physical Review Letters* (2006), vol. 96(3): p. 033001 (cit. on pp. 8, 34).
- [Mül09] H. MÜLLER, S.-W. CHIOU, S. HERRMANN, and S. CHU: ‘Atom interferometers with scalable enclosed area’. *Physical Review Letters* (2009), vol. 102(24): p. 240403 (cit. on pp. 8, 28, 34).
- [Cla09] P. CLADÉ, S. GUELLATI-KHÉLIFA, F. NEZ, and F. BIRABEN: ‘Large momentum beam splitter using Bloch oscillations’. *Physical Review Letters* (2009), vol. 102(24): p. 240402 (cit. on pp. 8, 28, 34).
- [McD13] G. D. McDONALD, N. KUHN, S. BENNETTS, J. E. DEBS, K. S. HARDMAN, M. JOHNSON, J. D. CLOSE, and N. P. ROBINS: ‘ $80\hbar k$ momentum separation with Bloch oscillations in an optically guided atom interferometer’. *Physical Review A - Atomic, Molecular, and Optical Physics* (2013), vol. 88(5): p. 053620 (cit. on pp. 8, 28, 34).
- [Rud15] J. RUDOLPH, W. HERR, C. GRZESCHIK, T. STERNKE, A. GROTE, M. POPP, D. BECKER, H. MÜNTINGA, H. AHLERS, A. PETERS, C. LÄMMERZAHN, K. SENGSTOCK, N. GAALOUL, W. ERTMER, and E. M. RASEL: ‘A high-flux BEC source for mobile atom interferometers’. *New Journal of Physics* (2015), vol. 17(6): p. 065001 (cit. on pp. 8, 53, 105).
- [Ven22] Z. VENDEIRO, J. RAMETTE, A. RUDELIS, M. CHONG, J. SINCLAIR, L. STEWART, A. URVOY, and V. VULETIĆ: ‘Machine-learning-accelerated Bose-Einstein condensation’. *Phys. Rev. Res.* (2022), vol. 4(4): p. 043216 (cit. on p. 8).
- [Che22] C. C. CHEN, R. GONZÁLEZ ESCUDERO, J. MINÁŘ, B. PASQUIOU, S. BENNETTS, and F. SCHRECK: ‘Continuous Bose–Einstein condensation’. *Nature* (2022), vol. 606(7915): pp. 683–687 (cit. on p. 8).
- [Gau09] A. GAUGUET, B. CANUEL, T. LÉVÈQUE, W. CHAIBI, and A. LANDRAGIN: ‘Characterization and limits of a cold-atom Sagnac interferometer’. *Physical Review A - Atomic, Molecular, and Optical Physics* (2009), vol. 80(6): p. 063604 (cit. on pp. 9, 42).

- [Sor14] F. SORRENTINO, Q. BODART, L. CACCIAPUOTI, Y. H. LIEN, M. PREVEDELLI, G. ROSI, L. SALVI, and G. M. TINO: ‘Sensitivity limits of a Raman atom interferometer as a gravity gradiometer’. *Physical Review A - Atomic, Molecular, and Optical Physics* (2014), vol. 89(2): p. 023607 (cit. on p. 9).
- [Jan22] C. JANVIER, V. MÉNORET, B. DESRUELLE, S. MERLET, A. LANDRAGIN, and F. PEREIRA DOS SANTOS: ‘Compact differential gravimeter at the quantum projection-noise limit’. *Physical Review A* (2022), vol. 105(2): p. 022801 (cit. on p. 9).
- [Ler10] I. D. LEROUX, M. H. SCHLEIER-SMITH, and V. VULETIĆ: ‘Implementation of cavity squeezing of a collective atomic Spin’. *Physical Review Letters* (2010), vol. 104(7): p. 073602 (cit. on p. 9).
- [Lou10] A. LOUCHET-CHAUVET, J. APPEL, J. J. RENEMA, D. OBLAK, N. KJAERGAARD, and E. S. POLZIK: ‘Entanglement-assisted atomic clock beyond the projection noise limit’. *New Journal of Physics* (2010), vol. 12(6): p. 065032 (cit. on p. 9).
- [Hos16] O. HOSTEN, N. J. ENGELSEN, R. KRISHNAKUMAR, and M. A. KASEVICH: ‘Measurement noise 100 times lower than the quantum-projection limit using entangled atoms’. *Nature* (2016), vol. 529(7587): pp. 505–508 (cit. on p. 9).
- [Gro10] C. GROSS, T. ZIBOLD, E. NICKLAS, J. ESTÈVE, and M. K. OBERTHALER: ‘Nonlinear atom interferometer surpasses classical precision limit’. *Nature* (2010), vol. 464(7292): pp. 1165–1169 (cit. on p. 9).
- [Rie10] M. F. RIEDEL, P. BÖHI, Y. LI, T. W. HÄNSCH, A. SINATRA, and P. TREUTLEIN: ‘Atom-chip-based generation of entanglement for quantum metrology’. *Nature* (2010), vol. 464(7292): pp. 1170–1173 (cit. on p. 9).
- [Lüc11] B. LÜCKE, M. SCHERER, J. KRUSE, L. PEZZÉ, F. DEURETZBACHER, P. HYLLUS, O. TOPIC, J. PEISE, W. ERTMER, J. ARLT, L. SANTOS, A. SMERZI, and C. KLEMP: ‘Twin matter waves for interferometry beyond the classical limit’. *Science* (2011), vol. 334(6057): pp. 773–776 (cit. on p. 9).
- [And21] F. ANDERS, A. IDEL, P. FELDMANN, D. BONDARENKO, S. LORIANI, K. LANGE, J. PEISE, M. GERSEMANN, B. MEYER-HOPPE, S. ABEND, N. GAALOUL, C. SCHUBERT, D. SCHLIPPERT, L. SANTOS, E. M. RASEL, and C. KLEMP: ‘Momentum Entanglement for Atom Interferometry’. *Physical Review Letters* (2021), vol. 127(14): p. 140402 (cit. on p. 9).
- [Yve03] F. YVER-LEDUC, P. CHEINET, J. FILS, A. CLAIRON, N. DIMARCQ, D. HOLLEVILLE, P. BOUYER, and A. LANDRAGIN: ‘Reaching the quantum noise limit in a high-sensitivity cold-atom inertial sensor’. *Journal of Optics B: Quantum and Semiclassical Optics* (2003), vol. 5(2): pp. 136–142 (cit. on p. 9).
- [Zoe10] T. van ZOEST, N. GAALOUL, Y. SINGH, H. AHLERS, W. HERR, S. T. SEIDEL, W. ERTMER, E. M. RASEL, M. ECKART, E. KAJARI, S. ARNOLD, G. NANDI, W. P. SCHLEICH, R. WALSER, A. VOGEL, K. SENGSTOCK, K. BONGS, W. LEWOCZKO-ADAMCZYK, M. SCHIEMANGK, T. SCHULDT, A. PETERS, et al.: ‘Bose-Einstein Condensation in Microgravity’. *Science* (2010), vol. 328(5985): pp. 1540–1543 (cit. on p. 10).

- [Mün13] H. MÜNTINGA, H. AHLERS, M. KRUTZIK, A. WENZLAWSKI, S. ARNOLD, D. BECKER, K. BONGS, H. DITTUS, H. DUNCKER, N. GAALOUL, C. GHERASIM, E. GIESE, C. GRZESCHIK, T. W. HÄNSCH, O. HELLMIG, W. HERR, S. HERRMANN, E. KAJARI, S. KLEINERT, C. LÄMMERZAHL, W. LEWOCZKO-ADAMCZYK, et al.: ‘Interferometry with Bose-Einstein condensates in microgravity’. *Physical Review Letters* (2013), vol. 110(9): p. 093602 (cit. on pp. 10, 12).
- [Ahl16] H. AHLERS, H. MÜNTINGA, A. WENZLAWSKI, M. KRUTZIK, G. TACKMANN, S. ABEND, N. GAALOUL, E. GIESE, A. ROURA, R. KUHL, C. LÄMMERZAHL, A. PETERS, P. WINDPASSINGER, K. SENGSTOCK, W. P. SCHLEICH, W. ERTMER, and E. M. RASEL: ‘Double Bragg Interferometry’. *Physical Review Letters* (2016), vol. 116(17): p. 173601 (cit. on pp. 10, 17, 35).
- [Kan21] S. KANTHAK, M. GEBBE, M. GERSEMANN, S. ABEND, E. M. RASEL, and M. KRUTZIK: ‘Time-domain optics for atomic quantum matter’. *New Journal of Physics* (2021), vol. 23(9): p. 093002 (cit. on p. 10).
- [Cam84] J. C. CAMPARO and R. P. FRUEHOLZ: ‘A dressed atom interpretation of adiabatic rapid passage’. *Journal of Physics B: Atomic and Molecular Physics* (1984), vol. 17(20): pp. 4169–4178 (cit. on p. 12).
- [Ger22] W. GERLACH and O. STERN: ‘Der experimentelle Nachweis der Richtungsquantelung im Magnetfeld’. *Zeitschrift für Physik* (1922), vol. 9(1): pp. 349–352 (cit. on p. 12).
- [Mor99] M. MORINAGA, I. BOUCHOULE, J. C. KARAM, and C. SALOMON: ‘Manipulation of motional quantum states of neutral atoms’. *Physical Review Letters* (1999), vol. 83(20): pp. 4037–4040 (cit. on p. 12).
- [Kov15a] T. KOVACHY, J. M. HOGAN, A. SUGARBAKER, S. M. DICKERSON, C. A. DONNELLY, C. OVERSTREET, and M. A. KASEVICH: ‘Matter wave lensing to picokelvin temperatures’. *Physical Review Letters* (2015), vol. 114(14): p. 143004 (cit. on p. 12).
- [Fat08] M. FATTORI, C. D’ERRICO, G. ROATI, M. ZACCANTI, M. JONA-LASINIO, M. MODUGNO, M. INGUSCIO, and G. MODUGNO: ‘Atom interferometry with a weakly interacting bose-einstein condensate’. *Physical Review Letters* (2008), vol. 100(8): p. 080405 (cit. on p. 13).
- [Ram50] N. F. RAMSEY: ‘A molecular beam resonance method with separated oscillating fields’. *Physical Review* (1950), vol. 78(6): pp. 695–699 (cit. on p. 13).
- [Bor04] C. J. BORDÉ: ‘Quantum theory of atom-wave beam splitters and application to multidimensional atomic gravito-inertial sensors’. *General Relativity and Gravitation* (2004), vol. 36(3): pp. 475–502 (cit. on p. 13).
- [Bon06] K. BONGS, R. LAUNAY, and M. A. KASEVICH: ‘High-order inertial phase shifts for time-domain atom interferometers’. *Applied Physics B: Lasers and Optics* (2006), vol. 84(4): pp. 599–602 (cit. on p. 13).
- [Rie91] F. RIEHLE, T. KISTERS, A. WITTE, J. HELMCKE, and C. J. BORDÉ: ‘Optical Ramsey spectroscopy in a rotating frame: Sagnac effect in a matter-wave interferometer’. *Physical Review Letters* (1991), vol. 67(2): pp. 177–180 (cit. on p. 15).

- [Kun96] S. KUNZE, S. DÜRR, and G. REMPE: ‘Bragg scattering of slow atoms from a standing light wave’. *Europhysics Letters* (1996), vol. 34(5): pp. 343–348 (cit. on p. 15).
- [Koz99] M. KOZUMA, L. DENG, E. W. HAGLEY, J. WEN, R. LUTWAK, K. HELMERSON, S. L. ROLSTON, and W. D. PHILLIPS: ‘Coherent splitting of bose-einstein condensed atoms with optically induced bragg diffraction’. *Physical Review Letters* (1999), vol. 82(5): pp. 871–875 (cit. on p. 15).
- [Tor00] Y. TORII, Y. SUZUKI, M. KOZUMA, T. SUGIURA, T. KUGA, L. DENG, and E. W. HAGLEY: ‘Mach-Zehnder Bragg interferometer for a Bose-Einstein condensate’. *Physical Review A - Atomic, Molecular, and Optical Physics* (2000), vol. 61(4): p. 4 (cit. on p. 15).
- [Mül08b] H. MÜLLER, S.-w. CHIOU, and S. CHU: ‘Atom-wave diffraction between the Raman-Nath and the Bragg regime: Effective Rabi frequency, losses, and phase shifts’. *Physical Review A - Atomic, Molecular, and Optical Physics* (2008), vol. 77(2): p. 023609 (cit. on pp. 15, 17).
- [Gad09] B. GADWAY, D. PERTOT, R. REIMANN, M. G. COHEN, and D. SCHNEBLE: ‘Analysis of Kapitza-Dirac diffraction patterns beyond the Raman-Nath regime’. *Optics Express* (2009), vol. 17(21): p. 19173 (cit. on p. 17).
- [Gie13] E. GIESE, A. ROURA, G. TACKMANN, E. M. RASEL, and W. P. SCHLEICH: ‘Double Bragg diffraction: A tool for atom optics’. *Physical Review A - Atomic, Molecular, and Optical Physics* (2013), vol. 88(5): p. 053608 (cit. on p. 17).
- [Mal10] N. MALOSSI, Q. BODART, S. MERLET, T. LÉVÈQUE, A. LANDRAGIN, and F. P. dos SANTOS: ‘Double diffraction in an atomic gravimeter’. *Physical Review A - Atomic, Molecular, and Optical Physics* (2010), vol. 81(1): p. 013617 (cit. on pp. 18, 19, 46, 97).
- [Phi91] W. D. PHILLIPS, P. D. LETT, S. L. ROLSTON, C. E. TANNER, R. N. WATTS, C. I. WESTBROOK, C. SALOMON, J. DALIBARD, A. CLAIRON, and S. GUELLATI: ‘Optical molasses: The coldest atoms ever’. *Physica Scripta* (1991), vol. 1991(T34): pp. 20–22 (cit. on p. 18).
- [Sal90] C. SALOMON, J. DALIBARD, W. D. PHILLIPS, A. CLAIRON, and S. GUELLATI: ‘Laser cooling of cesium atoms below $3\mu\text{K}$ ’. *Epl* (1990), vol. 12(8): pp. 683–688 (cit. on p. 18).
- [Lév09] T. LÉVÈQUE, A. GAUGUET, F. MICHAUD, F. PEREIRA DOS SANTOS, and A. LANDRAGIN: ‘Enhancing the area of a Raman atom interferometer using a versatile double-diffraction technique’. *Physical Review Letters* (2009), vol. 103(8): p. 080405 (cit. on pp. 19, 97).
- [Jaf18] M. JAFFE, V. XU, P. HASLINGER, H. MÜLLER, and P. HAMILTON: ‘Efficient Adiabatic Spin-Dependent Kicks in an Atom Interferometer’. *Physical Review Letters* (2018), vol. 121(4): p. 40402 (cit. on p. 19).

- [Har20] S. HARTMANN, J. JENEWEIN, S. ABEND, A. ROURA, and E. GIESE: ‘Atomic Raman scattering: Third-order diffraction in a double geometry’. *Physical Review A* (2020), vol. 102(6): p. 063326 (cit. on pp. 21, 88, 97).
- [Gie16] E. GIESE, A. FRIEDRICH, S. ABEND, E. M. RASEL, and W. P. SCHLEICH: ‘Light shifts in atomic Bragg diffraction’. *Physical Review A* (2016), vol. 94(6): p. 063619 (cit. on p. 21).
- [Geb20] M. GEBBE: ‘Atom Interferometry in a Twin Lattice’. PhD thesis. Universität Bremen, 2020 (cit. on pp. 21, 34).
- [Che08] P. CHEINET, B. CANUEL, F. P. DOS SANTOS, A. GAUGUET, F. YVER-LEDUC, and A. LANDRAGIN: ‘Measurement of the sensitivity function in a time-domain atomic interferometer’. *IEEE Transactions on Instrumentation and Measurement* (2008), vol. 57(6): pp. 1141–1148 (cit. on pp. 21, 96).
- [Bon15] A. BONNIN, N. ZAHZAM, Y. BIDEL, and A. BRESSON: ‘Characterization of a simultaneous dual-species atom interferometer for a quantum test of the weak equivalence principle’. *Physical Review A - Atomic, Molecular, and Optical Physics* (2015), vol. 92(2): p. 023626 (cit. on p. 21).
- [Déc19] B. DÉCAMPS, M. BORDOUX, J. ALIBERT, B. ALLARD, and A. GAUGUET: ‘Phase response of atom interferometers based on sequential Bragg diffractions’. *Journal of Physics B: Atomic, Molecular and Optical Physics* (2019), vol. 52(1): p. 015003 (cit. on p. 23).
- [Bar14] B. BARRETT, P. A. GOMINET, E. CANTIN, L. ANTONI-MICOLLIER, A. BERTOLDI, B. BATTELIER, P. BOUYER, J. LAUTIER, and A. LANDRAGIN: ‘Mobile and remote inertial sensing with atom interferometers’. *Proceedings of the International School of Physics "Enrico Fermi" on Atom Interferometry*. Ed. by G. M. TINO and M. A. KASEVICH. Vol. 188. 2014: pp. 493–555 (cit. on pp. 24, 60).
- [All66] D. W. ALLAN: ‘Statistics of Atomic Frequency Standards’. *Proceedings of the IEEE* (1966), vol. 54(2): pp. 221–230 (cit. on pp. 25, 51).
- [Ket92] W. KETTERLE and D. E. PRITCHARD: ‘Trapping and focusing ground state atoms with static fields’. *Applied Physics B* (1992), vol. 54(5): pp. 403–406 (cit. on p. 28).
- [Sau01] J. A. SAUER, M. D. BARRETT, and M. S. CHAPMAN: ‘Storage ring for neutral atoms’. *Physical Review Letters* (2001), vol. 87(27): p. 270401 (cit. on p. 28).
- [Arn04] A. S. ARNOLD: ‘Adaptable-radius, time-orbiting magnetic ring trap for Bose-Einstein condensates’. *Journal of Physics B: Atomic, Molecular and Optical Physics* (2004), vol. 37(2): p. L29 (cit. on pp. 28, 54, 64).
- [Wu07] S. WU, E. SU, and M. PRENTISS: ‘Demonstration of an area-enclosing guided-atom interferometer for rotation sensing’. *Physical Review Letters* (2007), vol. 99(17): p. 173201 (cit. on pp. 28, 54).

- [Moa20] E. R. MOAN, R. A. HORNE, T. ARPORNTHIP, Z. LUO, A. J. FALLON, S. J. BERL, and C. A. SACKETT: ‘Quantum Rotation Sensing with Dual Sagnac Interferometers in an Atom-Optical Waveguide’. *Physical Review Letters* (2020), vol. 124(12): p. 120403 (cit. on pp. 28, 34, 54).
- [Krz22] K. KRZYŻANOWSKA, J. FERRERAS, C. RYU, E. C. SAMSON, and M. BOSCHER: ‘Matter Wave Analog of a Fiber-Optic Gyroscope’. *arXiv:2201.12461* (2022), vol. (cit. on pp. 28, 54, 64).
- [Hei20] N. HEINE, J. MATTHIAS, M. SAHELGOZIN, W. HERR, S. ABEND, L. TIMMEN, J. MÜLLER, and E. M. RASEL: ‘A transportable quantum gravimeter employing delta-kick collimated Bose–Einstein condensates’. *European Physical Journal D* (2020), vol. 74(8): p. 174 (cit. on pp. 32, 60).
- [Dut16] I. DUTTA, D. SAVOIE, B. FANG, B. VENON, C. L. GARRIDO ALZAR, R. GEIGER, and A. LANDRAGIN: ‘Continuous Cold-Atom Inertial Sensor with 1 nrad/sec Rotation Stability’. *Physical Review Letters* (2016), vol. 116(18): p. 183003 (cit. on pp. 34, 107).
- [Sch11] K. U. SCHREIBER, T. KLÜGEL, J. P. R. WELLS, R. B. HURST, and A. GEBAUER: ‘How to detect the Chandler and the annual wobble of the earth with a large ring laser gyroscope’. *Physical Review Letters* (2011), vol. 107(17): p. 173904 (cit. on pp. 34, 54).
- [Gei11] R. GEIGER, V. MÉNORET, G. STERN, N. ZAHZAM, P. CHEINET, B. BATTELIER, A. VILLING, F. MORON, M. LOURS, Y. BIDEI, A. BRESSON, A. LANDRAGIN, and P. BOUYER: ‘Detecting inertial effects with airborne matter-wave interferometry’. *Nature Communications* (2011), vol. 2(1): pp. 1–7 (cit. on pp. 35, 107).
- [Rud82] M. RUDEMO: ‘Empirical Choice of Histograms and Kernel Density Estimators’. *Scandinavian Journal of Statistics* (1982), vol. 9(2): pp. 65–78 (cit. on p. 36).
- [Kov15b] T. KOVACHY, P. ASENBAUM, C. OVERSTREET, C. A. DONNELLY, S. M. DICKERSON, A. SUGARBAKER, J. M. HOGAN, and M. A. KASEVICH: ‘Quantum superposition at the half-metre scale’. *Nature* (2015), vol. 528(7583): pp. 530–533 (cit. on pp. 37, 61, 82).
- [Jen22] J. JENEWEIN, S. HARTMANN, A. ROURA, and E. GIESE: ‘Bragg-diffraction-induced imperfections of the signal in retroreflective atom interferometers’. *Physical Review A* (2022), vol. 105(6): p. 063316 (cit. on p. 39).
- [Sie23] J.-N. SIEMSS: ‘Theory of Large-Momentum-Transfer Atom Interferometry in the Quasi-Bragg Regime’. PhD thesis. Leibniz Universität Hannover, 2023 (cit. on p. 40).
- [Eks93] C. R. EKSTROM: ‘Experiments with a Separated Beam Atom Interferometer’. PhD thesis. Massachusetts Institute of Technology, 1993 (cit. on p. 40).
- [Ase17] P. ASENBAUM, C. OVERSTREET, T. KOVACHY, D. D. BROWN, J. M. HOGAN, and M. A. KASEVICH: ‘Phase Shift in an Atom Interferometer due to Spacetime Curvature across its Wave Function’. *Physical Review Letters* (2017), vol. 118(18): p. 183602 (cit. on p. 42).

- [Dur06] D. S. DURFEE, Y. K. SHAHAM, and M. A. KASEVICH: ‘Long-term stability of an area-reversible atom-interferometer sagnac gyroscope’. *Physical Review Letters* (2006), vol. 97(24): p. 240801 (cit. on p. 42).
- [Rud16] J. RUDOLPH: ‘Matter-Wave Optics with Bose-Einstein Condensates in Microgravity’. PhD thesis. Leibniz Universität Hannover, 2016 (cit. on p. 44).
- [Abe17] S. ABEND: ‘Atom-chip Gravimeter with Bose-Einstein Condensates’. PhD thesis. Leibniz Universität Hannover, 2017 (cit. on p. 44).
- [Agu14] D. AGUILERA, H. AHLERS, B. BATTELIER, A. BAWAMIA, A. BERTOLDI, R. BONDARESCU, K. BONGS, P. BOUYER, C. BRAXMAIER, L. CACCIAPUOTI, C. CHALONER, M. CHWALLA, W. ERTMER, M. FRANZ, N. GAALOUL, M. GEHLER, D. GERARDI, L. GESA, N. GÜRLEBECK, J. HARTWIG, M. HAUTH, et al.: ‘Erratum: STE-QUEST - Test of the universality of free fall using cold atom interferometry (Classical and Quantum Gravity)’. *Classical and Quantum Gravity* (2014), vol. 31(15) (cit. on p. 44).
- [Ave20] D. C. AVELINE, J. R. WILLIAMS, E. R. ELLIOTT, C. DUTENHOFFER, J. R. KELLOGG, J. M. KOHEL, N. E. LAY, K. OUDRHIRI, R. F. SHOTWELL, N. YU, and R. J. THOMPSON: ‘Observation of Bose–Einstein condensates in an Earth-orbiting research lab’. *Nature* (2020), vol. 582(7811): pp. 193–197 (cit. on p. 44).
- [Fry21] K. FRYE, S. ABEND, W. BARTOSCH, A. BAWAMIA, D. BECKER, H. BLUME, C. BRAXMAIER, S.-W. CHIOU, M. A. EFREMOV, W. ERTMER, P. FIERLINGER, T. FRANZ, N. GAALOUL, J. GROSSE, C. GRZESCHIK, O. HELLMIG, V. A. HENDERSON, W. HERR, U. ISRAELSSON, J. KOHEL, M. KRUTZIK, et al.: ‘The Bose-Einstein Condensate and Cold Atom Laboratory’. *EPJ Quantum Technology* (2021), vol. 8(1): p. 1 (cit. on pp. 44, 60).
- [Bev16] N. BEVERINI, A. D. VIRGILIO, J. BELFI, A. ORTOLAN, K. U. SCHREIBER, A. GEBAUER, and T. KLÜGEL: ‘High-Accuracy Ring Laser Gyroscopes: Earth Rotation Rate and Relativistic Effects’. *Journal of Physics: Conference Series* (2016), vol. 723(1): p. 012061 (cit. on p. 54).
- [Ber21] A. BERTOLDI, C. H. FENG, D. S. NAIK, B. CANUEL, P. BOUYER, and M. PREVEDELLI: ‘Fast Control of Atom-Light Interaction in a Narrow Linewidth Cavity’. *Physical Review Letters* (2021), vol. 127(1): p. 013202 (cit. on pp. 56, 60).
- [Ita93] W. M. ITANO, J. C. BERGQUIST, J. J. BOLLINGER, J. M. GILLIGAN, D. J. HEINZEN, F. L. MOORE, M. G. RAIZEN, and D. J. WINELAND: ‘Quantum projection noise: Population fluctuations in two-level systems’. *Physical Review A* (1993), vol. 47(5): pp. 3554–3570 (cit. on p. 60).
- [San99] G. SANTARELLI, P. LAURENT, P. LEMONDE, A. CLAIRON, A. G. MANN, S. CHANG, A. N. LUITEN, and C. SALOMON: ‘Quantum projection noise in an atomic fountain: A high stability cesium frequency standard’. *Physical Review Letters* (1999), vol. 82(23): pp. 4619–4622 (cit. on p. 60).

- [Bec18] D. BECKER, M. D. LACHMANN, S. T. SEIDEL, H. AHLERS, A. N. DINKELAKER, J. GROSSE, O. HELLMIG, H. MÜNTINGA, V. SCHKOLNIK, T. J. WENDRICH, A. WENZLAWSKI, B. WEPS, R. CORGIER, T. FRANZ, N. GAALOUL, W. HERR, D. LÜDTKE, M. POPP, S. AMRI, H. DUNCKER, M. ERBE, et al.: ‘Space-borne Bose-Einstein condensation for precision interferometry’. *Nature* (2018), vol. 562(7727): pp. 391–395 (cit. on p. 60).
- [Bon19] K. BONGS, M. HOLYSKI, J. VOVROSH, P. BOUYER, G. CONDON, E. M. RASEL, C. SCHUBERT, W. P. SCHLEICH, and A. ROURA: ‘Taking atom interferometric quantum sensors from the laboratory to real-world applications’. *Nature Reviews Physics* (2019), vol. 1(12): pp. 731–739 (cit. on pp. 60, 106).
- [Pan23a] C. D. PANDA, M. TAO, J. EGELHOFF, M. CEJA, and V. XU: ‘Minute-scale gravimetry using a coherent atomic spatial superposition’. *arXiv:2210.07289* (2023), vol. (cit. on p. 60).
- [Gor94] F. GORI: ‘Flattened gaussian beams’. *Optics Communications* (1994), vol. 107(5): pp. 335–341 (cit. on p. 62).
- [Bag96] V. BAGINI, D. AMBROSINI, G. S. SPAGNOLO, R. BORGHI, F. GORI, A. M. PACILEO, and M. SANTARSIERO: ‘Propagation of axially symmetric flattened Gaussian beams’. *Journal of the Optical Society of America A* (1996), vol. 13(7): p. 1385 (cit. on p. 62).
- [Bor01] R. BORGHI: ‘Elegant Laguerre–Gauss beams as a new tool for describing axisymmetric flattened Gaussian beams’. *Journal of the Optical Society of America A* (2001), vol. 18(7): p. 1627 (cit. on p. 62).
- [Hof00] J. A. HOFFNAGLE and C. M. JEFFERSON: ‘Design and performance of a refractive optical system that converts a Gaussian to a flattop beam’. *Applied Optics* (2000), vol. 39(30): p. 5488 (cit. on p. 62).
- [She06] D. L. SHEALY and J. A. HOFFNAGLE: ‘Laser beam shaping profiles and propagation’. *Applied Optics* (2006), vol. 45(21): pp. 5118–5131 (cit. on p. 62).
- [Fri65] B. R. FRIEDEN: ‘Lossless Conversion of a Plane Laser Wave to a Plane Wave of Uniform Irradiance’. *Applied Optics* (1965), vol. 4(11): pp. 1400–1403 (cit. on p. 65).
- [Kre69] J. L. KREUTZER: *Coherent light optical system yielding an output beam of desired intensity distribution at a desired equiphase surface*. U.S. Patent No. 3 476 463, 1969 (cit. on p. 65).
- [Rou14] A. ROURA, W. ZELLER, and W. P. SCHLEICH: ‘Overcoming loss of contrast in atom interferometry due to gravity gradients’. *New Journal of Physics* (2014), vol. 16: p. 123012 (cit. on p. 68).
- [Tak82] M. TAKEDA, H. INA, and S. KOBAYASHI: ‘Fourier-transform method of fringe-pattern analysis for computer-based topography and interferometry’. *Journal of the Optical Society of America* (1982), vol. 72(1): pp. 156–160 (cit. on p. 72).

- [Mie19] N. MIELEC: ‘Études pour un résonateur optique à profil d’intensité plat et son application à l’interférométrie atomique’. PhD thesis. Université PSL, 2019 (cit. on p. 72).
- [Mor93] A. MORINAGA, T. TAKO, and N. ITO: ‘Sensitive measurement of phase shifts due to the ac Stark effect in a Ca optical Ramsey interferometer’. *Physical Review A* (1993), vol. 48(2): pp. 1364–1368 (cit. on p. 81).
- [Mül95] J. H. MÜLLER, D. BETTERMANN, V. RIEGER, K. SENGSTOCK, U. STERR, and W. ERTMER: ‘Topological phase shift in a cold-atom interferometer’. *Applied Physics B Laser and Optics* (1995), vol. 60(2-3): pp. 199–204 (cit. on p. 81).
- [Dei08] B. DEISSLER, K. J. HUGHES, J. H. T. BURKE, and C. A. SACKETT: ‘Measurement of the ac Stark shift with a guided matter-wave interferometer’. *Physical Review A - Atomic, Molecular, and Optical Physics* (2008), vol. 77(3): pp. 1–4 (cit. on p. 81).
- [Cro09] A. D. CRONIN, J. SCHMIEDMAYER, and D. E. PRITCHARD: ‘Optics and interferometry with atoms and molecules’. *Reviews of Modern Physics* (2009), vol. 81(3): pp. 1051–1129 (cit. on p. 81).
- [Kim20] M. KIM, R. NOTERMANS, C. OVERSTREET, J. CURTI, P. ASENBAUM, and M. A. KASEVICH: ‘40 W, 780 nm laser system with compensated dual beam splitters for atom interferometry’. *Optics Letters* (2020), vol. 45(23): p. 6555 (cit. on pp. 82, 87).
- [Che21] M. CHEREDINOV: ‘A laser system for absolute light-shift compensation in a twin-lattice interferometer’. Master thesis. Leibniz Universität Hannover, 2021 (cit. on p. 83).
- [Han18] S. HANNIG, J. MIELKE, J. A. FENSKE, M. MISERA, N. BEEV, C. OSPELKAUS, and P. O. SCHMIDT: ‘A highly stable monolithic enhancement cavity for second harmonic generation in the ultraviolet’. *Review of Scientific Instruments* (2018), vol. 89(1): p. 013106 (cit. on p. 83).
- [Sha21] J. C. SHAW, S. HANNIG, and D. J. MCCARRON: ‘Stable 2 W continuous-wave 261.5 nm laser for cooling and trapping aluminum monochloride’. *Optics Express* (2021), vol. 29(23): p. 37140 (cit. on p. 83).
- [Han80] T. W. HANSCH and B. COULLAUD: ‘Laser frequency stabilization by polarization spectroscopy of a reflecting reference cavity’. *Optics Communications* (1980), vol. 35(3): pp. 441–444 (cit. on p. 83).
- [Tom81] W. J. TOMLINSON, R. E. WAGNER, T. S. STAKELON, T. W. CLIME, and R. B. JANDER: ‘Coupling efficiency of the optics in single-mode and multimode fiber components’. *Integrated Optics and Optical Fiber Communication*. Ed. by M. BARNOWSKI, J. G. GIALLORENZI, J. GOELL, J. MIDWINTER, and S. Y. Optica Publishing Group, 1981: TUL2 (cit. on p. 86).
- [Say22] J. SAYWELL, M. CAREY, N. DEDES, I. KUPROV, and T. FREEGARDE: ‘Efficient state-symmetric beamsplitters and mirrors for atom interferometers using optimized pulses’. *Journal of Physics B: Atomic, Molecular and Optical Physics* (2022), vol. 55(20): p. 205501 (cit. on p. 88).

- [Lor19b] S. LORIANI, A. FRIEDRICH, C. UFRICHT, F. DI PUMPO, S. KLEINERT, S. ABEND, N. GAALLOUL, C. MEINERS, C. SCHUBERT, D. TELL, É. WODEY, M. ZYCH, W. ERTMER, A. ROURA, D. SCHLIPPERT, W. P. SCHLEICH, E. M. RASEL, and E. GIESE: ‘Interference of clocks: A quantum twin paradox’. *Science Advances* (2019), vol. 5(10): eaax8966 (cit. on p. 88).
- [Rou20] A. ROURA: ‘Gravitational Redshift in Quantum-Clock Interferometry’. *Physical Review X* (2020), vol. 10(2): p. 21014 (cit. on p. 88).
- [Ufr20] C. UFRICHT, F. DI PUMPO, A. FRIEDRICH, A. ROURA, C. SCHUBERT, D. SCHLIPPERT, E. M. RASEL, W. P. SCHLEICH, and E. GIESE: ‘Atom-interferometric test of the universality of gravitational redshift and free fall’. *Physical Review Research* (2020), vol. 2(4): p. 043240 (cit. on p. 88).
- [Kaw07] T. KAWANISHI, T. SAKAMOTO, and M. IZUTSU: ‘High-speed control of lightwave amplitude, phase, and frequency by use of electrooptic effect’. *IEEE Journal on Selected Topics in Quantum Electronics* (2007), vol. 13(1): pp. 79–90 (cit. on p. 92).
- [Zhu18] L. ZHU, Y.-H. LIEN, A. HINTON, A. NIGGEBaum, C. RAMMELOO, K. BONGS, and M. HOLYNSKI: ‘Application of optical single-sideband laser in Raman atom interferometry’. *Optics Express* (2018), vol. 26(6): pp. 6542–6553 (cit. on pp. 93, 94).
- [Pan23b] H. J. PANDIT, A. TYAGI, H. VAID, R. DHAWAN, and A. CHOUDHARY: ‘Single sideband modulation formats for quantum atom interferometry with Rb atoms’. *Applied Physics B* (2023), vol. 129(1): p. 24 (cit. on p. 93).
- [Wen10] T. J. WENDRICH: ‘High resolution rotation sensor based on cold atom interferometry’. PhD thesis. Leibniz Universität Hannover, 2010 (cit. on p. 93).
- [Car12] O. CARRAZ, R. CHARRIÈRE, M. CADORET, N. ZAHZAM, Y. BIDEL, and A. BRESSON: ‘Phase shift in an atom interferometer induced by the additional laser lines of a Raman laser generated by modulation’. *Physical Review A - Atomic, Molecular, and Optical Physics* (2012), vol. 86(3): p. 033605 (cit. on pp. 93, 94).
- [Wan17] Y. WANG, J. ZHONG, H. SONG, L. ZHU, Y. LI, X. CHEN, R. LI, J. WANG, and M. ZHAN: ‘Location-dependent Raman transition in gravity-gradient measurements using dual atom interferometers’. *Physical Review A* (2017), vol. 95(5): p. 053612 (cit. on p. 93).
- [Sar22] S. SARKAR, R. PICCON, S. MERLET, and F. PEREIRA DOS SANTOS: ‘Simple and robust architecture of a laser system for atom interferometry’. *Optics Express* (2022), vol. 30(3): p. 3358 (cit. on p. 93).
- [Jia22] B. N. JIANG: ‘Low noise phase-locked laser system for atom interferometry’. *Applied Physics B: Lasers and Optics* (2022), vol. 128(4): p. 71 (cit. on p. 93).
- [Mac21] C. D. MACRAE, K. BONGS, and M. HOLYNSKI: ‘Optical frequency generation using fiber Bragg grating filters for applications in portable quantum sensing’. *Optics Letters* (2021), vol. 46(6): p. 1257 (cit. on p. 93).

- [Ram20] C. RAMMELOO, L. ZHU, Y.-H. LIEN, K. BONGS, and M. HOLYNSKI: ‘Performance of an optical single-sideband laser system for atom interferometry’. *Journal of the Optical Society of America B* (2020), vol. 37(5): p. 1485 (cit. on pp. 93, 102).
- [Ham14] HAMAMATSU PHOTONICS: *Technical note / Si Photodiodes*. Tech. rep. February. 2014: pp. 1–4 (cit. on p. 94).
- [Wan22] G. WANG, M. YANG, E. WANG, X. ZHANG, A. JIA, L. ZHU, S. YAN, and J. YANG: ‘In situ probing and stabilizing the power ratio of electro-optic-modulated laser pairs based on VIPA etalon for quantum sensing’. *Optics Letters* (2022), vol. 47(12): p. 2983 (cit. on p. 94).
- [Rei99] J. REICHEL, W. HÄNSEL, and T. W. HÄNSCH: ‘Atomic micromanipulation with magnetic surface traps’. *Physical Review Letters* (1999), vol. 83(17): pp. 3398–3401 (cit. on p. 95).
- [Ris18] I. RISCHKOPF: ‘Phasenstabilisierung zweier schmalbandiger faserbasierter Laser für die Präzisionsmetrologie’. Bachelor thesis. Leibniz Universität Hannover, 2018 (cit. on p. 97).
- [Zho15] L. ZHOU, S. LONG, B. TANG, X. CHEN, F. GAO, W. PENG, W. DUAN, J. ZHONG, Z. XIONG, J. WANG, Y. ZHANG, and M. ZHAN: ‘Test of Equivalence Principle at 10^{-8} Level by a Dual-Species Double-Diffraction Raman Atom Interferometer’. *Physical Review Letters* (2015), vol. 115(1): p. 013004 (cit. on p. 97).
- [Ste01] D. A. STECK: *Rubidium 87 D Line Data*. Tech. rep. University of Oregon, 2001 (cit. on p. 97).
- [Abe23] S. ABEND, B. ALLARD, A. S. ARNOLD, T. BAN, L. BARRY, B. BATTELIER, A. BAWAMIA, Q. BEAUFILS, S. BERNON, A. BERTOLDI, A. BONNIN, P. BOUYER, A. BRESSON, O. S. BURROW, B. CANUEL, B. DESRUELLE, I. DROUGKAKIS, R. FORSBERG, N. GAALLOU, A. GAUGUET, M. GERSEMANN, et al.: ‘Technology roadmap for Cold-Atoms based Quantum Inertial Sensor in Space’. *AVS Quantum Sci.* (2023), vol. 5(1): p. 019201 (cit. on p. 106).
- [Nar22] F. A. NARDUCCI, A. T. BLACK, and J. H. T. BURKE: ‘Advances toward fieldable atom interferometers’. *Advances in Physics: X* (2022), vol. 7(1): p. 1946426 (cit. on p. 106).
- [Boc17] M. BOCHKATI, S. SCHON, D. SCHLIPPERT, C. SCHUBERT, and E. M. RASEL: ‘Could cold atom interferometry sensors be the future inertial sensors? - First simulation results’. *2017 DGON Inertial Sensors and Systems (ISS)*. 2017: pp. 1–20 (cit. on p. 106).
- [Bla20] A. T. BLACK, J. KWOLEK, C. FANCHER, and M. BASHKANSKY: ‘Decoherence and dynamics in continuous 3D-cooled atom interferometry’. (2020), vol. 1129607(February 2020): p. 20 (cit. on p. 106).
- [Rak14] A. V. RAKHOLIA, H. J. MCGUINNESS, and G. W. BIEDERMANN: ‘Dual-axis high-data-rate atom interferometer via cold ensemble exchange’. *Physical Review Applied* (2014), vol. 2(5): p. 054012 (cit. on p. 107).

- [Le 08] J. LE GOUËT, T. E. MEHLSTÄUBLER, J. KIM, S. MERLET, A. CLAIRON, A. LANDRAGIN, and F. P. dos SANTOS: ‘Limits to the sensitivity of a low noise compact atomic gravimeter’. *Applied Physics B: Lasers and Optics* (2008), vol. 92(2): pp. 133–144 (cit. on p. 107).
- [Lau14] J. LAUTIER, L. VOLODIMER, T. HARDIN, S. MERLET, M. LOURS, F. PEREIRA DOS SANTOS, and A. LANDRAGIN: ‘Hybridizing matter-wave and classical accelerometers’. *Applied Physics Letters* (2014), vol. 105(14): p. 144102 (cit. on p. 107).
- [Bar16] B. BARRETT, L. ANTONI-MICOLLIER, L. CHICHET, B. BATTELIER, T. LÉVÈQUE, A. LANDRAGIN, and P. BOUYER: ‘Dual matter-wave inertial sensors in weightlessness’. *Nature Communications* (2016), vol. 7: p. 13786 (cit. on p. 107).
- [Ten21] B. TENNSTEDT, N. WEDDIG, and S. SCHÖN: ‘Improved Inertial Navigation With Cold Atom Interferometry’. *Gyroscopy and Navigation* (2021), vol. 12(4): pp. 294–307 (cit. on p. 107).
- [Tem22] S. TEMPLIER, P. CHEINEY, Q. d’Armagnac de CASTANET, B. GOURAUD, H. PORTE, F. NAPOLITANO, P. BOUYER, B. BATTELIER, and B. BARRETT: ‘Tracking the Vector Acceleration with a Hybrid Quantum Accelerometer Triad’. *Science Advances* (2022), vol. 8(45): eadd3854 (cit. on pp. 107, 108).
- [Guz14] F. GUZMÁN CERVANTES, L. KUMANCHIK, J. PRATT, and J. M. TAYLOR: ‘High sensitivity optomechanical reference accelerometer over 10 kHz’. *Applied Physics Letters* (2014), vol. 104(22): p. 221111 (cit. on pp. 107, 111).
- [Hin20] A. HINES, L. L. RICHARDSON, H. WISNIEWSKI, and F. GUZMÁN CERVANTES: ‘Optomechanical inertial sensors’. *Applied Optics* (2020), vol. 59(22): G167 (cit. on pp. 107, 111).
- [Ric20] L. L. RICHARDSON, A. RAJAGOPALAN, H. ALBERS, C. MEINERS, D. NATH, C. SCHUBERT, D. TELL, É. WODEY, S. ABEND, M. GERSEMANN, W. ERTMER, E. M. RASEL, D. SCHLIPPERT, M. MEHMET, L. KUMANCHIK, L. COLMENERO, R. SPANNAGEL, C. BRAXMAIER, and F. GUZMÁN: ‘Optomechanical resonator-enhanced atom interferometry’. *Communications Physics* (2020), vol. 3(1): p. 208 (cit. on pp. 107, 111).
- [Lan12] S. Y. LAN, P. C. KUAN, B. V. ESTEY, P. HASLINGER, and H. MÜLLER: ‘Influence of the coriolis force in atom interferometry’. *Physical Review Letters* (2012), vol. 108(9): p. 090402 (cit. on p. 108).
- [Coo21] N. COOPER, L. A. COLES, S. EVERTON, I. MASKERY, R. P. CAMPION, S. MADKHALY, C. MORLEY, J. O’SHEA, W. EVANS, R. SAINT, P. KRÜGER, F. ORUČEVIĆ, C. TUCK, R. D. WILDMAN, T. M. FROMHOLD, and L. HACKERMÜLLER: ‘Additively manufactured ultra-high vacuum chamber for portable quantum technologies’. *Additive Manufacturing* (Apr. 2021), vol. 40 (cit. on p. 110).
- [Bid18] Y. BIDEL, N. ZAHZAM, C. BLANCHARD, A. BONNIN, M. CADORET, A. BRESSON, D. ROUXEL, and M. F. LEQUENTREC-LALANCETTE: ‘Absolute marine gravimetry with matter-wave interferometry’. *Nature Communications* (2018), vol. 9(1): p. 627 (cit. on p. 110).

- [Chr19] M. CHRIST, A. KASSNER, R. SMOL, A. BAWAMIA, H. HEINE, W. HERR, A. PETERS, M. C. WURZ, E. M. RASEL, A. WICHT, and M. KRUTZIK: ‘Integrated atomic quantum technologies in demanding environments: development and qualification of miniaturized optical setups and integration technologies for UHV and space operation’. *CEAS Space Journal* (2019), vol. 11(4): pp. 561–566 (cit. on p. 111).
- [Kas19] A. KASSNER, M. RECHEL, H. HEINE, W. HERR, M. CHRIST, M. KRUTZIK, E. M. RASEL, and M. C. WURZ: ‘Atom chip technology for use under UHV conditions’. *Smart Systems Integration; 13th International Conference and Exhibition on Integration Issues of Miniaturized Systems*. April. Barcelona: VDE, 2019: pp. 69–75 (cit. on p. 111).
- [Kul18] P. KULIK, G. KASPROWICZ, and M. GASKA: ‘Driver module for quantum computer experiments: Kasli’. *Proc. SPIE 10808, Photonics Applications in Astronomy, Communications, Industry, and High-Energy Physics Experiments 2018*. Ed. by R. S. ROMANIUK and M. LINCZUK. Vol. 1080845. 2018: p. 223 (cit. on p. 112).
- [Kas20] G. KASPROWICZ, P. KULIK, M. GASKA, T. PRZYWOZKI, K. POZNIAK, J. JAROSINSKI, J. W. BRITTON, T. HARTY, C. BALANCE, W. ZHANG, D. NADLINGER, D. SLICHTER, D. ALLCOCK, S. BOURDEAUDUCQ, R. JÖRDENS, and K. POZNIAK: ‘ARTIQ and Sinara: Open software and hardware stacks for quantum physics’. *Quantum 2.0 Conference 2020*. Ed. by M. RAYMER, C. MONROE, and R. HOLZWARH. 2020 (cit. on p. 112).
- [AOS] AOSense: *Gravimeter*. URL: <https://aosense.com/products/atom-optic-sensors/gravimeter/> (visited on 07/16/2023) (cit. on p. 112).
- [Las] M. S. LASERS: *Quantum Gravimeter*. URL: https://m2lasers.com/images/M_Squared_Gravimeter_Handout_Web.pdf (visited on 07/16/2023) (cit. on p. 112).
- [Muq] MUQUANS: *Absolute quantum gravimeter*. URL: https://www.muquans.com/wp-content/uploads/2019/03/muquans_aqg.pdf (visited on 07/16/2023) (cit. on p. 112).

List of Figures

1.1	Vertical or horizontal optical manipulation	3
1.2	Vertical and horizontal optical manipulation	4
2.1	Vacuum chamber setup of the QUANTUS-1 experiment	10
2.2	Space-time diagram of a Mach-Zehnder-type like atom interferometer	14
2.3	Energy-momentum diagrams for single and double Bragg transitions	16
2.4	Energy-momentum diagrams for single and double Raman transitions	19
2.5	Higher order double Raman diffraction	20
2.6	Sensitivity functions for a Mach-Zehnder type atom interferometer	23
2.7	Sequential sensitivity functions	25
2.8	Sensitivity transfer functions	27
3.1	Flow diagram of the atom-chip fountain gravimeter sequence	30
3.2	Setup of the atom-chip fountain gravimeter	31
3.3	Flow diagram of the twin-lattice atom interferometer sequence	33
3.4	Setup of the twin-lattice atom interferometer	34
3.5	Histogram distribution for the twin-lattice interferometer	36
3.6	Atom number fluctuations at the twin-lattice interferometer	37
3.7	Twin lattice coherence time evaluation	38
3.8	Contrast decay of the twin lattice interferometer	39
3.9	Flow diagram of a dual BEC atom interferometer sequence	42
3.10	Setup of the dual BEC atom interferometer	43
3.11	Multi-axis extension of the dual BEC atom interferometer	45
3.12	Multi-axis geometry under the influence of gravity	47
3.13	Histogram distribution for the dual BEC interferometer	50
3.14	Allan deviation for the dual BEC interferometer	51
3.15	Flow diagram of the multi-loop atomic Sagnac interferometer sequence	55
3.16	Setup of the multi-loop atomic Sagnac interferometer	56
3.17	Space time diagram of the multi-loop geometry	57
4.1	Theoretical prediction of a flat-top beam profile after propagation	63
4.2	Half-section through the experimental vacuum chamber of QUANTUS-1	64
4.3	Mechanical assembly of the flat-top beam shaping optics	65
4.4	Comparison of theoretical flat-top profile and measured profile	67
4.5	Flat-top intensity measurement setup	67

4.6	Measured flat-top intensity profile	69
4.7	Contrast loss production for a flat-top profile in a twin-lattice interferometer . .	70
4.8	Flat-top beam phase measurement setup	71
4.9	Flat-top beam phase profiles measured by SHS and Michelson interferometer .	73
4.10	Algorithm for wavefront aberration analysis based on Michelson interference . .	74
4.11	Flat-top beam phase profile	75
4.12	Normalized intensity profile of a diffracted Gaussian beam	77
4.13	Normalized intensity profile of flat-top beams with and without diffraction . . .	78
4.14	Beam splitter capabilities of the flat-top and the Gaussian beam profiles	79
4.15	Comparison of the temporal-spatial stability of Gaussian and flat-top beam . .	80
4.16	Light shift compensation scheme	81
4.17	Optical setup for generating a light shift compensated light field	82
4.18	Comparison of the conversion efficiencies of the frequency doubling cavities . .	84
4.19	Performance of an interference filter for the superposition of light fields	86
4.20	Rubidium D ₂ level schemes	88
4.21	Schematic setup of a fiber based laser system	89
4.22	Setup of a spectroscopy unit for an absolute reference frequency	90
4.23	Generation steps of Raman frequencies based on electro-optical modulation . .	92
4.24	Optical sideband suppression for the Raman light field	94
4.25	Phase noise density of the Raman light field	96
4.26	Compensation of the differential AC-Stark shift for Raman	98
4.27	Examples of atomic density distributions after double Raman diffraction	100
4.28	Rabi oscillations for Raman double diffraction	101
4.29	Atomic density distribution after third order Raman double diffraction	101
6.1	Flow diagram of the operating principle of hybrid inertial navigation	108
6.2	Sensor head of the gyro-stabilized quantum navigation sensor	109
6.3	KVANTUM laser system	111

List of Tables

3.1	Parameters of the dual BEC interferometer	49
3.2	Sensitivity limit estimations for the dual BEC interferometer	53
3.3	Comparison of the advanced interferometry schemes	59
4.1	Specified surface quality of commercially available optical components	76
4.2	Integrated phase noise densities of the electronic components for Raman	97
5.1	Sensitivity limit estimations	105

Abbreviations and acronyms

AOM	- Acousto-optical modulator
ARTIQ	- Advanced real-time infrastructure for quantum physics
ARP	- Adiabatic rapid passage
BEC	- Bose-Einstein condensate
DDS	- Direct digital synthesizer
DKC	- Delta-kick collimation
dPD	- differential Photodiode
ECL	- External cavity single-frequency laser
EFL	- Effective focal length
EOM	- Electro-optic modulator
FBG	- Fiber Bragg grating
FD	- Fermi-Dirac (function)
FPGA	- Field-programmable gate array
FSR	- Free spectral range
FWHM	- Full width at half maximum
GNSS	- Global navigation satellite systems
GPS	- Global positioning system
HV	- High-vacuum
HOT	- Hannoversches Zentrum für optische Technologien
IBS	- Ion beam sputtering
IGP	- Ion Getter pump
IMU	- Inertial measurement unit
KDE	- Kernel density estimation
$\lambda/2$	- Half wave plate
$\lambda/4$	- Quarter wave plate
MEMS	- Micro-electro-mechanical systems
MOT	- Magneto-optical trap
MZI	- Mach-Zehnder type interferometer
NEG	- Non-evaporable getter
PBS	- Polarizing beam splitter
PCA	- Principal component analysis
PD	- Photodiode
PI	- Proportional-integral controller
PPLN	- Periodically poled lithium niobate
PSD	- Power spectral density
PV	- Peak-to-valley
QUANTUS	- Quantengase unter Schwerelosigkeit
RF	- Radio frequency
RMS	- Root-mean-square
RPC	- Remote procedure call
SFG	- Sum frequency generation
SHG	- Second harmonic generation
SHS	- Shack-Hartmann sensor
SQL	- Standard quantum limit
UHV	- Ultra-high vacuum
ZARM	- Zentrum für angewandte Raumfahrttechnik

Open Access

Some materials used or adapted in this work are from publications licensed under a Creative Commons Attribution 4.0 International License, which permits use, sharing, adaptation, distribution and reproduction in any medium or format. Appropriate credit was given to the original author(s) and the source, and changes were indicated. A link to the Creative Commons Attribution 4.0 International License is provided below. To view a copy of this license, visit <http://creativecommons.org/licenses/by/4.0/>.

Publications

Peer-reviewed

1. S. ABEND, M. GEBBE, **M. Gersemann**, H. AHLERS, H. MÜNTINGA, E. GIESE, N. GAALOUL, C. SCHUBERT, C. LÄMMERZAHL, W. ERTMER, W. P. SCHLEICH, and E. M. RASEL: ‘Atom-chip fountain gravimeter’. *Physical Review Letters* (2016), vol. 117(20): p. 203003.
2. **M. Gersemann**, M. GEBBE, S. ABEND, C. SCHUBERT, and E. M. RASEL: ‘Differential interferometry using a Bose-Einstein condensate’. *European Physical Journal D* (2020), vol. 74(10): p. 203.
3. L. L. RICHARDSON, A. RAJAGOPALAN, H. ALBERS, C. MEINERS, D. NATH, C. SCHUBERT, D. TELL, É. WODEY, S. ABEND, **M. Gersemann**, W. ERTMER, E. M. RASEL, D. SCHLIPPERT, M. MEHMET, L. KUMANCHIK, L. COLMENERO, R. SPAN-NAGEL, C. BRAXMAIER, and F. GUZMÁN: ‘Optomechanical resonator-enhanced atom interferometry’. *Communications Physics* (2020), vol. 3(1): p. 208.
4. F. ANDERS, A. IDEL, P. FELDMANN, D. BONDARENKO, S. LORIANI, K. LANGE, J. PEISE, **M. Gersemann**, B. MEYER-HOPPE, S. ABEND, N. GAALOUL, C. SCHUBERT, D. SCHLIPPERT, L. SANTOS, E. M. RASEL, and C. KLEMP: ‘Momentum Entanglement for Atom Interferometry’. *Physical Review Letters* (2021), vol. 127(14): p. 140402.
5. M. GEBBE, J.-N. SIEMSS, **M. Gersemann**, H. MÜNTINGA, S. HERRMANN, C. LÄMMERZAHL, H. AHLERS, N. GAALOUL, C. SCHUBERT, K. HAMMERER, S. ABEND, and E. M. RASEL: ‘Twin-lattice atom interferometry’. *Nature Communications* (2021), vol. 12(1): p. 2544.
6. S. KANTHAK, M. GEBBE, **M. Gersemann**, S. ABEND, E. M. RASEL, and M. KRUTZIK: ‘Time-domain optics for atomic quantum matter’. *New Journal of Physics* (2021), vol. 23(9): p. 093002.
7. C. SCHUBERT, S. ABEND, **M. Gersemann**, M. GEBBE, D. SCHLIPPERT, P. BERG, and E. M. RASEL: ‘Multi-loop atomic Sagnac interferometry’. *Scientific Reports* (2021), vol. 11(1): p. 16121.
8. S. ABEND, B. ALLARD, A. S. ARNOLD, T. BAN, L. BARRY, B. BATTELIER, A. BAWAMIA, Q. BEAUFILS, S. BERNON, A. BERTOLDI, A. BONNIN, P. BOUYER, A. BRESSON, O. S. BURROW, B. CANUEL, B. DESRUELLE, I. DROUGKAKIS, R. FORSBERG, N. GAALOUL, A. GAUGUET, **M. Gersemann**, et al.: ‘Technology roadmap for Cold-Atoms based Quantum Inertial Sensor in Space’. *AVS Quantum Sci.* (2023), vol. 5(1): p. 019201.

Proceedings

1. S. ABEND, **M. Gersemann**, H. AHLERS, M. SAHELGOZIN, J. MATTHIAS, N. GROVE, H. HEINE, N. GAALOUL, W. HERR, C. SCHUBERT, W. ERTMER, E. M. RASEL, M. GEBBE, H. MÜNTINGA, C. LÄMMERZAHL, L. TIMMEN, and J. MÜLLER: ‘Atom-chip-based quantum gravimetry with BECs’. *Proceedings of the International School of Physics "Enrico Fermi" on Foundations of Quantum Theory*. Ed. by E. M. RASEL, W. P. SCHLEICH, and S. WÖLK. Vol. 197. 2019: pp. 393–397.
2. S. ABEND, **M. Gersemann**, C. SCHUBERT, D. SCHLIPPERT, E. M. RASEL, M. ZIMMERMANN, M. A. EFREMOV, A. ROURA, F. A. NARDUCCI, and W. P. SCHLEICH: ‘Atom interferometry and its applications’. *Proceedings of the International School of Physics "Enrico Fermi" on Foundations of Quantum Theory*. Ed. by E. M. RASEL, W. P. SCHLEICH, and S. WÖLK. Vol. 197. 2019: pp. 345–392.

Curriculum Vitae

Name Matthias Gersemann

Bildungsweg

- 08/2002–06/2009 Allgemeine Hochschulreife, Gymnasium Burgdorf
- 07/2009–03/2010 Zivildienst, Institut für klinische Biochemie der Medizinischen Hochschule Hannover
- 04/2010–07/2010 freier Mitarbeiter, Institut für klinische Biochemie der Medizinischen Hochschule Hannover
- 10/2010–09/2013 Bachelor of Science, Physik, Leibniz Universität Hannover
- 10/2013–02/2016 Master of Science, Physik, Leibniz Universität Hannover
- 03/2016–10/2023 Promotionsstudium, Physik, Leibniz Universität Hannover

Acknowledgments

An dieser Stelle ist es an der Zeit, all den Menschen zu danken, die mich während der Zeit meiner Promotion unterstützt und begleitet haben.

Beginnen möchte ich mit **Ernst Rasel**, der mich stets gefördert und mir die Möglichkeit gegeben hat, in seiner Arbeitsgruppe ohne Wenn und Aber zu forschen. Nur dadurch konnten die in dieser Arbeit vorgestellten Ergebnisse überhaupt erst erzielt werden. Ebenfalls seit dem Beginn meiner Zeit am Institut für Quantenoptik hat mich **Sven Abend** begleitet, von dem ich unglaublich viel lernen durfte. Dafür bin ich sehr dankbar.

Erwähnen möchte ich auch das langjährige Forschungsvorhaben QUANTUS, das viele Universitäten kooperativ miteinander verbindet. Eine große Herausforderung, deren Anstrengung sich meines Erachtens absolut lohnt. Für mich persönlich bedeutet dies eine enge Verbindung zu dem Experiment QUANTUS-1, aber natürlich umso mehr auch zu den großartigen Kollegen. Aus Bremen sind dies **Ekim Hanmeli**, **Sven Herrmann** und **Hauke Müntinga**, die seit vielen Jahren die Forschung mit der Infrastruktur am Fallturm überhaupt erst möglich machen. Zusammen mit **Martina Gebbe** durfte ich zu Beginn an zahlreichen, gemeinsamen Tagen im Labor das Experiment mit all seinen Eigenheiten kennen lernen. Aus Berlin soll hier noch **Simon Kanthak** erwähnt sein, der mich mit seinem unermüdlichen Anreisen aus dem 'fernen Berlin' und Schaffungswillen immer wieder beeindruckt. Mit **Mikhail Cheredinov** haben wir jemanden aus Hannover im Team, der ebenfalls begeistert die Forschung vorantreibt und bereit ist, neue Rekorde zu erzielen.

Aber wo wären unsere Experimente ohne die theoretischen Arbeiten?! Ich möchte daher insbesondere **Enno Giese**, **Alexander Friedrich**, **Naceur Gaaloul** und **Klemens Hammerer** für die unermüdliche Auseinandersetzung mit uns Experimentatoren und die vielen hervorragenden Diskussionen danken. Außerdem auch **Jan-Niclas Kirsten-Siemß** im Speziellen für die ausdauernden Debatten über die Flugbahnsimulationen.

Am Institut für Quantenoptik habe ich viele Freunde und Kollegen gefunden, bei denen ich mich für die gute Zusammenarbeit, tolle Gemeinschaft und immer freundliche Atmosphäre bedanken möchte. Dies sind **Hendrik** und **Nina Heine**, die ich schon während des Studiums kennen und schätzen lernen durfte, **Dorthe Leopoldt**, **Étienne Wodey**, **Maik Lachmann**, **Dorothee Tell**, **Jonas Böhm**, **Alexandros Papakonstantinou**, **Wolfgang Bartosch**, **Jonas Matthias**, **Henning Albers**, **Klaus Zipfel**, **Holger Ahlers**, **Thijs Wendrich**, **Baptist Piest**, **Sebastian Bode**, **Waldemar Herr**, **Dennis Schlippert** und **Christian Schubert**.

Aber auch die noch nicht genannten Personen des QGyro-Teams möchte ich hier explizit erwähnen: **Mouine Abidi**, **Philipp Barbey**, **Ashwin Rajagopalan**, **Ann Sabu** und **Yueyang Zou**.

Mein Dank gilt auch der Feinmechanikerwerkstatt, in Person **Jonas Peter** und **Alexander Vocino**, die eine Unmenge von Bauteilen gefertigt haben, egal wie gewagt meine Entwürfe waren oder wie ehrgeizig die Spezifikationen auch gewesen sein mögen.

In der Elektronik Werkstatt von **Kai-Martin Knaak** konnte ich aus einem schier unendlichen Pool von Wissen schöpfen und habe dort einen Großteil meines Elektronikwissens erworben.

Auch den Sekretariaten des Instituts und der QUEST-LFS gebührt mein Dank, oft wird unterschätzt wie wichtig die dort geleistete Arbeit für uns alle doch ist.

Am Ende möchte ich noch meinen Eltern **Christiane** und **Joachim** danken, die mein gesamtes Leben stets für mich da waren und auf die ich mich immer verlassen kann.

Nicht zuletzt geht mein Dank auch an meine gesamte Familie, insbesondere **Sabine** für ihre bedingungslose, liebevolle und stets bestärkende Unterstützung.